

Modelling of Alkali-Silica Reaction under Multi-Axial Load

THÈSE N° 5982 (2013)

PRÉSENTÉE LE 28 OCTOBRE 2013

À LA FACULTÉ DES SCIENCES ET TECHNIQUES DE L'INGÉNIEUR
LABORATOIRE DES MATÉRIAUX DE CONSTRUCTION
PROGRAMME DOCTORAL EN GÉNIE CIVIL ET ENVIRONNEMENT

ÉCOLE POLYTECHNIQUE FÉDÉRALE DE LAUSANNE

POUR L'OBTENTION DU GRADE DE DOCTEUR ÈS SCIENCES

PAR

Alain Benjamin GIORLA

acceptée sur proposition du jury:

Prof. K. Beyer, présidente du jury
Prof. K. Scrivener, Dr C. Dunant, directeurs de thèse
Dr B. Bary, rapporteur
Prof. J.-F. Molinari, rapporteur
Dr S. Multon, rapporteur



ÉCOLE POLYTECHNIQUE
FÉDÉRALE DE LAUSANNE

Suisse
2013

The only reason for time is so that
everything doesn't happen at once
— Albert Einstein

To my parents.

Acknowledgements

I would like to express my gratitude to the Swiss Federal Office for Energy (OFEN) and Suisse-lectric Research for their financial support during this thesis.

I would like to thank my supervisor Karen Scrivener for letting me explore in details the numerical methods for visco-elasticity, even if that was not the primary aim of this work. I am grateful for her comments and her support during the course of this Ph.D.

I would like to thank my co-supervisor Cyrille Dunant for his input on the numerical methods and most notably the damage algorithm, and for the hours spent proof-reading this thesis, making comments and remarks that helped me improve the content and presentation of this manuscript.

I would like to thank Amor Guidoum and Philippe Vulliemin for their support through the thesis and their major contribution to the experimental part of this work. Building the tri-axial cells would not have been possible without their skill and knowledge. I would also like to thank the technical staff of the LMC, notably Lionel Sofia-Gabrion for his helpfulness and cheerfulness.

I would like to thank Daniele Inaudi from SMARTEC and Giovanni Centorbi from DIAMOND for their help and advice on the technical design of the fibre-optic sensors.

Finally I would like to thank all post-docs, Ph.D. candidates, master students, or visitors I met during this thesis, and who enlightened the work at LMC with a good dose of barbecues, beer, coffee, and good humour.

Lausanne, 26 August 2013

Alain Giorla

Abstract

Alkali-Silica Reaction (ASR) is a deleterious expansion phenomenon which affects the long-term behaviour of concrete. Its origin is a chemical reaction between amorphous silica present in the aggregates and alkali ions from the concrete pore solution. The silica gel produced is highly hydrophilic and swells by absorbing surrounding water. The induced pressure causes a macroscopic expansion and internal damage in the material microstructure.

In ASR-affected structures the overall expansion depends notably on the service load of the structure. Previous studies have shown that application of an uni-axial load reduces or eliminates the expansion in the direction of the load, but can increase the expansion in the lateral directions in a non-linear way. The influence of multi-axial stress states have rarely been studied, and experimental data are still needed. In this study, an experimental apparatus based on tri-axial cells is developed for the study of ASR-reactive concrete under multi-axial loads. The lateral and vertical deformations are measured in-situ with fibre-optic sensors cast in the concrete. The setup is designed to withstand the aggressive experimental conditions in terms of temperature, pressure, and alkali concentration for an extended period of time.

Numerical models are required to characterise and understand the different components of the measured strains. An existing microstructural model is extended to account simultaneously for the damage process and the stress relaxation which occurs in the visco-elastic cement paste. A numerical method based on finite elements in space and time was developed and implemented to represent the continuous growth of the ASR products in time. This method is complemented with a novel, thermodynamic compliant, continuum damage algorithm which can be applied concurrently with the viscous relaxation of the material

This model is applied to the analysis of the stress distribution in the microstructure of ASR-affected concrete. It is shown that both the internal damage and the stress relaxation must be accounted for in order to model the influence of applied stress on ASR. The model allows a reinterpretation of the accelerated tests commonly used in ASR testing and should allow these test results to be better related to field performance.

Keywords: Alkali-Silica Reaction, Continuum Damage, Creep, Finite Element Method, Space-Time Methods, Tri-Axial Cells

Résumé

La réaction alcali-granulats (RAG) est un phénomène d'expansion et de dégradation au long terme du béton causé par une réaction chimique entre des phases de silice amorphe contenue dans les granulats et les ions alcalins provenant de la solution de pore du béton. Le gel de silice produit par la réaction est hautement hydrophile et gonfle par absorption des molécules d'eau environnantes. La pression induite se traduit en une expansion à l'échelle macroscopique et un endommagement interne à l'échelle microscopique.

L'expansion d'une structure affectée par la RAG dépend notamment des charges auxquelles elle est soumise. Des études précédentes ont montré que l'application d'une contrainte uni-axiale réduit l'expansion dans la direction de chargement, mais l'augmente dans la direction latérale de manière non-linéaire. L'influence de contraintes multi-axiales reste peu étudié. Dans cette thèse, un montage expérimental inspiré des cellules tri-axiales est développé pour étudier le comportement de béton affecté par la RAG sous contrainte multi-axiales. Les déformations latérales et verticales sont mesurées in-situ avec des capteurs en fibre optique coulés dans le béton. Le setup est dimensionné de manière à résister pour une longue durée aux conditions expérimentales, particulièrement agressives en terme de température, pression et concentration en ions alcalins.

L'analyse des expériences sous contrainte nécessite l'élaboration de modèles numériques à l'échelle de la microstructure. Un modèle existant est complété par un modèle de visco-élasticité pour représenter le couplage entre endommagement et relaxation des contraintes dans la pâte de ciment. Une méthode numérique basée sur les éléments finis espace-temps est développée et implémentée. Cette méthode permet de représenter la croissance continue des produits de RAG avec le temps ainsi que l'irréversibilité thermodynamique du système.

La répartition des contraintes dans une microstructure de béton affectée par la RAG est étudiée grâce à ce modèle. L'endommagement et la visco-élasticité doivent être pris en compte simultanément pour reproduire les effets des contraintes sur l'expansion induite par la RAG. Le modèle permet une réinterprétation des tests accélérés et une meilleure corrélation avec les conditions réelles.

Mots-clés : Réaction Alcali-Granulats, Endommagement, Fluage, Méthode des Éléments Finis, Méthodes Espace-Temps, Cellules Tri-Axiales

Contents

Acknowledgements	v
Abstract	vii
Résumé	ix
Contents	xi
List of Figures	xv
List of Tables	xix
1 Introduction	1
2 ASR under multi-axial load: literature and experimental setup	5
2.1 ASR in structures	5
2.2 State of the art	6
2.2.1 Restrained expansion on mortar	6
2.2.2 Uni-axial imposed stress on concrete	7
2.2.3 Mixed imposed stress and displacements on concrete	10
2.2.4 Multi-axial imposed stress on concrete	12
2.2.5 Summary	13
2.3 Tri-axial experimental setup	15
2.3.1 Measurements	15
2.3.2 Prototype 1	16
2.3.3 Prototype 2	18
2.3.4 Prototype 3	21
2.3.5 Final design	23
2.3.6 Dimensioning the cell	24
2.4 Materials and experimental conditions	27
2.4.1 Materials	28
2.4.2 Boundary conditions	28
3 A review of ASR models	33
3.1 Macrostructural models for ASR	34

Contents

3.1.1	Phenomenological models	34
3.1.2	Poro-mechanical models	37
3.1.3	Reaction rim models	39
3.2	Micro-structural models for ASR	40
3.2.1	Expanding aggregates models	40
3.2.2	Gel pockets models	41
3.2.3	Effect of shape on ASR	44
3.3	Role of creep in ASR	47
4	Numerical modelling of creep	51
4.1	Modified ASR model	51
4.2	Linear visco-elasticity	53
4.2.1	Constitutive relation	53
4.2.2	Equivalence with generalised rheological models	54
4.2.3	Equivalence between the rheological models	56
4.3	Rheological model for cement paste	57
4.3.1	Visco-elastic and damage model for cement paste	58
4.3.2	Identification of the cement paste visco-elastic properties	59
4.3.3	Influence of the microstructure	61
4.4	Numerical techniques for space-time differential equations	63
4.4.1	Statement of the problem	63
4.4.2	Finite Differences	65
4.4.3	Finite Elements	66
4.5	Space-time finite elements formulation for generalised visco-elastic materials	68
4.5.1	Weak form	68
4.5.2	Constitutive relationship	69
4.5.3	Finite Element discretisation	70
4.5.4	Assembly	72
4.5.5	Generalisation to arbitrary linear visco-elastic behaviour	74
4.6	Stability and convergence properties of the method	76
4.6.1	Properties of the elementary matrices	76
4.6.2	Stability	80
4.6.3	Convergence	81
4.7	Representation of moving boundaries	85
4.7.1	Space-time conforming mesh	85
4.7.2	Extended finite elements in space and time	90
4.7.3	Conclusion	92
5	Continuum damage in space-time finite elements	95
5.1	Modelling degradation of quasi-brittle materials	95
5.1.1	Discrete crack	95
5.1.2	Continuum damage	96
5.2	Numerical methods for continuum damage mechanics	97

5.2.1	Numerical non-linear solvers	97
5.2.2	Algorithmically irreversible mechanics	98
5.3	Damage algorithm in space and time	99
5.3.1	Properties of the series of (t_n)	100
5.3.2	Thermodynamics of visco-elasticity and continuum damage	102
5.3.3	Influence of the damage path on the damage pattern	104
5.4	Failure criterion of cement paste	107
5.4.1	Effect of stress	108
5.4.2	Effect of strain rate	109
5.4.3	Identification of the cement paste rupture properties	110
5.5	Visco-elastic properties of damaged heterogeneous materials	114
6	Combined modelling of creep and ASR	121
6.1	Parameters of the model	121
6.1.1	Mechanical parameters	122
6.1.2	Morphological parameters	124
6.2	ASR simulations with a simplified damage approach	125
6.2.1	Simulations without damage	126
6.2.2	Simple damage in the cement paste	128
6.2.3	Simple damage in the aggregates	129
6.3	Combined effect of creep and ASR on simplified microstructure	132
6.3.1	Free expansion	133
6.3.2	Effect of load	134
6.3.3	Effect of creep and damage in the cement paste	137
6.4	Combined effect of creep and ASR on concrete microstructures	139
6.5	Conclusions	146
7	Conclusion	147
	References	149
A	Mechanical design of the tri-axial cells	161
B	Finite Differences scheme for visco-elastic materials	171
	Curriculum Vitae	175

List of Figures

1.1	Separation between the chemical and mechanical aspects of ASR	3
2.1	Crack pattern of ASR-affected cylinders under vertical load	9
2.2	Experimental setup for the study of ASR under uni-axial load	9
2.3	Experimental setup for the study of ASR under uni-axial load with lateral restraint	11
2.4	Comparison of experimental results of ASR expansion under uni-axial load . . .	14
2.5	Fibre-optic strain rosette placed in a mould before casting.	17
2.6	Step-by-step assembly of the prototype 2.	19
2.7	Detail of the intermediate ring used in the prototype 2	20
2.8	Application of the vertical load.	20
2.9	Hydraulic setup for the pressurisation of an alkaline solution	21
2.10	Ball joint placed under the sample to ensure co-axiality with the piston	22
2.11	Buckling failure of a fibre-optic sensor under 5 MPa water pressure	22
2.12	Scheme of the reinforced sensors	23
2.13	Detail of the O-ring groove in the prototype 3	26
2.14	PSD of the reactive and non-reactive aggregates	29
2.15	Final assembly	30
3.1	Expansion modelled as a sigmoidal function of time (arbitrary units).	34
3.2	Reduction of the final expansion with the applied stress as proposed by Leger .	36
3.3	Influence of the location of the gel pockets on the crack pattern obtained with the model of Çopuroglu	41
3.4	Damage pattern obtained with the model of Dunant compared with experimental pattern	43
3.5	Experimental and simulated expansion for different PSD obtained with the model of Dunant	43
3.6	Illustration of the influence of the load on the orientation of the cracks as estimated with the model of Dunant	43
3.7	Experimental and simulated expansion curves under uni-axial stress obtained with the model of Dunant	44
3.8	Influence of the aggregate shape on the anisotropy of free expansion	45
3.9	Influence of the aggregate shape on the damage pattern	46
3.10	Average stress induced by ASR in the cement paste with different reaction kinetics	48

List of Figures

4.1 Boltzmann superposition principle	53
4.2 Rheological models for linear elasticity and linear viscosity.	54
4.3 Common rheological models for linear visco-elasticity	55
4.4 Rheological model for visco-elastic cement paste.	59
4.5 Uni-axial creep simulation for a concrete microstructure.	60
4.6 Microstructure with circular, ellipsoidal, and triangular aggregates.	61
4.7 Simulated creep as a function of aggregate shape	62
4.8 Representation in space and time of the domain and its boundaries.	64
4.9 Representation of space-time finite elements	70
4.10 Experimental and numerical creep function for concrete	82
4.11 Deformation of an homogeneous visco-elastic plate.	83
4.12 Convergence properties for the visco-elastic homogeneous plate.	84
4.13 Two different representations of growing gel pockets	85
4.14 Iso-parametric transformation between reference and transformed elements	86
4.15 Deformation of a shrinking visco-elastic plate.	89
4.16 Convergence properties for the visco-elastic shrinking plate.	90
4.17 Expansion and stress imposed by a XFEM gel pocket	92
5.1 Influence of the time tolerance on the simulated damage pattern	105
5.2 Number of elements damaged at each step of the algorithm	106
5.3 Strain as a function of time for different levels of sustained loads	108
5.4 Stress-strain diagram for concrete when subject to different loading rates	109
5.5 Dimensions for the wedge splitting test	110
5.6 Load-displacement curves for the wedge splitting test	113
5.7 Damage pattern for the wedge splitting test	114
5.8 Stress relaxation at different degrees of stages of the material degradation	115
5.9 Microstructures with increasing artificially-induced damage.	117
5.10 Relation between elastic and visco-elastic damage	118
6.1 Simulated expansion and average stress in the cement paste without damage	127
6.2 Critical degree of reaction in absence of damage	128
6.3 Expansion under uni-axial load with homogeneous damage in the cement paste	129
6.4 Homogeneous damage in the paste under different loads.	130
6.5 Expansion under uni-axial load with homogeneous damage in the aggregates	131
6.6 Homogeneous damage in aggregates of different size	131
6.7 Homogeneous damage in the aggregates under different loads.	133
6.8 Quantity of damage and expansion of a single aggregate with different fracture criterion	135
6.9 Damage pattern in a single aggregate with different failure criteria	136
6.10 Quantity of damage in a single aggregate under uni-axial or bi-axial load	136
6.11 Damage pattern in a single aggregate under 5 MPa uni-axial or 5 MPa bi-axial load	137
6.12 Quantity of damage in a single aggregate with visco-elastic or visco-brittle cement paste	138

6.13 Damage pattern in a single aggregate with visco-elastic or visco-brittle cement paste	138
6.14 Expansion as a function of the damage in a simulated concrete microstructure	142
6.15 Damage pattern induced by ASR and creep in a concrete microstructure	143
6.16 Expansion and damage versus degree of reaction	145
A.1 Top plate	162
A.2 Intermediate plate	163
A.3 Bottom plate	164
A.4 Cell wall	165
A.5 Piston	166
A.6 Support plate	167
A.7 Ball joint support plate	168
A.8 Aluminium base	169
B.1 Properties of the Finite Differences scheme for generalised Maxwell materials .	172

List of Tables

2.1	Experimental conditions of previous studies of ASR under load	13
2.2	list of prototypes used during the study	16
2.3	Design parameters of the final tri-axial cells	24
2.4	Aggregate types used in the present study	28
2.5	Mix design for the reactive and non-reactive concretes	29
2.6	List of loading conditions used in the tri-axial cells	31
4.1	Material properties for the creep simulations	61
4.2	Elastic moduli of the paste as a function of aggregate shape	62
4.3	Material parameters for the Burger's model	82
4.4	Material parameters for the growing inclusion example.	92
5.1	Back-calculations of the failure criterion for the wedge splitting test	112
5.2	Volume fraction in percent of each phase for the creep-damage test.	116
6.1	List of mechanical parameters for the ASR model.	122
6.2	List of loading conditions used in the creep ASR simulations.	126
6.3	Ratio between maximum and minimum strength from different studies	140

1 Introduction

The alkali-silica reaction (ASR) is a concrete durability issue that was described by Stanton in the 1940s [1]. Since then, cases of ASR have been reported in various concrete structures, including bridges, tunnels, and dams. Affected concrete is subject to expansion and an internal degradation, which may affect the long-term serviceability of the structure.

In existing massive structures it is not feasible to stop the reaction itself. The expansion and degradation might be mitigated by repairing the structure. It is then critical from a management perspective to predict when the structure must be repaired and how it will evolve after the repairs. In extreme cases, it might even be necessary to replace the structure rather than to repair it.

The prediction of the service life of ASR-affected structures requires the development of numerical models able to represent accurately the phenomenon. Building these models requires an understanding of the underlying physics and the morphology of the affected material, complemented with parametric studies to assess the influence of the various parameters and feed models with realistic values.

ASR is caused by the reaction between amorphous silica contained in the aggregates and alkali ions from the concrete pore solution. The hydroxide ions break the structure of the silica so that alkali ions can penetrate it and form a gel. This gel is highly hydrophilic and swells by absorbing the surrounding water. The simultaneous presence of amorphous silica, alkali ions, and moisture are necessary for ASR to occur and cause deleterious expansion.

ASR is a complex chemical, physical and mechanical phenomenon. The nature of the gel changes with different alkali ions [2]; the permeability of the concrete affects the transport of water, and therefore the swelling process of the gel [3]; the nature of the aggregates changes the morphology of the mechanical degradation [4]; the orientation of the induced micro-cracks might affect the spatial distribution of the expansion [5].

Previous studies suggest a separation between the chemical processes on the one hand, and the mechanical consequences on the other hand. Ben Haha quantified with image analysis the degree of reaction of ASR-affected mortars and concretes, with different aggregate types and chemical conditions [6, 7]. He found a unique relation between the measured degree of reaction, the expansion, and the amount of aggregates in the system.

This indicates that the relation between degradation and expansion can be studied and modelled independently of the environmental conditions. This is essential since massive structures are subject to various stress conditions which affects the expansion and degradation of the structure.

The effect of applied load on ASR was studied in the successive works of Le Roux [8], Larive [9], Multon [10] and Dunant [11]. They showed that application of a uni-axial load on a reacting specimen reduces the expansion in the direction of the load, and even negates it if the load is high enough. However, the expansion in the lateral direction changes non-linearly as a function of the load and the lateral restraint.

The effect of multi-axial load remains unclear. Multon used steel rings to restraint the expansion in the lateral direction, but this is a passive restraint: the stress in the sample increases with the advancement of the reaction. To characterise the influence of the load on the ASR-induced expansion experiments under constant multi-axial load are still required.

In this thesis, an apparatus based on tri-axial cells has been designed for the analysis of ASR-affected concrete under multi-axial load. The setup allows application of independent vertical and radial loads on concrete cylinders. The expansion is measured in-situ with fibre-optic sensors cast in the concrete. The design of this equipment has taken four years so it has not been possible to generate results for comparison with the models.

The micro-mechanical analysis of these experiments requires the use of numerical models which characterise the degradation in the material microstructure. Indeed, the damage pattern depends on the geometry of the microstructure and the boundary conditions, which indicates that application of multi-axial load will strongly affect the orientation of the micro-cracks by modifying the distribution of the stresses in the microstructure.

The cement paste can also change the stress distribution in the material through creep and stress relaxation. Understanding how creep affects the expansion and degradation is critical for the analysis of structures. ASR spans decades in field conditions, while accelerated tests used in the lab to characterise the reaction typically take months or years, depending on the method. Given the large difference in time scales, it seems that visco-elasticity must play a role in the micro-mechanics of ASR. However, all ASR models in which the microstructure is explicitly represented neglect the time- and history-dependent behaviour of the cement paste.

In this work, the micro-mechanical model of Dunant [12, 11] is extended to account for creep in the cement paste. The model is purely micro-mechanical and aims at characterising the expansion and damage in the microstructure as a function of the amount of gel produced. In this work, we further consider the rate at which the gel is produced as an additional input of the model. The parameters affecting the model are represented schematically in Figure 1.1. In this work, only the mechanical aspect of ASR is considered.

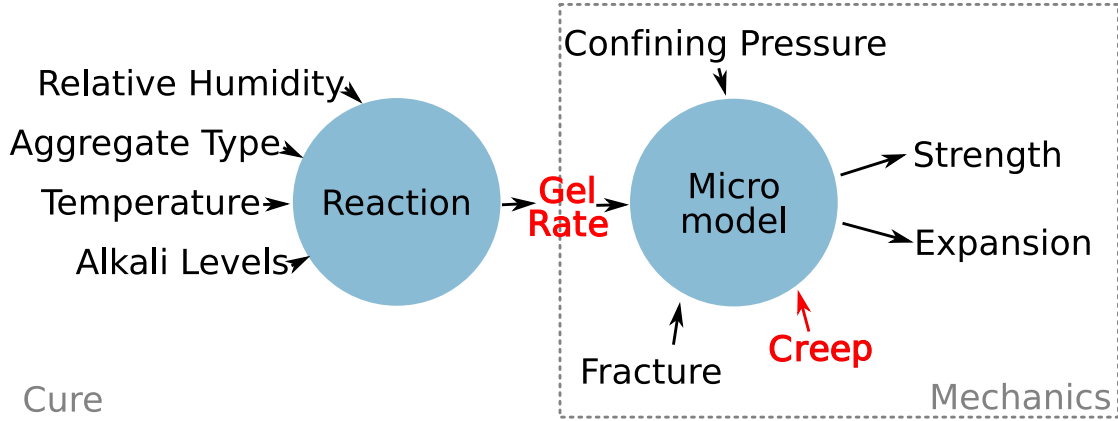


Figure 1.1: Separation between the chemical and mechanical aspects of ASR

The insertion of visco-elasticity in the numerical model necessitates the development of appropriate numerical methods. Indeed, the microstructure of an ASR-affected concrete changes with time, and traditional methods based on finite differences cannot account for a continuous growth of the silica gel.

A novel numerical method for the modelling of creep based on finite elements in space and time is proposed in this work. The method is applicable to any kind of rheological model composed by springs and dashpots placed in parallel or in series. It can represent geometries that change with time either with a conforming space-time mesh or with extended finite elements in space-time.

The method is complemented with a damage algorithm which computes explicitly the instants at which damage grows in the microstructure. This is critical in the case of heterogeneous materials since we show that the damage pattern is highly dependent on the order in which the elements are damaged. With this algorithm, the interaction between creep and damage is accurately accounted for, and the thermodynamic admissibility of the system is ensured at each step of the algorithm.

The visco-elastic model and damage algorithm are combined to study the effect of creep ASR. Two failure criteria are investigated, corresponding to a lower and upper bound of the material behaviour with respect to the strain rate. We show that in both cases creep reduces the damage induced in the microstructure, and therefore the macroscopic expansion. This indicates that purely elastic models might overestimate the material degradation caused by ASR.

Thesis outline

Chapter 1 is this introduction.

Chapter 2 first surveys the existing literature on the influence of applied load on ASR, and then describes the cells designed for the analysis of ASR under multi-axial load.

Chapter 3 reviews ASR models sorted by scope of application and underlying hypotheses.

Chapter 4 focuses on the modelling of creep: the physical aspects of the visco-elasticity of the cement paste are discussed first to propose an appropriate spring-dashpot rheological model; then numerical methods for visco-elastic materials are discussed. The finite element method in space and time is presented in detail, and its ability to represent time-dependent geometries proven with simple examples.

Chapter 5 describes the damage algorithm. The method is demonstrated on simple examples, and the mechanical properties of the cement paste are characterised with the analysis of wedge splitting tests from the literature.

Chapter 6 presents the consequences of including creep in the ASR model, and the need for a complete micro-damage model for the analysis of ASR under load.

Chapter 7 presents the conclusions and perspectives.

2 ASR under multi-axial load: literature and experimental setup

Applied loads are one of the numerous parameters which affects the development of ASR. Taking them into account is particularly important for the practical applicability of the models. Experimental evidence suggests that compressive stress reduces the imposed expansion in the direction of the load, and nullifies it if the load is high enough. The expansion in the other directions is affected in a non-linear way, and mechanical damage seems to increase as well. This effect has been characterised by several studies in uni-axial compression or in uni-axial compression with lateral restraint, but not under constant multi-axial loads. A design for a tri-axial device is therefore proposed to measure the ASR-induced expansion under a wide range of stress states.

2.1 ASR in structures

Concrete in structures is subject to various stress states, distributed in the structure depending on geometry, material properties, restraint, and applied forces. In dams, these forces include the dead weight of the structure, the pressure applied by the reservoir, thermal deformations, creep, and shrinkage. The structure is designed to accommodate for all these loads. However, the design does not account for the extra loads and the material degradation caused by ASR.

Numerical models are necessary for the analysis and prognosis of ASR-affected structures. Their accuracy and predictive abilities depend on how well the model represents the underlying physics. Standard tests for ASR are carried out in the absence of external forces to isolate the ASR phenomenon itself. Translating the results from the laboratory to the field conditions requires understanding how the stress state in the material affects the reaction and its characteristic expansion. This calls for sets of experiments to identify and characterise the influence of the loads on the development of the reaction.

ASR can be described as two simultaneous but uncoupled processes: the production of expansive silica gel, and its mechanical consequences. *A priori*, mechanical stress can affect both of these processes. Indeed, some chemical reactions and dissolution processes are known to be hindered or promoted by external pressure. However, The results from Larive indicate that such phenomena do not occur in ASR, at least in the range of stresses encountered in the field [9]. Still, mechanical loads affect the fracture processes in the material, and therefore the expansion as it is, in ASR, strongly coupled with internal damage.

In general, crack propagation in quasi-brittle materials depends on the type of mechanical boundary conditions. These are classified in two categories: imposed stresses and imposed displacements. These two types of boundary conditions affect fracture propagation at the micro and the macro scale, as they condition the stability of the crack growth. Imposed stresses cover all external and internal loads the structure is subject to. They can be surface stresses like the fluid pressure applied by the reservoir on a dam, or volumic stresses such as the dead weight of the structure. Imposed displacements cover the restraints of the structure by its surrounding environment or its reinforcements.

The study of both type of boundary conditions is therefore critical to understand the behaviour of structures affected by ASR. Experiments carried out in earlier works are reviewed below.

2.2 State of the art

Experimental studies of the influence of mechanical boundary conditions on ASR are quite scarce, notably because of the difficulty of implementing such test in the aggressive conditions which accelerate the reaction and for the extended periods of time typical of such studies (between 1 to 10 years). In the following, the main studies found in the literature are presented by type of boundary conditions and choice of materials.

2.2.1 Restrained expansion on mortar

Larive reported that the first experiments on the influence of restraint on ASR-induced expansion is the study of McGowan in 1955, who studied the expansion of highly-reactive mortars under load [13, 9]. In his study, the low level of the imposed stress (less than 1 MPa) was sufficient to reduce the expansion initially. However, after removal of the load the samples started to expand again.

Hobbs repeated this experiment later on with different aggregates, and showed a non-linear behaviour between the applied load and the expansion [14, 9]. The expansion curves were affected both in term of magnitude and rate of expansion. Furthermore, at the higher load, the measured expansion was higher than the expansion of the unloaded specimens.

Baulande measured the radial pressure imposed by reactive mortar samples which displacements were fully restrained in the axial direction [15, 9]. The application of a lateral confinement pressure reduced significantly the expansion of the samples. However, several questions arise from these tests:

- The experimental setups are not completely described, and information is missing both in terms of how the restraint was applied, and the nature of exposure conditions. These were certainly accelerated considering the short periods of observation (between one and four months), and so it is not obvious how the results from these short-term experiments would scale with time.
- The materials used were mortars with highly reactive opal. These aggregates were used in the early studies on ASR as model aggregates in order to identify the governing mechanisms. Such aggregates are not representative of what is used generally in the field, and it is not clear how slow-reactive aggregates would have behaved in such conditions. Furthermore, the results cannot be easily extrapolated to reactive concrete, because of the change in the aggregate content and particle size distribution.
- Finally, the level of the loads applied were quite small compared to the stress levels (around 3 MPa) induced by the development of ASR under restraint [16, 10].

2.2.2 Uni-axial imposed stress on concrete

Several authors have studied the influence of uni-axial loads on ASR expansion. These experiments are usually more completely described than the previous, and both the materials and the conditions relate more readily to the field conditions.

Study of Le Roux

The first reported experiment has been carried out by Le Roux [8]. He extracted cores from an ASR-affected bridge, and placed them in a vertical creep frame, itself immersed in either water or alkaline solutions. Some samples were stored unloaded in the same hygrometry conditions. The cores all came from the part of the bridge which showed extensive amounts of map cracking, and the reaction was assumed to be homogeneous across all samples.

Le Roux measured a reduction of the expansion in the vertical direction. At 5 MPa axial load, the measured expansion was found to be negligible. Unfortunately, the radial deformations were not measured, and so there is no clear indication about the influence of stress on the volumetric expansion. Furthermore, the analysis of the residual expansion of extracted cores is a complex problem as there is a first stage of the deformation which is controlled by the recovery of the structural load, and which was not investigated in this context.

Study of Larive

Later, Larive did an extended study of ASR under load using reactive and non-reactive concrete samples cast specifically for the tests [9]. The samples were placed under vertical creep frames in a controlled temperature chamber at 38 °C and relative humidity between 96 and 98 %. The axial loads ranged between 5 and 20 MPa, which spans the values of loads observed in the field.

With scanning electron microscopy, Larive found silica gel products in all samples, and their apparition was not affected qualitatively by the load. The weight of the samples were monitored as well during the reaction: the weight gain in most samples followed a similar trend, except in a few random cases which were discarded in the analysis. This indicates that the samples were absorbing water at a similar rate, and were therefore reacting similarly in terms of the dissolution-precipitation process of gel formation.

The expansion was measured with external extensometers, and the measure showed large uncertainties, as the in the unloaded specimens the final expansion reached values ranging between 0.5 and 1.5 mm/m. The vertical expansion was decreased in all loaded specimens, and was negligible at the highest load levels. The lateral expansion showed a different trend: it was found to be higher for loads of 5 and 10 MPa. However, the lateral expansion under 20 MPa was approximately the same as the unloaded specimen. In all cases, the lateral expansion differed both in terms of magnitude and in terms of rate.

The volumetric expansion varied non-linearly with the applied load. However, the authors suggested that up to 10 MPa, the volumetric expansion could be considered independent of the load, even though differences up to 30% were reported between the loaded and unloaded specimens.

Some samples were unloaded at different points of the reaction. In all cases these samples showed first a constant residual deformation, and then followed the expansion curve of the unloaded specimens when they reached and exceeded the initial residual deformation. This, coupled with the weight measurements and the microscopy observations, indicates that at these load, the chemical reaction is not significantly affected by the mechanical boundary conditions.

Mechanical tests on the loaded samples have been mentioned in the study, but no result is shown, except that at 20 MPa the Young's modulus of the samples was reduced by half after one year of reaction.

A surface crack pattern was observed in all the cases. For unloaded specimen, the samples showed a map cracking typical for well-developed ASR. Applying load had two effects: more cracks appear as the load increases, and the cracks are oriented in the direction of the load (see Figure 2.1). This can be understood as further evidence that the influence of the load on the vertical and lateral expansions is essentially mechanical.

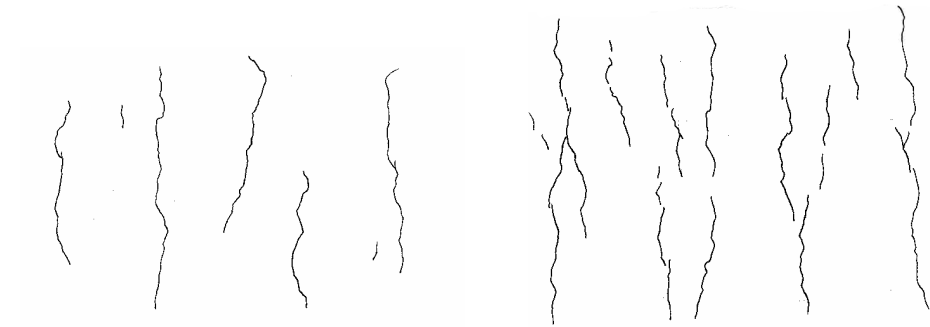


Figure 2.1: Crack pattern of ASR-affected cylinders under 5 MPa (left) and 10 MPa (right) vertical load [9].

Study of Dunant

A third study of the influence of uni-axial stress on ASR is found in the work of Dunant [12, 17]. In this study, the samples were directly immersed in an alkaline solution chosen to approximate the composition of the cement pore solution, and so minimise leaching compared to immersion in pure or tap water or even controlled relative humidity conditions. Loads ranged between 5 and 15 MPa. The mechanical setup is shown in Figure 2.2.



Figure 2.2: Experimental setup for study of ASR under uni-axial load and immersion in alkaline solution from [12].

The vertical and radial deformations of the samples were measured with embedded fibre-optic strain sensors placed outside the 45° perturbation cone near the flat surfaces of the cylinders, and adapted from the work of Inaudi [18]. The vertical sensors contained two fibres, one restrained for the measure of the expansion, and one free for the measure of the temperature. Using the knowledge of the expansion coefficient of the concrete the strains measured were corrected for the small temperature variations.

As in the previous studies, the vertical expansion is decreased as the load increases, and vanishes for loads higher than or equal to 10 MPa. However, the lateral expansion showed a different behaviour as that measured by Larive. The lateral expansion was in all cases lower than for unloaded specimen, and the lowest lateral expansion was found for the lowest load. Both the amount of expansion and its rate were modified, and it was found that the rate of lateral expansion is accelerated with increasing load. The volumetric expansion followed a similar trend to the lateral expansion as the vertical expansion vanishes in most loaded cases.

Dunant attributed the change in the expansion process to a change in the micromechanical degradation and used micro-mechanical modelling to evaluate that effect. Simulations for low level of loads showed indeed a reduction in the volumetric expansion [17]. However, no mechanical testing or microscopy analysis was done to characterise the internal damage of the samples and validate or invalidate this hypothesis.

2.2.3 Mixed imposed stress and displacements on concrete

Study of Berra

In his paper, Berra studied the influence of uni-axial loads on two different reactive aggregates, and with different alkali contents in the initial mix [19]. The samples were stored at 38 °C in 100% relative humidity. Further, no analysis of the advancement of the chemical reaction was done, and thus it is difficult to establish relations between the experimental results as a function of the alkali content in the mix.

The mechanical setup in this experiment differs from the three previous cases: instead of hydraulic pistons, the stress was imposed by a steel plate placed atop of each sample and maintained in position by pre-stressed bolts. This setup corresponds to a stress relaxation experiment, while the previous are creep experiments. Furthermore, the expansion of the sample deforms the plate in a way which was neither measured or accounted for by the authors, presumably because the plate was supposed thick enough to be considered as perfectly rigid.

As no non-reactive control samples were used, the creep and elastic deformations of the samples were calculated by extrapolation from the Young's moduli measured after 7 and 28 days using the European norm for the design and analysis of concrete structures [20]. This calculation method is empirical and might not give the right approximation for the creep deformation.

For all these reasons, the results from this study are not straightforward to interpret. The expansion in the direction of the load was reduced with increasing pre-stress, but the lateral expansion follows different relations depending on the aggregate type and the chemical conditions. This might be caused by the nature of the aggregates, as Ponce and co-workers showed that slow-reactive and high-reactive aggregates lead to different crack patterns in the microstructure [4, 21].

Study of Multon

Multon studied the development of ASR under both imposed stress in one direction and restrained displacements in the others [10]. The experimental setup is similar to the one used in the study of Larive, except that steel rings are used to provide a passive restraint in the lateral direction. Varying the thickness of the rings varies the degree of restraint of the setup.

Because of the rings, the restrained samples cannot exchange water with the surrounding environment. All samples in this study were sealed to prevent water loss and ensure the homogeneity of the chemical reaction in the different samples.

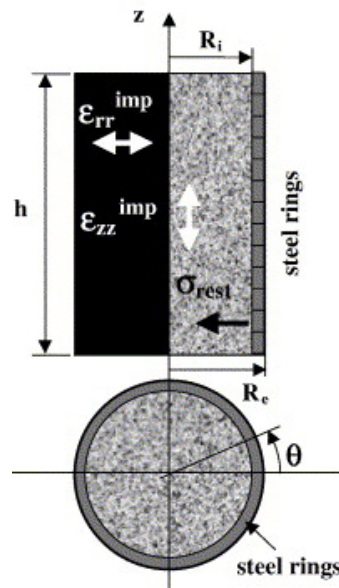


Figure 2.3: Experimental setup of ASR under uni-axial load with lateral restraint. Figure from [10].

The external displacements of the rings were measured with extensometers. Knowing the thickness and stiffness of the steel rings one can calculate the pressure exerted by the ASR-expanding sample on the ring. However, the calculation of the actual strain in the concrete samples can only be achieved under the assumption that the material is purely elastic and that no mechanical degradation occurs. The lateral stress measured was always found to be smaller than the imposed vertical stress, except for the unloaded but restrained specimen.

The anisotropy of the expansion was calculated as a function of the applied load and the degree of restraint. For unloaded specimens this coefficient did not change much because of the low magnitude of the stress imposed by the restrained expansion. For the specimen loaded at 10 MPa, the anisotropy coefficients were similar with and without restraint. Finally, for the specimen loaded at 20 MPa, the axial strain was found significantly higher than in the unrestrained specimen.

The volumetric expansion measured showed a strong non-linear behaviour as well. At constant degree of restraint, the volumetric expansion was the highest for the unloaded specimen, and the smallest for the specimen loaded at 10 MPa. At constant imposed load, the highest expansion was found with the highest degree of restraint, the smallest with the intermediate degree of restraint. Despite the large scatter in the results (from 1.5 to 3.5 mm/m), the authors concluded that the volumetric expansion was constant for every load-restraint combination considered.

The authors further proposed to represent the influence of multi-axial stress on ASR in structural codes with an anisotropic coefficient of expansion which is a non-linear function of the difference between the axial and average stress. The coefficients found in this formulation were fitted on the experimental curves, which makes it difficult to generalise to different concrete mixes.

2.2.4 Multi-axial imposed stress on concrete

The only ASR experiment conducted in multi-axial imposed stress states is found in the work of Gravel [22]. He monitored the strains of an ASR-reactive concrete cube subject to a multi-axial loading sequence. The stress was imposed independently in two directions, while the third was free of restraint. The concrete was placed in contact with a water tank through its unloaded face, providing water for the reaction to take place.

The aim of this experiment was to determine whether applying a load post-ASR would reduce or cancel the rate of expansion. Therefore, the cube was left to expand for two years before the first load was applied. Three load increments separated by 250 days were applied, two in the vertical direction and one in the lateral direction.

Application of a high enough load in one direction indeed stabilised the expansion in that direction. However, after application of a load in the transverse direction the expansion started again.

The analysis of this experiment is difficult as no control sample gave the unloaded ASR expansion or the creep deformations. Furthermore, the weathering conditions were not homogeneous within the sample, and therefore the cube cannot be simply treated as though the reaction occurred homogeneously in its bulk.

2.2.5 Summary

The influence of stress on ASR have been studied in a few mechanical and environmental conditions, as gathered in Table 2.1. These studies have provided valuable information on the phenomenon:

- The influence of the mechanical boundary conditions on ASR can be considered to be essentially mechanical.
- The expansion is reduced in the direction of the highest restraint, whether this restraint is stress- or displacement-controlled. If the restraint is high enough, the expansion disappears in that direction. Mechanical degradation is oriented in that direction.
- The expansion in the less-restrained direction is affected in a non-linear and non-monotonic way.
- The total volumetric expansion decreases with the average imposed stress in a non-linear way, but might increase in some cases. The results from the studies of Larive, Multon and Dunant are gathered in Figure 2.4. In most cases the volumetric expansion decreases with a small level of load, and then increases again. The experimental results show a huge scatter which might have been caused by differences in the curing condition or differences between materials.
- The relation between the applied stress and the macroscopic expansion might be influenced by the aggregate type the same way the mechanical properties are.

Table 2.1: Experimental conditions of previous studies of the influence of load on ASR. In [8, 12, 22] the samples were immersed in alkaline solution.

Reference	Boundary conditions	Geometry	Moisture conditions
Le Roux [8]	uni-axial load	cylinder (cores)	immersion
Larive [9]	uni-axial load	cylinder	relative humidity
Dunant [12]	uni-axial load	cylinder	immersion
Berra [19]	uni-axial restraint	prism	relative humidity
Multon [10]	uni-axial load + lateral restraint	cylinder	sealed
Gravel [22]	bi-axial load	cube	immersion

These phenomena have sometimes be referred as *transfer of expansion*. However, this term suggests that at the microstructure level, the pressure applied locally by the silica gel depends on the macroscopic stress, which seems a rather large simplification. Dunant suggested that this phenomenon is driven by preferred orientation of the microcracks induced by the reaction [12, 17]. Charpin confirmed this hypothesis with the application of micro-mechanical models at the level of a reacting aggregate [23]. In order to validate this hypothesis, a mechanical experiment where ASR-induced expansion and damage can both be measured needs to be undertaken.

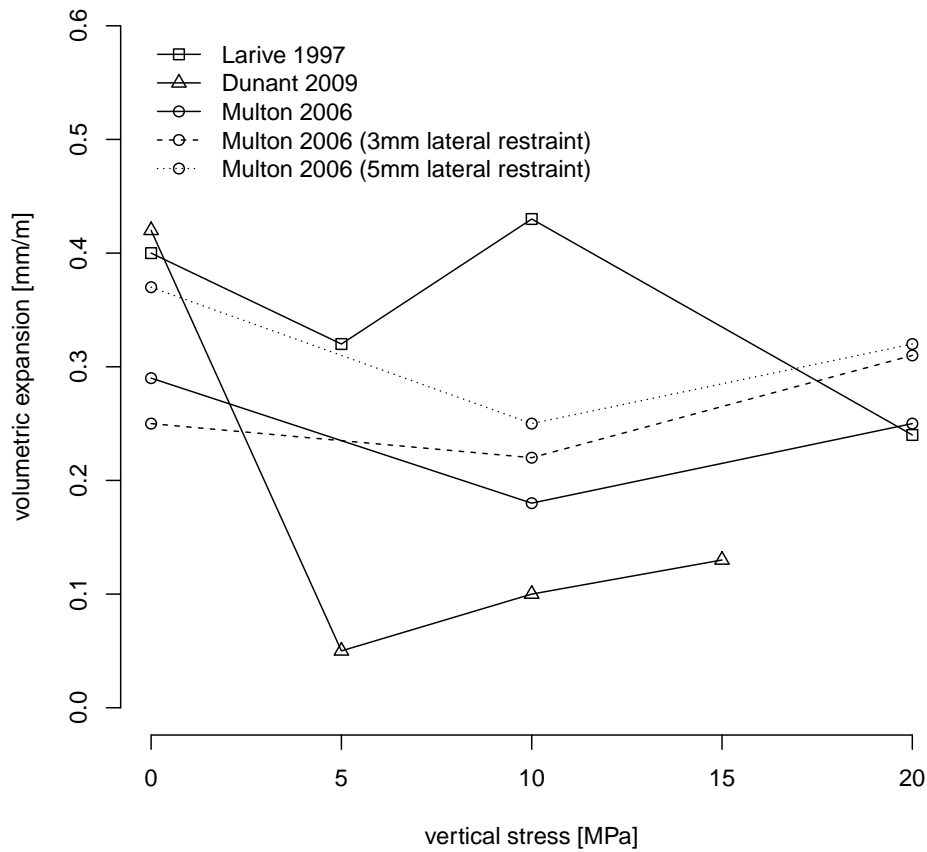


Figure 2.4: Comparison of experimental results of Larive, Multon and Dunant for the volumetric expansion unduced by ASR under uni-axial load, with and without lateral restraint. Data gathered from [9, 12, 10].

2.3 Tri-axial experimental setup

In this section a mechanical device for the analysis of ASR under complex stress states is described. The experimental setup satisfies the following conditions:

- Application of multi-axial mechanical loads. The loads on each axis should be independent.
- Environmental conditions suitable for ASR: increased temperature, high alkali concentration, constant hygrometry and sufficient supply of water.
- Measurements of the deformations and internal damage as a function of time.
- Several samples tested in the same conditions to verify the repeatability of the measure.

In practice, it is easier to apply bi-axial loads on cylinders rather than fully tri-axial loads on cubes. This is achieved by tri-axial cells, which were first introduced to analyse the failure of rock under multi-axial compression [24]. In concrete, they are mainly used to characterise the strength of the material under high confinement (see for example [25, 26, 27]), up to pressures of the order of 2 GPa [28], or the influence of load on permeability [29].

However, most of these tests are short-term experiments, and typically done in sealed condition to keep a constant moisture content. Most cells can hold only one sample, while several samples are required for ASR, including a non-reactive sample to identify the elastic and creep deformations. As these conditions do not meet all criteria stated above, a specific device was designed in this work.




The design phase was composed by three prototypes which allowed the identification of the technical difficulties relative to tri-axial cells, and to propose and test different solutions for the final design. The characteristics of these prototypes are summarised on Table 2.2.

2.3.1 Measurements

Deformations are measured using fibre-optic sensors cast in concrete. These sensors consist of a single fibre-optic held in tension on metallic supports. A Bragg network is engraved on the fibre. An optical mirror is chemically placed at the end of the wire. If a laser signal is sent through the fibre, it will be reflected by the mirror and the wave length of the reflected signal is shifted linearly with the deformation of the Bragg network.

Dunant showed that there is a good agreement between fibre-optic and external measures with extensometers [12]. This indicates that the perturbation caused by the presence of the sensors in the sample can be neglected. During a measurement, no additional perturbation is imposed to the system. Furthermore, these sensors show little uncertainties in the measure, as opposed to external extensometers.

Table 2.2: list of prototypes used during the study

Prototype			
Samples	1 cylinder $\varnothing 110$	2 cylinders $\varnothing 160$	3 cylinders $\varnothing 160$
Pressurised fluid	oil	oil	water

The sensors must be connected to the laser emitter via fibre-optic wires. The length of these wires is not limited, at least for lab applications, as Inaudi and co-workers reported successful measurements with wires as long as several kilometers [30]. However, this imposes finding a way to extract these wires from the cells without compromising the sealing.

2.3.2 Prototype 1

This prototype was a tri-axial cell lent by the Laboratory of Rock Mechanics (LMR) of the EPFL. It can hold a single sample of diameter 110 mm and height 220 mm. Its nominal pressure is 70 MPa, applied by oil. This prototype was used to test different technical solutions to the problems met in the design of the final cells:

Sealing

The wires of the fibre-optic sensors must be extracted from the cell while preserving its sealing. The LMR uses surface strain sensors to monitor their experiments, and extract the electric wires through holes filled with epoxy resin. The same approach was initially tried for the fibre-optic, yet the sealing was broken after a few hours at 15 MPa.

Commercial connectors from SERTO were chosen to make the fibre-optic wires pass through the cell walls. However, oil broke through the coating of the wires which resulted in a leak after one day at 15 MPa.

The fibre-optic wires were therefore protected by a teflon tube reinforced with a steel spring. With such assembly, deformations of a non-reactive concrete sample were measured for five months at 15 MPa without leaks.

Sensors

A fibre-optic rosette was initially used to measure the deformations. This sensor consists of a single fibre-optic wire placed on a triangular support, with one Bragg network engraved on each edge of the triangles (see Figure 2.5). These sensors can measure the strain in the axial and in one radial direction, and are smaller than the sensors previously used in the study of Dunant [12].

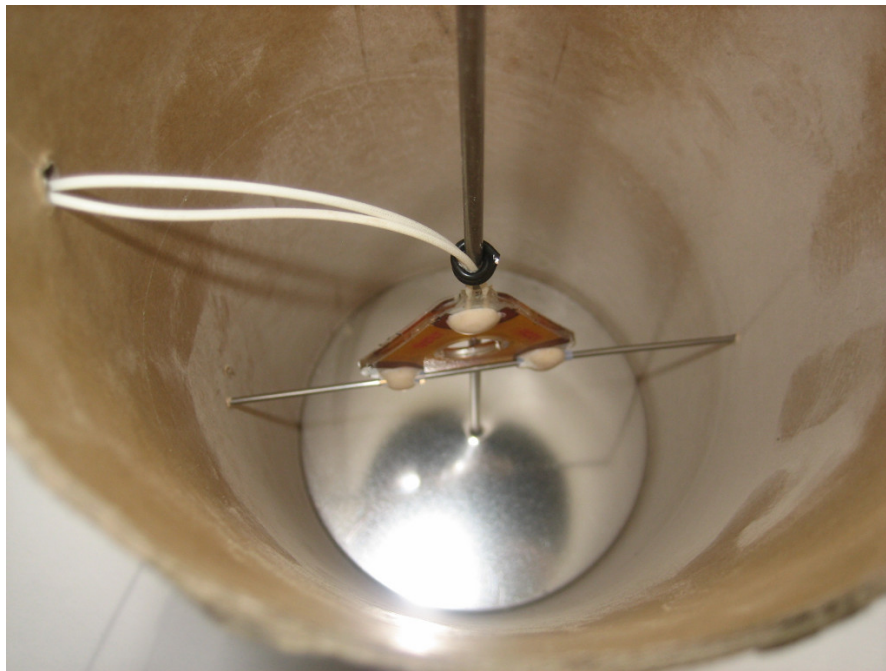


Figure 2.5: Fibre-optic strain rosette placed in a mould before casting.

However, the rosette is quite fragile, and in all tests done with it the signal was lost in one of the sensors during the first day of the test. As the sensors are wired in series, if one fails then all subsequent sensors in the series are lost too.

Therefore the sensors used in [12] are used in this study as well. These sensors consist of a single fibre held in tension between two metallic supports. A Bragg network is carved on the fibre and measures the length change between the two supports. Some sensors contain a second fibre that is not held by the supports. The measure of its deformation gives a measure of the temperature using the known thermal expansion coefficient of the fibre.

Pressurised fluid

This prototype used oil as it was the easiest to manipulate with the equipment available in the lab. Notably, oil pumping devices need not to be corrosion-resistant. The LMR uses rubber membranes to protect their samples from any oil infiltration. However, the long-term permeability of these membranes was unknown, so a concrete sample was exposed to a 15 MPa oil pressure for four months. That sample did not contain any sensor as it was not clear how to make the wires pass through the membrane while maintaining it sealed. The rubber was forced into the air voids at the concrete surface, and traces of oil were found at the surface of the sample and near its edges, indicating that the membrane does not protect samples from oil ingress in the long run.

A further disadvantage is that in ASR, the reaction occurs only if the sample contains enough water. A sealed sample will not react and expand as much as if it were immersed in alkaline solution.

Some tri-axial apparatus are able to provide additional water to the sample through pipes going through the piston. However, doing so does not ensure the homogeneous distribution of water through the sample, and this design solution was therefore rejected.

Therefore, it was chosen to directly apply the lateral pressure with water, without any protecting membrane, even though that might force the pressurised water to penetrate somewhat in the cement porosity.

2.3.3 Prototype 2

This prototype was designed as a realistic model of the final cell. It can hold 2 standard concrete cylinders (diameter 160 mm, length 320 mm), and operates with oil. The designed service pressure is 20 MPa.

Assembly

The guiding idea for this prototype was to build it in layers. The pressure vessel was divided into two parts by a steel ring, so that the assembly could be done easily step-by-step from bottom to top (see Figure 2.6). The passages for the fibre-optic wires were pierced through the intermediate ring, as shown in Figure 2.7. The assembly procedure is:

1. Place the bottom cylinder and the bottom part of the tube
2. Place the intermediate ring (Figure 2.6 left)
3. Make the wires from the bottom cylinder pass through the ring
4. Place the top cylinder

5. Make the wires from the top cylinder pass through the ring
6. Place the top part of the tube and seal the cell (Figure 2.6 right)



Figure 2.6: Step-by-step assembly of the prototype 2.

Even though this design makes the assembly easier, it increases the risk of leakage. Indeed, one of the joints of the ring was extruded after a few hours under a pressure of 10 MPa. This extrusion was caused by a wrong design of the O-ring groove, as the gap between the mechanical pieces was not small enough. To minimise risk of leakage, a third prototype was designed without an intermediate ring, and with a stricter tolerance on the O-ring groove.

Vertical load

The first prototype was small enough to fit under an existing creep frame. The load was transmitted from the piston to the sample by a cylinder which passes through the upper plate of the cell. However, the prototype 2 was too large for the loading frames available in the LMC, and a specific solution was developed.

The threaded shafts maintaining the plates are used as a frame. They are extended by 500 mm and support a third plate to which a piston is attached. The piston transmits the load to the samples the same way as in prototype 1. The assembly is shown in Figure 2.8.

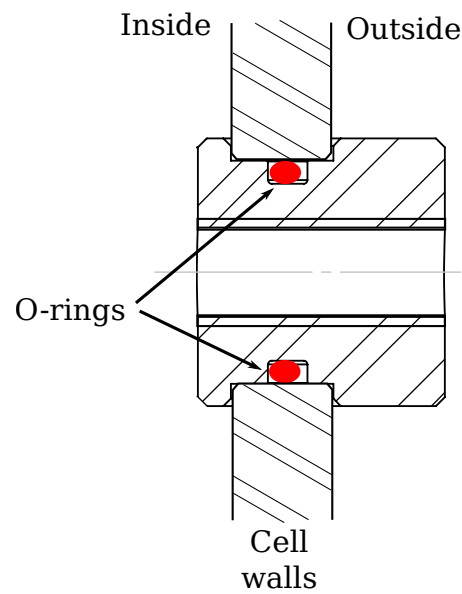


Figure 2.7: Detail of the intermediate ring used in the prototype 2. The fibre-optic wires are extracted through the threaded passages. Tolerances for the O-ring groove were not precise enough and caused the extrusion of the joint.

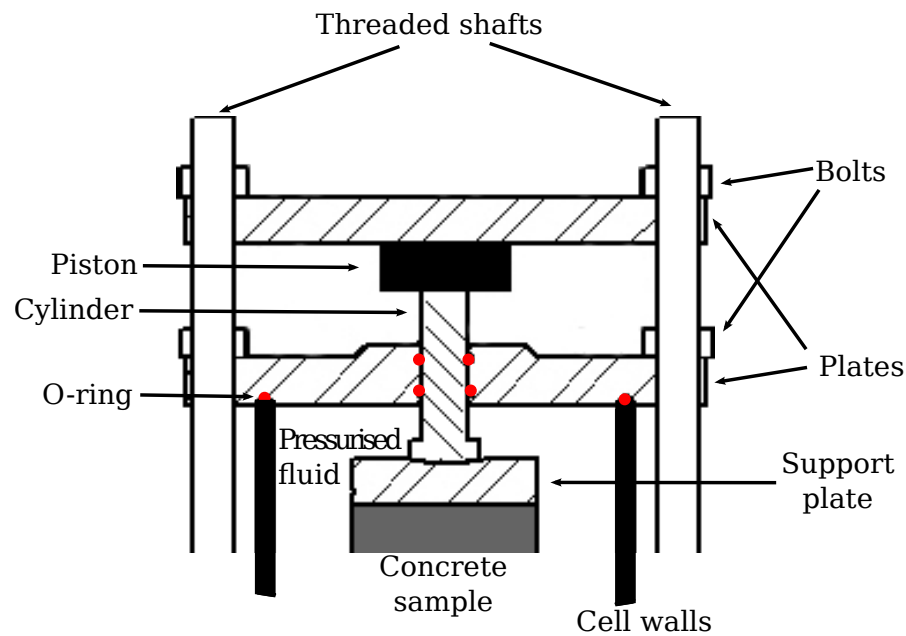


Figure 2.8: Application of the vertical load.

2.3.4 Prototype 3

The last prototype is very close to the final design of the cell. The tube is kept in a single block as opposed to the prototype 2. This prototype is designed to operate with alkaline solution, up to 30 MPa.

Pressurised fluid

A coupling device is required to pressurise an alkaline solution. It was achieved by applying an oil pressure to an alkaline solution via a pressure transfer chamber. A sketch of the hydraulic assembly is shown in Figure 2.9.

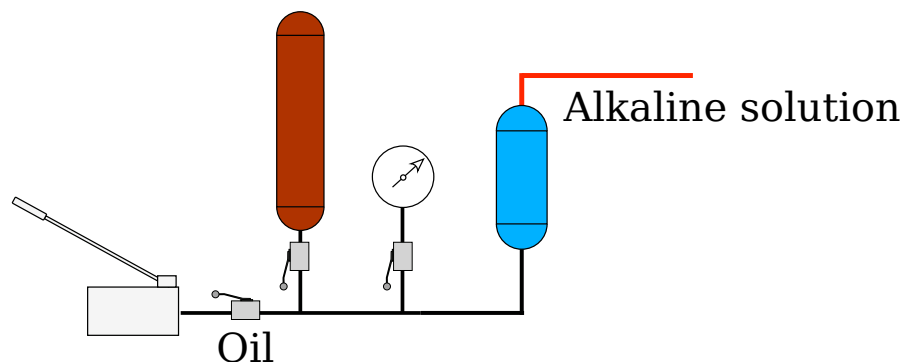


Figure 2.9: Hydraulic setup for the pressurisation of an alkaline solution

Alignment

During the assembly of this prototype, the samples were not aligned with the axis of the cell with an angle of approximately 0.6° . This results in a misalignment of around 10 mm at the top of the sample column, and which prevented a proper application of the force by the vertical piston. In the final design, a ball joint is added at the bottom of the column to ensure the alignment of the samples with the piston (see Figure 2.10).

Sensors

Applying a water pressure directly to the sample without membrane increases the pressure in the concrete porosity. The sensors were exposed to that pressure and collapsed after twelve hours under 5 MPa water pressure (see Figure 2.11). Water leaked through the fibre-optic wires and the signal of the sensors was lost.

Sensors were covered with a thermoformable tube, cast in concrete and then exposed to a 5 MPa water pressure. The sensors were indeed water-proof, but the thermal treatment affected the fibres and the signal was lost in all treated samples.

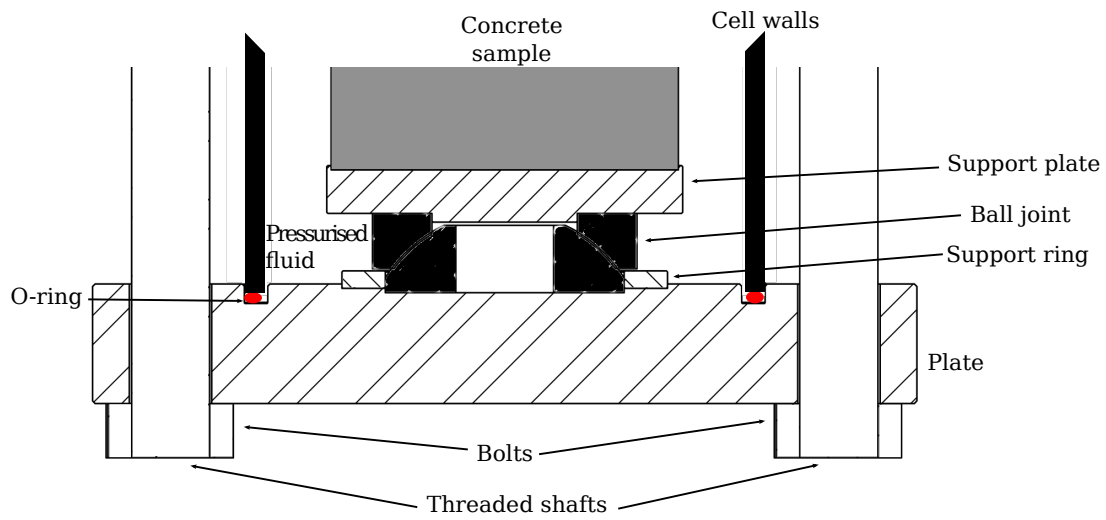


Figure 2.10: Ball joint placed under the sample to ensure co-axiality with the piston. The support ring is placed to limit the maximum angle of the ball joint.



Figure 2.11: Buckling failure of a fibre-optic sensor cast in a concrete sample exposed to 5 MPa water pressure.

Therefore, the design of the sensors was changed to ensure their sealing. The metallic supports of the sensors are threaded to mechanical bulkheads similar to the ones used to pass through the cell walls. The intermediate plastic tube is reinforced with a steel tube. The design of these sensors is pictured in Figure 2.12.

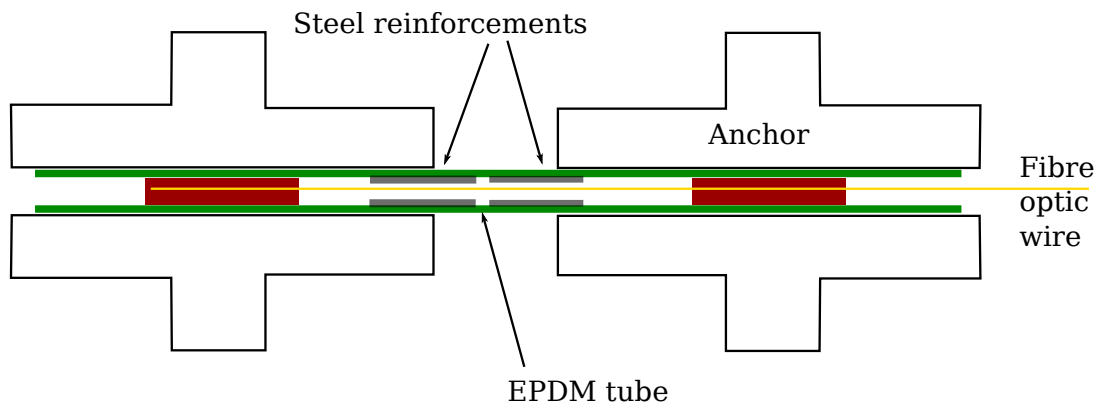


Figure 2.12: Scheme of the reinforced sensors. Dimensions not to scale.

2.3.5 Final design

A set of six cells was built using the experience gained from the three previous prototypes. The main design choices are:

- Each cell holds three concrete cylinders in a large steel tube held between two circular plates. The plates are bolted to eight threaded shafts. A piston is placed above the upper plate; the force is transmitted to the samples via a cylinder which goes through the top plate. A third plate fixed to the shafts maintains the piston. A ball joint placed under the samples ensures the alignment of the samples with the piston.
- The cells are designed to apply independent axial and radial pressures from 0 to 15 MPa. The lateral pressure is applied with an alkaline solution directly in contact with concrete. The cells are placed in a hot room with a controlled temperature of 38 °C.
- The strains are measured with fibre-optic sensors placed in the axial and radial direction of each sample. The sensors are sealed, and the fibre-optic wires are protected with a tube reinforced with a spring. The wires are passed through the lower plate through standard mechanical connections used in hydraulic construction.
- The damage can be characterised at discrete instants during the experiment: if the load is changed for a short period of time and then restored, the measure of the additional deformation provides the value of the effective stiffness of the sample at that instant. This test could however impose non-recoverable deformations and can therefore will be carried out a limited amount of time during the experiment [31].

- The temperature is monitored in the room and in each sample using a temperature fibre-optic sensors. Manometers are connected to each cell and piston to control their pressure.

2.3.6 Dimensioning the cell

The design described above imposes severe restrictions on the dimensions of the cells. The different parameters involved in the cell design and their final numerical values are listed in Table 2.3.

Table 2.3: Design parameters of the final tri-axial cells

Parameter	Symbol	Value
Maximum pressure of the alkaline solution	P_{solution}	15 MPa
Maximum pressure applied by the piston on the samples	P_{piston}	15 MPa
Elastic limit of the tube	$R_{\text{e,tube}}$	280 MPa
Poisson's ratio of the tube	ν_{tube}	0.27
Young's modulus of the shafts	E_{shaft}	193 GPa
Internal radius of the tube	r_{in}	111 mm
External radius of the tube	r_{out}	120 mm
Radius of a concrete sample	r_{samples}	80 mm
Radius of the threaded shafts	r_{shaft}	18 mm
Radius of the O-rings	$r_{\text{O-ring}}$	3.5 mm
Length of the threaded shafts	l_{shaft}	1110 mm
Number of threaded shafts	n_{shaft}	8
Number of O-rings	$n_{\text{O-ring}}$	2

Cell walls

The maximum pressure P_{solution} in the chamber depends on the inner and outer radii r_{in} , r_{out} of the tube as well as the elastic limit $R_{\text{e,tube}}$ of the material.

$$P_{\text{solution}} = R_{\text{e,tube}} \frac{r_{\text{out}}^2 - r_{\text{in}}^2}{r_{\text{out}}^2 + r_{\text{in}}^2} \quad (2.1)$$

The inner diameter must be chosen as small as possible to limit the amount of pressurised fluid, but large enough to be able to manoeuvre the fibre-optic wires around the samples. Indeed, sharp angles can weaken the signal from the sensors, and so a distance of 30 mm is required between the samples and the tube. The inner radius of the tube is therefore at least 110 mm.

Application of (2.1) with the dimensions and material properties of the tube gives a maximum service pressure of 42 MPa, which is well above the required pressure of 15 MPa.

Pre-stressing of the bolts

The alkali solution applies a strong pressure on the upper and lower plates, and so does the piston. This force is transmitted to the shafts via the bolts, which must be pre-stressed to a value high enough to ensure the sealing. The pre-stress to apply in each bolt is:

$$P_{\text{prestress}} \geq \frac{P_{\text{solution}} r_{\text{in}}^2 + P_{\text{piston}} r_{\text{samples}}^2}{n_{\text{shaft}} r_{\text{shaft}}^2} \quad (2.2)$$

However, the pre-stress is limited: indeed, applying this pre-stress compresses the O-rings which ensures the sealing, and these should not be compressed more than 70%, otherwise they might collapse and not ensure the sealing [32]. This gives the following upper bound for the pre-stress:

$$P_{\text{prestress}} \leq 0.6 E_{\text{shaft}} \frac{n_{\text{O-ring}} r_{\text{O-ring}}}{l_{\text{shaft}}} \quad (2.3)$$

Considering the dimensions of the cells, the O-rings and the material properties, the pre-stress in the bolts must be between 72 and 76 MPa.

The bolts apply a compressive load on the cell tube, which therefore must be checked for buckling. The equation for the critical buckling pressure P_{crit} for a thin-walled cylinder in axial compression is given by [33]:

$$P_{\text{crit}} = 0.6 E_{\text{tube}} \frac{r_{\text{out}} - r_{\text{in}}}{r_{\text{in}}} \quad (2.4)$$

Numerical application gives a critical load of 9 GPa, which rules out the possibility of axial buckling of the cell tube.

O-ring grooves

If the water pressure is too high, the O-ring can be extruded from its groove through the gap between the tube and the groove (see Figure 2.13). The dimension of this gap depends on the shore hardness of the O-ring and the service pressure and must be as small as possible. Given the diameter and hardness of the O-ring chosen, the maximum admissible gap is 0.13 mm.

However, the gap must be large enough to allow the mechanical pieces to fit in one another. Notably, the tolerances must be set so that the pieces are not in contact with each other.

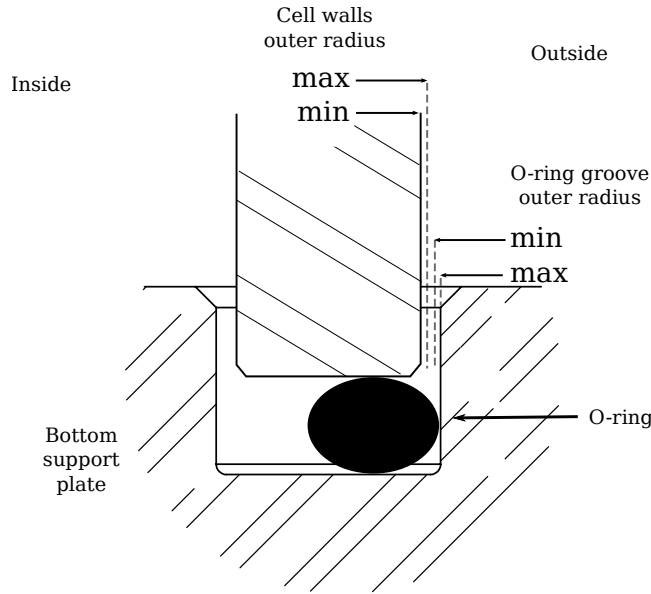


Figure 2.13: Detail of the O-ring groove in the prototype 3 with indications of the tolerance on the radii of the cell walls and the groove (dimensions not to scale).

The tube being under the pressure of the alkaline solution, the gap in service conditions is lower than the gap as drawn. The displacement of the external surface of the tube is given by:

$$u(r_{out}) = \frac{(1 - \nu_{tube}^2)}{E_{tube}} \frac{r_{in}^2 r_{out}}{(r_{out}^2 - r_{in}^2)} P_{solution} \quad (2.5)$$

Given the dimensions of the tube and the pressure conditions, the displacement of the external surface of the tube is 0.10 mm, which means the admissible gap in the drawing is 0.23 mm.

In the drawing, the groove and the tube are separated by a maximum of 0.2 mm. The tolerances are set to 0.05 mm for each piece, which still leaves a minimum gap of 0.1 mm between them.

Sensors

During the testing of the prototype 3, the sensors failed in radial buckling under the high internal pressure. The sensors are therefore reinforced with two internal steel cylinders. These are not in contact with one each other in order to avoid restraining the deformation of the sensors itself. The critical buckling pressure P_{crit} for a thin-walled cylinder in lateral compression is given by [33]:

$$P_{\text{crit}} = \frac{\pi^2 D}{l^2 \beta^2} \left[(1 + \beta^2)^2 + \frac{12 Z^2}{\pi^4 (1 + \beta^2)^2} \right] \quad (2.6)$$

Where D is the cylinder flexural stiffness per unit width, Z the curvature parameter of the cylinder, l its length, and β the buckling parameters which depends on the geometry of the cylinder and the number of axial and radial buckling waves. By varying β in (2.6) one can find the minimal critical buckling pressure and the corresponding number of buckling waves.

Numerical application with the dimensions of the tube indicates that the critical buckling pressure is equal to 10.5 MPa, which is lower than the imposed alkali pressure. However, this value does not account for the mechanical restraint of the tube, which increases the critical buckling pressure by approximately 50% [33]. The critical buckling pressure is further increased by the presence of the outer plastic tube.

The reinforced sensors were placed in pressurised oil at 20 MPa in the prototype 1. The sensor showed no sign of collapse and the signal from the sensor was read without change. This validates the design of the sensors in the experimental conditions.

The sensors being larger than in their original design, the measure of the concrete deformations might be affected as well [34]. This influence can be measured by comparing the Young's modulus of a concrete cylinder obtained from external strain gauges and from the embedded sensor.

2.4 Materials and experimental conditions

As shown before, stress has a complex non-linear influence on ASR expansion. Therefore, a set of mechanical loads ranging from uni-axial to isotropic pressures must be investigated. Six tri-axial cells were built with the design described above. Each of these cells operates at different load levels. They contain two reactive and one reactive concrete samples. The materials used and the mechanical boundary conditions are described below.

2.4.1 Materials

The mix design is chosen to be as close as possible to the one used in the work of Dunant to provide immediate comparison between the results of the present study and his.

Two set of aggregates are used in this study. They come from the quarries dug during the construction of two dams in the Swiss Alps, and were well characterised during the previous studies of Ben Haha, Dunant and Chappex [6, 12, 35]. They have similar mechanical properties, except that the reactive aggregate exhibits a strong anisotropy due to its layered mineralogy. Their main properties are gathered on Table 2.4

Table 2.4: Aggregate types used in the present study

Aggregate	Reactive	Non-Reactive
Designation in this work	R	NR
Designation in [6]	A	B
Designation in [12]	SI	SK
Designation in [35]	Swiss Alps aggregates	
Porosity [%]	4	1.5
Tensile strength [MPa]	10	11
Young's modulus [GPa]	60	64

Both aggregates had a diameter range of 16 to 32 mm. They were crushed and sieved to best approach Bolomey reference curve [36]. The finest aggregates (diameter < 200 μm) were removed from the distribution to avoid an early non-deleterious reaction. The final distribution is shown in Figure 2.14.

The expansion caused by the reactive aggregate does not decrease when the concentration in alkali increases; the alkalinity of the mix can therefore be chosen without restriction [6, 35].

The cement is Pur 4 cement from Holcim. It is a CEM I 42.5 cement according to the European standard nomenclature. It has a low content in alkali ($\text{Na}_2\text{O}_{\text{eq}} = 0.5 \%$) which allows the adjustment the alkali content in the mix by adding sodium hydroxide in the mix water. The water-to-cement ratio is set to 0.47 as in the study of Dunant and the alkali content to 1% of the weight of cement. The final mix design is shown on Table 2.5.

2.4.2 Boundary conditions

The samples are subject to the combined load of the alkaline solution and the axial piston force, as described in Figure 2.15. The axial load is therefore equal to the sum of both, while the radial load is equal to the fluid pressure. This setup cannot apply a radial load higher than the axial load. The operating loads for each cell are listed on Table 2.6.

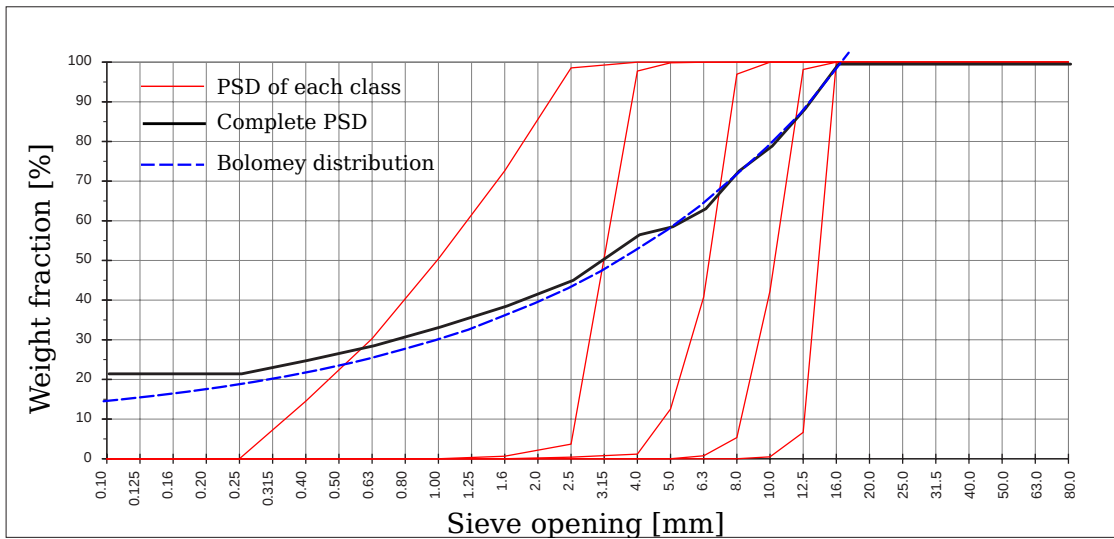


Figure 2.14: Particle size distribution of each reactive aggregate class (red), of the final concrete mix (black), and reference Bolomey curve (blue). The curve accounts for the particle size distribution of the cement.

Table 2.5: Mix design for the reactive and non-reactive concretes. Proportions are given for 50 litres of concrete, enough for 6 cylinders.

Material	Quantity [kg]
Cement Holcim Pur 4	18.2
Water	7.8
Aggregate (0.2-2.5 mm)	23.5
Aggregate (2.5-4 mm)	14.1
Aggregate (4-8 mm)	23.5
Aggregate (8-12.5 mm)	18.8
Aggregate (12.5-16 mm)	14.1
Sodium hydroxide	0.1
Super-plastisizer	0.2

The radial pressure drops in the first days after loading as the solution equilibrates with the concrete pore pressure. The fluid pressure is therefore manually increased to compensate for this pressure loss. Manometers connected to the cells record the pressures every 6 hours. The pressurised fluid is a NaOH solution of concentration 0.9 M as used by Chappex with the same reactive aggregates [35].

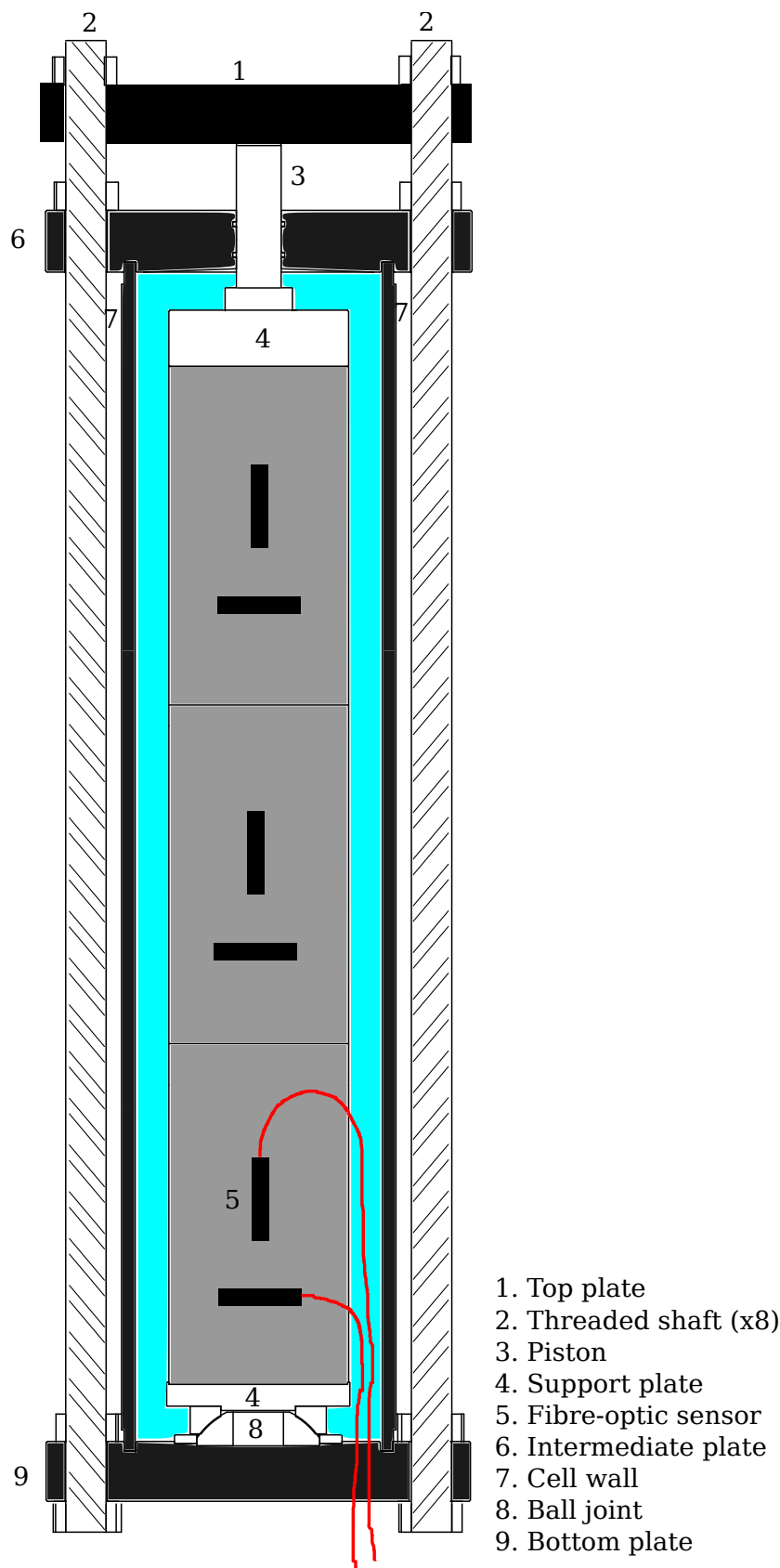


Figure 2.15: Final assembly of the tri-axial cells (not to scale).

2.4. Materials and experimental conditions

Table 2.6: List of loading conditions used in the tri-axial cells (in MPa)

Designation	Fluid pressure	Piston pressure	Total radial load	Total axial load
A5R5	5	0	5	5
A10R5	5	5	5	10
A15R5	5	10	5	15
A10R10	10	0	10	10
A15R10	10	5	10	15
A15R15	15	0	15	15

3 A review of ASR models

ASR models fall into two main categories: macrostructural models concerned with the analysis of structures affected by the reaction, and microstructural models which aim to link the chemical process of the reaction to its impact at the material level.

Macrostructural models require the input of a wide range of properties. In the case of ASR, this includes heat and water flows, the imposed expansion, creep, etc, which in fact depend on the material microstructure which cannot be explicitly represented at such scale. Macroscopic constitutive laws are developed to approximate the processes that occur within the material. These laws can be either empirically derived from the fitting of experiments, or from multi-scale models based on the knowledge of the physical processes at the microscale.

Microstructural models describe explicitly the concrete microstructure, typically with a finite element (FE) discretisation. This limits the size of the sample represented (≈ 10 cm), and are usually developed for the analysis of laboratory experiments. The modelling effort can therefore be focused on a few select phenomena as only a limited number of parameters are varied in those experiments. These models are useful not only to understand the mechanisms of ASR, but also to help in the construction of macroscopic constitutive laws.

In this chapter, models from the literature are reviewed, according to their scope of application. It is shown that most of these models ignore the possible interaction between ASR and the creep in the material. A modification of the model of Dunant is proposed, which accounts for visco-elasticity of the cement paste. The constitutive hypotheses of the modified model are summarised at the end of the chapter. The numerical developments will be described in the chapters 4 and 5.

3.1 Macrostructural models for ASR

Macrostructural models are developed for the analysis of large concrete structures. These models can be classified according to how they represent the alkali silica gel. In most of these models, the expansion or the degree of reaction are typically expressed as sigmoidal functions of time. These functions are used because of their similarity with the free expansion measured experimentally. They suggest however an exhaustion of the process which is rarely observed in the field.

3.1.1 Phenomenological models

Phenomenological models simulate the ASR expansion and induced damage from macroscopic laws derived from experimental measurements. In the earliest models reported by Léger in [37], the ASR expansion was uniformly distributed in the concrete structure. At that time, it was easier to impose an equivalent homogeneous thermal loading rather than deriving and implementing a specific constitutive law. Later, such analysis was refined by varying the imposed expansion across the structure as a function of temperature, relative humidity, concentration of reactive components or compressive stress.

These early models use three main parameters: the asymptotic expansion $\varepsilon_{\text{ASR}}^{\infty}$ which controls the amplitude of the deformation, the latency τ_{lat} which controls the induction period of the reaction, and the acceleration characteristic time τ_{acc} which controls the main slope of the sigmoid (see Figure 3.1). For example, Larive proposed the following expression for the imposed expansion as a function of time $\varepsilon_{\text{ASR}}^0(t)$ [9]:

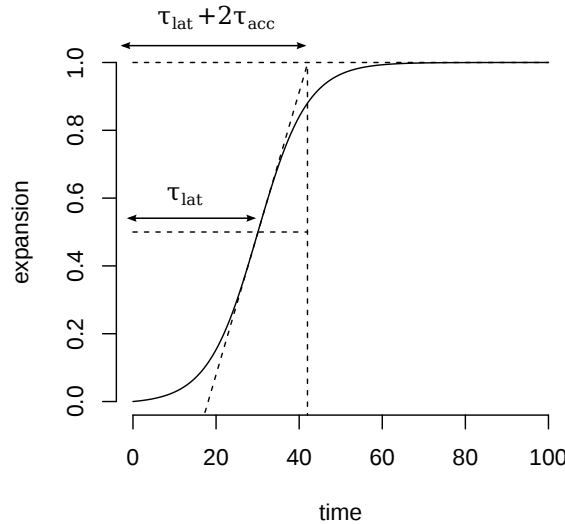


Figure 3.1: Expansion modelled as a sigmoidal function of time (arbitrary units).

$$\varepsilon_{\text{ASR}}^0(t) = \frac{1 - e^{-t/\tau_{\text{acc}}}}{1 + e^{(\tau_{\text{lat}} - t)/\tau_{\text{acc}}}} \varepsilon_{\text{ASR}}^{\infty} \quad (3.1)$$

Lab experiments conducted at different relative humidities have shown that the final expansion decreases with a decrease in the saturation degree in the material. There is a threshold under which little or expansion occurs, which itself depends on temperature, as shown for example by Poyet in [3]. In models like the model of Bažant or Capra [38, 39], this is accounted for by multiplying the final expansion $\varepsilon_{\text{ASR}}^{\infty}$ by a factor h between 0 and 1 which depends on the degree of saturation in the material and is fitted on experiments.

The temperature modifies the characteristic times τ_{lat} and τ_{acc} with an Arrhenius law. The activation energies for the latency $E_{a,\text{lat}}$ and the acceleration $E_{a,\text{acc}}$ are different, and are measured experimentally from expansion curves at different temperatures. Larive and Ben Haha (among others) have measured activation energies between 40 to 45 kJ · mol⁻¹ for the acceleration characteristic time [9, 6].

The activation energy for the latency period is more difficult to determine, as it notably depends on the water availability as shown by Larive. In the model of Saouma [40], this activation energy is chosen between 75 to 80 kJ · mol⁻¹. This value corresponds to the activation energy of the dissolution of silica in alkaline solution, and was measured experimentally by Larive in [9].

The effect of external load on the expansion is usually accounted for by reducing the asymptotic expansion the same way the relative humidity does. In his early model, Leger proposed to use the following relation between the expansion and the applied load [37]:

$$\varepsilon_{\text{ASR}}(\sigma) = \begin{cases} \varepsilon_{\text{ASR}}^0 & \text{if } \sigma < \sigma_L \\ \varepsilon_{\text{ASR}}^0 - K \log_{10}(\sigma/\sigma_L) & \text{if } \sigma_L < \sigma < \sigma_{\text{max}} \\ 0 & \text{if } \sigma > \sigma_{\text{max}} \end{cases} \quad (3.2)$$

σ_L is the stress imposed by the expansion under free loading conditions; the expansion is not affected if the applied stress is below this value. K controls the slope of the expansion, and σ_{max} is the stress above which no expansion occurs. The function is shown on Figure 3.2.

However, this function does not consider the effect on lateral expansion, and Leger found that the parameters must be adapted on a case by case basis. This limits the application of the model, several authors enhanced this formulation by considering the volumetric expansion. For example, Saouma distinguished two distinct effects of the applied stress [40]:

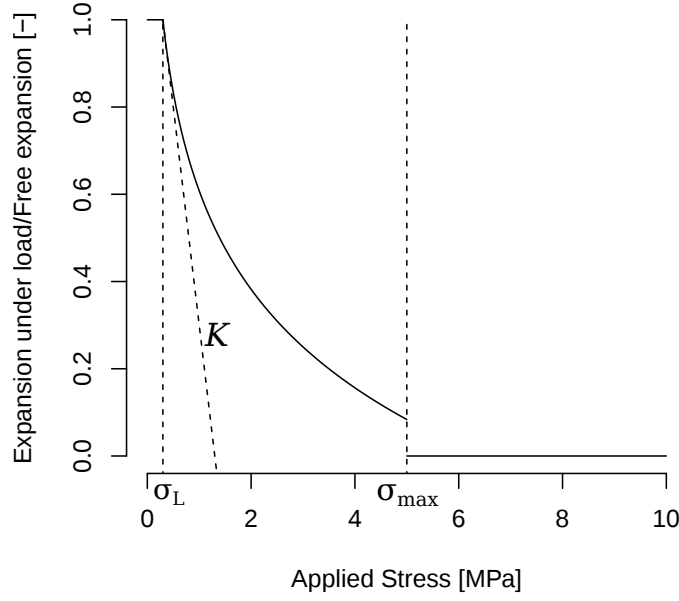


Figure 3.2: Reduction of the final expansion as a function of the applied stress in the macrostructural model of Leger [37].

- The imposed strain tensor along each axis is weighted by a factor that depends on the tri-axial stress state of the material. Saouma identified nine cases from free expansion to isotropic compression and attributed weights based on mechanical assumptions. However, in all cases, the volumetric imposed expansion remains the same, which is in contradiction with the experimental results from Larive, Multon or Dunant.
- The latency τ_{lat} is increased in case of compressive stress by a factor which depends on the compressive strength of the material f'_c and the trace of the stress tensor σ . In (3.3), ϕ is a parameter that is equal to 1 if the material is in tension, or a value calibrated on the experiment of Multon if the material is in compression [10].

$$\tau_{\text{lat}}(T, \sigma, f'_c) = \underbrace{\left(1 + \phi \frac{\text{tr}(\sigma)}{3f'_c}\right)}_{\text{stress}} \underbrace{\left(e^{E_{a,\text{lat}}(1/T - 1/T_0)}\right)}_{\text{temperature}} \tau_{\text{lat}}(T_0) \quad (3.3)$$

3.1.2 Poro-mechanical models

These models are based upon the assumption that the expansive silica gel forms inside the concrete porosity. The amount of gel formed is assumed to be a sigmoidal function of time to reflect the experimental expansion curves. The gel exerts a pressure on the pore walls, which translates to a macroscopic expansion. However, for the gel to form in the porosity, it must be either highly fluid to move from the aggregates to the paste, or formed by through-solution reactions, which does not correspond to experimental evidence from Bulteel or Ben Haha [41, 7].

The macroscopic constitutive material law in these models follows (3.4), where \mathbb{B} is equivalent to the Biot tensor used in poro-mechanics [42], and refers to the amount of gel-filled pores and their geometry, and σ_{ASR} is the pressure imposed by the gel.

$$\sigma = \mathbb{C} : \varepsilon + \mathbb{B} : \sigma_{\text{ASR}} \quad (3.4)$$

These two parameters correspond to an idealisation of the material microstructure and cannot be measured experimentally. They can be fitted for a specific concrete mix, or they can be derived using analytical homogenisation schemes. Doing so introduces additional fitting parameters, as these schemes are based information on the microstructure that are not readily available, like the amount of porosity accessible to the gel or in some cases the geometry of the pores.

In his model, Li assumed that the pores where the gel forms are ellipsoidal, and that the aspect ratio of these pores changes during the course of the reaction because of micro-cracking [43]. The coefficient \mathbb{B} therefore changes as the cracks propagate, and the model was able to reproduce the trends observed in the uni-axial experiments of Larive. However, the aspect ratio of the idealised pore was calibrated on the experiments, and the model cannot determine how this aspect ratio evolves with the advancement of the chemical reaction.

Capra used the gel pressure to estimate the damage caused by ASR, which in turn translates into imposed strains [44]. In his model, the gel can exert pressure on the solid skeleton only after it has already filled the accessible porosity, or the cracks opened during the ASR process (3.5). This delays the occurrence of expansion the same way the latency time does in the phenomenological models.

$$\sigma_{\text{ASR}} = (V_{\text{gel}} - V_{\text{accessible porosity}} - V_{\text{cracks}}) \mathbb{C}_{\text{gel}} : \mathbf{I} \quad (3.5)$$

Capra identified relations between $V_{\text{accessible porosity}}$, σ_{ASR} , V_{gel} , V_{cracks} and the global strain tensor ε using assumptions on the microstructure of the ASR-affected concrete. Replacing these relations in (3.5) gives σ_{ASR} as a function of the volume of gel formed and the current strain in the material. However, the coefficients for these relations cannot be measured experimentally and must be calibrated for each set of experiments. They further don't consider the fact that these relations might change in the presence of applied stress. The total strain is the sum of the elastic strain, ASR-imposed strains, and mechanical anelastic strains caused by mechanical damage in tension or in compression. These anelastic strains were calculated with a damage model that did not account for the loss in compressive strength due to ASR observed by numerous authors, nor for the fact that this loss depends strongly on the aggregate type as shown by Giaccio [21].

Grimal used a variation of the model of Capra which aims to account for creep at the structural level [45]. The creep properties of the material are calibrated on non-reactive experiments and are assumed independent of the occurrence of ASR. In his model, the rate of ASR expansion and damage d_{ASR} are coupled by the following differential equation:

$$\dot{\varepsilon}_{\text{ASR}}(t) = \frac{\dot{d}_{\text{ASR}}(t)}{(1 - d_{\text{ASR}}(t))^2} \varepsilon_{\text{ASR}}^{\infty} \quad (3.6)$$

In this model, d_{ASR} is calculated from the gel pressure with a relation similar to (3.5), which further accounts for the saturation degree and the temperature. This model also accounts for the pressure in the water-filled porosity. However, the Biot coefficients of the gel and of water are related to the morphology of the pores, their volume fraction and the mechanical properties of the fluid they are filled with. All these microstructural parameters change during the reaction, notably because of the opening of cracks, and therefore these coefficients should not be constants as proposed in this work. Furthermore, the creep properties of a material are affected by damage in a non-trivial way, as shown theoretically by Budyanski in [46], and experimentally by Denarié and co-workers in [47].

Various authors have proposed variants of such poro-mechanical models. For example, the model of Bangert describes explicitly the water movements in the microstructure, and uses it to compute the gel pressure [48]. However, the damage is computed macroscopically as an empirical function of the maximum strain in the sample, which leads to unrealistically high damage, even after a few days of reaction. In the model of Pesavento, the Biot coefficient of the gel accounts for the fact that the gel forms inside the aggregate porosity [49]. However, even if the damage in the microstructure is accounted for in the expression of the mechanical equilibrium and the water movements, it was not considered in the calibration of the model.

The constitutive models for structures derived from poro-mechanics suffer from the simplistic description of the solid phase. First, these models are multi-scale schemes, and therefore should consider all heterogeneities of similar scale including cracks and aggregates. Second, ASR damage is not distributed uniformly across the solid skeleton, and this requires a distinction between aggregates and cement paste. Finally, they typically rely on a number of parameters which are impossible to measure experimentally. These models require a large number of fitting parameters, and so cannot be easily extrapolated from one reactive concrete to another.

3.1.3 Reaction rim models

Reaction rims models were developed to propose a better representation of the microstructure than the poro-mechanical models. In these models, each aggregate is considered separately in a representative elementary volume of cement paste. The reaction is assumed to occur around the aggregates in the interfacial transition zone (ITZ). This corresponds to high-reactive aggregates like opal, but cannot be applied to the slow-reactive aggregates commonly used in structures.

For example, Bažant divided his model into a chemical component which controls the rate of reaction, and a fracture mechanics component which describes the cracking of the cement paste [38, 50]. The crack around each aggregate is assumed to be a ring which propagates in a plane. The final isotropic expansion is obtained by integrating over all possible crack orientations. The model does not consider the interactions between each crack, and so it is restricted to low volume fractions of aggregates. The model can be fitted to capture the expansion caused by highly-reactive glassy aggregates with a uniform PSD, but then fails to represent the loss in compressive or tensile strength. However, the mechanical manifestations of ASR are different in slow-reactive aggregates, which represent the majority of aggregates used in the field. For these reasons this model is of no practical use.

The model of Suwito also assumes that the silica gel forms a layer around the aggregates [51]. The volume of gel formed is calculated using a chemical kinetics model accounting for the mineralogy of the aggregate, the composition of the concrete pore solution, and diffusion of the reactants through the aggregate, the cement paste and the ITZ. The chemical composition of the gel is an output of the model, and is based to estimate the pressure it applies. The macroscopic expansion is calculated using models previously developed to estimate the thermal expansion coefficient of heterogeneous materials (see for example the work of Pierard for a comprehensive review of these models [52]). In such scheme, all phases are purely elastic, and therefore the model cannot capture effects of internal damage or applied stress on the imposed expansion. Furthermore, it predicts that all the aggregates react, while Ben Haha showed with image analysis that in slow-reactive aggregates less than 3 % of the aggregate area are affected [7].

In his model, Charpin considered different fracture mechanisms happening simultaneously around the aggregate: debonding around the aggregate and propagation of penny-shaped cracks in three orthogonal direction [23]. An homogenisation approach is used to consider the complete particle size distribution. He accounted for the fact that crack propagation changes the morphology of the microstructure, and therefore changes the weights calculated during the homogenisation procedure. His model was able to capture PSD effects [53] and to some extent the effect of applied load. However, when the load is too high, the model overestimates the debonding of the aggregates, and underestimates the overall expansion. This can be explained by the fact that the morphology of the reaction and the crack propagation are ill-represented, but also by the fact that no creep was accounted for in the model. Indeed, crack growth in visco-elastic media might be slower than in purely elastic material, which could explain the overestimation of the damage by the model.

These models might be improved if they would describe the gel formation in the aggregate rather than around it. For example, Reinhardt used fracture mechanics at the aggregate level to describe the fracture of rocks placed in alkaline solutions. With his model he was able to predict the critical pressure of the gel required to break apart an aggregate as a function of the size of the aggregate [54]. Using this model in a multi-scale approach as the one proposed by Charpin might lead to more accurate macroscopic constitutive laws.

3.2 Micro-structural models for ASR

In these models, the microstructure of concrete is explicitly represented with a FE discretisation. The pressure imposed by the silica gel opens cracks in the microstructure, with a complex geometry which cannot be represented using analytical schemes. The location at which the gel forms is an important parameter which dictates where the cracks initiate and how they propagate.

3.2.1 Expanding aggregates models

In these models, the expansion is caused either around the aggregates similar to the reaction rim models detailed above, or by an homogeneous expansion of the aggregate themselves.

Comby-Peyrot modelled a mortar bar affected by ASR with three-dimensional FE [55]. In her simulations, only the larger aggregates were considered, as the computational resources necessary to discretised the full PSD were too high. This might have undesired effects in the simulation, as Dupray showed that for this kind of simulation the smallest aggregates have a significant influence on the crack propagation in the microstructure [56]. This, combined with the fact that the expansion was driven by an homogeneous expansion of the aggregates, lead to an unrealistically dense damage pattern in the paste.

Schlangen used a lattice model to simulate crack propagation caused by ASR [57]. In this model, the gel is not explicitly described: some zone of the microstructure are described as "expanding". The total area of these zones does not change with the reaction, but the expansion coefficients does using an empirical kinetic law. Schlangen tried three different configurations: the ITZ expands, the ITZ and the formed cracks expand, or all the aggregates expand homogeneously. The damage is calculated with a local algorithm which shows huge dependency to the mesh [58]. The pattern was compared with images of microbar samples obtained with back-scattered electron microscopy. The aggregates used were highly-reactive basalt aggregates with different PSDs. With these simulations, the authors concluded that the first loading scenario (expanding ITZ) gave the best match for the fracture pattern. The second scenario (expanding ITZ and cracks) lead to early failure in the cement matrix. The last scenario (expanding aggregate) caused a dense crack pattern which did not match the observations. However, no comparison was done for the total expansion of the sample. Furthermore, the simulation attempted to reproduce a micro-bar test, which is known to have poor correlation with what happens in the field as shown for example by Lu and co-workers in [59].

3.2.2 Gel pockets models

In these models, the expansion is caused by gel pockets in the aggregates.

Çopuroglu modified the model of Schlangen so that the gel forms in gel pockets either in the aggregate, in the paste or in the ITZ [60]. In the simulation, the volume of the gel formed is constant, but the ASR-imposed expansion depends on the advancement of the chemical reaction. This model showed the expected result that the location of the gel pockets dominates the crack pattern in the material (see Figure 3.3). However, several concerns are raised from this simulation: the quantity of gel formed seems large compared to the values measured experimentally by Ben Haha [7]; only one aggregate was simulated, which is not representative of a concrete or mortar microstructure; and no comparison was made with experimental expansion curves. This model is therefore ill-suited for the study of ASR.

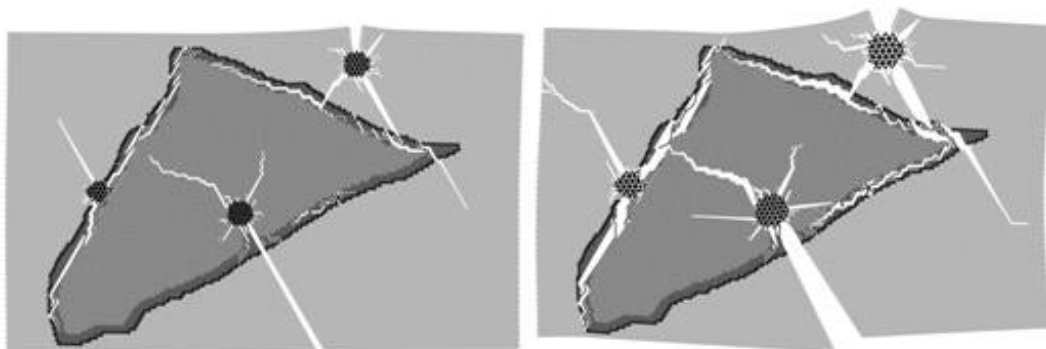


Figure 3.3: Influence of the location of the gel pockets on the crack pattern obtained with the model of Çopuroglu. Figure from [60].

Dunant proposed a model where the gel pockets grow within the aggregates as the reaction advances [12, 11]. This model follows the experimental evidence of Ben Haha, further confirmed by Dunant, who suggested that the macroscopic expansion depends only on the amount of gel formed, and not on its rate [7, 12]. In this model, the effects of chemical processes are therefore reduced to a volume of gel formed. The crack pattern and the expansion depends only on the number and location of the gel zones and the mechanical boundary conditions applied to the sample.

In this model, the concrete microstructure is discretised in two dimensions using a C++ FE framework called AMIE. The aggregates are represented as circular inclusions embedded in a cement paste matrix. Their behaviour is elastic-brittle, and their mechanical properties distributed according to a Weibull law to account for the heterogeneity of the material. The dimensions of the microstructure are identical to the dimensions of the samples tested in the laboratory (4 cm for a mortar bar, 7 cm for a concrete prism), which allows the direct comparison between the simulation with the experiments.

The mechanical degradation is described with a non-local continuum damage model. Indeed, the crack network caused by ASR is very dense, and would be numerically too intensive to represent with a discrete crack approach. The damage algorithm uses the fact that the fracture criterion evolves monotonically with the load. This way, it is possible to predict which elements are damaged first, and therefore how the damage propagates in the microstructure, without using a Newton-Raphson iterative solver. The thermodynamic equilibrium is naturally enforced by the algorithm [61].

The gel pockets are randomly distributed in the aggregates. They are represented in the model using extended finite elements (XFEM). Indeed, they are too small to be meshed explicitly, and their growth would require re-meshing. Their mechanical behaviour and imposed expansion does not depend on the chemical advancement of the reaction, only their size does. Their nucleation in the aggregates induce a crack pattern similar to the one observed experimentally for slow-reactive aggregates (see Figure 3.4).

The mechanical properties of the aggregates were measured by Ben Haha in [6]. The elastic properties of the cement paste were back-calculated from the initial deformation of the uni-axial experiments [5], and the fracture properties of these two phases measured from destructive tests on mature cement paste samples. The expansive coefficient of the gel was fixed to 0.5, value which corresponds to the 50% increase in volume reported by Garcia-Diaz and co-workers in [62]. The stiffness of the gel was fitted on free expansion experiments, and was fixed at 22 GPa, which is within the range of the moduli measured experimentally by Leemann and co-workers using nano-indentation [63].

Dunant used this model to estimate the influence of the aggregate PSD [17]. In the model, it is possible to change the aggregate PSD, and also the way the gel pockets are distributed in the aggregates. For example, it is possible to consider that only the larger aggregates are reactive by only placing gel pockets in these. The model captured well the effect of the aggregate PSD after

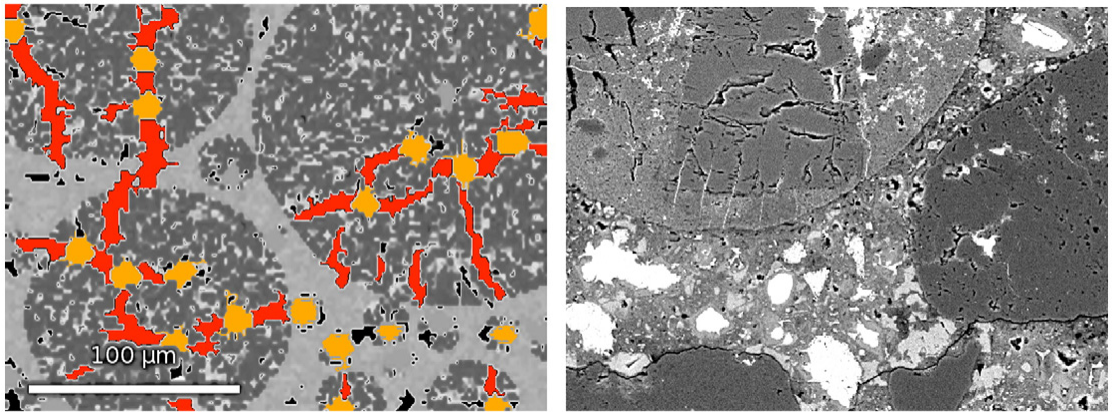


Figure 3.4: Damage pattern obtained with the model of Dunant compared with experimental pattern obtained by semi-electron microscopy (right). Figure from [11].

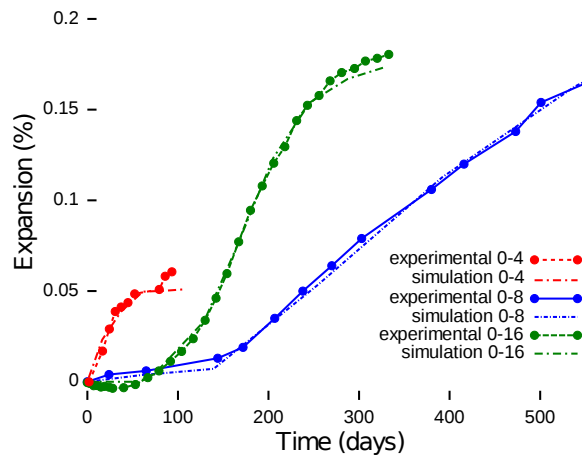


Figure 3.5: Experimental and simulated expansion for different PSD. Figure from [12].

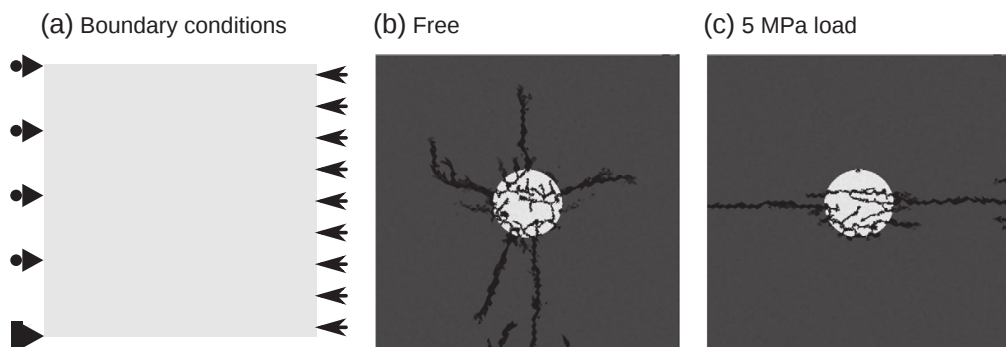


Figure 3.6: Illustration of the influence of the load on the orientation of the cracks as estimated with the model of Dunant. Figure from [5].

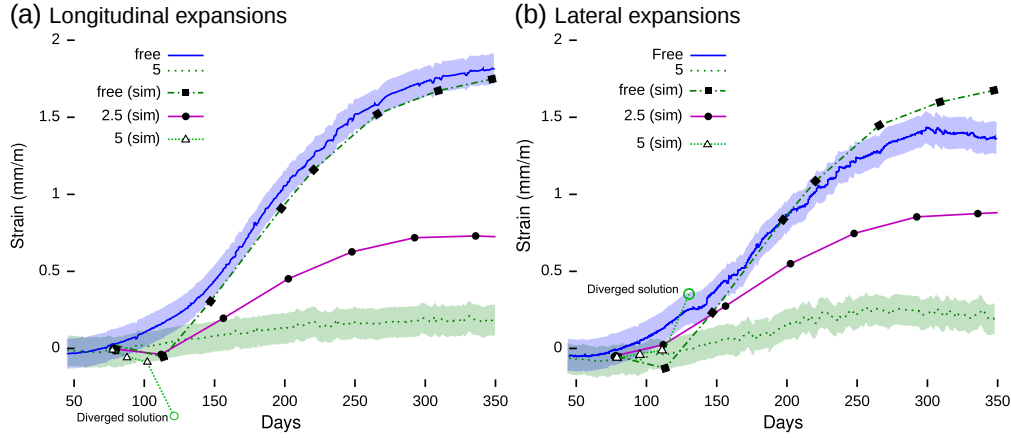


Figure 3.7: Experimental and simulated expansion curves under uni-axial stress obtained with the model of Dunant. Figure from [5].

calibration of the kinetics as a linear function of time, as shown on Figure 3.5. The dependence of the kinetics to the size of the aggregates can be attributed to diffusion effects through the aggregates and to mechanical effects since each aggregate size splits at a different gel pressure, as shown by Reinhardt in [54].

In this model, the effect of uni-axial load can be simulated by applying a constant stress on one edge of the sample [5]. By doing so, the cracks in the aggregates are forced in the direction of the load (see Figure 3.6). Under low applied stress, the model predicts a reduction of the expansion in the direction of the load and in the lateral direction, which is consistent with the experimental results (see Figure 3.7). However, the model overestimates the damage for applied loads higher than 5 MPa, as in the 2D setup used damage propagates through the paste and breaks completely the sample. This can be explained by the crack coalescence which might happen earlier in two dimensions than in three, and by the absence of creep in the material model of the cement paste.

3.2.3 Effect of shape on ASR

The model of Dunant can be used to investigate several morphological parameters of ASR, such as the location where the gel forms, the effect of particle size distribution, or the shape of aggregates.

The expansion induced by ASR has been shown to be anisotropic with respect to the casting direction, even in the case of free expansion. The degree of anisotropy changes from one author to another, and a large scatter exists depending on the type of the aggregate or the shape of the specimen. The shape of the aggregates was often proposed to explain this anisotropy of the expansion.

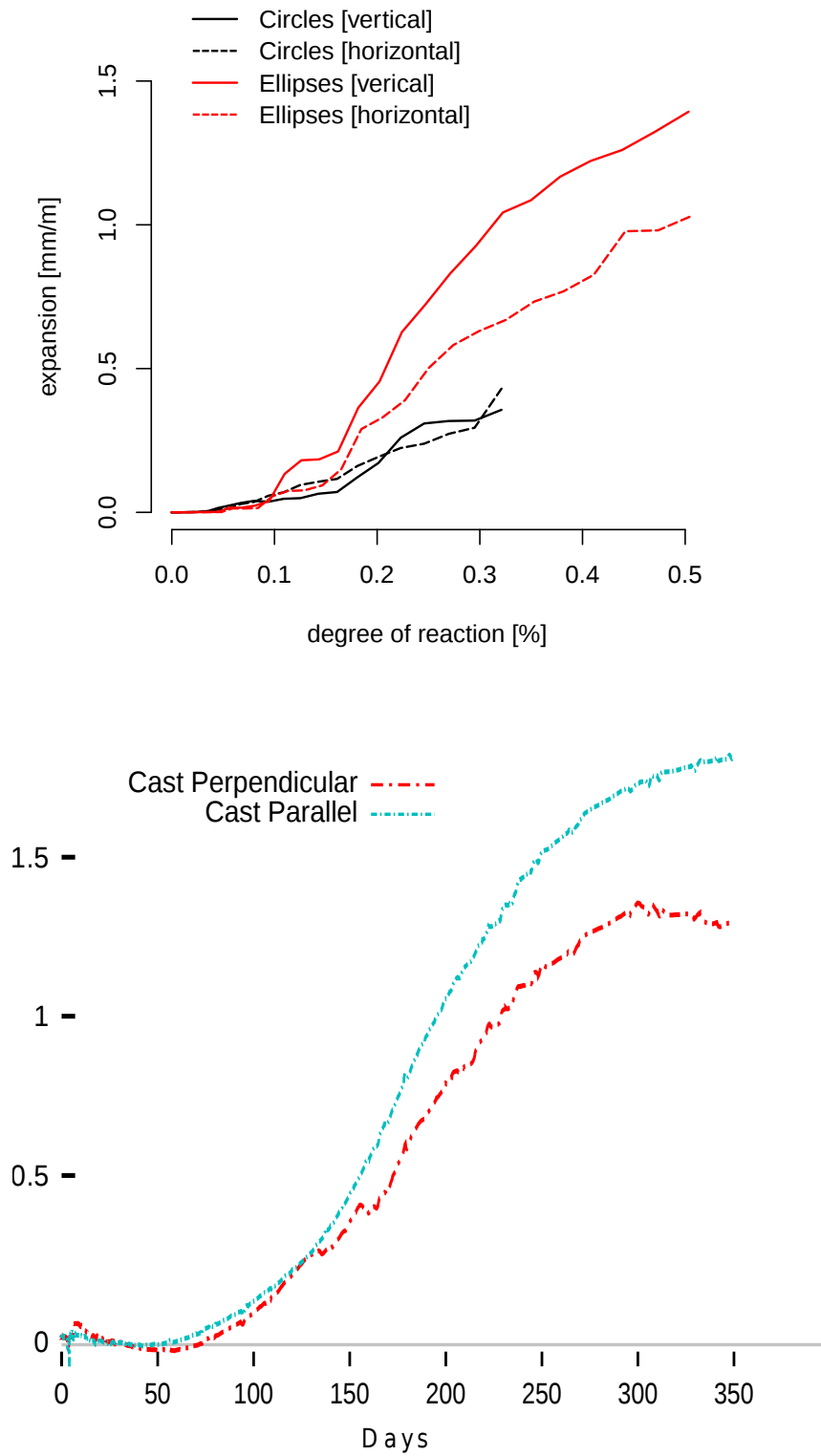


Figure 3.8: Influence of the aggregate shape on the anisotropy of free expansion (left) and comparison with experimental data from Dunant [12] (right).

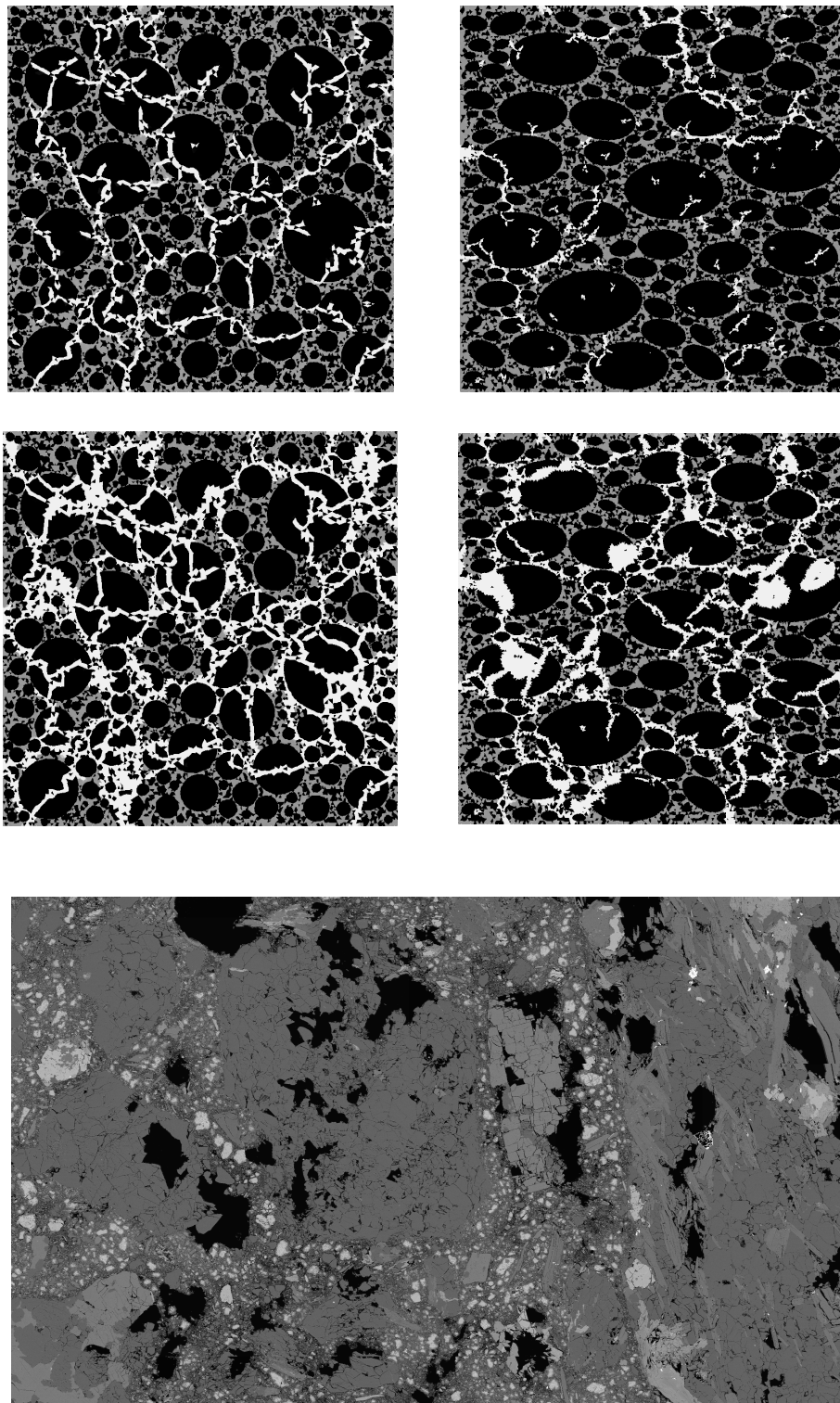


Figure 3.9: Influence of the aggregate shape on the damage pattern at two different degrees of reaction. Comparison with experimental damage pattern obtained at high degrees of reaction.

Dunant measured the expansion from cylinders cored in a concrete cube in two different directions, using the same reactive aggregates as in this study [12]. The ratio between the axial expansion of the cylinder cored in the direction perpendicular to casting and the axial expansion of the cylinder cored in the casting direction was approximately 0.8. A similar value was found in chapter 4 for the uni-axial creep using ellipsoidal aggregates.

In this section the model of Dunant is used with two different aggregate shapes: circles and ellipses with an aspect ratio of 0.6 as in chapter 4. The major axis of the ellipses is oriented preferably along the horizontal direction to simulate the effect of casting direction.

The expansion with the two different particles shape as a function of degree of reaction is reported in Figure 3.8, and compared with the experimental results from Dunant [12]. The expansion caused by circular aggregates is isotropic as expected, even though variations can be seen because of the heterogeneity of the sample and the reaction. Ellipsoidal aggregates provide an anisotropic expansion with a trend similar to what is found in experiments.

The damage pattern induced by the two microstructures is shown for two different degrees of reaction in Figure 3.9. In terms of amount, the damage in both microstructures is similar. However, their morphology is different. In case of circles the damage forms clear cracks that propagate easily in the microstructure. For the ellipses, the damage tends to spread in large zones around the gel pockets rather than to propagate. The curvature of the aggregate boundary makes it more difficult for a crack to cross it. This forms highly damaged areas similar to what is sometimes observed in experiments after a long period of time. These areas would tend to weaken more the material than the diffuse crack pattern, which explains the difference observed in expansion and diminishes the damage spread in the cement paste.

Indeed, the cement paste is highly damaged in the case of the circular aggregates, while the damage is mostly concentrated in the aggregates in the semi-electron microscopic observations of Ben Haha or Dunant. This very high damage in the paste might as well be induced by the absence of creep in the model, as discussed below.

3.3 Role of creep in ASR

ASR is a very long process that lasts for decades in structures. As concrete exhibits a strongly visco-elastic mechanical behaviour, it is natural to verify if and how creep affects ASR. Some macrostructural models like the model of Poyet [64], Grimal [45] or Saouma [40] account for creep at the structural scale. However, these interactions remain phenomenological, and there is no influence of ASR on the creep of concrete, or vice-versa.

The stress induced by ASR in the material can be dissipated in two different ways: opening of cracks or visco-elasticity. These two effects are both rate-dependent and temperature-dependent. Notably, if the activation energy of creep is highly different than the activation energy for ASR expansion, then the extrapolation of accelerated tests to structure requires a more careful treatment in the model. Indeed, the accelerated tests might overestimate the degree of reaction at which the damage propagates through the paste. Understanding these relations between visco-elasticity and damage is therefore critical to propose a better understanding of the long-term behaviour of structures subject to ASR.

For example, Figure 3.10 shows the simulated average stress induced by ASR in a visco-elastic cement paste, without accounting for damage, and with different reaction kinetics. The instantaneous case corresponds to the purely elastic case. Creep reduces significantly the stress in the paste, and delays the degree of reaction at which the material reaches its tensile limit. The mechanical behaviour of ASR-affected concrete might therefore be dominated by damage in short-term laboratory conditions, and by creep in long-term field conditions.

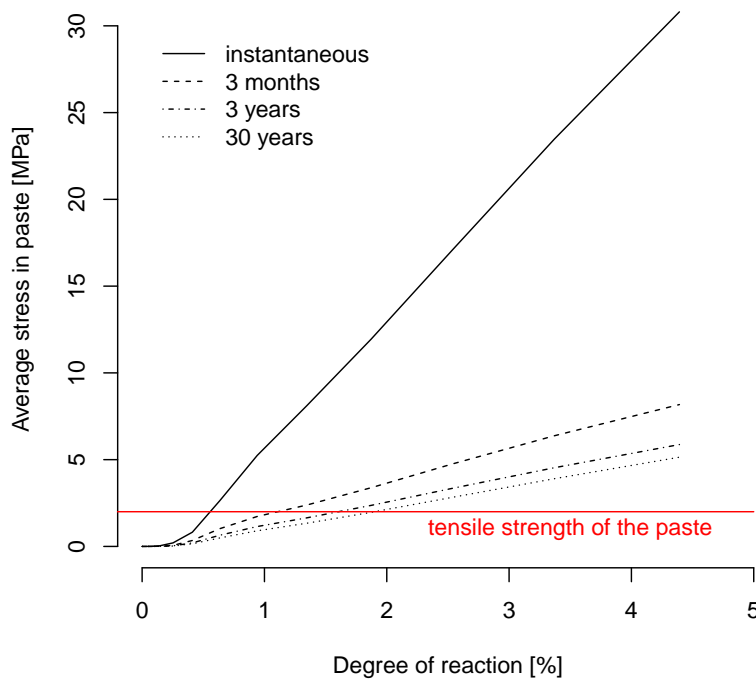


Figure 3.10: Average stress induced by ASR in the cement paste, with different reaction kinetics. Creep is accounted for but not damage. The degree of reaction at which the paste reaches its tensile limit is delayed by the creep phenomenon.

In a previous work, Willis showed that the crack propagation in a uniform visco-elastic media was slowed down by the stress relaxation in the material [65]. In a more recent study, Cécot confirmed this result for multiple discrete cracks propagating in a concrete microstructure discretised with FE [66]. He notably found that different cracks were activated depending on the loading rate.

The microstructural model described above can provide a very fine characterisation of the damage pattern in the microstructure. They show that this pattern is very complex and depends in a non trivial way on the concrete matrix-inclusion arrangement and the location of the gel formation. Crack initiation and propagation in a material depend in turn on the stress distribution in the material. As the cement paste is a visco-elastic material, this stress distribution is likely overestimated by the model.

The apparition of cracks in the material modifies its apparent visco-elastic properties. Budiansky further proved that the crack connectivity has a great influence on these properties [46], and Denarié showed that the relaxation properties of a damaged concrete are strongly affected by the amount of damage [47]. These effects show the influence of the crack geometry at the microstructure level on the macroscopic properties, which is a factor that macrostructural models typically either approximate or neglect.

Since none of the microstructural models account for creep in the cement paste, the principal aim of this thesis is to propose a microstructural ASR model which accounts for the interaction between creep and damage in the cement paste. The model of Dunant is used as a basis since it already provides good agreement with the experiments. The numerical method for the modelling of visco-elasticity is described in chapter 4. In chapter 5, it is completed with a damage algorithm that accounts for the interaction between creep and damage. In chapter 6, application of the model shows the increase in damage in the microstructure caused by accelerated conditions as opposed to field conditions.

4 Numerical modelling of creep

The ASR model of Dunant was modified to investigate the interaction between creep and ASR. A linear visco-elastic behaviour of the cement paste was added to the constitutive hypotheses of the model. This introduces in the material equilibrium additional differential equations which can be interpreted as equivalent springs and dashpots arranged in series and in parallel in the material. A generalised Kelvin-Voigt model is proposed to model the linear creep of the cement paste. The arising constitutive equations are then integrated using a novel space-time finite element approach. The method is unconditionally stable and convergent in time and can represent geometries which evolve continuously in time such as the ASR gel pockets.

Some parts of this chapter have been submitted for publication in *International Journal for Numerical Methods in Engineering* [67].

4.1 Modified ASR model

The model of Dunant is used as a basis for an ASR model to which a visco-elastic behaviour of the cement paste was added. The model is built to be as generic as possible in order to explore the different aspects of ASR such as the influence of the microstructure, the material constitutive laws, or the boundary conditions. A number of assumptions in the original model are eliminated to assess their effects. The hypotheses of the modified model and differences with the original are summarised below:

Microstructure: the material is modelled as a three-phases composite with gel pockets embedded in aggregates embedded in a cement paste matrix. Several parameters can be controlled independently: the size of the simulated sample, the volume fraction of aggregate, their PSD, their shape, the number of gel pockets zones, and their specific location. These parameters can be for example chosen to represent ASR expansion of mortars or concrete, or different reactive aggregates. This is similar to the original model except for the shape of the aggregates.

Discretisation: the sample is discretised in two dimensions with FE. The gel pockets are represented with XFEM as they are too small to be meshed explicitly. They grow as a function of time which results from the kinetics of all chemical processes. This function of time can be chosen independently of other parameters to represent the difference between ASR in accelerated conditions and in field conditions. This was possible in the previous model, but has no consequences on the final result if visco-elasticity is not accounted for.

Mechanical behaviour: the cement paste is represented as a quasi-brittle visco-elastic material, the aggregates as a quasi-brittle material, and the gel pockets as an elastic material with imposed expansion. All the mechanical properties can be measured from mechanical tests. The simulation is conducted at constant temperature. The thermal deformation is neglected in the model, but the creep properties can be adjusted to simulate the effect of temperature on creep.

Boundary conditions: mechanical boundary conditions in stress or in displacement can be imposed on any edge of the sample. These mechanical conditions have no influence on the material behaviour. Anisotropy of the expansion or the damage is a consequence of the model, not an input.

The model is implemented in the FE framework AMIE. Several extensions were made to the framework, notably in the damage algorithm and the assembly of the system in space and time. Further, the numerical efficiency of certain operations was improved.

As opposed to the model of Dunant, the proposed one is strongly time-dependent: the rate of gel formation is now an input of the model. This therefore requires a robust and stable numerical integration scheme. The following aspects required specific developments:

- The gel pockets should grow continuously with time as they do in experiments. If not, the creep and damage propagation are too dependent on the size of the time step. Given the very long time scale of ASR, it would be too costly from a computational perspective to use a large number of time steps, and using large time step would lead to an inaccurate estimation of the stress relaxation, and therefore the damage.
- It should be possible to change the time step easily during the simulation. Indeed, the damage algorithm of Dunant searches for the elements that are damaged first, which means the instants at which these elements are damaged. The algorithm is extended to the time domain, so that an increase in damage corresponds to an increase in time. The model should therefore be able to change the time step with a minimal computational cost.

To this effect, a novel numerical method based on finite elements in space and time was developed and implemented. This proposed method can account for gel zones growing with arbitrary functions of time, and the cost of a change in the time step is minimal. It is coupled with the extended damage algorithm based on the one proposed by Dunant in chapter 5.

4.2 Linear visco-elasticity

In this section the constitutive relations for linear visco-elastic materials are presented in the form of rheological models composed by springs and dashpots assembled in series and in parallel. In general a given linear creep or relaxation function can be approximated by an infinite number of such models, as shown by Roscoe [68] or Biot [69, 70]. This is not true in the non-linear case, and the choice of rheological model for the cement paste should be as close as possible to the physical phenomena that occurs in the material.

4.2.1 Constitutive relation

The constitutive law of linear visco-elastic materials depends on the complete strain and stress history of the system. This is equivalent to the Boltzmann superposition principle, which states that the response of a material to a series of solicitations is equal to the sum of the elementary contribution of each solicitation (see Figure 4.1). In concrete, this is valid as long as the stress in the material remains low compared to its strength (see for example Neville [71] or Bažant [72]).

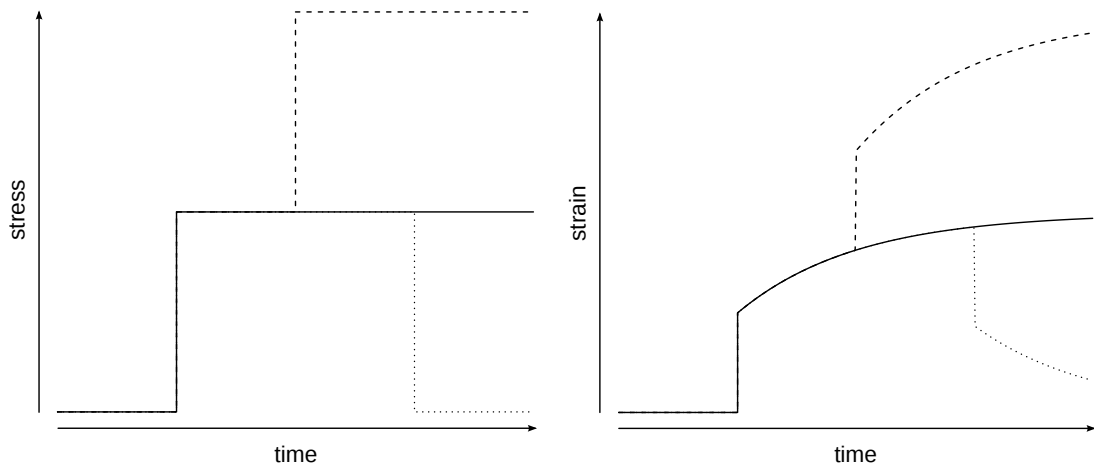


Figure 4.1: Illustration of Boltzmann superposition principle for linear non-ageing visco-elastic materials.

Chapter 4. Numerical modelling of creep

The constitutive law can be written in integral form as (4.1), where \mathbb{J} is the creep function of the material, and \mathbb{R} the relaxation function. Both are fourth-order tensors with the same symmetries as the material elastic stiffness tensor.

$$\begin{cases} \varepsilon(t) &= \int_0^t \mathbb{J}(t, t') : \frac{\partial \sigma(t')}{\partial t'} dt' \\ \sigma(t) &= \int_0^t \mathbb{R}(t, t') : \frac{\partial \varepsilon(t')}{\partial t'} dt' \end{cases} \quad (4.1)$$

\mathbb{J} and \mathbb{R} can be measured independently from creep or stress relaxation experiments, the former being more common as it is easier in practice to apply a load on a sample rather than controlling its deformation. However, they are not independent functions, as their convolution gives the fourth-order identity tensor \mathbb{I} (see for example Drozdov for a more complete proof [73]). One set of experiments is therefore sufficient to characterise completely the material behaviour.

$$\int_0^t \mathbb{J}(t, t') : \frac{\partial \mathbb{R}(t', 0)}{\partial t'} dt' = \int_0^t \mathbb{R}(t, t') : \frac{\partial \mathbb{J}(t', 0)}{\partial t'} dt' = \mathbb{I} \quad (4.2)$$

Inserting these constitutive equations in a FE program necessitates the storage of the entire stress and strain history of the system. This approach would lead to problems too large from a computational perspective to be used in practice. Therefore, visco-elastic materials are more preferably considered as springs and dashpots assembled in series or in parallel.

4.2.2 Equivalence with generalised rheological models

Indeed, any creep or relaxation function can be approximated by springs and dashpots assembled in series or in parallel. The constitutive equation for the linear elastic spring and the linear dashpots are:


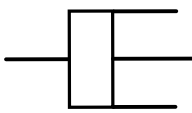
Spring:	$\sigma(t) = \mathbb{C} \varepsilon(t)$	
Dashpot:	$\sigma(t) = \mathbb{E} \dot{\varepsilon}(t)$	

Figure 4.2: Rheological models for linear elasticity and linear viscosity.

By assembling these two elements in parallel or in series, one finds the Kelvin-Voigt or the Maxwell models respectively. These elementary rheological modules are themselves of little interest for the modelling of concrete and cementitious materials: indeed the Kelvin-Voigt model does not exhibit an initial elastic deformation nor stress relaxation, while the Maxwell model predicts creep at constant rate, which is not observed for concrete as the rate of the creep deformations decreases with time. However, they can be used to build more complex visco-elastic models, as shown in Figure 4.3.

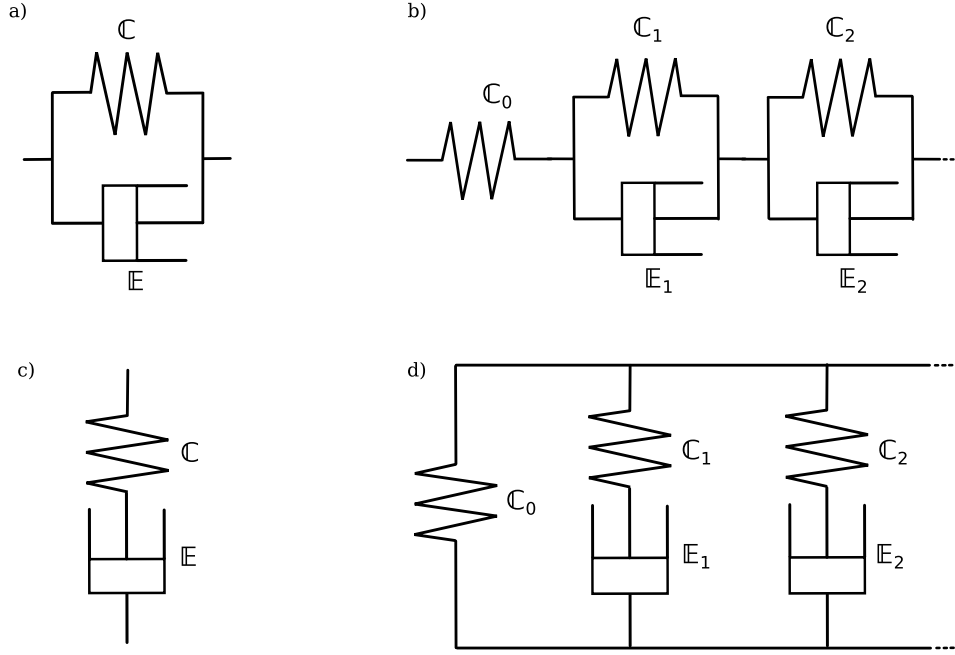


Figure 4.3: Rheological models for linear visco-elasticity: a) Kelvin-Voigt model, b) generalised Kelvin-Voigt model, c) Maxwell model d) generalised Maxwell model.

A generalised Kelvin-Voigt material is constructed by m Kelvin-Voigt modules placed in series. \mathbb{C}_p refers to the stiffness tensor of the p^{th} spring in the assembly, and $\mathbb{E}_p = \tau_p \mathbb{C}_p$ to the viscosity tensor of the corresponding dashpot. The stresses in all modules are equal to the total stress, and the total strain in the material is equal to the sum of all partial strains. Under a constant load σ_0 applied at $t' = 0$ the strain ε is given by:

$$\varepsilon(t) = \left[\sum_{p=1}^m \mathbb{C}_p^{-1} (1 - e^{-t/\tau_p}) \right] : \sigma_0 \quad (4.3)$$

Since any creep function can be approximated as a sum of exponentials (known as Dirichlet series), any visco-elastic material can be represented by a generalised Kelvin-Voigt model.

Similarly, a generalised Maxwell material is composed by m Maxwell modules placed in parallel. The total stress in the material is equal to the sum of the stresses in each module, and the strain in all modules are equal to the total strain. Under a constant strain ε_0 applied at $t' = 0$, the stress $\sigma(t)$ is given by:

$$\sigma(t) = \left[\sum_{p=1}^m \mathbb{C}_p (1 - e^{-t/\tau_p}) \right] : \varepsilon_0 \quad (4.4)$$

Any visco-elastic material can therefore be approximated by a generalised Maxwell model after expansion in a Dirichlet series of its stress relaxation function.

4.2.3 Equivalence between the rheological models

The generalised Kelvin-Voigt and Maxwell models are two among the many possibilities of arranging springs and dashpots in series or in parallel. By nature, they are mathematical approximations of the creep and relaxation functions, but they do not represent necessarily the physical processes in the material.

Constructing a material as an assembly of spring and dashpot is equivalent to considering that the internal energy of the material depends on the total strain ε and m "internal variables" α_p [69, 70]. When the system is deformed, it dissipates energy proportionally to the rate of deformation. These variables are called "internal" as they correspond to processes that cannot be measured experimentally in general nor acted upon. Therefore, there exists a set of m *homogeneous* differential equations which relates ε with the α_p and their respective rates. The system can be written as:

$$\begin{bmatrix} \mathbb{C}_{00} & \dots & \mathbb{C}_{0p} & \dots \\ \vdots & & & \\ \mathbb{C}_{0p} & & \mathbb{C}_{pq} & \\ \vdots & & & \end{bmatrix} \begin{bmatrix} \varepsilon \\ \vdots \\ \alpha_p \\ \vdots \end{bmatrix} + \begin{bmatrix} \mathbb{E}_{00} & \dots & \mathbb{E}_{0p} & \dots \\ \vdots & & & \\ \mathbb{E}_{0p} & & \mathbb{E}_{pq} & \\ \vdots & & & \end{bmatrix} \begin{bmatrix} \dot{\varepsilon} \\ \vdots \\ \dot{\alpha}_p \\ \vdots \end{bmatrix} = \begin{bmatrix} \sigma \\ \vdots \\ 0 \\ \vdots \end{bmatrix} \quad (4.5)$$

In (4.5), the variables ε , α_p and σ are second-order tensors, while the coefficients \mathbb{C}_{pq} and \mathbb{E}_{pq} are fourth order tensors corresponding respectively to the stiffnesses of the springs and the viscosities of the dashpots in the assembly. The α_p have the same symmetry properties than ε and σ .

(4.5) shows that the choice of the α_p is actually free, and that any independent linear combination of these will represent the same linear creep or relaxation function.

In particular, if the system is diagonalised it transforms into the generalised Maxwell model.

$$\begin{bmatrix} \sum_q \mathbb{C}_q & \dots & -\mathbb{C}_p & \dots \\ \vdots & \ddots & & 0 \\ -\mathbb{C}_p & & \mathbb{C}_p & \\ \vdots & 0 & & \ddots \end{bmatrix} \begin{bmatrix} \varepsilon \\ \vdots \\ \alpha_p \\ \vdots \end{bmatrix} + \begin{bmatrix} 0 & \dots & 0 & \dots \\ \vdots & \ddots & & 0 \\ 0 & & \mathbb{E}_p & \\ \vdots & 0 & & \ddots \end{bmatrix} \begin{bmatrix} \dot{\varepsilon} \\ \vdots \\ \dot{\alpha}_p \\ \vdots \end{bmatrix} = \begin{bmatrix} \sigma \\ \vdots \\ 0 \\ \vdots \end{bmatrix} \quad (4.6)$$

The corresponding system for the generalised Kelvin-Voigt model is:

$$\begin{bmatrix} \mathbb{C}_0 & -\mathbb{C}_0 & \dots & -\mathbb{C}_0 \\ -\mathbb{C}_0 & \ddots & & \mathbb{C}_0 \\ \vdots & & \mathbb{C}_0 + \mathbb{C}_p & \\ -\mathbb{C}_0 & \mathbb{C}_0 & & \ddots \end{bmatrix} \begin{bmatrix} \varepsilon \\ \vdots \\ \alpha_p \\ \vdots \end{bmatrix} + \begin{bmatrix} \mathbb{E}_0 & -\mathbb{E}_0 & \dots & -\mathbb{E}_0 \\ -\mathbb{E}_0 & \ddots & & \mathbb{E}_0 \\ \vdots & & \mathbb{E}_0 + \mathbb{E}_p & \\ -\mathbb{E}_0 & \mathbb{E}_0 & & \ddots \end{bmatrix} \begin{bmatrix} \dot{\varepsilon} \\ \vdots \\ \dot{\alpha}_p \\ \vdots \end{bmatrix} = \begin{bmatrix} \sigma \\ \vdots \\ 0 \\ \vdots \end{bmatrix} \quad (4.7)$$

4.3 Rheological model for cement paste

A specific model must be chosen to represent the cement paste in the modified ASR model. The choice can be driven by the ease of fitting the experimental results, or by the ease of the numerical method. For example, it is more practical to use the generalised Kelvin-Voigt model to fit creep experiments, but the generalised Maxwell model proposes a system which is diagonal, and therefore is more practical from a numerical perspective.

Even though the choice of rheological assembly is *a priori* free, it is necessary to understand what are the driving physical processes and at which scale they occur. Indeed, when damage propagates through the cement paste, its apparent visco-elastic behaviour will be changed in a non-trivial way. Notably, Budiansky showed cracks in a visco-elastic media affected each component of the matrices in the system (4.5) in a different way [46]. This means that the damage is *a priori* not distributed equally on each spring or dashpot of the assembly. In (4.5), the variables α_p represent the strain history of the system. In polymers, these are commonly associated with molecular segments of different lengths (see for example Drozdov [73]). In concrete, some of these are related to the internal structure of the C-S-H phase, but the exact mechanism for creep at the micro-scale remains still an open question (see for example the work of Tamtsia for a comprehensive review of mechanisms proposed in the literature [74]). Acker proposed to distinguish two mechanisms for creep [75]: a short-term hygral mechanism through which the air and water are redistributed in the microstructure, and a long-term mechanical behaviour which can be described by sliding of the C-S-H layers on each other.

A major difficulty in the analysis of concrete creep is that the microstructure evolves a lot during the first days of hydration. This ageing modifies the apparent behaviour of concrete. De Schutter tried to link the creep properties of the cement paste to the advancement of the hydration reaction, yet the relations remained empirical and difficult to extrapolate from one concrete mix to another [76]. Van Damme measured with nano-indentation the basic creep of C-S-H at different positions in the microstructure and different instants [77]. Linking these properties to a macroscopic creep function for cement paste requires complex numerical tools like the one proposed by Davydov [78] or Do [79]. The nanostructure of C-S-H is still ill-understood, and therefore there doesn't seem to be a mechanistic model able to give a definitive spring-dashpot assembly for C-S-H yet.

Even if the physical origin of the rheological model of C-S-H remains unknown it is possible to assume a rheological model for the cement paste, and to fit its properties to experimental measurements.

4.3.1 Visco-elastic and damage model for cement paste

In the visco-elastic and damage ASR model proposed, cement paste is represented with a damageable generalised Kelvin-Voigt model. The undamaged material has one elastic branch (stiffness \mathbb{C}_0) and two visco-elastic branches. The first Kelvin-Voigt module (stiffness \mathbb{C}_1 and viscosity \mathbb{E}_1) represents short-term creep caused by water redistribution in the microstructure. The second Kelvin-Voigt module (stiffness \mathbb{C}_2 and viscosity \mathbb{E}_2) represents long-term creep caused by the sliding of the C-S-H sheets.

The first elastic stiffness can be decomposed in a weighted sum of the different constituents of the cement paste: anhydrous cement, C-S-H, portlandite, ettringite, porosity, etc. The weights of each constituent can be determined by analytical or numerical homogenisation at the cement paste level as proposed for example by Bernard and co-workers [80]. It is critical to consider that these weights depend strongly on the cement microstructure, and that they evolve in a non trivial way when cracks propagate in the material.

The damage is represented by a single damage parameter d which is function of time and the state of the material. However, each spring \mathbb{C}_i (respectively dashpot \mathbb{E}_i) is affected in a different way through functions $d_i^c(d)$ (respectively $d_i^e(d)$). Damage occurs when a specific criterion is met. See chapter 5 for more details on the damage algorithm. The corresponding rheological assembly is described in Figure 4.4.

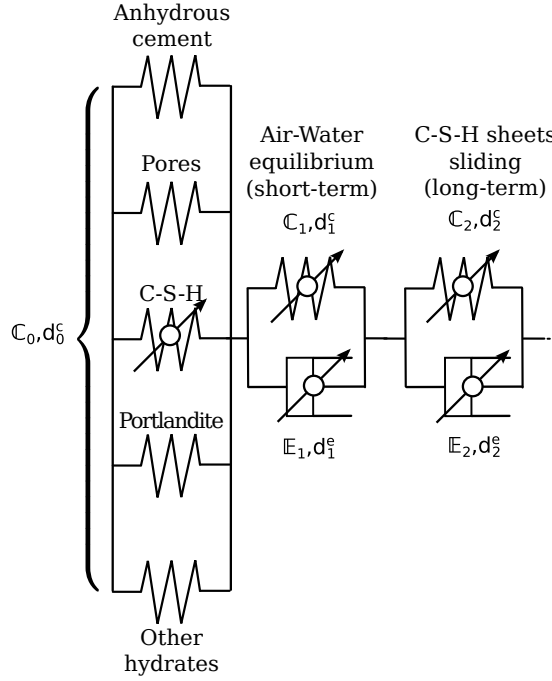


Figure 4.4: Rheological model for visco-elastic cement paste.

The constitutive set of differential equations for the cement paste is:

$$\begin{bmatrix} (1 - d_0^c(d))C_0 & -(1 - d_0^c(d))C_0 & -(1 - d_0^c(d))C_0 \\ -(1 - d_0^c(d))C_0 & (1 - d_0^c(d))C_0 + (1 - d_1^c(d))C_1 & (1 - d_0^c(d))C_0 \\ -(1 - d_0^c(d))C_0 & (1 - d_0^c(d))C_0 & (1 - d_0^c(d))C_0 + (1 - d_2^c(d))C_2 \end{bmatrix} \begin{bmatrix} \varepsilon \\ \alpha_1 \\ \alpha_2 \end{bmatrix} + \begin{bmatrix} 0 & 0 & 0 \\ 0 & (1 - d_1^e(d))E_1 & 0 \\ 0 & 0 & (1 - d_2^e(d))E_2 \end{bmatrix} \begin{bmatrix} \varepsilon \\ \dot{\alpha}_1 \\ \dot{\alpha}_2 \end{bmatrix} = \begin{bmatrix} \sigma \\ 0 \\ 0 \end{bmatrix} \quad (4.8)$$

4.3.2 Identification of the cement paste visco-elastic properties

The undamaged visco-elastic properties of the cement paste are fitted on the uni-axial experiments of Dunant with non-reactive aggregates [17]. The method is detailed so that it can easily be repeated for different aggregates or environmental conditions. Notably, given the role of water in the creep of C-S-H, the creep in the tri-axial experiments proposed in chapter 2 is likely to change with the applied fluid pressure.

Chapter 4. Numerical modelling of creep

Consider a concrete sample represented in two dimensions at its meso-scale. The sample is a square of 80×80 millimetres containing circular elastic aggregates embedded in a visco-elastic matrix. Aggregates are generated so that they follow a Bolomey reference curve with a maximum aggregate diameter of 16 mm as in the experiments. They are randomly placed in the sample so that they don't intersect, and the minimum distance between each aggregate is equal to 0.01 mm. This minimum distance is required in order to avoid artificial connection between the aggregates after the FE discretisation.

At $t = 0$, a vertical load of 10 MPa is applied on the upper edge of the sample. The lower edge can move only along the horizontal direction and the left edge only along the vertical direction. The microstructure and boundary conditions are gathered in Figure 4.5.

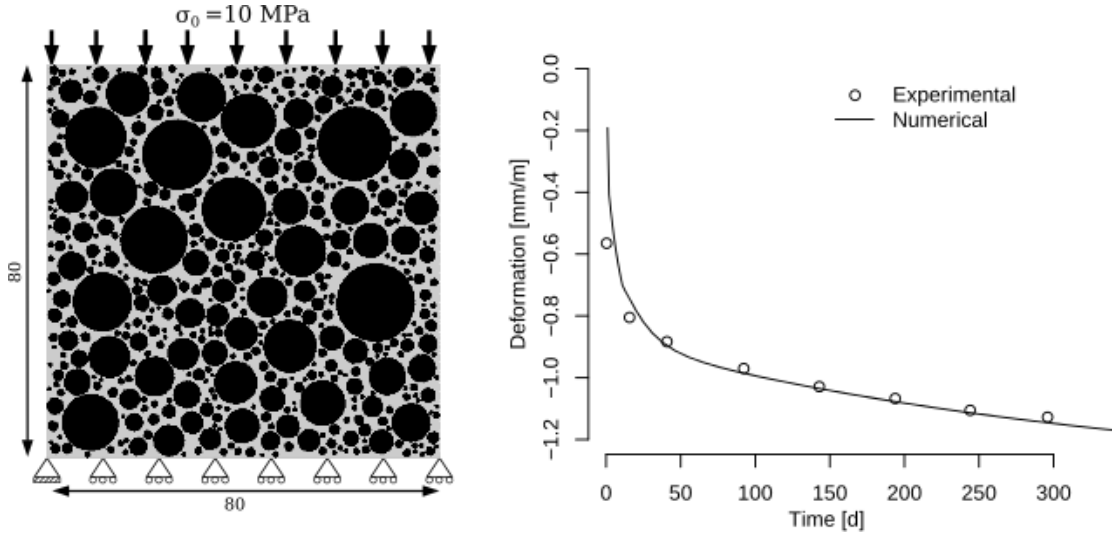


Figure 4.5: Microstructure and boundary conditions for the uni-axial creep test experiment on concrete sample (left). Comparison between numerical and experimental creep curves (right). Data from Dunant [17]

The elastic properties of the aggregates and the cement paste are the same as proposed by Dunant, and are gathered in Table 4.1. The visco-elastic properties of the paste (C_1, E_1) , (C_2, E_2) are varied until agreement between the numerical and the experimental results. The damage is kept equal to 0 as the load in this test is supposed low enough compared to the concrete strength. Figure 4.5 shows the good correlation between the numerical and experimental curves. The damage properties of the material will be investigated in the next chapter.

Table 4.1: Material parameters for the aggregates and cement paste. Elastic properties from [17]. Viscous properties of the paste fitted from experiments using circular aggregates.

Properties [unit]	Aggregates	Cement paste		
		Spring 0	Kelvin-Voigt 1	Kelvin-Voigt 2
Young's modulus [GPa]	58	12	4	4.5
Poisson ratio [-]	0.3	0.3	0.3	0.3
Characteristic time [day]	-	-	10	300

4.3.3 Influence of the microstructure

The overall properties of concrete are highly dependent on its microstructure. The shape of the aggregates plays an important role, and the most simple hypothesis is to consider them circular. However, aggregates in the field vary in terms of shape and angularity, and this can affect the simulated mechanical properties. For example, Du showed that concrete modelled with angular aggregates was more brittle than concrete modelled with circular aggregates [81]. Neville recorded that creep is anisotropic with respect to casting direction, with an anisotropy ratio between 0.6 to 0.8 depending on the aggregates [71].

In the following, three different aggregate shapes were investigated: circles, equilateral triangles, and ellipses (aspect ratio = 0.6). The particle size distribution were generated so that the area covered by a certain aggregate was equal to the area covered by the corresponding circular aggregate. The triangles are the most extreme case of isotropic angular aggregates, while the circles are the most extreme case of smooth aggregates. These two microstructures serve therefore as bounds for the mechanical properties of the simulated concrete. The aggregates are randomly oriented. For the ellipses, the orientation is biased so that the preferred orientation is in the direction of the load, as shown in Figure 4.6.

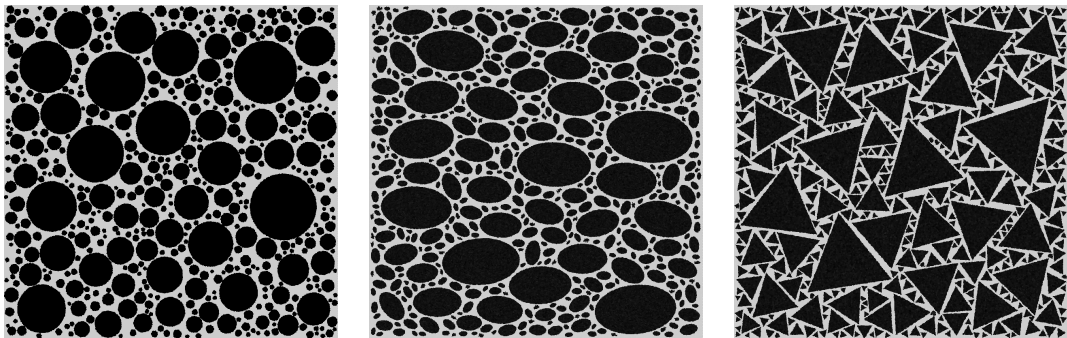


Figure 4.6: Microstructure with circular, ellipsoidal, and triangular aggregates.

For all samples two loading scenario are tested: first a constant load in the vertical direction, then a constant load in the lateral direction. Anisotropy of creep refers to the ratio between the uni-axial creep obtained with the lateral load and the uni-axial creep obtained with the vertical load. The results are shown in Figure 4.7. In these conditions, ellipsoidal aggregates provide an approximation of the anisotropy of creep in the range reported by Neville [71].

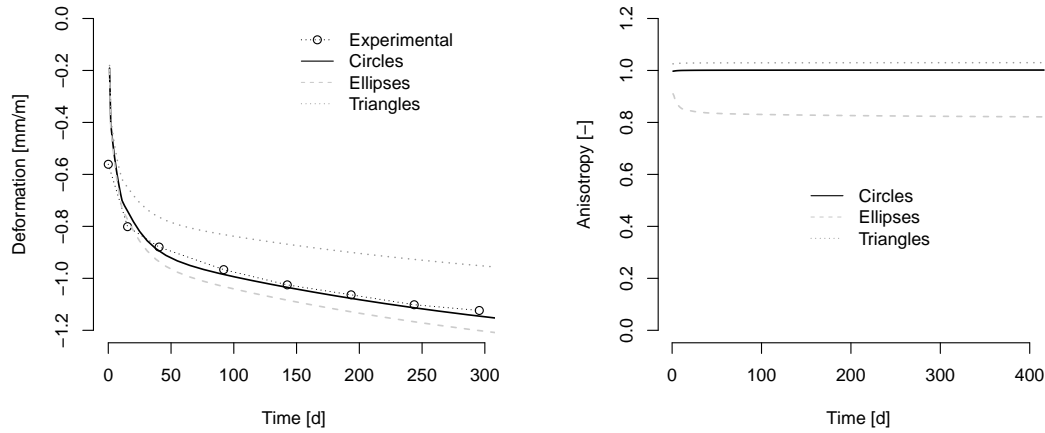


Figure 4.7: Simulated creep curves with different microstructures (left). Anisotropy of creep with respect to casting direction (left).

The effect of the type of aggregates with the same mechanical properties is reported in Figure 4.7. Using triangular aggregates makes the material stiffer as the stress concentrates around the aggregate tips and therefore reduces the importance of the relaxation in the microstructure. The mechanical properties of the cement paste can be adjusted so that the triangular microstructure fits the experimental creep curve. This gives an upper bound of the cement paste properties, as reported in Table 4.2. More precise values could be obtained with a realistic representation of the concrete microstructure as the one obtained from 3D tomography by Escoda and co-workers [82].

Table 4.2: Elastic moduli of the two Kelvin-Voigt elements of the cement paste model fitted with different types of aggregates.

Microstructure	Young's modulus[GPa]	
	Kelvin-Voigt 1	Kelvin-Voigt 2
Circles	4.0	4.5
Ellipses	4.1	4.6
Triangles	3.0	3.7

4.4 Numerical techniques for space-time differential equations

The numerical resolution of the differential equations (4.8) requires a robust integration method in both space and time. The choice of numerical method for the modified ASR model depends on the ability of the method to adapt to different rheological models, the ease of changing the time step during the course of the simulation, and the ability to represent the continuous growth of the gel pockets.

4.4.1 Statement of the problem

Consider a compressible, linear, viscoelastic solid \mathcal{S} occupying a spatial region $\Omega_S(t)$ during a period of time Ω_T which starts at $t = 0$. $\Omega_{S \times T}$ denotes the cartesian product of the space and time domains. From Newton's second law of motion we obtain the balance of momentum of the system:

$$\rho \ddot{\mathbf{u}}(x, y, z, t) - \nabla \cdot \boldsymbol{\sigma}(x, y, z, t) = \mathbf{f}(x, y, z, t), \quad \forall (x, y, z, t) \in \Omega_{S \times T} \quad (4.9)$$

The displacements are equal to a known displacement field \mathbf{u}^F on a boundary of the space domain $\Gamma_{S \times T}^F$ (4.10), while a traction \mathbf{q} is applied to the complementary boundary $\Gamma_{S \times T}^Q$ (4.11).

$$\text{Imposed displacements:} \quad \mathbf{u}(x, y, z, t) = \mathbf{u}^F(x, y, z, t), \quad \forall (x, y, z, t) \in \Gamma_{S \times T}^F \quad (4.10)$$

$$\text{Imposed stress:} \quad \boldsymbol{\sigma}(x, y, z, t) \cdot \mathbf{n}(x, y, z) = \mathbf{q}(x, y, z, t), \quad \forall (x, y, z, t) \in \Gamma_{S \times T}^Q \quad (4.11)$$

The initial displacements are given, which means that $\Gamma_{S \times T}^F$ includes the complete solid at $t = 0$. Furthermore, $\Gamma_{S \times T}^F$ and $\Gamma_{S \times T}^Q$ are constructed so that both of them are not empty at any instant in time. The domain decomposition and boundary conditions are summarised in Figure 4.8.

$$\text{Imposed displacements:} \quad \begin{cases} \Gamma_{S \times T}^F \cap \Omega_S(t = 0) & = \Omega_S(t = 0) \\ \Gamma_{S \times T}^F \cap \Omega_S(t \neq 0) & \neq \emptyset \end{cases} \quad (4.12)$$

$$\text{Imposed stress:} \quad \begin{cases} \Gamma_{S \times T}^Q \cap \Omega_S(t = 0) & = \emptyset \\ \Gamma_{S \times T}^Q \cap \Omega_S(t \neq 0) & \neq \emptyset \end{cases} \quad (4.13)$$

$$\text{Complementarity:} \quad \Gamma_{S \times T}^F \cap \Gamma_{S \times T}^Q = \emptyset \quad (4.14)$$

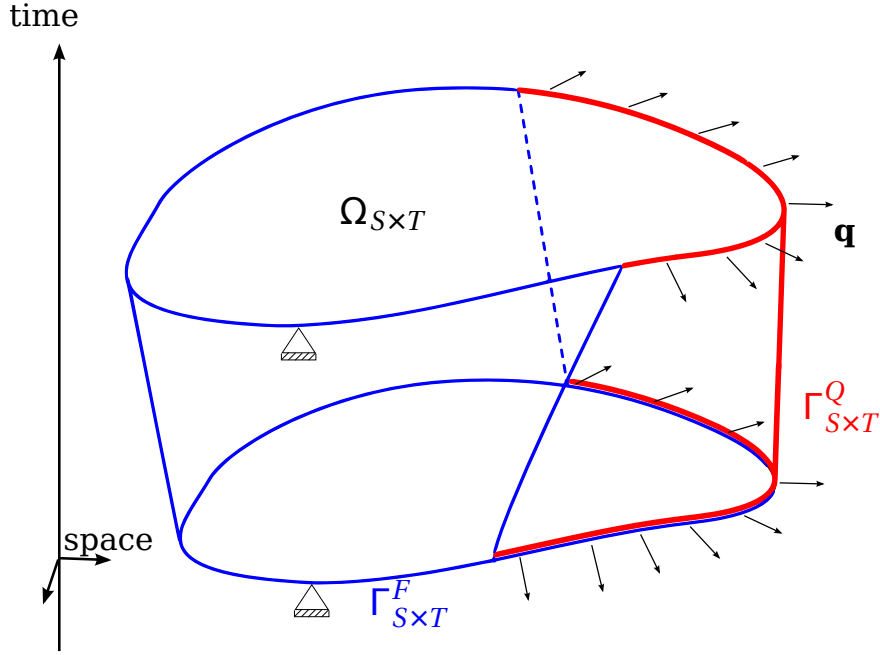


Figure 4.8: Representation in space and time of the domain and its boundaries.

The material behaviour is described by (4.5), in which the material parameters are known functions of space and time. The system of differential equations composed by (4.5, 4.9-4.14) cannot be solved analytically in the general case. It can be solved numerically with FE, FD, or both. The basic concepts of these two methods are:

- The FD method consists in finding the values of \mathbf{u} and its derivatives at specific coordinates. The linear system is composed by (4.9) written at each of the coordinates considered, and approximations of the differential operators to relate \mathbf{u} to its derivative. The displacement between the coordinates is *a priori* unknown.
- In the FE method, the displacement function \mathbf{u} is approximated by a linear combination of functions which derivatives and integrals can be easily calculated (typically, polynomials by parts). The coefficients for the linear combination are the solution of a system of linear equations which is derived from the weak form of the material equilibrium (4.9).

The main difference between FE and FD is that the first approximates the function \mathbf{u} , while the second approximates the integro-differential operators that appear in the constitutive equations. In both cases, the choice of the approximation has a strong influence on the convergence and stability properties of the method. Both approaches have been proposed in the literature for visco-elastic materials, and their advantages and drawbacks are reviewed below.

4.4.2 Finite Differences

The common approach for visco-elasticity is to use FE in space and FD in time. This was first proposed by Zienkiewicz in 1968 for the generalised Kelvin-Voigt material [83]. Later, other integration schemes were proposed, mostly based on the generalised Maxwell model, as in the work of Bažant [84], Guidoum [85], or Zocher [86], among others.

The time domain is divided into a series of discrete instants (t_n). At each of these instants, the displacement and all its time-derivatives are discretised with FE. The resulting system has too many unknowns, so FD are used to provide the necessary additional relations. The state of the system at instant t_{n+1} can then be calculated from the load at that instant and the state of the system at a limited number of previous instant t_n to t_{n-p+1} , where p of the order of the scheme in time. Most schemes are written so that $p = 1$ to reduce the memory cost of the scheme.

Each scheme is specific to a single rheological model. Using the internal structure of the matrices in (4.5) the material behaviour can be rewritten in a form similar to a thermo-elastic material:

$$\sigma(t_{n+1}) = \mathbb{C}^{\text{eq}}(t_{n+1}) : \varepsilon(t_{n+1}) + \sigma_{\text{imp}}^{\text{eq}}(t_{n+1}) \quad (4.15)$$

In (4.15), the equivalent stiffness tensor $\mathbb{C}^{\text{eq}}(t_{n+1})$ and the visco-elastic imposed stress $\sigma_{\text{imp}}^{\text{eq}}(t_{n+1})$ depend on the mechanical properties of each spring and dashpot in the model, their parallel/serial assembly, the length of a time step $\Delta t_{n+1} = t_{n+1} - t_n$, and the values of the strains and the internal variables at the previous instant t_n .

This formulation is compact in term of computational memory, which was a limiting factor at the time these methods were developed. It is furthermore easy to implement in commercial FE programs, as they typically allow the user to write their own iterative procedures. However, the gain in memory comes at the cost of computational time. Indeed, $\sigma_{\text{imp}}^{\text{eq}}(t_{n+1})$ must be recalculated at each time step, and therefore must be the forces applied to the FE system. Furthermore, if the time step changes, then $\mathbb{C}^{\text{eq}}(t_{n+1})$ changes and the whole FE system must be re-assembled again.

Most schemes are restricted to a single rheological model with mechanical properties independent of time, like the first scheme proposed by Zienkiewicz [83] or the one proposed by Zocher [86]. Indeed, the construction of (4.15) changes in a non-trivial way if the stiffness and viscosity tensors of the spring and dashpots change with time, or if the rheological arrangement of the spring and dashpot changes, both of which happening in the case of damage propagation in a visco-elastic media.

$\mathbb{C}^{\text{eq}}(t_{n+1})$ and $\sigma_{\text{imp}}^{\text{eq}}(t_{n+1})$ are determined using FD time-stepping schemes, the exact scheme varying from one author to another. Zienkiewicz and co-workers showed in 1984 that all these schemes belong to a more general family of time-stepping schemes similar to the Newmark θ -method [87, 88, 89, 90]. Their convergence and stability depends strongly on the values of the θ parameters used during the integration. For certain combinations of these parameters, the method is stable only if the time step is small enough. The properties of the chosen method must therefore be checked with care before using it.

In FD schemes, the differentiation is carried out separately in the space and the time domains. It means that the spatial discretisation must remain the same from one time step to another. This can be illustrated by the numerical method of Cecot [66]: he studied discrete crack propagation in an heterogeneous visco-elastic material. In his model, the crack grows discontinuously at discrete instants, and geometry remains constant between instants. This will not allow for the continuous growth of features such as silica gel pockets with time.

For these reasons, these approaches might not be the best suited for the study of ASR. An example of such scheme for the generalised Maxwell model is given in appendix B.

4.4.3 Finite Elements

The idea of FE in space and time was first proposed in 1969 independently by Argyris and Fried for the analysis of time-dependent phenomena [91, 92]. Later, It was used by Hughes, French or Bajer (amongst others) for the analysis of wave propagation in purely elastic media [93, 94, 95], by Adelaide for the analysis of contact friction between elastic solids [96], or by Idesman and co-workers for generalised Maxwell materials [97, 98, 99].

In space-time FE, the displacements are considered a function of both space and time. The velocities, accelerations, strains, strain rates can be obtained at any point of space and time by differentiation of the displacement function, as opposed to FD schemes which are discrete by nature. The displacement field is continuous in space and time, but the derivatives are not.

This makes possible the simulation of spatial domains which change in time, as for example gel pockets growing in the aggregates. Furthermore, since the state of the system is known at any instant, it is possible to characterise precisely the time at which damage initiates in the microstructure.

Still, several concerns are raised for the formulations in the literature:

- A two-field approach is usually preferred, where the velocity field follows a different discretisation than the displacement field. Jump operators in space and time are used to enforce the continuity of the fields from one element to another. An additional set of equations is provided to equate the time-derivative of the displacement field with the velocity field. This improves in some cases the convergence properties of the method but this is at the expense of the symmetry of the system [93]. Therefore such two-field

discretisation cannot be used for large-scale practical engineering applications, nor for the analysis of ASR.

- The discretisation follows generally a Galerkin approach, which is a generalisation of the FE method. In this approach, the virtual function is not chosen in the same space as the displacement function. The convergence properties of the method can be improved with the right shape of the space-time elements [100] or the right choice of the virtual functions [101], but this makes the stability of the method dependent on the length of the time step. Such formulations should therefore be avoided in the case of ASR simulations, where the time step would be changed a lot during the course of the simulation.

A one-field FE discretisation preserves both the symmetry and stability of the system. The size of the system is proportional to the fineness of the time discretisation, and therefore would be too large to solve directly if a large number of steps were to be considered at once. However, the system matrix exhibits a layered structure which allows a step-by-step resolution as proposed for example by Howard in the context of sound waves propagation [102] or Adelaide for frictional contact between elastic solids [96]. With such approach, the size of the subsystem to be solved at each step is equal to the size of the equivalent purely-spatial problem. With the right choice of shape functions, the elementary matrices scale directly with the length of a time interval, which facilitates the change of the time step during the course of the simulation.

The only formulation of the method for visco-elastic materials known to the author was proposed by Idesman and co-workers, based on a generalised Maxwell model. However, his derivation of the method suffers from the two issues described above. In this chapter we propose an original derivation of FE in space and time which does not suffer from the aforementioned limitations. The method is of practical interest for the analysis of ASR as it exhibits the following properties:

- It can represent any spring-dashpot rheological assembly.
- It can account for material properties which change in time.
- It can account for spatial domains which change in time.
- It is unconditionally stable.
- The system to be solved at each step is symmetric.
- With the right choice of shape functions, the elementary matrices scale linearly with the length of a time step.

4.5 Space-time finite elements formulation for generalised visco-elastic materials

In this section, the space-time FE formulation for the linear elastic spring and the linear viscous dashpots are presented.

4.5.1 Weak form

The solid satisfies the equilibrium at any point in time, which translates to the following integral, in which the trial functions \mathbf{v} are chosen in the Sobolev space \mathcal{V}_S^1 defined by the space of derivable functions of (x, y, z) which first derivatives can be integrated.

$$\int_{\Omega_S(t)} \mathbf{v}(x, y, z)^\top (\rho \ddot{\mathbf{u}}(x, y, z, t) - \nabla \cdot \boldsymbol{\sigma}(x, y, z, t)) d\Omega_S = \int_{\Omega_S(t)} \mathbf{v}(x, y, z)^\top \mathbf{f}(x, y, z, t) d\Omega_S \quad (4.16)$$

$\forall t \in \Omega_T \text{ and } \forall \mathbf{v} \in \mathcal{V}_S^1$

\mathbf{v} are chosen as kinematically admissible functions, and therefore obey to the displacements boundary condition (4.10). Integration by part of (4.16) reads:

$$\begin{aligned} & \int_{\Omega_S(t)} \left(\mathbf{v}(x, y, z)^\top \rho \ddot{\mathbf{u}}(x, y, z, t) + \nabla \mathbf{v}(x, y, z)^\top \boldsymbol{\sigma}(x, y, z, t) \right) d\Omega_S \\ &= \int_{\Gamma_S^Q(t)} \mathbf{v}(x, y, z)^\top \mathbf{q}(x, y, z, t) d\Gamma_S^Q + \int_{\Omega_S(t)} \mathbf{v}(x, y, z)^\top \mathbf{f}(x, y, z, t) d\Omega_S \end{aligned} \quad (4.17)$$

\mathbf{v} are chosen in the Sobolev space $\mathcal{V}_{S \times T}^3$, which consists of derivable functions of (x, y, z, t) which third derivatives can be integrated. The third-derivative is justified by the stress rate that appears in (4.19), and which is proportional to the second time-derivative of the strain in the case of visco-elastic materials.

In (4.17) \mathbf{v} can be considered as functions of time. The expression is then derived and integrated over the time domain, which leads ((x, y, z, t) coordinates are omitted):

$$\int_{\Omega_T} \frac{\partial}{\partial t} \left[\int_{\Omega_S} (\mathbf{v}^\top \rho \ddot{\mathbf{u}} + \nabla \mathbf{v}^\top \boldsymbol{\sigma}) d\Omega_S \right] d\Omega_T = \int_{\Omega_T} \frac{\partial}{\partial t} \left[\int_{\Gamma_S^Q} \mathbf{v}^\top \mathbf{q} d\Gamma_S^Q \right] d\Omega_T + \int_{\Omega_T} \frac{\partial}{\partial t} \left[\int_{\Omega_S} \mathbf{v}^\top \mathbf{f} d\Omega_S \right] d\Omega_T \quad (4.18)$$

4.5. Space-time finite elements formulation for generalised visco-elastic materials

The time-derivative operator is switched with the spatial integral, and distributed over the different terms. An additional integration by part over the time domain reduces the order of the third time-derivative which appears on the acceleration term. Finally, the weak form of the material equilibrium reads:

$$\int_{\Omega_{S \times T}} \left(\dot{\mathbf{v}}^T \rho \ddot{\mathbf{u}} + \dot{\mathbf{v}}^T \rho \dot{\mathbf{u}} + \dot{\mathbf{v}}^T \sigma + \nabla \mathbf{v}^T \dot{\sigma} \right) d\Omega_{S \times T} = \int_{\Gamma_{S \times T}^Q} \left(\dot{\mathbf{v}}^T \mathbf{q} + \mathbf{v}^T \dot{\mathbf{q}} \right) d\Gamma_S^Q + \int_{\Omega_{S \times T}} \left(\dot{\mathbf{v}}^T \mathbf{f} + \mathbf{v}^T \dot{\mathbf{f}} \right) d\Omega_{S \times T} \quad (4.19)$$

The calculation of these integrals and derivatives is straight-forward when the spatial domain does not change in time. In this case, the spatial and temporal terms are uncoupled and can be carried out separately. This is however not true in the general case, and will be detailed later.

4.5.2 Constitutive relationship

Hooke's law for linear elastic springs $\sigma = \mathbb{C} \varepsilon$ in (4.19) gives:

$$\int_{\Omega_{S \times T}} \left(\dot{\mathbf{v}}^T \rho \ddot{\mathbf{u}} + \dot{\mathbf{v}}^T \rho \dot{\mathbf{u}} + \dot{\mathbf{v}}^T \mathbb{C} \nabla \mathbf{u} + \nabla \mathbf{v}^T \mathbb{C} \dot{\mathbf{u}} \right) d\Omega_{S \times T} = \int_{\Gamma_{S \times T}^Q} \left(\dot{\mathbf{v}}^T \mathbf{q} + \mathbf{v}^T \dot{\mathbf{q}} \right) d\Gamma_S^Q + \int_{\Omega_{S \times T}} \left(\dot{\mathbf{v}}^T \mathbf{f} + \mathbf{v}^T \dot{\mathbf{f}} \right) d\Omega_{S \times T} \quad (4.20)$$

Similarly, a linear viscous damper defined by its constitutive law $\sigma = \mathbb{E} \dot{\varepsilon}$:

$$\int_{\Omega_{S \times T}} \left(\dot{\mathbf{v}}^T \rho \ddot{\mathbf{u}} + \dot{\mathbf{v}}^T \rho \dot{\mathbf{u}} + \dot{\mathbf{v}}^T \mathbb{E} \dot{\mathbf{u}} + \nabla \mathbf{v}^T \mathbb{E} \dot{\mathbf{u}} \right) d\Omega_{S \times T} = \int_{\Gamma_{S \times T}^Q} \left(\dot{\mathbf{v}}^T \mathbf{q} + \mathbf{v}^T \dot{\mathbf{q}} \right) d\Gamma_S^Q + \int_{\Omega_{S \times T}} \left(\dot{\mathbf{v}}^T \mathbf{f} + \mathbf{v}^T \dot{\mathbf{f}} \right) d\Omega_{S \times T} \quad (4.21)$$

(4.20) and (4.21) both assume that the mechanical properties are independent of space and time. If not, then the right-side integral must be completed with the term corresponding to their respective derivatives.

The space-time finite element method is first described using these two elementary operators, then extended to general visco-elastic material laws.

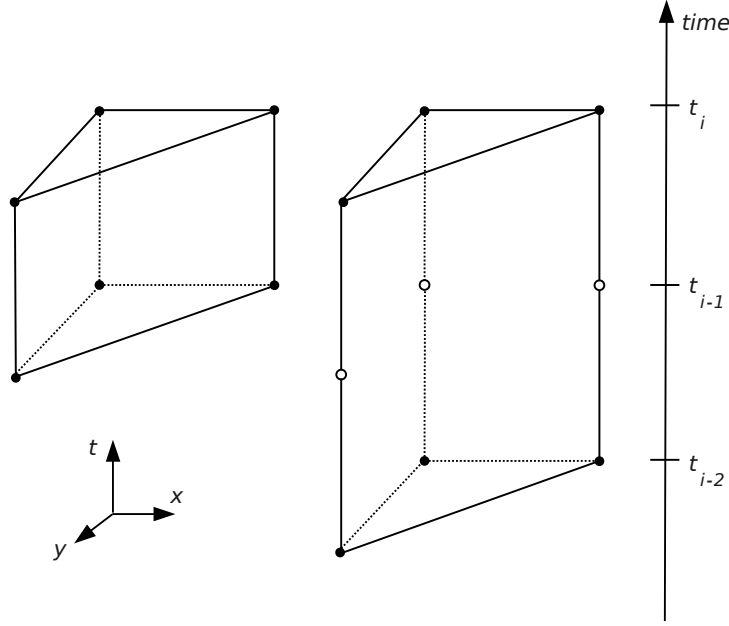


Figure 4.9: Representation of space-time finite elements with two spatial dimensions and time-linear (left) or time-quadratic (right) shape functions.

4.5.3 Finite Element discretisation

A space-time finite element is composed by a single, manifold, space-time domain $\Omega_{S \times T}$, and n nodes defined by their space-time coordinates. The nodes are usually placed on the boundaries of the element, but that is not necessary. The nodes can be further discriminated in p sets (or time planes), the q^{th} time plane containing n_q nodes all located at the same instant t_q . The element then covers the time interval $[t_1, t_p]$. In space-time FE, the term “time slab” is commonly used instead of “time interval” or “time step”. This specific designation emphasises the fact that the state of the material is described continuously, as opposed to FD where the state of the material is only known at discrete instants in time.

In the element, the displacement field is approximated by shape functions $N(x, y, z, t)$. The following derivation is thus equally valid for generalised Galerkin, spectral, or mesh-free methods. Examples of two-dimensional space-time elements are shown in Figure 4.9.

$$\mathbf{u}(x, y, z, t) = \sum_{i=1}^n N_i(x, y, z, t) \mathbf{u}_i, \quad \forall (x, y, z, t) \in \delta\Omega_{S \times T} \quad (4.22)$$

4.5. Space-time finite elements formulation for generalised visco-elastic materials

The time-derivative of their space-derivatives must be integrable and non-zero, which can be enforced by choosing each shape function as the product of a function of space by a function of time. These elements are sometimes referred to as prismatic in the literature [103, 104]. The most immediate choice of shape function are Lagrange polynomials in space multiplied by Lagrange polynomials in time. The orders of the polynomials in time and in space can be chosen independently. If the time function is chosen as piece-wise linear, then all second time-derivatives disappear, leading to a quasi-static form of the equilibrium of momentum. The method still applies for discontinuous functions of space and/or time. In finite elements, the trial functions are chosen in the same space with associated nodal trial displacements \mathbf{v}_i , which can be simplified after insertion in (4.20-4.21).

After discretisation, the material equilibrium in Ω_S is represented by a system of linear equations which unknowns are the nodal displacements \mathbf{u}_i . We introduce the elementary matrices \mathbf{M} , \mathbf{K} , \mathbf{L} , and vectors \mathbf{q} , \mathbf{f} . Under the assumption that the material properties (density, stiffness and viscosity) are constant in space, these matrices and vectors can be written by block so that the block $_{ij}$ represents the interaction between the i^{th} and j^{th} nodes:

$$\mathbf{M}_{ij} = \int_{\Omega_{S \times T}} [\dot{\mathbf{N}}_i \rho \ddot{\mathbf{N}}_j + \ddot{\mathbf{N}}_i \rho \dot{\mathbf{N}}_j + \dot{\mathbf{N}}_i \dot{\rho} \dot{\mathbf{N}}_j] d\Omega_{S \times T} \quad (4.23)$$

$$\mathbf{K}_{ij} = \int_{\Omega_{S \times T}} [\dot{\mathbf{N}}_i \mathbf{C} \dot{\mathbf{N}}_j + \nabla \mathbf{N}_i \mathbf{C} \nabla \mathbf{N}_j + \nabla \mathbf{N}_i \dot{\mathbf{C}} \nabla \mathbf{N}_j] d\Omega_{S \times T} \quad (4.24)$$

$$\mathbf{L}_{ij} = \int_{\Omega_{S \times T}} [\dot{\mathbf{N}}_i \mathbf{E} \dot{\mathbf{N}}_j + \nabla \mathbf{N}_i \mathbf{E} \nabla \mathbf{N}_j + \nabla \mathbf{N}_i \dot{\mathbf{E}} \nabla \mathbf{N}_j] d\Omega_{S \times T} \quad (4.25)$$

$$\mathbf{q}_i = \int_{\Gamma_{S \times T}^Q} [\dot{\mathbf{N}}_i \mathbf{q}_i + \mathbf{N}_i \dot{\mathbf{q}}_i] d\Gamma_{S \times T}^Q \quad (4.26)$$

$$\mathbf{f}_i = \int_{\Omega_{S \times T}} [\dot{\mathbf{N}}_i \mathbf{f}_i + \mathbf{N}_i \dot{\mathbf{f}}_i] d\Omega_{S \times T} \quad (4.27)$$

The discretised form of the material equilibrium for the spring and the dashpot elements are:

$$\text{spring: } \forall i \in [1, n], \quad \sum_{j=1}^n [\mathbf{M}_{ij} + \mathbf{K}_{ij}] \mathbf{u}_j = \mathbf{q}_i + \mathbf{f}_i \quad (4.28)$$

$$\text{dashpot: } \forall i \in [1, n], \quad \sum_{j=1}^n [\mathbf{M}_{ij} + \mathbf{L}_{ij}] \mathbf{u}_j = \mathbf{q}_i + \mathbf{f}_i \quad (4.29)$$

In these vectors and matrices, larger blocks can be identified based on the time plane decomposition of the element. Each line of block corresponds to the material equilibrium at a certain time plane. Each column of blocks corresponds to the influence of a certain time plane on all others.

In (4.28), the indices i and j can be read as the indices of the time planes rather than the indices of the nodes, and they cover the interval $[1, p]$ rather than $[1, n]$. From now on, the indices in the matrices always refer to the indices of the time planes, unless stated otherwise.

The elements are hereafter assembled to provide a complete discretisation of the space-time domain. The assembly is described here only for spring elements. Dashpot elements are treated similarly.

4.5.4 Assembly

The solid is discretised into a set of nodes and associated linear elastic elements. This divides the time domain into a set of time planes (or instants) separating the time slabs. In any time slab, the elementary contributions from all elements are assembled the same way as the purely spatial FE in this slab. However, the assembly in time of time slabs does not follow this rule. Indeed, at the boundary between two consecutive elements, the material equilibrium is provided either by the element before, or by the element after. Their nodal contributions are opposite one from each other, and only one of them is required.

The final system is constructing by choosing, for each instant, the corresponding line of block in the assembled matrices of the time slab just before that instant¹. The final assembled matrix has a structure in blocks similar to the elements, where each line of blocks represents the material equilibrium at an instant. The matrix is banded by blocks and asymmetric.

For example, the final system for time-linear elements has the following structure after application of the initial boundary condition. In that case, $\mathbf{M} = 0$ and is omitted without loss of generality. The structure of the matrix in (4.30) is consistent with the one found by Adelaide for friction problems [96].

$$\begin{bmatrix} \mathbf{I} & 0 & 0 & 0 & \dots \\ \mathbf{K}_{01} & \mathbf{K}_{11} & 0 & 0 & \dots \\ 0 & \mathbf{K}_{12} & \mathbf{K}_{22} & 0 & \dots \\ & & \ddots & \ddots & \ddots \end{bmatrix} \begin{bmatrix} \mathbf{u}_0 \\ \mathbf{u}_1 \\ \mathbf{u}_2 \\ \vdots \end{bmatrix} = \begin{bmatrix} \mathbf{u}_0 \\ \mathbf{q}_1 + \mathbf{f}_1 \\ \mathbf{q}_2 + \mathbf{f}_2 \\ \vdots \end{bmatrix} \quad (4.30)$$

¹The time slab after could be chosen as well. This corresponds to the problem where the final state of the system is known, and the solution is therefore its initial state. This approach is however not suitable in the case of irreversible phenomena, and therefore only the causal approach is described.

4.5. Space-time finite elements formulation for generalised visco-elastic materials

The system can then be solved as a block-diagonal system. This pivot involves the inversion or solving of blocks of the global matrix corresponding to single time slabs. This iterative approach is similar to the one proposed earlier by Howard or Bajer [102, 95].

$$[\mathbf{M}_{ii} + \mathbf{K}_{ii}] \mathbf{u}_i = \mathbf{q}_i + \mathbf{f}_i - \sum_{j=i-p}^{i-1} [\mathbf{M}_{ji} + \mathbf{K}_{ji}] \mathbf{u}_j \quad (4.31)$$

Thus, at each step of the pivot only the elements from a single time slab need to be assembled. \mathbf{u}_j are known either from the boundary conditions or from the previous iterations. The number of unknowns in (4.31) is equal to the number of unknowns of the purely spatial system with the same spatial discretisation. This makes the proposed method suitable for large engineering problems. The system for linear viscous elements is:

$$[\mathbf{M}_{ii} + \mathbf{L}_{ii}] \mathbf{u}_i = \mathbf{q}_i + \mathbf{f}_i - \sum_{j=i-p}^{i-1} [\mathbf{M}_{ji} + \mathbf{L}_{ji}] \mathbf{u}_j \quad (4.32)$$

Springs and dashpots are described by the same iterative procedure, and so are their combinations in series and parallel. In the most general case, the system is:

$$\mathbb{K}_{ii} \mathbf{x}_i = \mathbf{b}_i - \sum_{j=i-p}^{i-1} \mathbb{K}_{ji} \mathbf{x}_j \quad (4.33)$$

\mathbb{K} is referred to hereafter as the assembled matrix, and the block \mathbb{K}_{ii} as the system matrix. The system matrix is squared, positive definite as proven below.

By identification with (4.31-4.32), the assembled matrices and vectors for the spring and the dashpot are:

$$\text{Spring: } \mathbb{K} = \mathbf{M} + \mathbf{K}, \quad \mathbf{x} = \mathbf{u}, \quad \mathbf{b} = \mathbf{q} + \mathbf{f} \quad (4.34)$$

$$\text{Dashpot: } \mathbb{K} = \mathbf{M} + \mathbf{L}, \quad \mathbf{x} = \mathbf{u}, \quad \mathbf{b} = \mathbf{q} + \mathbf{f} \quad (4.35)$$

4.5.5 Generalisation to arbitrary linear visco-elastic behaviour

In this section, the expression of \mathbb{K} is given first for the Kelvin-Voigt and Maxwell elementary modules as examples, and then for any visco-elastic material obeying to (4.5).

Kelvin-Voigt material

The constitutive equation of a Kelvin-Voigt module of stiffness \mathbb{C} and viscosity \mathbb{E} is:

$$\sigma = \mathbb{C} \varepsilon + \mathbb{E} \dot{\varepsilon} \quad (4.36)$$

This relation can be inserted in (4.19) and subsequent relations. The resulting assembled matrix is therefore simply the sum of the elementary contributions of the spring and the dashpot, reading:

$$\text{Kelvin-Voigt: } \mathbb{K} = \mathbf{M} + \mathbf{K} + \mathbf{L}, \quad \mathbf{x} = \mathbf{u}, \mathbf{b} = \mathbf{q} + \mathbf{f} \quad (4.37)$$

Maxwell material

The constitutive equation for a Maxwell module of stiffness \mathbb{C} and viscosity \mathbb{E} depends on one additional internal variable α :

$$\sigma = \mathbb{C} (\varepsilon - \alpha) \quad (4.38)$$

$$\sigma = \mathbb{E} \dot{\alpha} \quad (4.39)$$

α is a second-order tensor with the same symmetry properties than σ . It derives then from a displacement field \mathbf{a} the same way ε derives from \mathbf{u} .

(4.38) can be inserted in the FE approach described above using $\mathbf{u} - \mathbf{a}$ as the unknown field, and so can (4.39) using \mathbf{a} as the unknown field. This gives the following system:

4.5. Space-time finite elements formulation for generalised visco-elastic materials

$$[\mathbf{M} + \mathbf{K}] [\mathbf{u} - \mathbf{a}] = \mathbf{f} + \mathbf{q} \quad (4.40)$$

$$[\mathbf{M} + \mathbf{L}] [\mathbf{a}] = \mathbf{f} + \mathbf{q} \quad (4.41)$$

After rearrangement of the terms, the system reads:

$$\left[\begin{bmatrix} \mathbf{M} & 0 \\ 0 & 0 \end{bmatrix} + \begin{bmatrix} \mathbf{K} & -\mathbf{K} \\ -\mathbf{K} & \mathbf{K} \end{bmatrix} + \begin{bmatrix} 0 & 0 \\ 0 & \mathbf{L} \end{bmatrix} \right] \begin{bmatrix} \mathbf{u} \\ \mathbf{a} \end{bmatrix} = \begin{bmatrix} \mathbf{f} + \mathbf{q} \\ 0 \end{bmatrix} \quad (4.42)$$

Therefore, the assembled matrix, unknowns and right-side vectors for the Maxwell material are:

$$\text{Maxwell: } \mathbb{K} = \begin{bmatrix} \mathbf{M} + \mathbf{K} & -\mathbf{K} \\ -\mathbf{K} & \mathbf{K} + \mathbf{L} \end{bmatrix}, \quad \mathbf{x} = \begin{bmatrix} \mathbf{u} \\ \mathbf{a} \end{bmatrix}, \quad \mathbf{b} = \begin{bmatrix} \mathbf{q} + \mathbf{f} \\ 0 \end{bmatrix} \quad (4.43)$$

Generalisation

In (4.42), \mathbf{K} and \mathbf{L} are arranged in matrices which have the exact same block decomposition as the rheological matrices of the thermodynamical system (4.5) adapted for Maxwell materials. Generalisation is therefore immediate. Using p and q as the indices of the stiffness and viscosity tensors in (4.5), the assembled matrix for generalised visco-elastic material reads:

$$\text{General case: } \mathbb{K} = \begin{bmatrix} \mathbf{M} + \mathbf{K}_{00} + \mathbf{L}_{00} & \dots & \mathbf{K}_{0p} + \mathbf{L}_{0p} & \dots \\ \vdots & & & \\ \mathbf{K}_{0p} + \mathbf{L}_{0p} & & \mathbf{K}_{pq} + \mathbf{L}_{pq} & \\ \vdots & & & \end{bmatrix}, \quad \mathbf{x} = \begin{bmatrix} \mathbf{u} \\ \vdots \\ \mathbf{a}_p \\ \vdots \end{bmatrix}, \quad \mathbf{b} = \begin{bmatrix} \mathbf{q} + \mathbf{f} \\ \vdots \\ 0 \\ \vdots \end{bmatrix} \quad (4.44)$$

Notably, the assembled matrix corresponding to the cement paste behaviour (4.8) is:

$$\text{Cement paste: } \mathbb{K} = \begin{bmatrix} \mathbf{M} + \mathbf{K}_0 & -\mathbf{K}_0 & -\mathbf{K}_0 \\ -\mathbf{K}_0 & \mathbf{K}_0 + \mathbf{K}_1 + \mathbf{L}_1 & \mathbf{K}_0 \\ -\mathbf{K}_0 & \mathbf{K}_0 & \mathbf{K}_0 + \mathbf{K}_2 + \mathbf{L}_2 \end{bmatrix}, \quad \mathbf{x} = \begin{bmatrix} \mathbf{u} \\ \mathbf{a}_1 \\ \mathbf{a}_2 \end{bmatrix}, \quad \mathbf{b} = \begin{bmatrix} \mathbf{q} + \mathbf{f} \\ 0 \\ 0 \end{bmatrix} \quad (4.45)$$

The described method can therefore be used to simulate any rheological arrangement of springs and dashpots. Its stability and convergence properties are detailed in the following section.

4.6 Stability and convergence properties of the method

The elementary matrices are first expanded for shape functions expressed as traditional Lagrange polynomials. A simple dependency between these and the time discretisation is obtained, which makes it possible to assemble the system matrix only once during the course of the simulation. Using these relations, the stability of the method is formally proved. Then the convergence properties are numerically estimated.

In this section only, the indices i and j refer to the nodes of the element, and indices k and l to its time planes.

4.6.1 Properties of the elementary matrices

Here the elementary matrices for spring and dashpot elements are derived in some detail for specific elements. It is shown that under some conditions (easily verified), the elastic, viscous and acceleration terms of the assembled matrix scale with Δt the length of a time slab the following way:

$$\mathbf{K} \propto 1 \quad (4.46)$$

$$\mathbf{L} \propto \frac{1}{\Delta t} \quad (4.47)$$

$$\mathbf{M} \propto \frac{1}{\Delta t^2} \quad (4.48)$$

Under these conditions, the system matrix need only to be assembled for the first step of the simulation. At any other step it is sufficient to multiply the first system matrix by the appropriate factor to obtain the system matrix at that step. This property makes it very easy to adjust the time step during the course of the simulation, for example to characterise sudden increases in boundary conditions or damage.

The conditions and proof of these properties are given below.

Conditions

Consider a prismatic space-time finite element. Such element contains $n^S \times n^T$ nodes discriminated by their coordinates in space and in time. Each node can be identified by the indices $s \in [0, n^S]$ and $t \in [0, n^T]$. The time coordinates vary from 0 to Δt . The material properties are taken constant in both space and time. The nodal coordinates of the node (s, t) are given by:

$$(x, y, z, t)_{st} = ((x, y, z)_s, t_t) \quad (4.49)$$

The shape functions are taken as product of functions of space multiplied by functions of time:

$$N_{st}(x, y, z, t) = N_s^S(x, y, z) \times N_t^T(t) \quad (4.50)$$

Partition of unity is enforced in both domains:

$$\sum_{s=0}^{n^S} N_s^S = \sum_{t=0}^{n^T} N_t^T = 1 \quad (4.51)$$

Notably:

$$\sum_{t=0}^{n^T} \dot{N}_t^T = \sum_{t=0}^{n^T} \ddot{N}_t^T = 0 \quad (4.52)$$

The iso-parametric transformation from the real time $t \in [0, \Delta t]$ to the reference time $\theta \in [0, 1]$ gives:

$$\forall t \in [0, n^T] \quad \dot{\mathbf{N}}_t^T \propto \frac{1}{\Delta t} \quad (4.53)$$

$$\forall t \in [0, n^T] \quad \ddot{\mathbf{N}}_t^T \propto \frac{1}{\Delta t^2} \quad (4.54)$$

Elements which respect this conditions are referred thereafter as time-regular elements.

Stiffness matrix

The elastic term (4.24) can be integrated in the time domain first, leading to:

$$\mathbf{K}_{ij} = \left[\mathbf{N}_{t_i}^T \mathbf{N}_{t_j}^T \right]_0^{\Delta t} \int_{\Omega_S} \nabla \mathbf{N}_{s_i}^S \mathbb{C} \nabla \mathbf{N}_{s_j}^S d\Omega_S \quad (4.55)$$

Blocks can be therefore discriminated according to the position of the nodes i and j in time:

$$\left[\mathbf{N}_{t_i}^T \mathbf{N}_{t_j}^T \right]_0^{\Delta t} = 1 \quad \text{if } t_{t_i} = t_{t_j} = \Delta t \quad (4.56)$$

$$\left[\mathbf{N}_{t_i}^T \mathbf{N}_{t_j}^T \right]_0^{\Delta t} = -1 \quad \text{if } t_{t_i} = t_{t_j} = 0 \quad (4.57)$$

$$\left[\mathbf{N}_{t_i}^T \mathbf{N}_{t_j}^T \right]_0^{\Delta t} = 0 \quad \text{otherwise} \quad (4.58)$$

\mathbf{K} is independent of time as is $\int_{\Omega_S} \nabla \mathbf{N}_{s_i}^S \mathbb{C} \nabla \mathbf{N}_{s_j}^S d\Omega_S$. Furthermore, the assembled matrix \mathbf{K} is diagonal by blocks, and each diagonal block corresponds to the purely spatial FE system at that time. This proves that the elastic term in the system matrix is positive definite.

$$\mathbf{K}_{kl} = 0 \quad \forall k \neq l \quad (4.59)$$

Viscosity matrix

The same way, the viscous term (4.25) becomes:

$$\mathbf{L}_{ij} = \left[\mathbf{N}_{t_i}^T \dot{\mathbf{N}}_{t_j}^T \right]_0^{\Delta t} \int_{\Omega_S} \nabla \mathbf{N}_{s_i}^S \mathbb{E} \nabla \mathbf{N}_{s_j}^S d\Omega_S \quad (4.60)$$

Which gives depending on the position of the nodes i and j in time:

$$\left[\mathbf{N}_{t_i}^T \dot{\mathbf{N}}_{t_j}^T \right]_0^{\Delta t} = \dot{\mathbf{N}}_{t_j}^T(\Delta t) \quad \text{if } t_{t_i} = \Delta t \quad (4.61)$$

$$\left[\mathbf{N}_{t_i}^T \dot{\mathbf{N}}_{t_j}^T \right]_0^{\Delta t} = -\dot{\mathbf{N}}_{t_j}^T(0) \quad \text{if } t_{t_i} = 0 \quad (4.62)$$

$$\left[\mathbf{N}_{t_i}^T \dot{\mathbf{N}}_{t_j}^T \right]_0^{\Delta t} = 0 \quad \text{otherwise} \quad (4.63)$$

Therefore \mathbf{L} is inversely proportional to the time interval Δt . Furthermore, the following relation between the blocks of the assembled matrix \mathbf{L} is verified:

$$\sum_{l=k-n^T}^k \mathbf{L}_{lk} = 0 \quad (4.64)$$

This further proves that the viscous term in the system matrix is positive definite.

Mass matrix

Finally, the acceleration term (4.23) follows a similar treatment where the $\dot{\mathbf{N}}^T$ are replaced with $\ddot{\mathbf{N}}^T$ and $\nabla \mathbf{N}^S$ by \mathbf{N}^S . Therefore \mathbf{M} is inversely proportional to the time interval squared, and the relation between the blocks \mathbf{M}_{ji} is verified:

$$\sum_{l=k-n^T}^k \mathbf{M}_{lk} = 0 \quad (4.65)$$

This further proves that the acceleration term in the system matrix is positive definite. Therefore, the system matrix is positive definite as a sum of positive definite matrices.

4.6.2 Stability

The method is unconditionally stable, which allows to choose freely the time step during the course of the simulation. This is proved here with a Kelvin-Voigt material. The proof extends to any visco-elastic material by decomposing its behaviour in a mass, a viscous and an elastic term. The elements use the same space-time discretisation and shape functions as in the previous section.

If we impose the following boundary conditions (4.66-4.68), the method is stable if $\lim_{k \rightarrow \infty} \mathbf{u}_k = 0$.

$$\mathbf{u}_{l \in [0, n^T - 1]} = \mathbf{u}_0 \quad > \quad 0 \quad (4.66)$$

$$\mathbf{f}(t) = 0, \quad \forall t \in \Omega_T \quad (4.67)$$

$$\mathbf{q}(t) = 0, \quad \forall t \in \Omega_T \quad (4.68)$$

Insertion of (4.59) in the system matrix yields:

$$[\mathbf{M}_{kk} + \mathbf{K}_{kk} + \mathbf{L}_{kk}] \mathbf{u}_k = - \sum_{l=k-n^T}^{k-1} [\mathbf{M}_{lk} + \mathbf{L}_{lk}] \mathbf{u}_l \quad (4.69)$$

If $0 < \mathbf{u}_l \leq \mathbf{u}_{l_0}$, which is true for the initial boundary conditions (4.66):

$$0 < [\mathbf{M}_{kk} + \mathbf{K}_{kk} + \mathbf{L}_{kk}] \mathbf{u}_k \leq - \left[\sum_{l=k-n^T}^{k-1} [\mathbf{M}_{lk} + \mathbf{L}_{lk}] \right] \mathbf{u}_{l_0} \quad (4.70)$$

Then, using relations (4.64) and (4.65):

$$0 < \mathbf{u}_k \leq [\mathbf{M}_{kk} + \mathbf{L}_{kk}] [\mathbf{M}_{kk} + \mathbf{K}_{kk} + \mathbf{L}_{kk}]^{-1} \mathbf{u}_{l_0} \quad (4.71)$$

Using λ_{kk} the highest eigenvalue of $[\mathbf{M}_{kk} + \mathbf{L}_{kk}] [\mathbf{M}_{kk} + \mathbf{K}_{kk} + \mathbf{L}_{kk}]^{-1}$, and the fact that the matrices are positive definite:

$$0 < \mathbf{u}_k < e^{-\lambda_{kk} \Delta t} \mathbf{u}_{l_0} \quad (4.72)$$

Then the series of (\mathbf{u}_k) is bounded by 0 and by $e^{-\lambda_{kk} t_k} \mathbf{u}_0$, the later tending toward 0 with increasing k . The algorithm is therefore unconditionnally stable and convergent and does not create artificial oscillations while converging to the solution.

In the next section, the convergence properties of the method are numerically investigated.

4.6.3 Convergence

The algorithm is used on a simple test case for which an analytic solution is known. In this numerical example, the spatial discretisation is kept the same from one simulation to another, but the time discretisation is refined. Comparison with the analytic solution gives an estimate of the error of the numerical method as a function of the fineness of the time discretisation.

Description of the problem

The sample is a homogeneous rectangular plate of size $w \times h = 1000 \times 1000$. At $t = 0$, a constant load σ_0 is applied on the upper edge of the sample. The bottom edge can only move along the horizontal axis and the bottom left corner fixed in the vertical direction to prevent global translation of the sample.

Distances are given in millimetres and durations in days.

Plane stress is assumed; this has no influence on the convergence properties of the method with respect to time. The geometry and mechanical boundary conditions of the plate are summarised in Figure 4.12.

Material behaviour

The sample is considered as an homogeneous Burgers' material, composed of a Maxwell and a Kelvin-Voigt module placed in series (see Figure 4.10) [105].

To represent this behaviour using the proposed method, two internal state variables are used: the displacement of the Maxwell dashpot \mathbf{a}_{MX} and the displacement of the Kelvin-Voigt module \mathbf{a}_{KV} . In (4.33), the final matrix and vectors are:

$$\text{Burgers' model: } \mathbb{K} = \begin{bmatrix} \mathbf{M} + \mathbf{L}_{MX} & -\mathbf{K}_{MX} & -\mathbf{K}_{MX} \\ -\mathbf{K}_{MX} & \mathbf{K}_{MX} + \mathbf{L}_{MX} & \mathbf{K}_{MX} \\ -\mathbf{K}_{MX} & \mathbf{K}_{MX} & \mathbf{K}_{MX} + \mathbf{K}_{KV} + \mathbf{L}_{KV} \end{bmatrix}, \quad \mathbf{x} = \begin{bmatrix} \mathbf{u} \\ \mathbf{a}_{MX} \\ \mathbf{a}_{KV} \end{bmatrix} \quad (4.73)$$

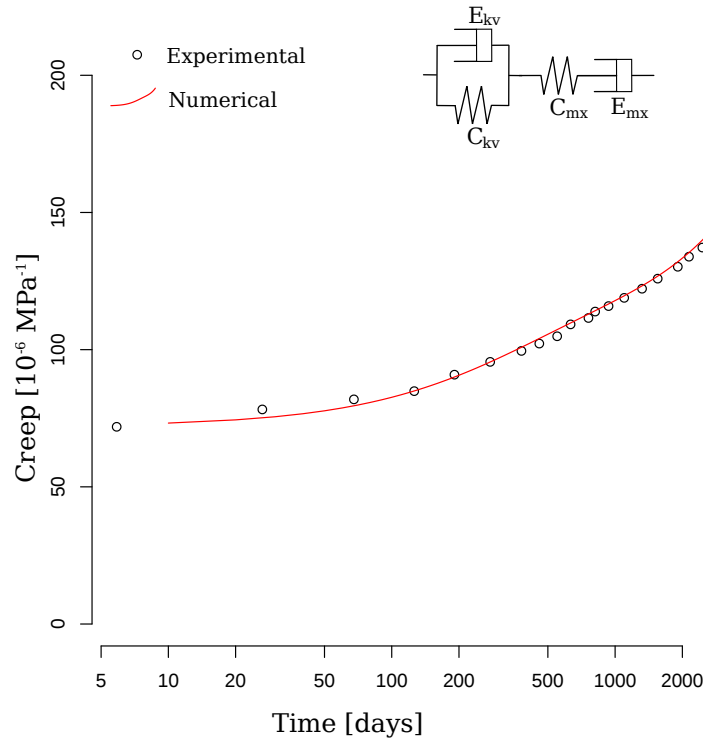


Figure 4.10: Experimental creep function of concrete (data from [106]) and numerical fit obtained with a Burgers' model.

This specific model is chosen as it provides a good approximation of homogenised concrete behaviour [107, 108]. Material parameters are identified from a long-term creep experiment from the work of Bengougam [106] (see Figure 4.10). Since the material is isotropic, four parameters were fitted: two Young's moduli and two characteristic times τ so that $\mathbb{E} = \tau \mathbb{C}$. The Poisson's ratio was assumed to be 0.3, which is commonly used for hardened concrete. The values are gathered in Table 4.3. Dynamic effects are neglected.

Table 4.3: Material parameters for the Burger's model

Properties [unit]	Maxwell module	Kelvin-Voigt module
Young's modulus [GPa]	14	30
Poisson ratio [-]	0.3	0.3
Characteristic time [day]	5000	300

Space-time discretisation

The sample is meshed with prismatic elements with a triangular base in the space domain as shown in Figure 4.9. A Delaunay triangulation is used to obtain a set of triangles which are then extruded in the time direction to complete the space-time mesh. The fineness of the time discretisation and the order of the shape functions in time are varied to evaluate their influence on the error estimates. The initial mesh and its deformed states at selected instants are shown in Figure 4.11.

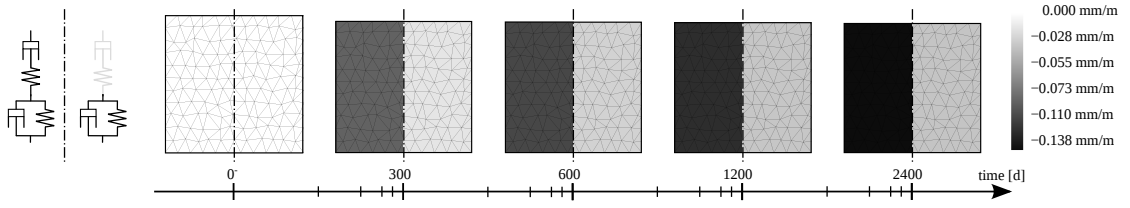


Figure 4.11: Initial and deformed states of the sample plate. The grey level shows the magnitude of the vertical total strain (left) and the vertical strain of the Kelvin-Voigt module (right).

Error estimates

The error in displacement and the error in energy are used to evaluate the convergence properties of the method with respect to the time discretisation. In the following, Δt is the interval between two consecutive time planes, and the $(\cdot)_{\Delta t}$ subscript denotes the numerical solution obtained in that interval. The displacements and the energy error are defined from the reference analytic solution (subscript $(\cdot)_R$):

$$\mathbf{e}(\Delta t) = \int_{\Omega_{S \times T}} \left| 1 - \frac{\mathbf{u}_{\Delta t}}{\mathbf{u}_R} \right| d\Omega_{S \times T} \quad (4.74)$$

$$\mathbf{E}(\Delta t) = \int_{\Omega_{S \times T}} \left| 1 - \frac{\boldsymbol{\varepsilon}_{\Delta t} : \boldsymbol{\sigma}_{\Delta t}}{\boldsymbol{\varepsilon}_R : \boldsymbol{\sigma}_R} \right| d\Omega_{S \times T} \quad (4.75)$$

In this case, the rectangular geometry is simple and an exact solution is known. The displacement field is given by the creep functions \mathbb{J} of the Maxwell and Kelvin-Voigt modules. The origin being located at the bottom-left corner, the analytic solution is:

$$\mathbb{J}_{MX}(t) = \frac{t + \tau_{MX}}{\tau_{MX} E_{MX}} \quad (4.76)$$

$$\mathbb{J}_{KV}(t) = \frac{1 - e^{-t/\tau_{KV}}}{E_{KV}} \quad (4.77)$$

$$\mathbf{u}_R = \begin{bmatrix} x [\mathbb{J}_{MX}(t) + \mathbb{J}_{KV}(t)] \sigma_0 \\ y [v_{MX} \mathbb{J}_{MX}(t) + v_{KV} \mathbb{J}_{KV}(t)] \sigma_0 \end{bmatrix} \quad (4.78)$$

The mechanical energy is uniform in the plate as are the strain and stress fields. The energy is:

$$\varepsilon_R : \sigma_R = [\mathbb{J}_{MX}(t) + \mathbb{J}_{KV}(t)] \sigma_0^2 \quad (4.79)$$

Convergence analysis

The error estimates in displacements and energy are plotted in Figure 4.12. The errors converge monotonically towards machine precision. Both error estimates converge linearly with respect to the time discretisation. The energy error and the displacement error follow the same trend since the stress is constant through space and time. This numerical results illustrate the convergence and stability of the proposed method for these specific problems.

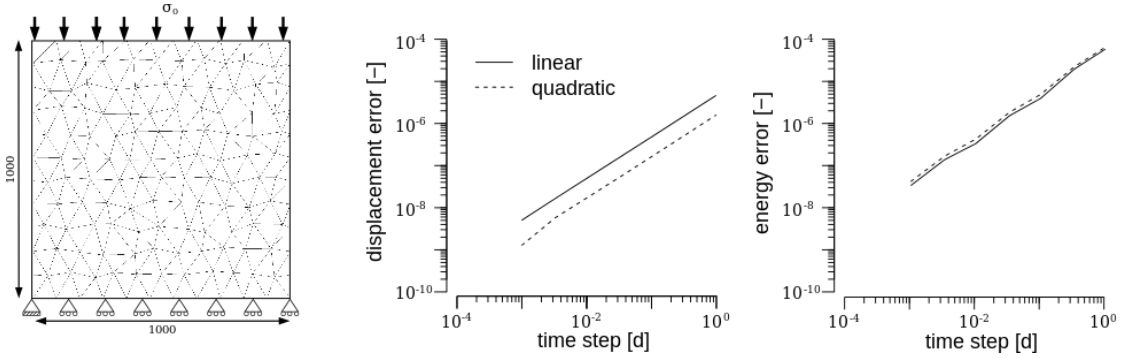


Figure 4.12: Boundary conditions (left), error in displacement as a function of the time step (middle), error in energy as a function of the time step (right) for the homogeneous plate problem. Time steps are normalised with the lowest characteristic time of the material. Error estimates are given for time-linear and time-quadratic elements.

The convergence rates are independent of the order of the time discretisation. This is consistent with known results on the convergence rates of FD schemes of the same order (see for example the work of Zienkiewicz and co-workers [87, 88, 89]). Indeed, the proposed method for any specific set-up could be understood as an implicit backward Euler scheme at the first order in time, or an implicit backward Houbolt scheme at the second order in time. However, it differs from these more common schemes by providing a single formulation which can integrate any shape functions of space and time, on any space-time domain, with non-constant material properties. This additional flexibility induces no penalty in the convergence or stability of the method. In the next section, we illustrate how moving boundaries can be represented.

4.7 Representation of moving boundaries

In this section, we propose two methods to represent material inclusions with time-dependent radius. The first method is based on a conforming meshing of the boundaries of the inclusion in space and time. The second method is based on extended finite elements (XFEM) in space and time. Both methods increase the computational cost. However, the first method induces mesh discrepancies effect, and therefore the second method is preferred.

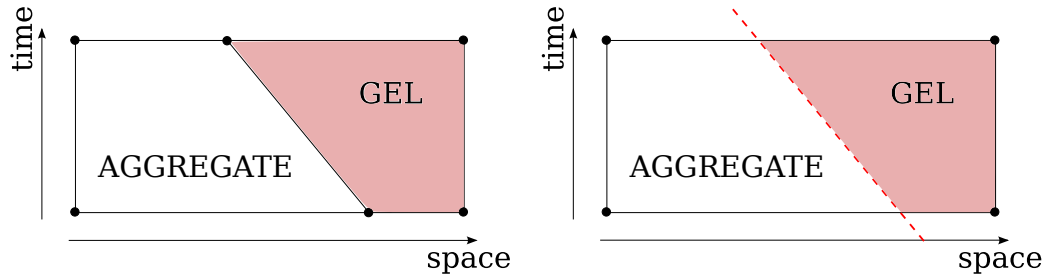


Figure 4.13: Representation of the growth of silica gel pockets in aggregates with time, with a conforming mesh (left) or XFEM (right).

4.7.1 Space-time conforming mesh

In this set-up, the domain covered by each space-time element adjacent to the growing inclusion is stitched so that it follows explicitly the boundaries of the inclusion, as shown in Figure 4.13. These elements do not respect the condition stated in section 4.6.1, and therefore their elementary matrices are non-trivial functions of the time interval.

Indeed, the elementary matrices are calculated as integrals over the space-time domain of the derivatives of shape functions. For time-regular elements, the integrals are uncoupled and can be carried out separately in space and in time. For time-irregular elements, the integrals cannot be uncoupled and the whole space-time domain must be treated as one single domain.

Time-irregular elements must be treated the same way irregular elements are treated in purely spatial FE. The shape functions are described on a simple reference element (also called iso-parametric element) on which the derivation and integration operators are easily calculated. The real element is given as the result of a specific geometrical transformation of the reference element (called the iso-parametric transformation). The shape functions of the real element are then equal to the composition of the iso-parametric transformation with the shape functions of the reference element.

In the following, we show how to calculate the high-order derivatives which appear in (4.23-4.25).

Statement of the problem

Consider a reference element with its associated local coordinates $\xi = (\xi, \eta, \zeta, \theta)$ and a transformed element with its associated coordinates $\mathbf{x} = (x, y, z, t)$ (see Figure 4.14). The coordinates in the transformed element are given from the coordinates in the reference element by the following geometrical transformation:

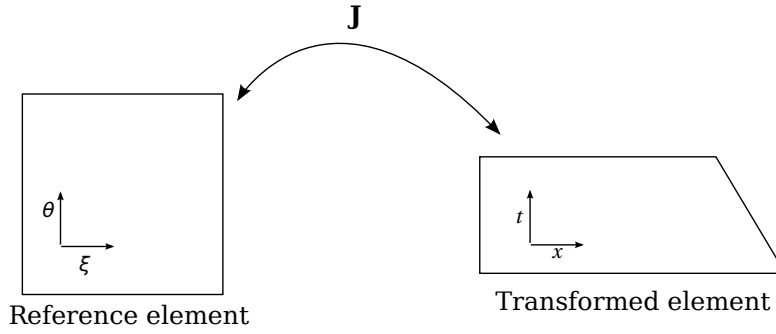


Figure 4.14: Reference element with local coordinates (left) and transformed element with global coordinates (right).

$$x_j = N_i(\xi) \bar{x}_{ij} \quad (4.80)$$

In (4.80) and throughout this section, the convention is that there is summation over repeated indices (Einstein notation), and derivation over indices is marked by commas. N_i is the i^{th} shape function in the *reference* element, and \bar{x}_i the global coordinates of the associated node in the *transformed* element¹.

¹The shape functions in (4.80) are the geometrical shape functions of the element. When using XFEM, these are not the same as the shape functions used for the approximation of the displacement in (4.22).

The calculations of the first derivatives are well-known in FE analysis. The calculations of the higher-order derivatives are more complex and rarely stated. Dhatt and Touzot gave expressions for the second-order derivatives in [109].

In the following section, we show how to calculate any high-order derivative from the iso-parametric elements. The index i refers to the indices of the nodes. The roman indices a, b, c, \dots refers to derivatives of the global coordinates, while the greek indices $\alpha, \beta, \gamma, \dots$ refers to derivatives of the local coordinates.

First derivatives

The derivative in the reference $\frac{\partial}{\partial \xi}$ and transformed $\frac{\partial}{\partial x}$ elements can be obtained by the chain derivation rule:

$$\frac{\partial}{\partial \xi} = \frac{\partial x}{\partial \xi} \frac{\partial}{\partial x} \quad (4.81)$$

The object $\frac{\partial x}{\partial \xi}$ is identified as the jacobian matrix J . Using this matrix, (4.81) is rewritten as:

$$\xi_{,\alpha} = J_{\alpha a} x_{,a} \quad (4.82)$$

The coefficients of J are calculated from the derivatives of the shape functions of the reference element and the coordinates of the nodes in the transformed element:

$$J_{\alpha a} = N_{i,\alpha} \bar{x}_{ia} \quad (4.83)$$

The inverse relation is more useful in practice:

$$x_{,a} = J_{a\alpha}^{-1} \xi_{,\alpha} \quad (4.84)$$

J and J^{-1} are actually second-order tensors, and their concept can be extended to any higher-order derivative. In the following, the chain derivation rule is thoroughly applied to obtain the second and third derivatives in the global coordinates as a function of the derivatives in the local coordinates. Their exact expressions are given in order to facilitate their implementation in a FE program.

Second derivatives

Chain derivation of (4.82) and (4.84) give the following relations:

$$\xi_{,\alpha\beta} = J_{\alpha a,\beta} x_{,a} + J_{\alpha a} J_{\beta b} x_{,ab} \quad (4.85)$$

$$x_{,ab} = J_{a\alpha,b}^{-1} \xi_{,\alpha} + J_{a\alpha}^{-1} J_{b\beta}^{-1} \xi_{,\alpha\beta} \quad (4.86)$$

In general, it is easier to calculate the derivatives of J rather than the derivatives of J^{-1} . Indeed, derivation of (4.83) gives:

$$J_{\alpha a,\beta} = N_{i,\alpha\beta} \bar{x}_{ia} \quad (4.87)$$

$$J_{\alpha a,\beta\gamma\dots} = N_{i,\alpha\beta\gamma\dots} \bar{x}_{ia} \quad (4.88)$$

Inserting (4.85) in (4.86) gives the following final expression for $x_{,ab}$:

$$x_{,ab} = \left[-J_{a\alpha}^{-1} J_{b\beta}^{-1} J_{\alpha a,\beta} J_{b\gamma}^{-1} \right] \xi_{,\gamma} + \left[J_{a\alpha}^{-1} J_{b\beta}^{-1} \right] \xi_{,\alpha\beta} \quad (4.89)$$

Third derivatives

Chain derivation of (4.85) gives:

$$\xi_{,\alpha\beta\gamma} = J_{\alpha a,\beta\gamma} x_{,a} + [J_{\alpha a,\beta} J_{\gamma b} + J_{\alpha a,\gamma} J_{\beta b} + J_{\alpha a} J_{\beta b,\gamma}] x_{,ab} + J_{\alpha a} J_{\beta b} J_{\gamma c} x_{,abc} \quad (4.90)$$

Insertion of (4.84) and (4.89) in (4.90) gives the final relation for $x_{,abc}$:

$$\begin{aligned}
 x_{,abc} = & \left[J_{a\alpha}^{-1} J_{b\beta}^{-1} J_{c\gamma}^{-1} \right] \left[\left(J_{\alpha d, \beta} J_{\gamma e} + J_{\alpha d, \gamma} J_{\beta e} + J_{\alpha d} J_{\beta e, \gamma} \right) \left(J_{d\delta}^{-1} J_{e\epsilon}^{-1} J_{\delta d, \epsilon} J_{e\zeta}^{-1} \right) \right. \\
 & \left. - J_{\alpha f, \beta \gamma} J_{f\zeta}^{-1} \right] \xi_{, \zeta} \\
 & - \left[J_{a\alpha}^{-1} J_{b\beta}^{-1} J_{c\gamma}^{-1} \right] \left[J_{\alpha d, \beta} J_{\gamma e} + J_{\alpha d, \gamma} J_{\beta e} + J_{\alpha d} J_{\beta e, \gamma} \right] \left[J_{d\delta}^{-1} J_{e\epsilon}^{-1} \right] \xi_{, \delta \epsilon} \\
 & + \left[J_{a\alpha}^{-1} J_{b\beta}^{-1} J_{c\gamma}^{-1} \right] \xi_{, \alpha \beta \gamma} \quad (4.91)
 \end{aligned}$$

Recursive relations for any higher order could be obtained but are not in the scope of the current work.

Numerical example

These relations are implemented and verified on a simple example for which the analytic solution is known. The solution of the problem shown in section 4.6.3 is independent of the actual dimensions of the plate, and these can change with time as long as the plate remains rectangular. The width of the plate is then changed in time with the following function: $w(t) = 800 + 200 e^{-t/300}$ (distances in millimetres, time in days). The space-time mesh is obtained by the appropriate homothety of the space-time mesh of the reference plate.

The deformed mesh at different instants is shown in Figure 4.15. The boundary conditions and convergence properties of this problem are gathered in Figure 4.16. The stresses and strains calculated are equal to the stresses and strains calculated for the reference plate, and the convergence rate is not affected. This proves the sound implementation of the method, as well as its ability to represent time-dependent material boundaries.

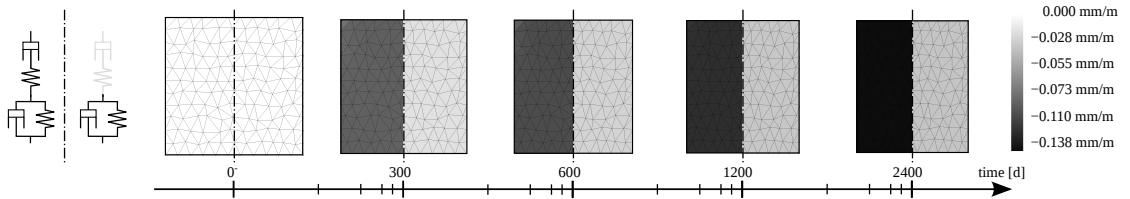


Figure 4.15: Initial and deformed states of the time-dependent plate. The grey level shows the magnitude of the vertical total strain (left) and the vertical strain of the Kelvin-Voigt module (right).

Summary

The first, second and third derivatives in the global coordinates are obtained from the first, second and third derivatives in the local coordinates by application of (4.84), (4.89) and (4.91). These are complex tensorial relations and their estimation requires intensive computations.

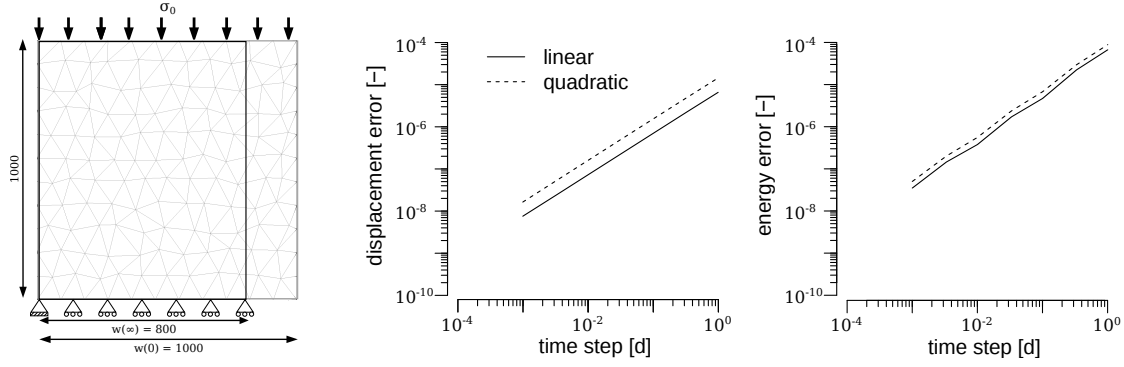


Figure 4.16: Boundary conditions (left), error in displacement as a function of the time step (middle), error in energy as a function of the time step (right) for the homogeneous time-dependent plate problem. Time steps are normalised with the lowest characteristic time of the material. Error estimates are given for time-linear and time-quadratic elements.

Given D the number of spatial dimensions of the domain, the number of operations to calculate the second (respectively third) derivatives of a function in the general case scales with $(D + 1)^3$ (respectively $(D + 1)^6$). However, if the element is regular in time, it scales only with D^2 for both the second and third derivatives. Indeed, if the element obeys to the condition stated in section 4.6.1, then all terms corresponding to the coupling between space and time disappear. The following relations are verified, where J^{-1*} is the inverse jacobian matrix of the equivalent purely-spatial element.

$$\begin{bmatrix} \frac{\partial^2}{\partial x \partial t} \\ \frac{\partial^2}{\partial y \partial t} \\ \frac{\partial^2}{\partial z \partial t} \end{bmatrix} = \frac{1}{\Delta t} J^{-1*} \begin{bmatrix} \frac{\partial^2}{\partial \xi \partial \theta} \\ \frac{\partial^2}{\partial \eta \partial \theta} \\ \frac{\partial^2}{\partial \zeta \partial \theta} \end{bmatrix}, \quad \begin{bmatrix} \frac{\partial^3}{\partial x \partial t^2} \\ \frac{\partial^3}{\partial y \partial t^2} \\ \frac{\partial^3}{\partial z \partial t^2} \end{bmatrix} = \frac{1}{\Delta t^2} J^{-1*} \begin{bmatrix} \frac{\partial^3}{\partial \xi \partial \theta^2} \\ \frac{\partial^3}{\partial \eta \partial \theta^2} \\ \frac{\partial^3}{\partial \zeta \partial \theta^2} \end{bmatrix} \quad (4.92)$$

In ASR, the silica gel pockets are very small, and meshing them with space-time conforming meshes as proposed in this section might lead to very large computational problems, and mesh artifacts. In his model, Dunant used extended finite elements to represent them without meshing. In the following, the XFEM approach is adapted to the time domain for the analysis of gel pocket growth.

4.7.2 Extended finite elements in space and time

In the extended finite element method, the displacement function is enriched with discontinuous functions which represent discontinuities of the material. Moës and co-workers developed it first for the analysis of crack growth [110], and then adapted it for holes and material inclusions in [111, 112]. In the later case, the enrichment functions are weakly discontinuous: the displacement is continuous over the boundaries of an inclusion, but the strain is not.

In any element that contains a XFEM discontinuity, the enriched displacement field reads:

$$\mathbf{u}(x, y, z, t) = \sum_{i=1}^n N_i(x, y, z, t) \mathbf{u}_i + \sum_{i=1}^n N_i(x, y, z, t) \phi_i(x, y, z, t) \bar{\mathbf{u}}_i \quad (4.93)$$

In (4.93), ϕ_i are the enrichment functions associated to the node i , and $\bar{\mathbf{u}}_i$ the associated nodal displacement. The enrichment function is a hat-like function adapted from [112]. It is given by (4.94), where (x_i, y_i, z_i) are the spatial coordinates of the node, proj_t the projection operator on the surface of the inclusion at instant t , and $\|\cdot\|$ the 3-D euclidian norm. The time appears implicitly in the projection operator. The function is maximum on the boundary and equal to 0 on any on the node.

$$\phi_i(x, y, z, t) = \|(x_i, y_i, z_i) - \text{proj}_t(x_i, y_i, z_i)\| - \|(x, y, z) - \text{proj}_t(x, y, z)\| \quad (4.94)$$

Using these functions, the space-time finite element approach described above can be used without modification.

Integration of this function is carried out on each element by extruding a regular grid of spatial Gauss points in the time direction. This creates a series of regular grids placed at instants corresponding to the Gauss points required for the temporal integration of the projection function appearing in (4.94). This increases the computational time by a factor scaling to g^D , where g is the number of divisions of the regular grid and D the number of spatial dimensions. However, at each Gauss points the derivatives are easily evaluated with use of (4.92).

Numerical example

In this section, we evaluate the performance of the method implementation of the method in AMIE. The sample consists in a homogeneous rectangular plate of size $w \times h = 1000 \times 1000$ containing a growing inclusion of radius $r = 200t$, with $t \in [0, 1]$. The inclusion and the plate are elastic in order to provide direct comparison with the spatial XFEM already implemented in AMIE. The mechanical properties of each phase in this setup are gathered in Table 4.4.

The average strain and stress in the sample are plotted as a function of the radius of the inclusion in Figure 4.17. The solution is compared with a purely spatial XFEM solution as implemented by Dunant in [12]. This proves the sound implementation of the method and its ability to represent silica gel pockets zones growing with arbitrary functions of time.

The small fluctuations appearing in the strain curves comes from instants where a new band of elements are enriched. The error in stress comes for the larger part from the band of interface elements, and while this error is quite large (on the order of the MPa) it is small compared

Table 4.4: Material parameters for the growing inclusion example.

Properties [unit]	Plate	Growing inclusion
Young's modulus [GPa]	60	22
Poisson ratio [-]	0.3	0.3
Imposed expansion [-]	-	0.5

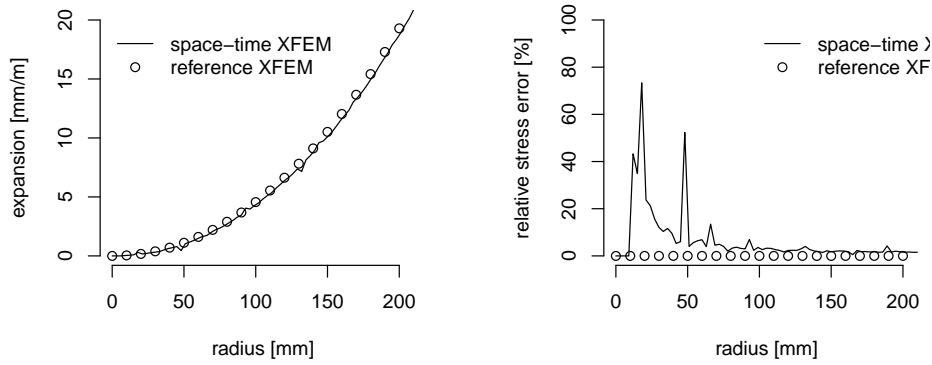


Figure 4.17: Average expansion (left) and stress (right) imposed by a single gel pocket as a function of the radius.

to the applied stress (on the order of the GPa). Furthermore, the error is concentrated in the elements lying at the interface between the growing inclusion and the plate. These errors are therefore related to the quadrature used to compute the forces on the interface elements, and are reduced when the number of Gauss points increases.

4.7.3 Conclusion

Two methods to account for moving boundaries in space-time FE were presented.

- A space-time conforming discretisation of the problem leads to heavy calculations when determining the derivatives of the shape functions, which makes difficult the assembly and the post-processing of the system. Furthermore, they can lead to meshing artifacts if the elements are too stretched compared to the reference elements.
- Space-time XFEM requires more Gauss points for their exact integration, but the determination of the derivatives of the shape functions at each of the Gauss points is simpler. However, this method introduces larger errors at the interface of the inclusion.

In both cases the elements do not satisfy the conditions established in section 4.6.1, meaning that the elementary matrices of these elements cannot be easily calculated when the time step changes.

Using XFEM in space and time is the natural extension of the model of Dunant for ASR. The error on the stress calculated in interface elements has little influence on the damage propagation in a visco-elastic ASR simulation since these elements cannot be damaged in the model of Dunant. This simplification represents the fact that the interface between the gel pocket and the aggregate is imperfect, and avoids the complete debonding of the gel pockets which is one cause of the overestimation of damage in the model of Charpin [23].

In the next chapter, the space-time finite element method is used as a basis for a visco-damage algorithm.

5 Continuum damage in space-time finite elements

In the previous chapter, a novel space-time finite element method was proposed to simulate linear visco-elastic materials such as the cement paste. In this chapter, it is completed with a continuum damage model. The damage is computed with an algorithm which searches for the instant at which damage occurs. By doing so, the energy dissipated by visco-elasticity is properly accounted for, and the irreversibility of the system is enforced through the simulation. This algorithm is independent to the size of the time step as opposed to other non-linear solvers. The method is validated with tensile tests on heterogeneous microstructures. This example proves the importance of the order in which the elements are damaged. Using this algorithm, the fracture criterion of the cement paste is identified based on available data from the literature.

5.1 Modelling degradation of quasi-brittle materials

The modelling of ASR at the microstructure level requires numerical tools that can capture when and where cracks will be opened, and how they propagate in time and space. In finite elements, two classes of methods are commonly used: discrete cracks and continuum damage approaches. They are reviewed below, and the damage approach is found to be the best suited for the microstructural simulation of ASR.

5.1.1 Discrete crack

In discrete crack approaches, the cracks are explicitly described as discontinuities in the microstructure. The easiest way to introduce such discontinuity is by disconnecting the elements one from another as the crack grows. Remeshing techniques are used to capture more precisely the geometry of the crack during its propagation, as for example in the work of Wang [113]. However, Jirásek and Patzák showed in [114] that each time the mesh is adapted, artificial oscillations are introduced in the stress and strain fields. This introduces in the simulation numerical artefacts that might dominate the crack propagation.

Discrete cracks can also be represented by extended finite elements (XFEM) as proposed first by Moës and co-workers [110]. With this technique, the shape functions of the element through which the crack lies are enriched with a discontinuity. This approach alleviates the issue of remeshing at the expense of a computationally intensive assembly of the FE system. However, remeshing is still frequently used to improve the precision of the solution around the crack tip.

Modelling of multiple discrete crack growth as in the case of ASR leads to numerical difficulties as it is not clear which crack must propagate at each step of the simulation. For example, Budyn and co-workers carry out a stability analysis at each crack tip that might grow to decide which one prevails [115]. Furthermore, crack initiation remains an open question. In the work of Wang and Cecot, pre-existing cracks are placed in the sample at specific locations before the simulation. For XFEM, cracks are initiated using criteria similar to non-local damage models, as did Areias and Belytschko in [116]. Merging and branching of cracks require dedicated algorithm and intensive geometry computations, notably in three dimensions where the crack pattern becomes highly complex.

In the current work, another difficulty lies in the representation in space-time finite elements of the propagating crack. Cecot used a simple approach by deciding that the crack propagates instantaneously at discrete instants, thus allowing a decoupling between visco-elasticity and crack growth [66]. This approach is highly dependent on the time step. The use of XFEM in space-time for crack propagation would provide a continuous crack growth, but this becomes a challenging task numerically as the crack geometry cannot be a priori known, and must be found with numerically costly iterations.

5.1.2 Continuum damage

In continuum damage mechanics, the material behaviour is supplemented with state variables representing defects, voids, or micro-cracks in the underlying microstructure. This approach was first introduced by Kachanov for the analysis of creep rupture of steel [117] and then became widespread for the analysis of quasi-brittle materials.

In this approach, the description of the damage in the material can be arbitrarily complex, and can therefore represent damage from different mechanical causes and simulate elaborate mechanical behaviours. For example, the Mazars model commonly used for concrete distinguishes between damage in tension and in compression, each of which having a different impact on the material behaviour [118]. The ASR structural models of Capra or Grimal account separately for the internal damage caused by ASR and mechanical damage caused by external loads [44, 45].

In damage models, the material behaviour is written using a non-linear relation between the stress and the strain. The damage variables are given as a monotonically increasing function of the maximum strain reached previously during the simulation. This ensures the irreversibility of the phenomenon as no additional damage can occur during unloading.

However, the method is very sensitive to the size and orientation of the elements in the mesh, as shown for example by de Borst [119] or Jirásek and co-workers [120]. Indeed, the damage localises in a band one element wide, which can then be arbitrarily small. This means that as the mesh is refined, the energy dissipated by the damage in the elements tends to 0 while it should converge towards a strictly positive value as proven by Rice in [121]. The rupture of the sample becomes more and more fragile as the mesh is refined, which is clearly un-physical as the material behaviour should not depend on the mesh, which is a purely numerical object.

This led to the development of non-local models as proposed by Pijaudier and Bažant in [122]. In non-local damage models, the state variables are averaged over a certain area for the purpose of determining the damage and its evolution. This area is an approximation of the size of a representative elementary volume of the underlying microstructure, and can be measured experimentally as the width of the fracture process zone [123].

In the case of ASR, the degradation in the microstructure forms a complex pattern as multiple cracks grow simultaneously in the aggregates and, at later age, in the cement paste. In that regard, continuum damage approaches are preferable to discrete crack approaches as the latter require specific and intensive developments to simulate the crack initiation, propagation, and junction in the microstructure.

5.2 Numerical methods for continuum damage mechanics

Using damage mechanics with finite elements requires the usage of non-linear solvers. The Newton-Raphson method is mostly used, possibly supplemented with arc-length control. The properties of these methods are well-known, and they can be found with examples of implementation in most reference books on the finite element method, see for example Dhatt and Touzot [109] or Zienkiewicz [103, 104]. More recently, Dunant and co-workers proposed a new class of iterative algorithm to treat such material behaviour [61, 124]. These two algorithms are detailed below and the algorithm of Dunant is chosen as a basis for a new damage algorithm.

5.2.1 Numerical non-linear solvers

In the Newton-Raphson method or similar non-linear solvers, the damage is calculated from a global perspective: the non-linear system of equations is transformed into a linear system from which the damage increment in all elements can be calculated. At each iteration, a lot of elements might be damaged, which might lead to cases where the crack band is actually larger than that which is imposed by the non-local nature of the model. Therefore, these algorithms require small loading steps in order to characterise precisely the damage propagation.

The sensitivity to the loading path is critical in the case of visco-elastic damage. Most visco-elastic damage models assume a constant damage rate over a time step as in the work of Kim and co-workers [125] or Darabi and co-workers [126, 127]. However, that might lead to onset of damage *before* the material reaches its stress or strain limit. As visco-elastic materials are history-dependent, miscalculating the history of the system leads to wrong estimations of the material response.

These issues are related to the fact that the Newton-Raphson method is a purely numerical approach which does not account for the physical nature of the problem. Indeed, this method solves for a final degraded state of the simulated sample. Given a non-linear material law, this has no unique solution from a mathematical perspective (notably, complete failure of the sample always satisfies the non-linear material law). This comes from the fact that each iteration of the Newton-Raphson procedure does not necessarily describe a feasible material state. Between two iterations some elements might be damaged even though they would not have reached their failure criterion when considering a continuous transition from one state to another.

The method therefore shows strong limitations when damage occurs in various different zones of the sample. For example, Comby-Peyrot used a non-local Mazars model in her ASR simulation [55]. The simulation predicted complete failure of the cement paste, which is not observed in reality and shows the need for a more elaborate damage algorithm.

5.2.2 Algorithmically irreversible mechanics

Dunant proposed in [61, 124] a novel class of algorithms that solve not only for the final state of the material, but for the complete transformation path that lead there. These are referred to as algorithmically irreversible mechanics as the algorithm imposes that the first and second principles of thermodynamics are satisfied during the entire damage process, while they are only satisfied at discrete instants in time with Newton-Raphson solvers. The damage found is the minimum damage such that no element is damaged before it reaches its failure criterion.

At each step of the algorithm, the final load is applied to the sample. Elements are sorted with respect to their failure criterion expressed as a monotonic function of the stress, the strain, or the other state variables. The set of elements with the highest criterion are damaged by an amount chosen so that at the next iteration, this set of elements changes. This specific value of the damage is determined using a bisection search at each step of the algorithm.

The algorithm defines a chain of events in which damage increases in the microstructure. Each event in the sequence is a valid transitional state of the material. One can find the load at which this event occurred, and therefore the corresponding instant. In turn, one can find the dissipation caused by visco-elasticity before this instant. The algorithm is therefore suited to characterise the interaction between creep and damage in visco-elastic models. The question of how much damage is introduced at each event remains open. Dunant was able to calculate

it by bisection since his simulations did not account for visco-elastic dissipation.

For visco-elastic material, this would require the damage to be expressed explicitly as a function of time, but it is not always possible to know a priori the nature of this function. Therefore, in the present work, we let the damage increase at each event by a fixed amount. This discontinuous description of the material behaviour naturally tends towards a continuous description when the damage increment tends toward 0.

5.3 Damage algorithm in space and time

In this section the algorithm of Dunant is modified to account for visco-elasticity of the material behaviour. The thermodynamic validity is demonstrated. Effect of tolerances on the time or damage increments are also discussed.

A quasi-brittle visco-elastic solid is simulated between two instants t_{init} and t_{final} . The algorithm aims at finding the degradation caused by given external forces $\mathbf{f}(t)$ and surface tractions $\mathbf{q}(t)$.

The material behaviour is supplemented with a damage parameter d so that:

$$(1-d) \begin{bmatrix} \mathbb{C}_{00} & \dots & \mathbb{C}_{0p} & \dots \\ \vdots & & & \\ \mathbb{C}_{0p} & & \mathbb{C}_{pq} & \\ \vdots & & & \end{bmatrix} \begin{bmatrix} \varepsilon \\ \vdots \\ \alpha_p \\ \vdots \end{bmatrix} + (1-d) \begin{bmatrix} \mathbb{E}_{00} & \dots & \mathbb{E}_{0p} & \dots \\ \vdots & & & \\ \mathbb{E}_{0p} & & \mathbb{E}_{pq} & \\ \vdots & & & \end{bmatrix} \begin{bmatrix} \dot{\varepsilon} \\ \vdots \\ \dot{\alpha}_p \\ \vdots \end{bmatrix} = \begin{bmatrix} \sigma \\ \vdots \\ 0 \\ \vdots \end{bmatrix} \quad (5.1)$$

In this chapter, a single scalar damage variable is used. However, the damage can be represented by more elaborate mathematical objects (vectors, tensors), and notably be distributed differently over each spring and dashpot as in the cement paste model proposed in the previous chapter.

The material is further defined by its failure surface in the stress-strain space. Any mechanical state above this surface is not physically valid and cannot be reached by the material at any point of space and time. All mechanical states below this surface are valid, and failure cannot occur until the material state has reached the failure surface.

The damage is a yet unknown function of time. In the general case, it is not possible to know a priori the nature of this function, so it is approximated here by a piece-wise constant function. The values of the function are fixed, but the location of the discontinuities in time are not: the aim of the algorithm is to find these specific instants. It is assumed that the damage can only take a finite number of values sorted by ascending order. Transition from one state of damage to the next only occurs when the material has reached its failure surface. The material can

only go to its next higher damage state.

By doing so, damage cannot decrease, and a damage state cannot be skipped in the process. By increasing the number of available states, the damage tends toward a continuous function of time.

The distance to the failure surface is characterised by a criterion C . This is a continuous and monotonic function of the mechanical state of the material (stress, strain, viscous strains, damage, or their derivatives). $C = 0$ defines the iso-surface at which damage occurs.

The algorithm aims at finding the series of instants (t_n) at which the material goes from one state of damage to another and the corresponding damage and displacement fields (d_n) and (\mathbf{x}_n) . It can be expressed as followed:

1. Start with known t_n , d_n and \mathbf{x}_n
2. Assemble a space-time finite element system between t_n and t_{final} as in the previous chapter
3. Resolution of the system gives $\mathbf{x}_{final}(d_n)$
4. Using \mathbf{x}_n and $\mathbf{x}_{final}(d_n)$, use the finite element approximation to calculate $C(t)$ for each element of the mesh
5. Find $t_{n+1} < t_{final}$ the first instant when an element reaches $C = 0$. Two cases arise:
 - If t_{n+1} does not exist, then the algorithm has converged; d_n, \mathbf{x}_{final} is the state of the material at t_{final}
 - Otherwise, increment the damage in that specific element and proceed to the next iteration

The algorithm starts with $t_0 = t_{init}$. d_0 and \mathbf{x}_0 are given by the initial boundary conditions. The algorithm imposes to re-assemble the FE system at each step. However, this is immediate in the case of space-time finite elements since the elementary matrices scale with the length of the time interval as proven in the previous chapter.

5.3.1 Properties of the series of (t_n)

The algorithm stated above constructs a series of strictly increasing (t_n) . Indeed, if $t_{n+1} < t_n$, it would mean that damage should have occurred in the past, and so that the state of the sample at t_n is not valid. This is proven more formally below.

The state of the sample at instant t_n is considered valid if no element e at that state is above its failure surface. Furthermore, since the damage is discontinuous at t_n , the criterion is also discontinuous and the following inequalities must be true before and after that instant.

$$\begin{cases} C_e(t_n^-) \leq 0 \\ C_e(t_n^+) \leq 0 \end{cases}, \forall e \quad (5.2)$$

It is assumed that the material is at equilibrium at t_{init} , and so that (5.2) is true and strictly enforced at t_0^+ :

$$C_e(t_0^+) < 0, \forall e \quad (5.3)$$

At constant damage d_0 , the material state variables are continuous between t_0 and t_{final} , and so is the criterion. The first instant at which any element in the mesh reaches $C = 0$ is therefore strictly higher than t_0 . Since the number of elements in the mesh is finite, t_1 is therefore strictly higher than t_0 .

In the following e^* denotes the set of elements that reach their criterion at t_0 . In practice, this set is restricted to one element, but this is not necessarily the case. The criterion right before t_1 takes the following values:

$$\begin{cases} C(t_1^-) = 0 & \text{if } e \in e^* \\ C(t_1^-) < 0 & \text{otherwise} \end{cases} \quad (5.4)$$

Only the elements in e^* are damaged at t_1 :

$$\begin{cases} d(t_1^+) > d(t_1^-) & \text{if } e \in e^* \\ d(t_1^+) = d(t_1^-) & \text{otherwise} \end{cases} \quad (5.5)$$

When the damage occurs, the state of the material can only move away from its failure surface. The value of the criterion can therefore only decrease when the damage increases. The following inequalities are then true:

$$\begin{cases} C(t_1^+) < C(t_1^-) = 0 & \text{if } e \in e^* \\ C(t_1^+) = C(t_1^-) < 0 & \text{otherwise} \end{cases} \quad (5.6)$$

By recurrence, for all n (5.2) is true and strictly enforced at t_n^+ , and $t_{n+1} > t_n$.

This result is obtained for a criterion that is strictly decreasing for increasing damage. If the criterion is constant for increasing damage, then the damage in the e^* must increase again at t_n until the criterion falls below 0 (or ceases to exist if the material becomes completely damaged). From a practical perspective, it means that some damage states in e^* never occur and can be removed from the series of damage states.

Furthermore, the series of (t_n) is finite since both the number of elements in the mesh and the number of possible states in each element are.

In the next section, it is shown that the algorithm respects the thermodynamics of the system, both in terms of visco-elasticity and damage.

5.3.2 Thermodynamics of visco-elasticity and continuum damage

The state of the material at any instant in time can be represented by its stress σ , its strain ε , the strains of the visco-elastic variables α_i , and a damage variable d . Its internal energy Ψ is function of ε , α_i and d .

A small variation $\dot{\varepsilon}$ of the strain causes a small variation in energy $\dot{\Psi}$. The second law of thermodynamics imposes the following inequality, commonly known as the Clausius-Duhem inequality:

$$\sigma : \dot{\varepsilon} - \dot{\Psi} \geq 0 \quad (5.7)$$

This inequality applies directly to visco-elastic materials. Indeed, the first term correspond to the work of the internal elastic forces in the material. For visco-elastic materials, this term should be completed by equivalent terms $\sigma_i : \dot{\alpha}_i$, where σ_i is the internal stress associated with the evolution of the variable α_i (not to be confused with the stresses of the springs and dashpots in the rheological assembly). As the α_i are internal variables, their associated stress is by definition equal to 0, as is the right-hand side of the corresponding line in the constitutive set of equations (5.1). This is consistent with the fact that visco-elasticity as described in the previous chapter is a reversible phenomena and therefore it occurs without any entropy increase.

Applying the chain derivation rule on $\dot{\Psi}$ in (5.7) yields, after rearrangement of the terms:

$$\left(\sigma - \frac{\partial \Psi}{\partial \varepsilon} \right) : \dot{\varepsilon} - \sum_i \frac{\partial \Psi}{\partial \alpha_i} \dot{\alpha}_i \geq \frac{\partial \Psi}{\partial d} \dot{d} \quad (5.8)$$

Since this must be true for any arbitrary evolution of the elastic and visco-elastic strains, this indicates that:

$$\sigma = \frac{\partial \Psi}{\partial \varepsilon} \quad (5.9)$$

$$0 = \frac{\partial \Psi}{\partial \alpha_i} \quad (5.10)$$

This is equivalent to the definition of the internal energy of the visco-elastic materials given for example by Biot [69, 70]. Since the contribution of the visco-elastic variables are again equal to 0, the internal mechanical energy can be written as:

$$\Psi = \sigma : \varepsilon \quad (5.11)$$

The internal energy can include other dissipative terms as well, like the energy required to open surfaces or the heat dissipated. These terms are added to $\sigma : \varepsilon$, which makes relation (5.11) an upper bound for the energy. Then, insertion in (5.8) gives:

$$\frac{\partial (\sigma : \varepsilon)}{\partial d} \dot{d} \leq 0 \quad (5.12)$$

Relation (5.12) is always satisfied if:

1. Damage always increases with time, and
2. Stress always diminishes with increasing damage

The first condition is imposed by the algorithm as proven in the previous section. The second condition is true by construction of the material behaviour (5.1).

The algorithm therefore satisfies the thermodynamics of the system at any point in time. Furthermore, the algorithm remains valid even though the internal variables are not affected by the damage the same way the stress is.

5.3.3 Influence of the damage path on the damage pattern

In the algorithm formulated above, only one element is damaged at each iteration. This might lead to a very large number of steps to reach convergence. The number of iterations can be reduced at the expense of accuracy by damaging at t_n all elements that reach their criterion between t_n and $t_n + \delta t$. By doing so, all elements that are expected to be damaged at very close instants are damaged simultaneously.

δt is a user-defined time tolerance. By increasing δt the number of elements that are damaged at each step increases. This modifies the series of (t_n) , (d_n) and (\mathbf{x}_n) , and therefore the final damage pattern. In this section, the influence of δt is investigated with a numerical tensile test on an heterogeneous material.

The sample is a two-dimensional representation of a concrete mesostructure containing 35% of aggregates. This low volume fraction of aggregates is chosen to provide comparison with results from the literature. The aggregates and the paste are purely elastic, and only the paste can be damaged. A displacement ramp is imposed on the upper edge of the sample between $t = 0$ and $t = 1$; the lower and left edge can only move along respectively the horizontal and the vertical direction. The microstructure, the boundary conditions and the imposed displacement are shown in Figure 5.1.

Experimentally, this kind of setup leads to the apparition of a crack band which width depends on the fineness of the material microstructure [129]. The crack is expected to initiate at a random point (depending on the heterogeneities and defects in the microstructure) and then to propagate in a line with an angle depending on the exact boundary conditions. A damage pattern obtained by numerical simulation will be considered valid if it exhibits this kind of features.

The simulation is run with time tolerances ranging from 10^{-2} to 10^{-9} . From a practical perspective, $\delta t = 0$ cannot be achieved and is bounded by the numerical machine precision.

The time tolerance has a huge influence on the ultimate crack pattern. For the lowest time tolerance, the damage localises in a band. The width of the band depends on the characteristic distance between the heterogeneities and not on the non-local behaviour of the cement paste. Very little damage is seen outside the band.

For strict time tolerances, a localised crack is still observed, even though its width decreases slightly as well. Micro-cracks are initiated around the aggregates. The density of these cracks increases when the time tolerance is loosened. During loading, these micro-cracks appear first. At some point during the simulation, one of these predominates and forms the localised band. This occurs earlier for stricter time tolerances. The angle of the crack band is the artificial friction that occurs at the edges of the sample.

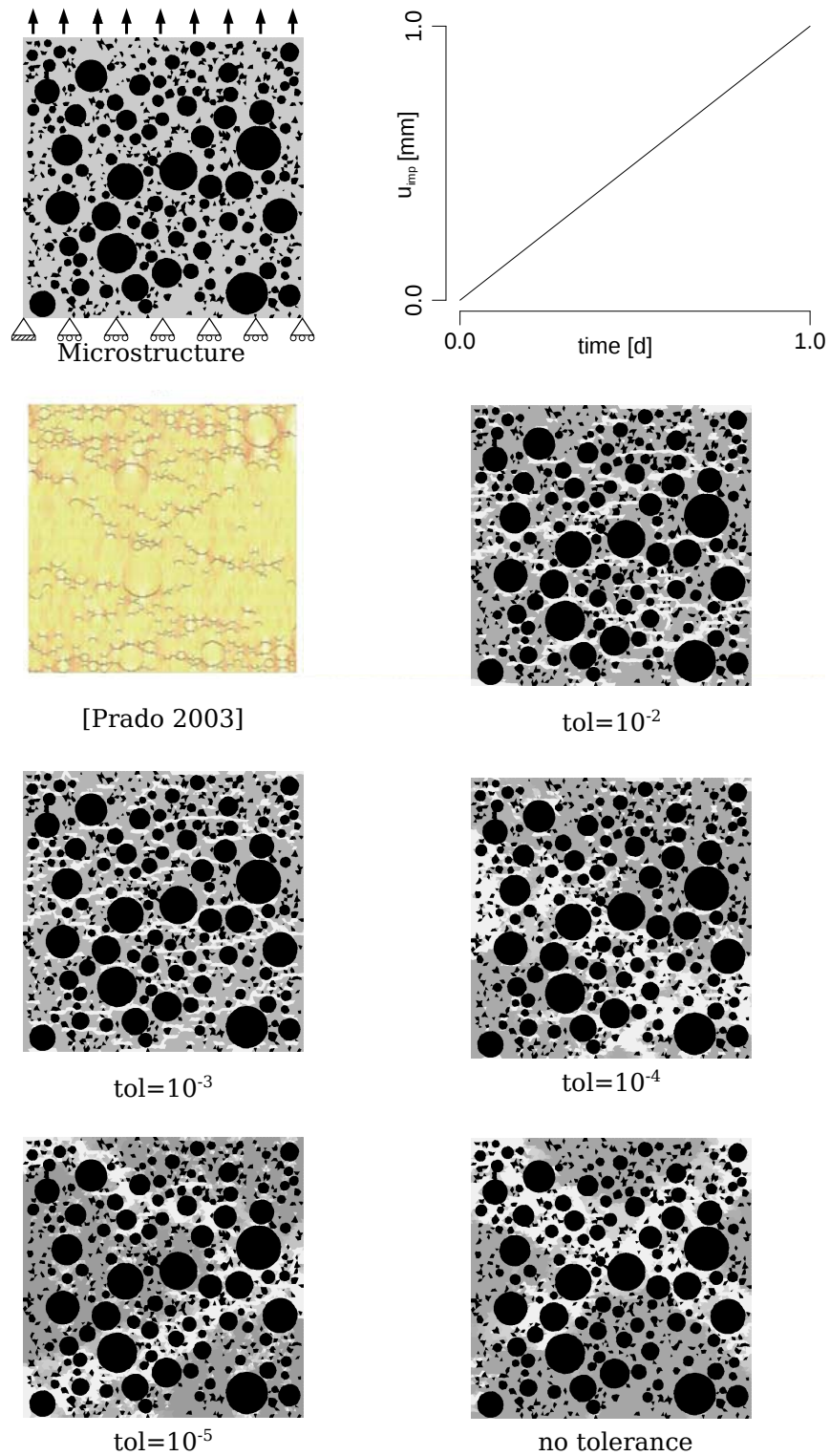


Figure 5.1: Evolution of the damage pattern with the time tolerance for a tensile test: the crack band appears only for the stricter time tolerances. Comparison with the damage pattern obtained with a similar microstructure by Prado and Van Mier [128]. Newton-Raphson methods are expected to produce patterns similar without a localised crack band.

For loose time tolerances, none of the micro-cracks predominates. They all propagate simultaneously in cracks that have a width which depends on the non-local properties of the cement paste. The crack patterns become comparable for example with patterns obtained by Prado and Van Mier with local lattice models on similar microstructures [128].

In Figure 5.2 the number of elements damaged at each step is shown as a function of the time tolerance. This number decreases with the time tolerance toward a converged value of 1 element damaged at each step of the damage algorithm. Furthermore, the localised crack band appears only when less than two elements are damaged at a single iteration.

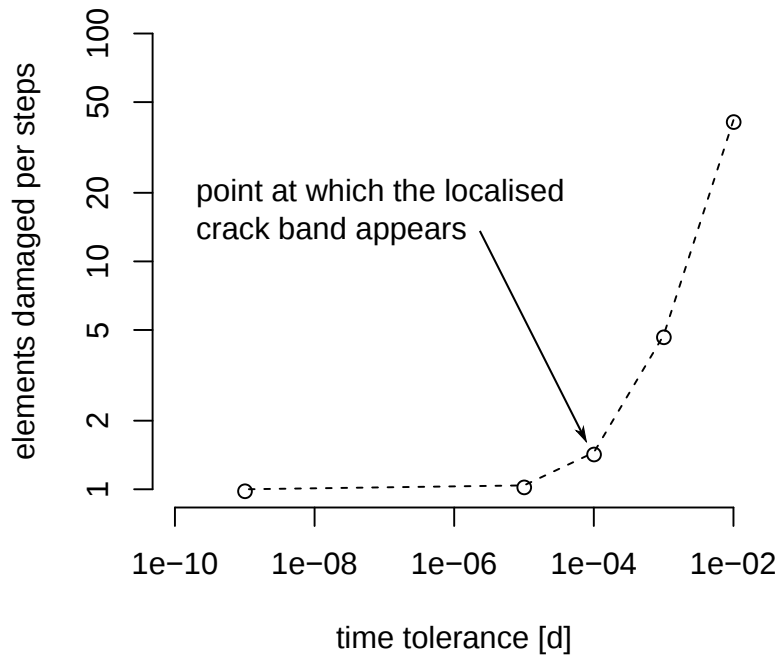


Figure 5.2: Number of elements damaged at each step of the simulation (out of 3936) as a function of the time tolerance.

This shows that the state of damage in heterogeneous materials is highly dependent on the damage path. The Newton-Raphson method and similar non-linear solvers don't account for that path and typically damage a large number of elements at each step. With the current framework, this is equivalent to using a very loose time tolerance, which leads then to damage patterns that don't match experiments.

This issue can be alleviated with Newton-Raphson methods by considering very small load increments. However, it is not always possible to identify beforehand what is the load increment “small enough” required to obtain a valid damage pattern. Furthermore, that load increment might change during the simulation because of variations of the loading or damage rates. Given Figure 5.2, at least 10^5 load steps should be necessary for the Newton-Raphson method to obtain a localised crack band, which seems unfeasible from a practical perspective.

With the proposed algorithm, this specific load increment is automatically found. When the time step is adjusted by the algorithm, the new time step is a) the smallest time step so that damage occurs in one element and b) the largest time step so that damage occurs only in that element. By doing so, the damage rate becomes an output of the algorithm, determined by the specific load and damage history, rather than an input coming from the material behaviour.

The algorithm is generic in the sense that it can be used to represent various types of material irreversibility, including for example plasticity. It does not depend on the exact nature of the failure criterion nor the constitutive behaviour of the material at each damage state. It is valid for more elaborate description of the damage variable, including material models in which each spring or dashpot are damaged independently.

To use this algorithm with a specific material, one needs to define a failure criterion that dictates when the material goes from one state to another, and the constitutive behaviour at each of these states. These two material characteristics are identified for cement paste in the next sections.

In the following, the failure criterion of the cement paste and its mechanical behaviour when damaged are discussed based on experimental evidence and numerical simulations.

5.4 Failure criterion of cement paste

Fracture experiments on paste samples are scarce because of the difficulty of making homogeneous samples free of spurious effects such as bleeding or shrinkage. They can be characterised and extrapolated from fracture experiments on concrete samples completed with numerical analysis. Indeed, the mechanical behaviour of concrete depends on the behaviour of cement paste and aggregates, the latter being more easily characterised with experiments.

Furthermore, concrete and cement share a similar morphology: they are both composite materials containing elastic inclusions embedded in a weaker visco-elastic matrix. Cement and concrete differ by the respective volume fraction of each phase, and by the contrast in the mechanical properties of each phase. As such, analysis of concrete as a composite material can give insights on the behaviour of the cement paste itself.

In the following sections, a failure criterion is proposed for cement paste. It is based on experimental evidence on the effect of stress and strain rates on the rupture of visco-elastic materials, and notably concrete. This criterion is then validated with simulations of wedge splitting tests on concrete specimens.

5.4.1 Effect of stress

Under a sustained load, the deformation of a visco-elastic sample can be divided into four stages [73]:

1. the initial elastic load;
2. the primary creep, during which the deformation rate starts at a high value and then drops significantly;
3. the secondary creep, during which the creep occurs at a somewhat constant creep rate;
4. the tertiary creep, during which the creep rate increases dramatically up to the failure of the material. This phase only occurs when the applied load is above a certain threshold.

An increase of the load accelerates all stages of the creep, and particularly the tertiary creep, as shown in Figure 5.3. In concrete, this threshold for tertiary creep is approximately 80% of the ultimate strength of the material, and the creep becomes non-linear for loads higher than 40% than the strength of the material [72, 71].

In practice, concrete itself is almost never subject to loads at which tertiary creep may happen. However, locally, the cement paste can be subject to tension high enough for the tertiary creep to occur.

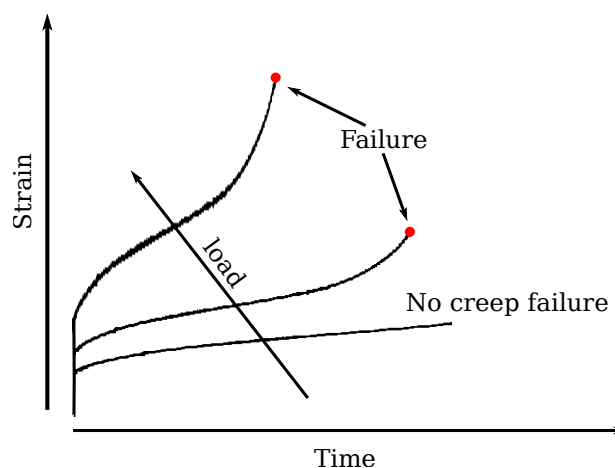


Figure 5.3: Representation of strain as a function of time for different levels of sustained loads.

From a phenomenological perspective, creep rupture relates to stable or unstable crack growth in the material. Below the creep rupture threshold, micro-cracks are induced in the microstructure but are stabilised by the stress relaxation. Above that threshold, the cracks can propagate faster than the material can relax stress and lead to the failure of the sample.

The presence of thresholds in terms of sustained loads indicates that the failure criterion is function of the stress. However, it is not sufficient as a criterion based entirely on the stress would not be able to characterise the delay at which the creep rupture occurs. Information based on the strain or the strain rate are required to complete the failure criterion.

5.4.2 Effect of strain rate

When subject to a constant strain rate, the strain-stress relation in a visco-elastic sample follows a typical bell-shaped curve as shown in Figure 5.6. When the strain rate increases, the height of the peak increases, and it is shifted depending on the strain rate. When it is subject to a slow strain rate, the material will be able to reach larger strains, but the stress at rupture will be lower. This is illustrated in Figure 5.4.

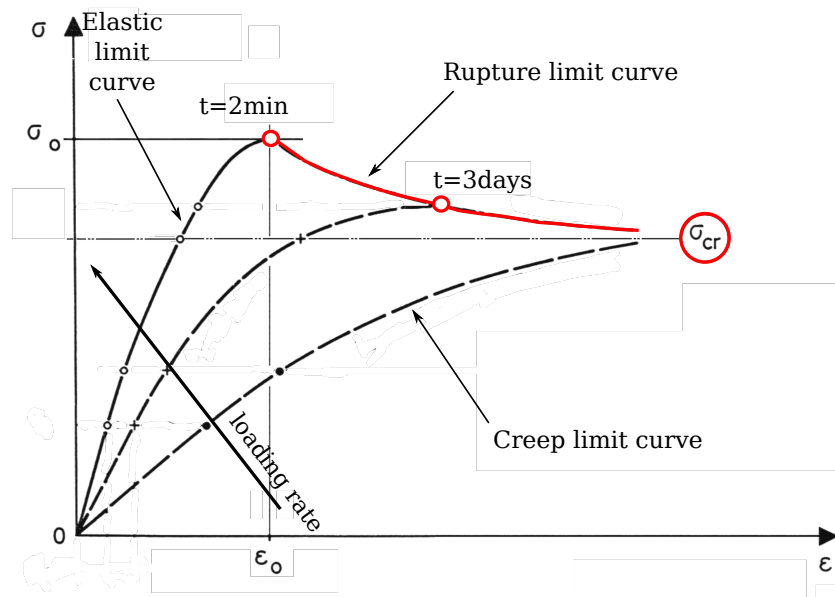


Figure 5.4: Stress-strain diagram for concrete when subject to different loading rates. Figure adapted from [130].

Such diagram cannot be captured by a criterion in strain or in strain rate. Indeed, if the criterion is only based on the strain rate, it would never predict failure of the sample for slow strain rates. If the criterion is only based on the strain, it could not account for the fact that the strain at rupture is shifted for the higher strain rates.

Challamel and co-workers proposed in [131] a modification of Mazars' model which is able to capture the influence of stress or strain rate on creep rupture. In this criterion, the damage is calculated as the root of an exponential function of the stress and the strain. However, using such elaborate criterion introduces additional material characteristics that are difficult to measure experimentally. Therefore, in this work a simpler fracture criterion based on strain is used, in which the only material parameter is the maximum tensile strain of the material. In the next section, we verify that this criterion can simulate the influence of strain rate on the rupture of concrete.

5.4.3 Identification of the cement paste rupture properties

The wedge splitting test is a common test in concrete mechanics. It was first introduced by Brühwiler and Wittman [132], and then notably used by Denarié to characterise the coupling between creep and crack propagation in concrete [133, 47].

The sample consists of a notched cube. A displacement is imposed at constant rate on the neck of the notch; a mechanism measures the force response. A crack propagates at the tip of the notch until complete failure of the sample. Since the boundary conditions are imposed by displacement, the rupture of the material is stable and the crack does not propagate further if the imposed displacement remains constant. The sample geometry and boundary conditions are shown in Figure 5.5.

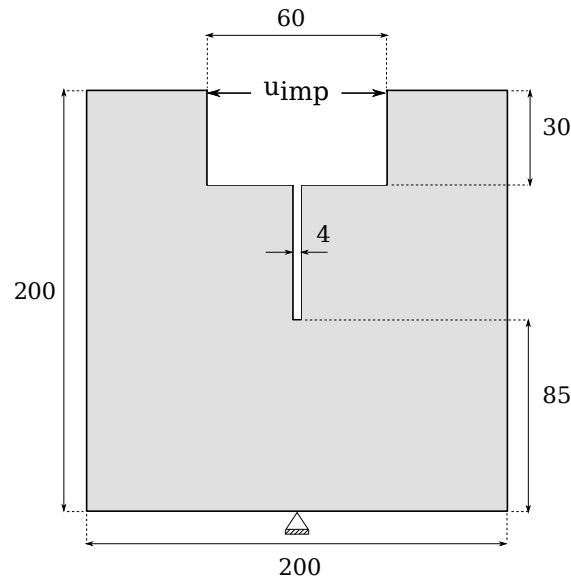


Figure 5.5: Dimensions (in millimetres) for the wedge splitting test. The displacement u_{imp} is imposed on the neck of the sample at a constant rate. Figure adapted from [47].

The sample is simulated with a two-dimensional slice. The heterogeneous microstructure is represented in the area below the notch where the crack is expected to propagate. Three different speeds are tested: 0.01 mm/day, 0.001 mm/day, and 0.0001 mm/day. These are very slow loading rates compared to similar experiments from the literature. For example, Denarié used loading rates ranging from 0.0005 to 0.5 mm/min, so 0.72 to 720 mm/day [133]. However, the paste model presented here does not account for the very short-term creep of the cement paste, and such short experiments would not show any distinctive results using the proposed model.

Material behaviour

The aggregates are purely elastic; in this simulation they cannot be damaged. This assumption is driven by the hypothesis that the aggregates are stiffer and stronger than the cement paste, and therefore the crack propagates only in the latter. The cement paste follows the mechanical behaviour described in the previous chapter (4.8), in which all branches are affected equally. The material is represented by 11 damage states equally distributed between 0 and 1. Two different fracture criteria are tested:

$$C = \sigma - \sigma_{cr} \quad (5.13)$$

$$C = \varepsilon - \varepsilon_{cr} \quad (5.14)$$

In (5.13-5.14) the highest principal components of the strain and stress are used as a scalar measure. The criterion in strain predicts failure under compressive loading because of the traction induced in the lateral directions. The criterion in strain never predicts failure under pure compressive loads. In composite materials like concrete, damage occurs mostly because parts of the microstructure are placed in tension, and therefore the failure of the cement paste in compression is neglected in the present model.

Non-local formulation

The proposed model uses a non-local formulation to reduce mesh dependency. Following the observations of Jirásek [134], only the strain field is smoothed. Other fields are then derived from the smoothed strain using the local material properties. The strain is averaged on a certain distance l_{char} which represents the characteristic length of the underlying microstructure of the material.

The choice of weighting function α has little impact of the results [135], and is formulated here as a truncated polynomial of the distance r to the local point considered:

$$\alpha(r) = \begin{cases} \left(\frac{r^2}{l_{\text{char}}^2} - 1 \right)^2 & \text{if } r < l_{\text{char}} \\ 0 & \text{otherwise} \end{cases} \quad (5.15)$$

Results

Figure 5.6 shows the load-displacement curves for the two different criteria, normalised by their peak value. Experimental results from [133] are also reported. The crack patterns are shown in Figure 5.7. The material parameters used for the different criterion are gathered on Table 5.1.

Table 5.1: Back-calculations of the failure criterion for the wedge splitting test

Tensile strength	σ_{cr}	1.5 MPa
Tensile strain	ε_{cr}	0.1 mm/m

The simulated behaviour follows the same trends as the experiments, even though the material properties for the paste and the aggregates have not been fitted for the materials used in Denarié's experiments, and that the microstructure is not represented in all the sample. The shape of the stress-strain curve and its evolution with the loading rate is dominated by the fracture criterion.

When the criterion is based on the stress, the displacement at the peak is delayed with decreasing loading rates. This is a direct effect of the stress relaxation, which delays the moment when the ultimate stress is reached. When the criterion is based on the strain, the peak occurs roughly at the same displacement but the ultimate force is significantly decreased when the strain rate decreases. This reduction is larger than what is observed in the experiment. This might be caused by the fact that the strain-based criterion is too brittle

In all simulated cases, the curves do not superpose after the peak as in the experiments. This could have different causes: the material model does not contain enough damage states, the microstructure contains only the largest aggregates. Having more states would lead to a finer characterisation of the post-peak behaviour. The finer aggregates would likely impede the crack propagation by strengthening the material in the fracture process zone. The post-peak response can also be influenced by the damaged behaviour of the cement paste as discussed in the next section.

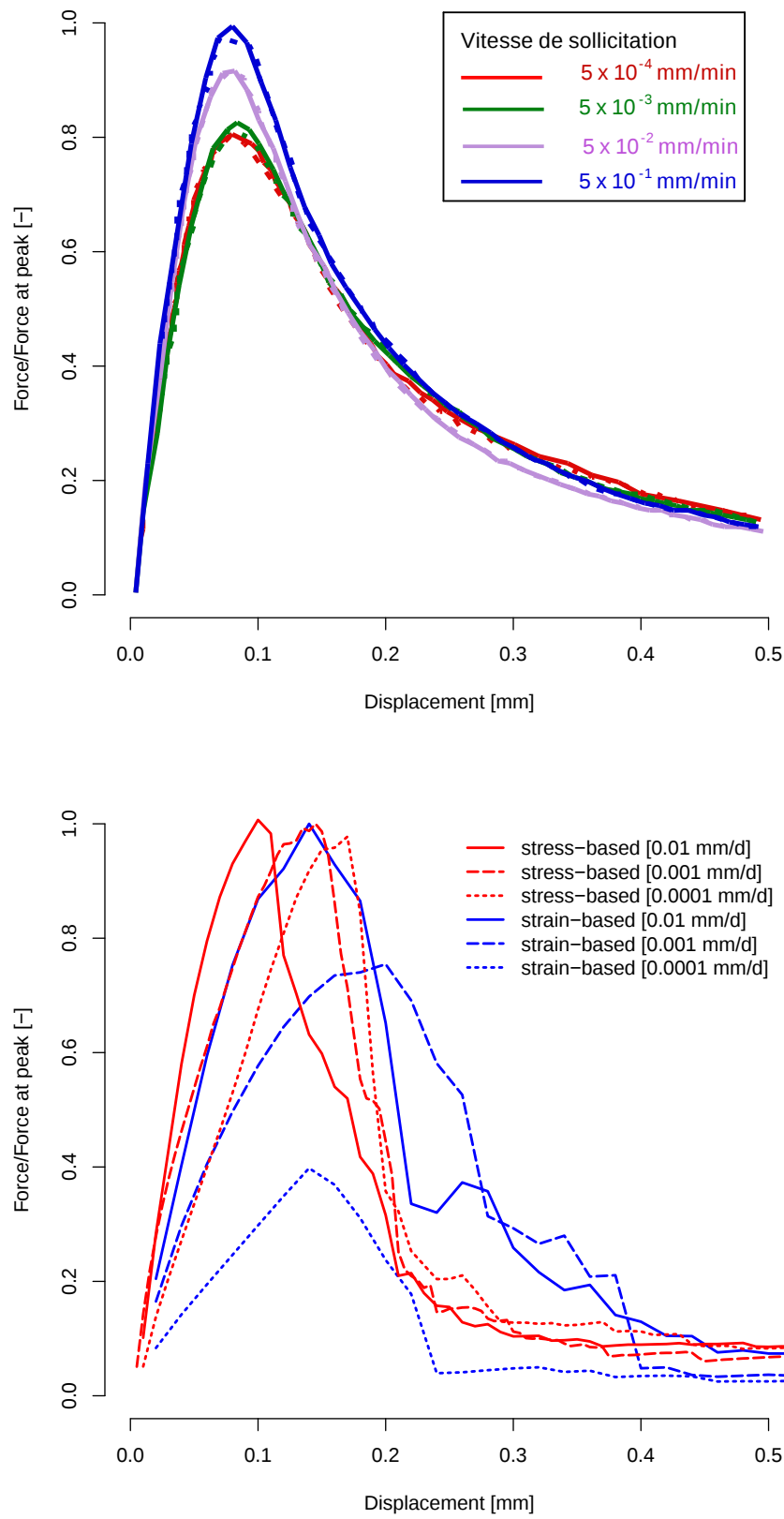


Figure 5.6: Experimental (top) and numerical (bottom) load-displacement curves for the wedge splitting test. Experimental results from [133].

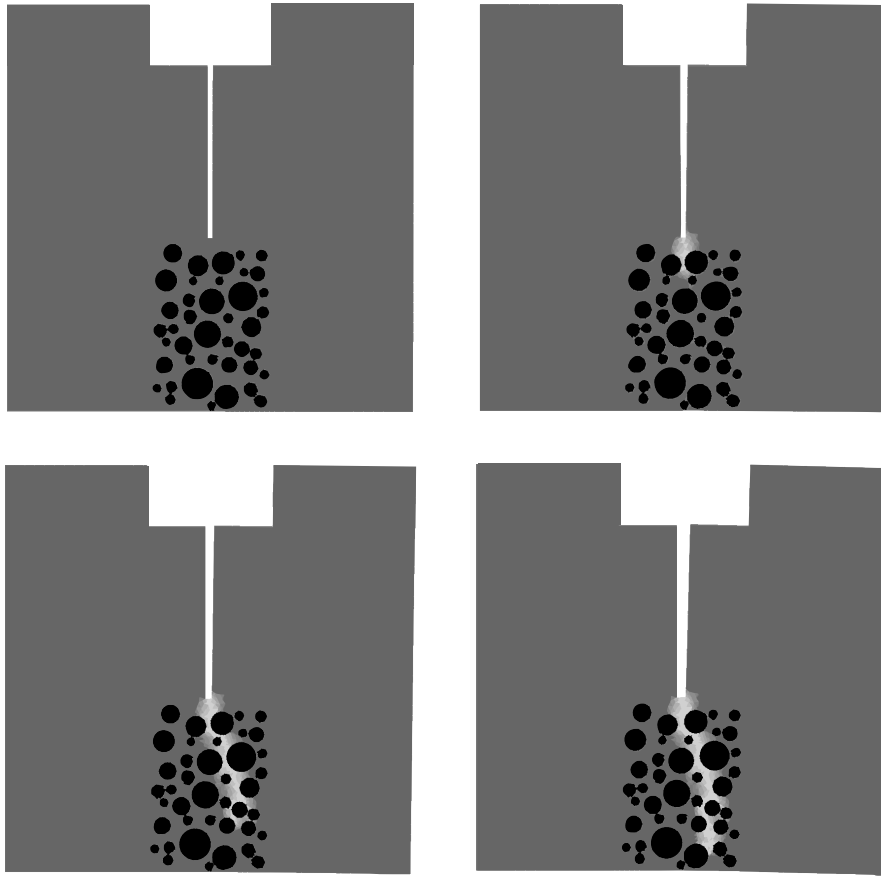


Figure 5.7: Damage pattern at different stages of the simulation.

5.5 Visco-elastic properties of damaged heterogeneous materials

In the previous simulations, it was assumed that all springs and dashpots in the model are affected equally. However, Denarié showed in [47] that the macroscopic (or apparent) stress relaxation of a damaged concrete sample is faster than for the sound material (see Figure 5.8). This indicates that for heterogeneous materials like concrete and by extension cement paste, damage affects differently each of branch in the rheological model. In this section, we show with numerical simulations that this is caused by the heterogeneous nature of the cement paste.

To verify the results of Denarié, the visco-elastic properties of numerical samples with different degrees of damage are estimated. Different microstructures with increasingly complex morphologies are investigated. Damage is artificially introduced in the microstructure with simplistic mechanisms. The visco-elastic properties are then estimated with a uni-axial creep experiment in which no element can be damaged. The average axial strain in the sample is measured as a function of time, and fitted with exponentials to obtain the material properties of the apparent generalised Kelvin-Voigt model.

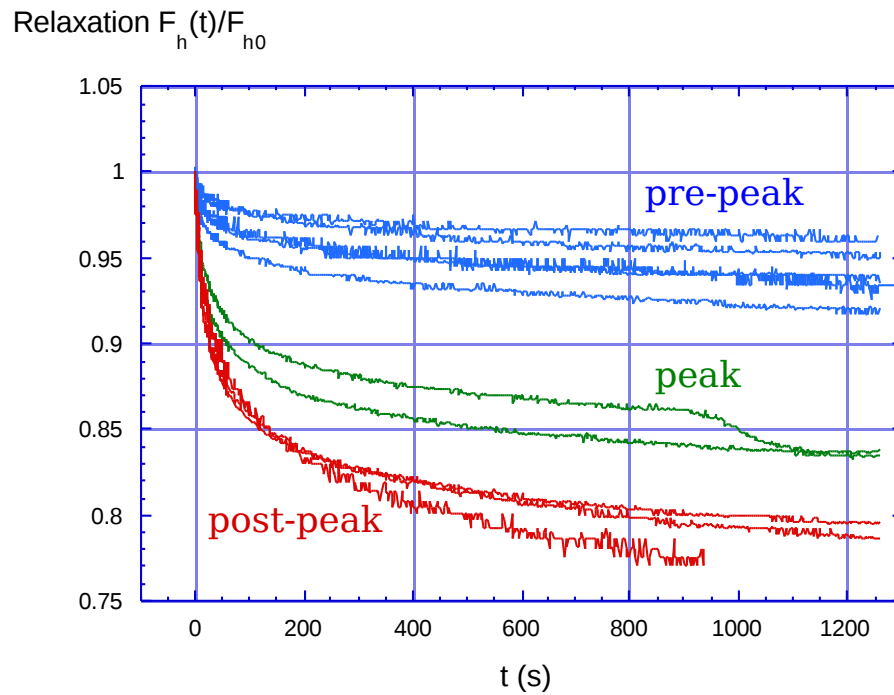


Figure 5.8: Stress relaxation at different degrees of stages of the material degradation. Figure adapted from [133].

The loss in the visco-elastic properties are found to be higher than the loss in the elastic properties, which corresponds to an acceleration of the apparent visco-elastic behaviour.

Microstructure

Three different microstructures are studied:

- Homogeneous visco-elastic material
- Heterogeneous material composed by elastic inclusions embedded in a visco-elastic matrix. The elastic inclusions have a volume fraction of 40%.
- Idealised cement microstructure composed by three set of elastic inclusions (representing unhydrated cement, ettringite, and portlandite) and capillary pores embedded in a bi-phasic visco-elastic matrix (representing inner and outer C-S-H). The volume fraction of each phase is chosen to approximate the phase assemblage of a cement paste with water/cement ratio of 0.45 and a degree of hydration of 90%. The specific size of each phase does not match experimental evidence and a more elaborate microstructure as the ones produced by the μ c hydration simulation software would improve the results [136].

The simulations are in two dimensions. The mechanical properties of each phase are taken from various experimental works and gathered by [79]. For the idealised cement paste, some hydrates like ettringite are assumed perfectly elastic, but might contribute to the creep of the material as well. The aim of these simulations is however not to reproduce the creep of cement paste, but to understand how damage affects the overall properties of the material.

Table 5.2: Volume fraction in percent of each phase for the creep-damage test.

Phase	Homogeneous	Heterogeneous	Idealised cement
Inner C-S-H	-	-	14
Outer C-S-H	100	60/80	40
Unhydrated cement	-	40/20	3
Portlandite	-	-	15
Ettringite	-	-	18
Capillary water	-	-	10

Artificially-induced damage

Different degrees of damage are artificially induced in the microstructure. In the homogeneous plate, this is done by adding randomly placed voids up to a specified volume fraction.

In the heterogeneous material and the idealised cement paste, an elastic tensile test is simulated first. The mechanical properties of the elements in the outer C-S-H phase with the highest stress are zeroed in order to represent the fact that these elements break first.

The damaged fraction in the microstructure can be controlled by adjusting the volume of damaged elements in the microstructure. The damage pattern differs from what is obtained with the damage algorithm presented in the previous chapter, but it is assumed that the increase in damage will change the apparent mechanical properties regardless of its exact morphology.

The three microstructures with increasing damage are pictured in Figure 5.9. The tests were repeated with randomised placements of the particles in order to obtain averaged values.

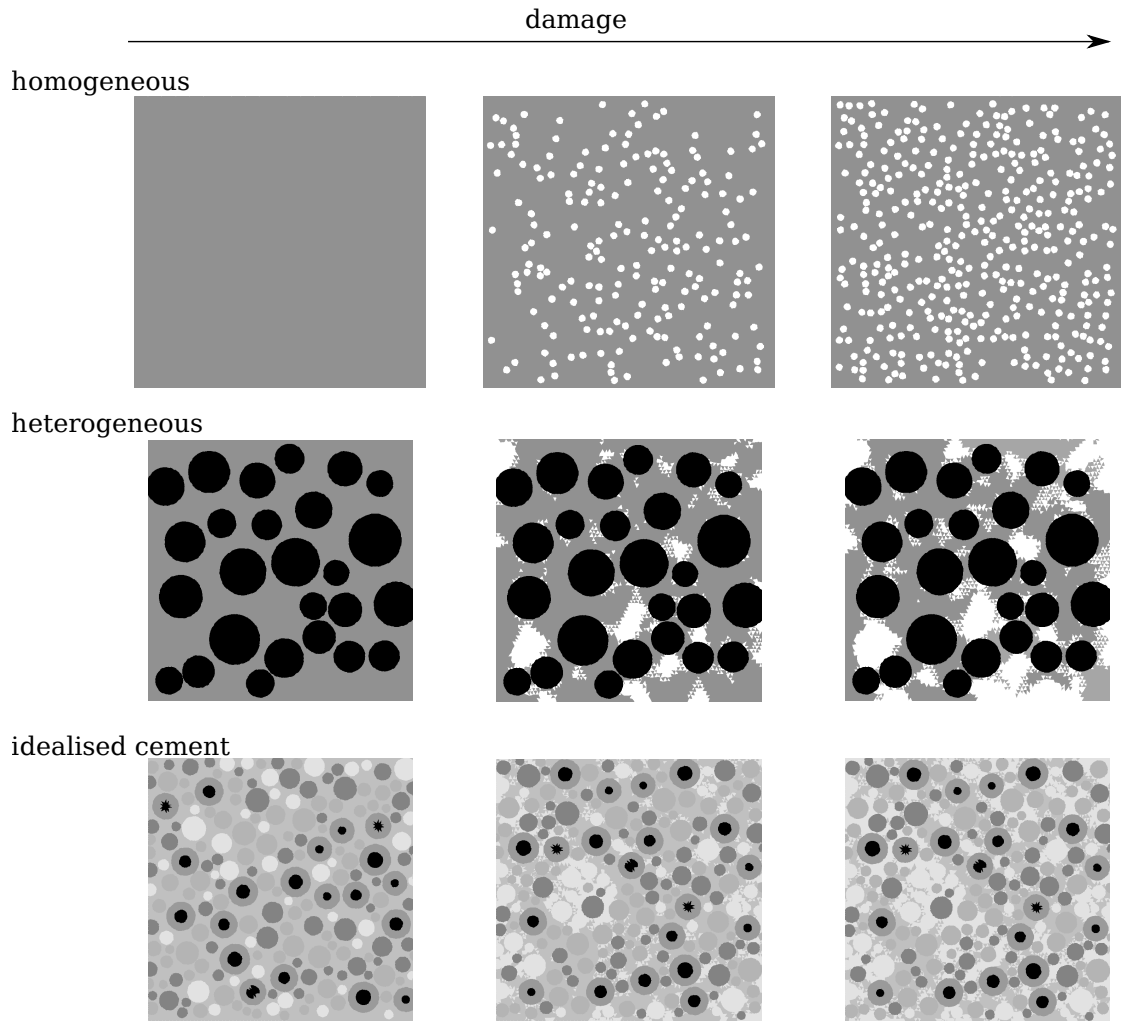


Figure 5.9: Microstructures with increasing artificially-induced damage.

Estimation of the visco-elastic properties

After the microstructures have been modified, a creep test is carried out to identify the visco-elastic properties of the material. The average strain in the sample is measured as a function of time. This function is then approximated by a set of two exponentials with fixed characteristic times to find the closest Kelvin-Voigt representation of the material. The approximation is determined with the least-squares estimates provided in the R software package [137]. The accuracy of the fitting process is verified since for the homogeneous plate without damage, the fitted creep curve is indeed equal to the creep curve prescribed.

Using this method, each branch in the rheological model can be attributed a damage parameter which depends on the damaged fraction of the material. In practice, it is easier to consider the loss in elastic properties rather than the damaged fraction, since it is the one used in the FE calculations. The damage in each viscous branch are shown as a function of the elastic damage in Figure 5.10, and compared with the experimental results of Denarié treated with the same analysis procedure except that the relaxation curve is fitted.

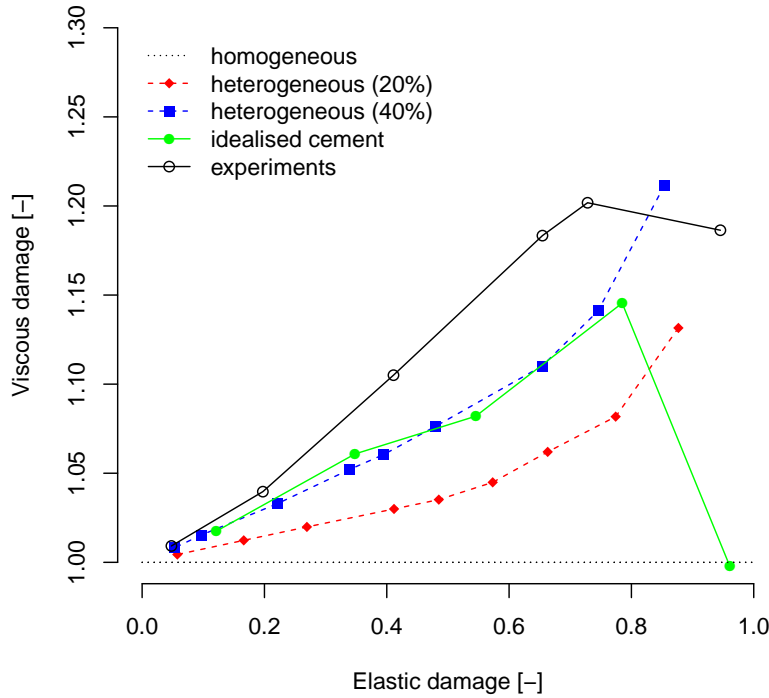


Figure 5.10: Relation between damage in the visco-elastic branches and in the elastic branch for different microstructures. Comparison with experimental results from Denarié [47].

The viscous damage in the homogeneous sample follows exactly the elastic damage. This was expected from known results on linear visco-elasticity. Indeed, the spatial and temporal parts of the constitutive differential equations can be solved for separately: the spatial distribution of the stress depends on the geometry of the sample, while its time evolution depends solely on the material properties. This is referred to as Alfrey's theorem, and a complete proof for stress- and displacement-controlled boundary conditions was given by Tsien in [138]. It follows that, in case of homogeneous visco-elastic materials, each spring and dashpot in the rheological model must be affected by damage the same way. However, this theorem is not applicable to strongly heterogeneous materials as the cement paste which contains elastic phases and visco-elastic phases with different characteristics times.

5.5. Visco-elastic properties of damaged heterogeneous materials

In the other microstructures, the viscous damage is higher than the elastic damage, and follows a trend similar to the experiments. In the case of the heterogeneous microstructure (elastic inclusions in visco-elastic C-S-H), the viscous damage does not seem to decrease at high elastic damage. This might be caused by the fact that in the idealised cement or in the damaged concrete, two visco-elastic phases cohabit (outer and inner C-S-H) and only one is damaged (outer C-S-H). The inner C-S-H still contributes to the visco-elastic behaviour of the material, even at high degrees of damage.

With these simulations we have outlined the influence of damage on the creep properties of heterogeneous materials such as cement paste. This influence is highly dependent on the microstructure of the simulated material, and needs to be characterised for cement paste on more realistic microstructure models. To avoid using a yet unknown parameter, this effect is neglected in the following ASR simulations, and all branches of the cement paste model are damaged the same way.

6 Combined modelling of creep and ASR

In chapters 4 and 5 a powerful numerical method was developed to simulate the behaviour of non-linear visco-elastic materials. In this chapter, the model is applied to the study of ASR at the microstructure level. First we identify the physical parameters required for the model, and from which experiments they can be measured or back-calculated. The model can be used with different microstructures in order to simulate mortar, concrete, or aggregates of different reactivity.

Then, we show through simple examples that oversimplified damage models give poor results for the expansion and damage inside the material. This demonstrates that homogenised approaches used in certain ASR models will always overestimate the damage induced in the microstructure, even if creep is introduced in the model. We further show that neglecting damage in the cement paste leads to unrealistic damage patterns and debonding of the aggregates.

Finally, the model is applied on a concrete microstructure with different rates of reaction. In so doing we demonstrate the ability of the model to represent the evolution of the expansion and damage with different reaction kinetics. The two different failure criteria proposed in the previous chapter are compared and used as lower and upper bound of the material behaviour. The strain-based criterion leads to an overbrittle behaviour of the concrete, and predicts the simultaneous failure of the paste and the aggregates. The stress-based criterion leads to an initiation of damage in the aggregates, followed by a propagation in the cement paste that depends on the rate of the reaction, which corresponds better to the field observations.

6.1 Parameters of the model

This section describes the parameters used in the model, and discusses their physical origin and the experiments required to measure them. The mechanical parameters are related to the material used in the concrete, while the morphological parameters relate to the microstructure and the proportion of each constituent in the composite.

6.1.1 Mechanical parameters

Table 6.1 lists the mechanical parameters of the model, as well as their origin. All of these parameters can either be measured experimentally, or back-calculated from creep or fracture experiments. In a given simulation, the cement paste fails according to either to a tensile strain limit or a tensile stress limit, not both. The choice of criterion is critical for the evaluation of the damage pattern, as discussed throughout this chapter.

Table 6.1: List of mechanical parameters for the ASR model.

Phase	Properties	Value	Origin
Aggregates	Young's modulus	60 GPa	Measured by Ben Haha on raw aggregate samples in [6]
	Poisson ration	0.3	
	Tensile stress limit	11 MPa	
Cement paste	Elastic modulus	12 GPa	Back-calculated by Dunant from non-reactive creep experiments [12]
	Poisson ration	0.3	
	Viscous modulus 1	4 GPa	Back-calculated in Chapter 4 from non-reactive creep experiments by Dunant [12]
	Characteristic time 1	10 days	
	Viscous modulus 2	4.5 GPa	
	Characteristic time 2	300 days	
	Tensile strain limit	0.1 mm/m	Back-calculated in Chapter 5 from wedge splitting test by Denarié [47]
	Tensile stress limit	1.5 MPa	
Gel	Elastic modulus	22 GPa	Measured by Leeman with nano-indentation [63]
	Poisson ration	0.499997	
	Imposed expansion	0.5	Calibrated by Dunant based on experimental observations of Garcia-Diaz and co-workers [62]

In the case of the Young's modulus of the cement paste, the back-calculation is easy and simple homogenisation schemes like the Mori-Tanaka estimate will provide good agreement with the finite element approximation [139, 140]. The value found by Dunant for the cement paste is within the range of experimental data found in the literature and (see for example [80]). For comparison, the finite element model of Do which describes explicitly the microstructure of the cement paste predicts a Young's modulus of 14 GPa with a water/cement ratio of 0.45 but a different cement composition [79].

For the creep and tensile strength of the cement paste, the back-calculation requires finite element simulations as shown respectively in chapter 4 and 5. The values of the fracture criteria for the cement paste are slightly lower than what is typically used. The creep properties identified in chapter 4 leads to a ratio between the instantaneous elastic modulus and the relaxed modulus (defined as the apparent modulus with an infinitely slow strain rate) equal to 6.66, which is close to the value of 7.5 found by analyzing the experimental data used by Tran on cement paste [141]. Direct comparison is however not possible since Tran did not specify the water/cement ratio or age of the cement paste.

For a full characterisation of the effect of temperature the activation energy of the creep is required. This activation energy varies a lot from one aggregate type to another, as Bengougam reported values ranging from 48 to 140 kJ · mol⁻¹ during his studies on dam concrete [106]. Since the activation energy of creep has not been characterised for the aggregates used in this study, the effect of the temperature is neglected in this section.

The reactive aggregates used in this study are highly anisotropic [6]. They have a layered structure, each layer being a few millimetres thick. The bond between each layer is very brittle, and Ben Haha recorded a tensile strength of 1.2 MPa in the perpendicualar direction of the layers. In his tests, the size of the sample was 180 × 70 × 70 millimetres. Considering the scale of the simulation, it is reasonable to assume that each aggregate is mono-phasic, and so the value used in this work is equal to the tensile strength measured by Ben Haha in the parallel direction, equal to 11 MPa.

The mechanical properties are varied from one element to another in order to account for the heterogeneity of the cement paste and the aggregate. In a given element, the properties \mathcal{P} is given by (6.1), in which ω is a random Weibull variable. This law ensures that the average properties of the simulated material is equal to the prescribed value.

$$\mathcal{P} = \mathcal{P}_{\text{prescribed}} \cdot (0.8 + 0.2 \omega) \quad (6.1)$$

The properties of the ASR gel are those used by Dunant in his previous simulations. The expansion coefficient is based on the stoichiometric volume balance between silica and ASR gel, as reported by Garcia-Diaz and colleagues [62]. Dunant calibrated the Young's modulus of the gel by first assuming it equal to the modulus of C-S-H, and then adjusting it until agreement between experimental and numerical curves [12]. Leemann and Lura measured with nano-indentation on ASR products an elastic modulus ranging from 5 to 45 GPa [63]. The gel is stiffer close to the cement paste, and softer close to the center of the aggregates. The value used in this study is within the experimental bounds, but the distribution of the stiffness of the gel within the aggregate is not accounted for.

Finally, Leemann and Lura found the gel is visco-elastic. However, they did not provide values for the creep properties of the silica gel, nor the time scale at which this creep occurs. The visco-elasticity of the silica gel is therefore ignored in this work to avoid fitting an unknown parameter. Introducing the creep of the silica gel in the model would reduce the applied pressure, and therefore the damage and the expansion.

6.1.2 Morphological parameters

The morphological parameters can be adjusted to simulate concrete or mortars with aggregates of different shape, particle size distribution, or reactivity. In the model, the reactivity of an aggregate is characterised by three values: the density of gel pockets, their growth as a function of time, and the overall area they cover at the end of the reaction. These parameters can be estimated using image analysis as in the work of Ben Haha [6, 7].

The density of gel pockets is chosen equal to 4 gel pockets per cm^2 of reactive aggregate, which is the value used by Dunant to model free expansion with the reactive aggregates considered. This value should be adjusted for different aggregates, and should be measured with a more extensive microscopic study of the material. The maximum area covered is chosen equal to 3% of the aggregate surface according to the values found by Ben Haha with these aggregates.

To determine the rate of gel formation the temperature and the chemical environment should be both considered. In accelerated tests alkali ions are added to the concrete mix and the temperature increased. The experimental studies of Larive and Ben Haha (among others) show that the temperature affects the reaction following an Arrhenius law [9, 6].

The dependence of the reaction on the amount of alkali is however not well understood and depends on the exact aggregate type. However, Ben Haha showed that for the reactive aggregates used in this study, the degree of reaction remains linear with respect to time in the range of concentrations and temperatures he studies.

Bulteel [41], and Yi [142] measured the degree of reaction of silica with nuclear magnetic resonance spectroscopy and image analysis respectively with other reactive aggregates and found linear relations between time and the degree of reaction. Dunant found in [12] that the use of linear kinetics in his model provided a good agreement with the experimental free expansion measured with the same reactive aggregates as in this study.

The present model does not yet enable full coupling between the environmental conditions and the mechanical consequences. The growth rate of the ASR gel pockets is varied arbitrarily. A more complete model can be expressed if the relation between the temperature, alkali concentration, and growth rate is identified. For the purpose of the mechanical simulations, this relation is not required.

In the following simulations, four different kinetics are investigated. The kinetics are expressed in term of the time at which the maximum amount of gel is reached.

- 100 days (\approx 3 months). This kinetics corresponds to an accelerated mortar bar test.
- 1 000 days (\approx 3 years). This kinetics corresponds to an accelerated concrete test with a low alkali content.
- 10 000 days (\approx 30 years). This kinetics is used to represent field structures.

- “Instantaneous”. For these simulations, the viscosity of the cement paste is neglected. This is used as a baseline to investigate the role of creep in the behaviour.

In this chapter, several modelling approaches are investigated. We demonstrate that a complete microstructural approach is required to reproduce the unique features of ASR expansion. Indeed, an ASR model must be able to predict the two following observations:

- A sample affected by ASR retains its macroscopic integrity. This notably means that a ASR model must predict a limited amount of damage in the cement paste.
- The expansion of a loaded sample affected by ASR is reduced in the direction of the load, and is affected non-linearly in the lateral direction, as shown by the studies of Larive or Dunant. A ASR model must predict a non-linear relation between the applied load and the volumetric expansion.

6.2 ASR simulations with a simplified damage approach

In this section, the need for a fine characterisation of the damage in the microstructure is established. If the average values of stress or strain are used for the estimation of damage (as what would happen with homogenisation schemes), then the expansion imposed by ASR leads to an almost complete failure of the material. First we show that a model without damage cannot reproduce the effects of load on ASR. The same conclusion is found for two models with a simplified damage approach.

The visco-elastic properties of the paste are accounted for to estimate the effects of creep on these simple models. Three cases are investigated:

- No damage is induced in the microstructure. All deformations are either elastic or visco-elastic. This corresponds to models which do not include damage in their formulation.
- Damage is spread homogeneously in the cement paste, but the aggregates remain undamaged.
- Damage is spread homogeneously in the aggregates. Each aggregate is damaged separately to account for the heterogeneity of the reaction as a function of the aggregate size.

The damage is attributed to each phase so that its average stress remains under the fracture criterion of the phase. This is equivalent to a material in which the characteristic length of the crack band would be equal to the size of the sample. This simple approach does not account for local effects, as what would happen with homogenisation procedures.

For each case the free expansion and the expansion under load are measured as a function of the degree of reaction. The loading cases are reported in Table 6.2. The expansion is calculated as the average strain in the sample, to which the creep strain measured with non-reactive aggregates was deducted.

For each loading scenario, the four kinetics defined in section 6.1 are investigated in order to identify the effect of the rate of reaction on the expansion and damage.

Table 6.2: List of loading conditions used in the creep ASR simulations.

Lateral load	0 MPa	5 MPa	10 MPa	15 MPa
Vertical load				
0 MPa	X			
5 MPa	X	X		
10 MPa	X	X	X	
15 MPa	X	X	X	X

6.2.1 Simulations without damage

In the simulations without damage, the ASR-induced expansion is independent of the load, as expected from the Boltzmann superposition principle. This is in contradiction with the experimental results on ASR under load, and confirms that internal damage must be accounted for in the modelling of ASR.

Figure 6.1 shows the expansion as a function of the degree of reaction in the unloaded case. The expansion curves are identical for all other loading scenarios. The comparison with experimental results from Ben Haha and Dunant [6, 12] shows that the expansion is too low at the beginning of the reaction, and too high towards the end. This is caused by the absence of damage, as it would increase the expansion by reducing the stiffness of the sample.

By adjusting the mechanical parameters of the gel (stiffness and imposed expansion), it is certainly possible to shift the curves so that it matches the experimental curves. However, this would hide the physical processes in the microstructure, and therefore would forbid the use of the model with different materials or boundary conditions.

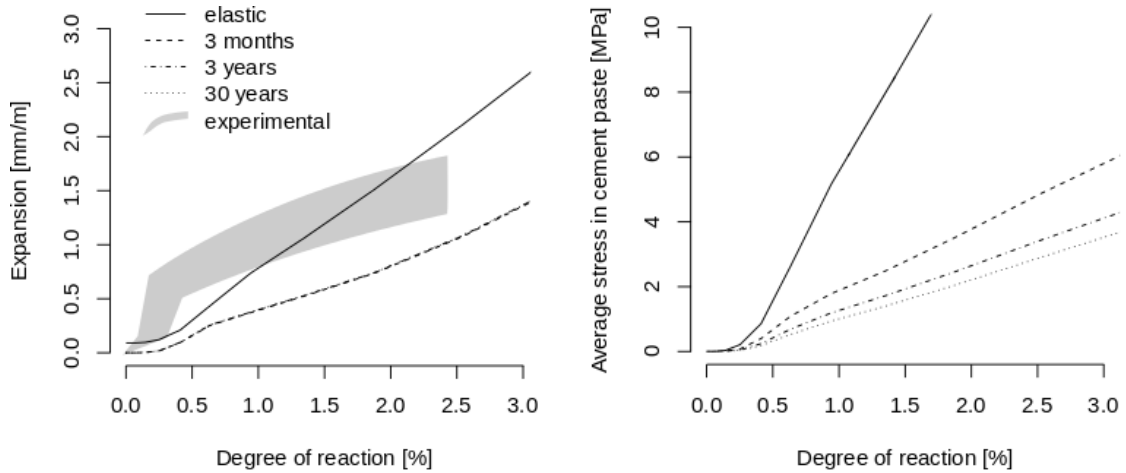


Figure 6.1: Simulated expansion (left) and stress in the cement paste (right) as a function of degree of reaction and reaction kinetics without damage in the microstructure. Comparison with experimental data from Ben Haha [6, 12]

In the elastic case, the expansion is significantly higher than that is estimated with viscoelasticity. In the latter case, the rate of reaction does not affect the expansion and all curves are superposed. This is caused by the fact that in the simulation, the expansion is imposed as a strain in the gel pockets. The setup corresponds to a relaxation test, and the stress is decreased when the rate of reaction decreases.

With an homogenised model, a phase in the material (cement paste or aggregate) would fail when its average stress reaches the failure criterion of that phase, as for example was proposed by Pichler and Hellmich in [143]. Here, we define the *critical degree of reaction* as the degree of reaction for which the cement paste fails.

The critical degree is plotted against the rate of reaction in Figure 6.2 for three different loading cases: unloaded, 5 MPa uni-axial, and 5 MPa bi-axial load.

With the criterion in strain, the rate of reaction has no influence on the critical degree of reaction. With the criterion in stress, we observe that the critical degree of reaction increases when the rate decreases. This indicates that for a slower reaction, the onset of damage in the cement paste is delayed, and so the damage in the material would be lower.

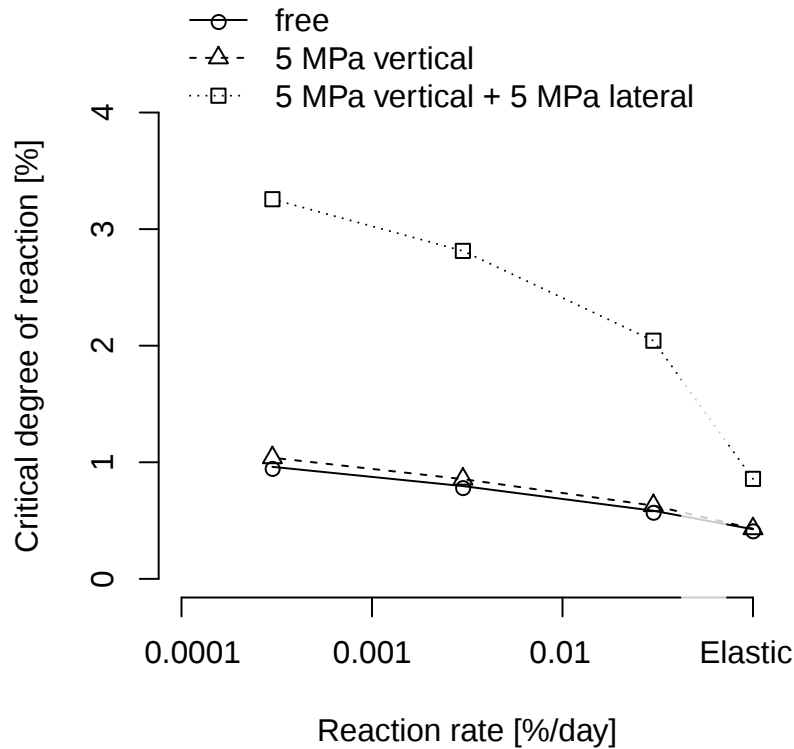


Figure 6.2: Critical degree of reaction in absence of damage as a function of the rate of reaction for different loads.

In all cases, the critical degree of reaction is increased under load. This indicates that applied stress strengthen the material, and impedes the crack propagation as proposed by Dunant in [5]. However, the effect remains small in the case of uni-axial load, while we would expect a decrease in the critical degree of reaction since experiments indicate an increase in damage. This shows that this approach will not provide a realistic behaviour of ASR-affected concrete under load, even if the mechanical parameters of the gel are well calibrated.

The stress-based criterion can then be understood as a lower bound of the damage behaviour, and the strain-based as an upper bound. We show in the following section that even with the stress-based criterion simplified damage models overestimate the damage in the microstructure.

6.2.2 Simple damage in the cement paste

In these simulations, the aggregates cannot be damaged, but the cement paste is damaged homogeneously. This can be compared to models in which concrete is damaged homogeneously, and expansion is imposed by a purely elastic medium.

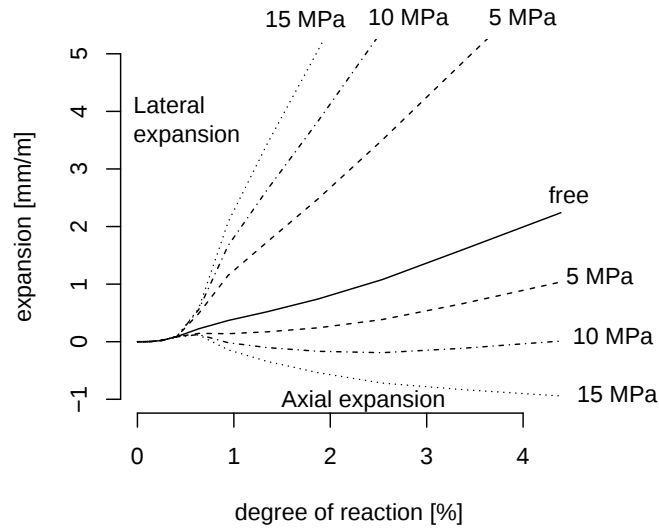


Figure 6.3: Axial and lateral expansion under uni-axial load with the 100 days kinetics and homogeneous damage in the cement paste.

Using this model, it is possible to partially reproduce the effects of uni-axial load on the expansion as shown in Figure 6.3. However, in these simulations, the lateral expansion under load is higher than the free expansion, and the axial expansion is reduced to the point that the material actually shrinks. This indicates that these models induce too much damage in the cement paste, and that orientation of damage plays an important role on how the expansion is affected by external loads.

Figure 6.4 shows the damage in the cement paste as a function of the degree of reaction. When the load increases, the damage decreases and its occurrence is delayed as expected from the results in the previous section. For the bi-axial load, the reduction is significantly higher than under uni-axial load. Furthermore, the damage is decreased when the rate of reaction decreases. Still, the damage reaches very high values compared to the loss of stiffness or compressive strength induced by ASR, which shows this kind of approaches cannot represent ASR.

6.2.3 Simple damage in the aggregates

The previous simulations show that damage must occur in the aggregates to reduce the stress in the cement paste and so be consistent with experimental observations. Here, the aggregates are damaged separately and homogeneously. To do so the average stress in each aggregate is computed and damage is applied so that it remains below its tensile limit. This way the heterogeneity of the reaction is better represented than with the previous model, and effects of aggregate size can be captured.

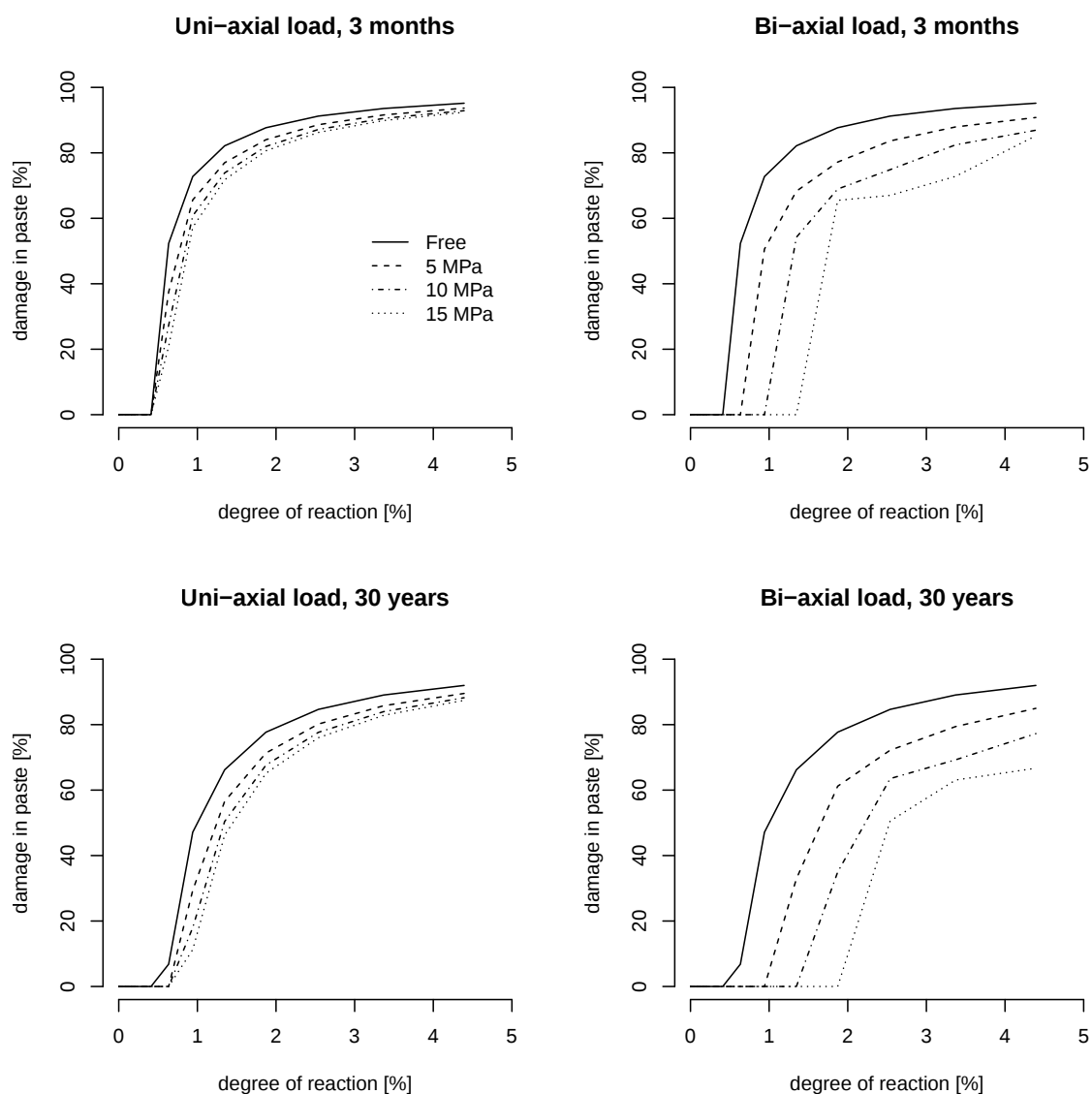


Figure 6.4: Homogeneous damage in the cement paste under uni-axial load (left) and bi-axial isotropic load (right), for 3 months (top) and 30 years kinetics (bottom).

The expansion for the 3 months kinetics under different uni-axial loads is shown in Figure 6.5. The influence of load follows a similar trend to what was found with the homogeneous damage in the cement paste, but with a smaller amplitude. Indeed, the damage is not enough to reduce or negate the expansion in the uni-axial case.

Each aggregate is damaged separately, and these simulations can capture the fact that the point at which each aggregate fails depends on its size. The damage for aggregates of different diameter is plotted as a function of the degree of reaction in each aggregate in Figure 6.6.

6.2. ASR simulations with a simplified damage approach

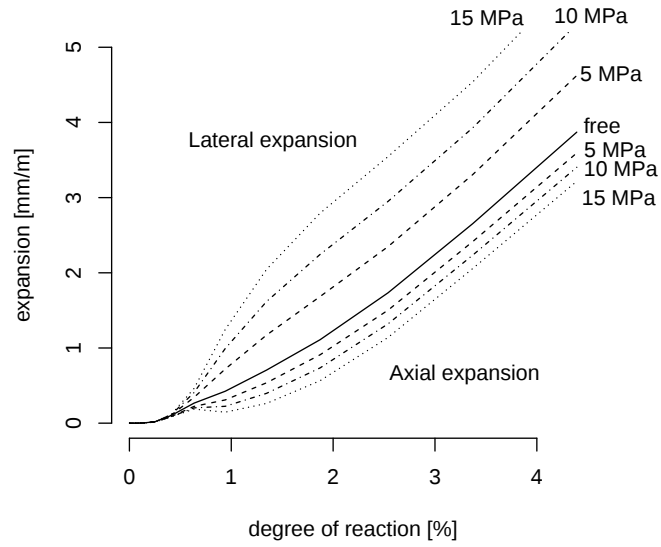


Figure 6.5: Axial and lateral expansion under uni-axial load with the 3 months kinetics and homogeneous damage in the aggregates.

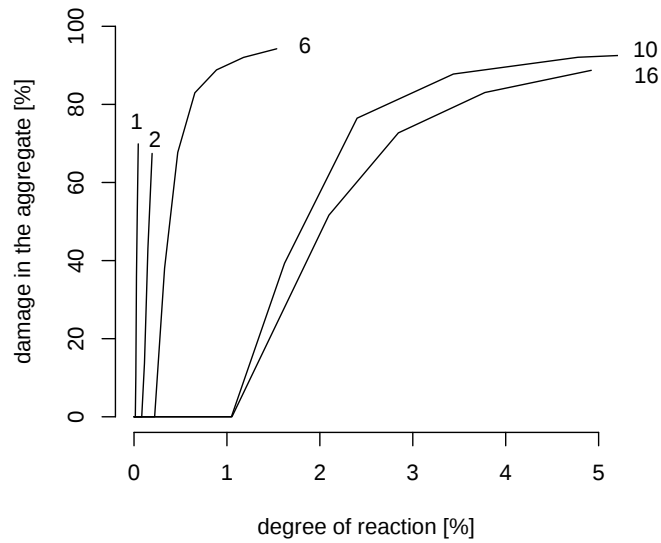


Figure 6.6: Homogeneous damage in aggregates of different diameter as a function of the degree of reaction in the aggregate. Aggregate size in millimetres.

The smaller aggregates are damaged for very low degrees of reaction, which is consistent with the experimental observations of Dunant on these aggregates and with the fracture mechanics model of Reinhardt and Mielich which predicts failure of the smallest aggregates for a lower level of gel pressure [54].

The overall damage in the simulated samples for different loads and kinetics is shown in Figure 6.4. All curves superpose as opposed to what happens in the case of cement paste. At the end of the simulation most reactive aggregates have reached a damage value very close to 1, and the damaged fraction in the aggregates tends toward the fraction of reactive aggregates.

ASR was simulated with simplified damage models. In all cases the effects of applied load on the expansion could not be reproduced, and the damage induced was very high compared to what happens in the field. The failure criterion used in these simulations is a lower bound of the material behaviour, indicating that other criteria will exhibit similar trends.

These simplified approaches still indicate that the main effect of creep is to reduce and delay the damage in the paste, and that the damage in the aggregate is mostly unaffected. This is consistent with the experimental observations of Ben Haha, who showed that the damage-expansion relation of ASR-affected concretes and mortars did not depend on the rate of the chemical reaction [6, 7].

Localisation and orientation of damage are two predominant features that are not considered by these simplified models. Indeed, the average values used here are wrong estimates of local behaviours. The stress imposed by ASR is so high that it can only be reduced by a complete failure of the sample. However, with a localised crack, only the elements close to the gel pockets will fail, and so the material will retain its integrity until the cracks percolate. In the next section we show through simple examples the effect of creep on the damage induced by ASR.

6.3 Combined effect of creep and ASR on simplified microstructure

Creep and damage must be both accounted for in the cement paste. If only creep is considered, the damage pattern in the aggregate shows a debonding of the aggregate which is not seen in experiments. For these simulations, a single aggregate is represented containing six randomly distributed gel pockets. With this simple setup we show the effects of creep or load by varying the conditions of the numerical experiments.

The aim of these simulations is not to reproduce the ASR expansion curves, but to illustrate with simple examples the behaviour of the system in different conditions in terms of material properties and rate of reaction.

6.3. Combined effect of creep and ASR on simplified microstructure

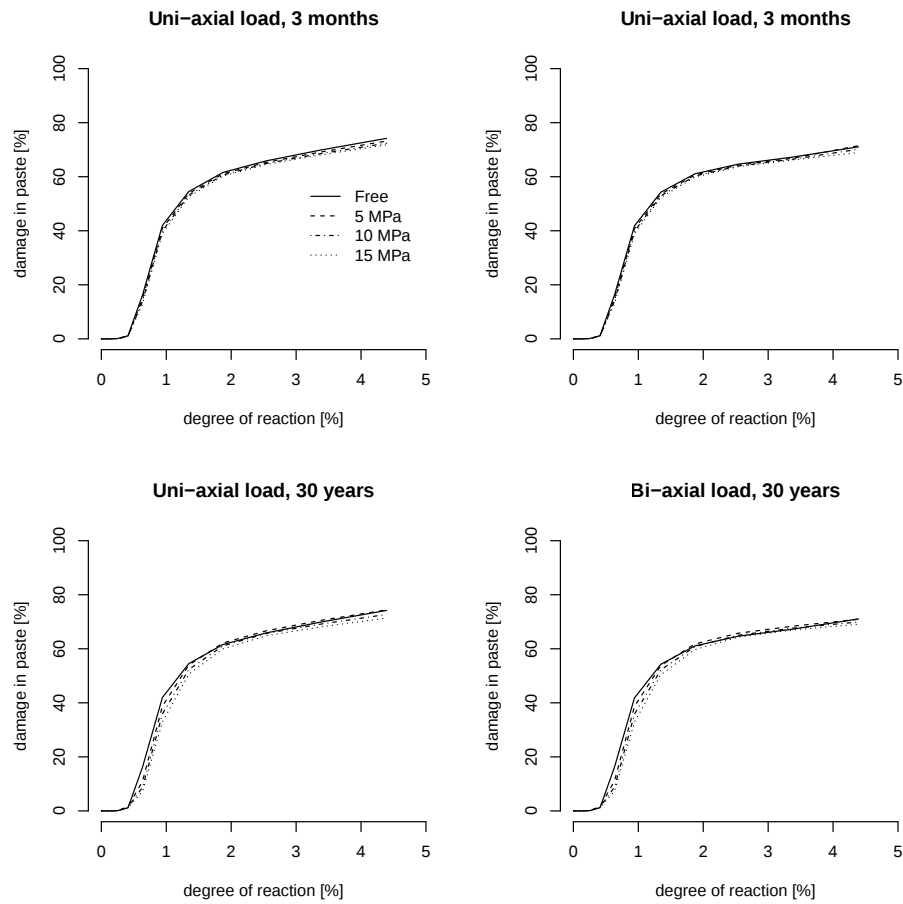


Figure 6.7: Homogeneous damage in the aggregates under uni-axial load (left) and bi-axial isotropic load (right), for 3 months (top) and 30 years kinetics (bottom).

In the following examples, the damage in the aggregate and the cement paste is explicitly accounted for with the damage algorithm presented in chapter 5. The discussion focuses on the comparison between the strain- and stress-based fracture criteria. In chapter 5, the strain-based criterion was preferred to simulate the wedge splitting tests of Denarié, but these were carried out at high strain rates, so it might not be directly applicable to slow strain rates as in ASR.

6.3.1 Free expansion

The influence of the failure criterion on the damage and expansion in unloaded conditions is investigated. The expansion of the system and induced damage are shown in Figure 6.8. The ultimate damage patterns are compared in Figure 6.9.

The fracture criterion has an important influence on the distribution of the damage in the microstructure: the strain-based criterion induces more damage in the cement paste, while the stress-based criterion induces more damage in the aggregate. The overall damage is lower for the stress-based criterion.

For the strain-based criterion, there is no clear influence of the kinetics. A lower reaction rate seems to reduce the amount of damage but increase the overall expansion. This effect might be caused by the simplistic microstructure: the sample loses very quickly its integrity, which makes the results obtained difficult to extrapolate to what would happen with more complete microstructures.

For the stress-based criterion, the trend is clearer: a lower reaction rate leads to less damage and less expansion. Furthermore, the rate of expansion with respect to the degree of reaction seems not to be affected by the rate of the reaction during the later stages. This is an illustration of the stability of the crack propagation in the sample. For the strain-based criterion, the propagation is unstable and the sample fails as soon as a crack initiates. For the stress-based criterion, the crack propagation is stabilised by the criterion and further delayed by the creep.

In both cases the damage sometimes decreases in the sample. This is caused by the growth of the gel pockets: the area they cover is not accounted for in the measure in damage. During their growth, some elements that were previously damaged are replaced with gel, and therefore are not counted as damaged afterwards.

Finally, in all cases the damage increases very rapidly at the beginning. The final value of that initial damage depends on the rate of reaction and the type of criterion. This indicates that creep does not affect the point at which the aggregate splits, but affects the damage caused during this event and the subsequent propagation.

6.3.2 Effect of load

We repeat the previous simulations with a 5 MPa uni-axial load or a 5 MPa bi-axial load, using the slowest kinetics. These setups induce a very high damage in the sample, up to the point that the samples fail in all conditions. The damage as a function of the degree of reaction and the load is reported in Figure 6.10.

This early failure is caused by the fact that the microstructure is not fully represented, and this numerical setup is too brittle compared to concrete. The damage pattern are reported in Figure 6.11.

The ultimate pattern shows oriented cracking in the uni-axial load, and to a lesser extent under bi-axial load. In this case, it forms a denser network of cracks. We observe that the damage remains higher in the aggregate for the stress-based criterion and higher in the paste for the strain-based criterion.

6.3. Combined effect of creep and ASR on simplified microstructure

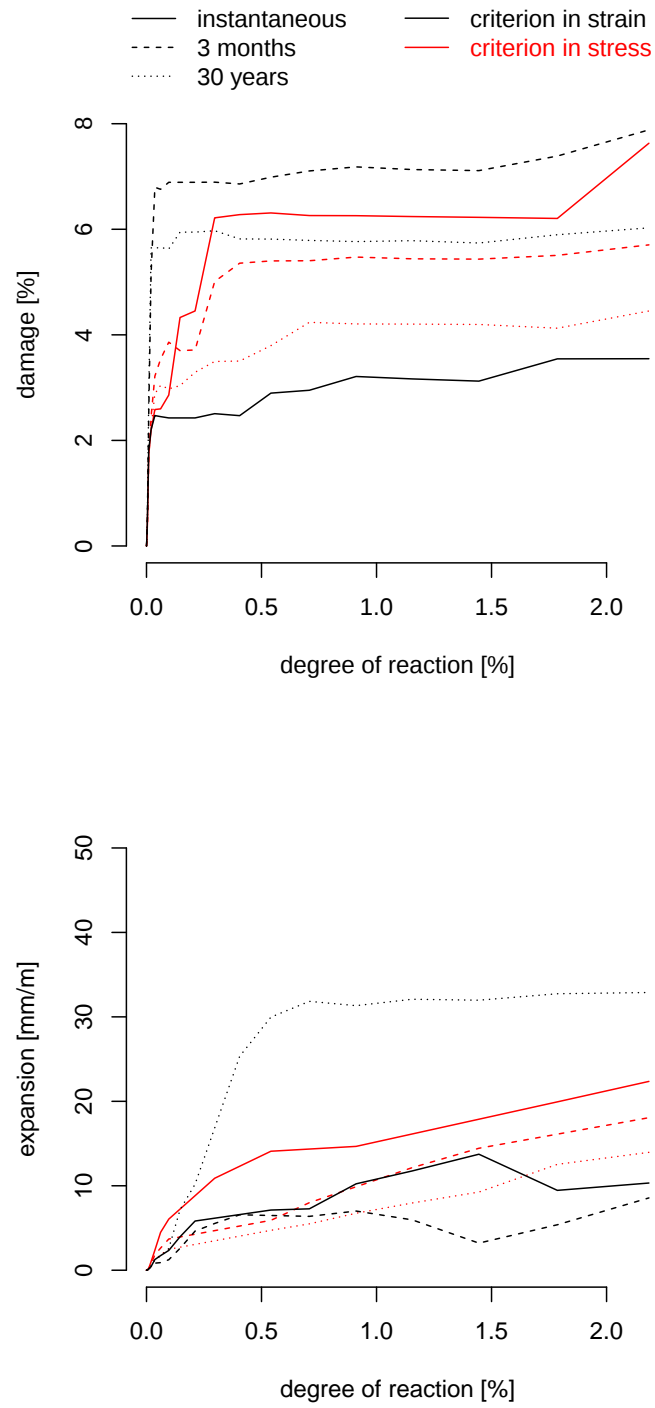


Figure 6.8: Quantity of damage (top) and expansion (bottom) induced by ASR in a single aggregate with different fracture criteria and reaction kinetics.

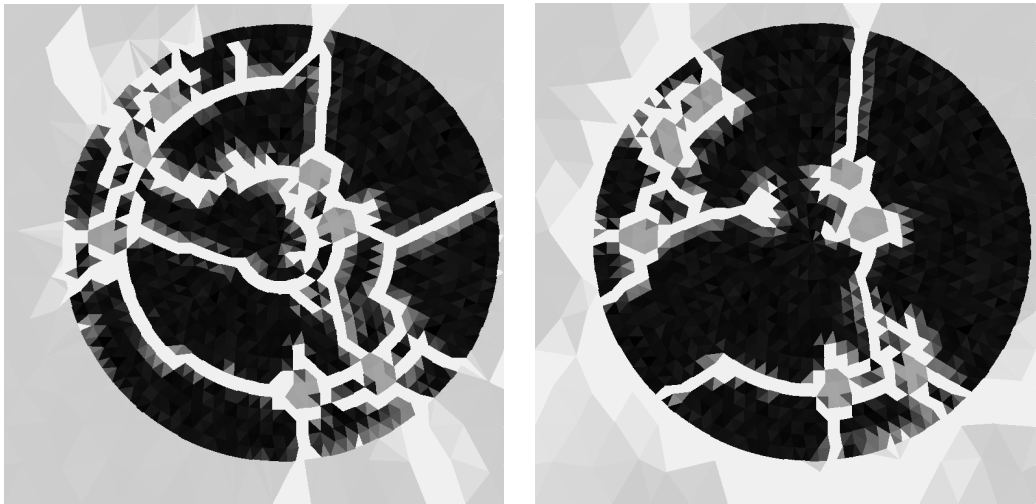


Figure 6.9: Pattern of damage induced by ASR using a stress-based (left) or strain-based (right) criterion in a single aggregate in unloaded conditions.

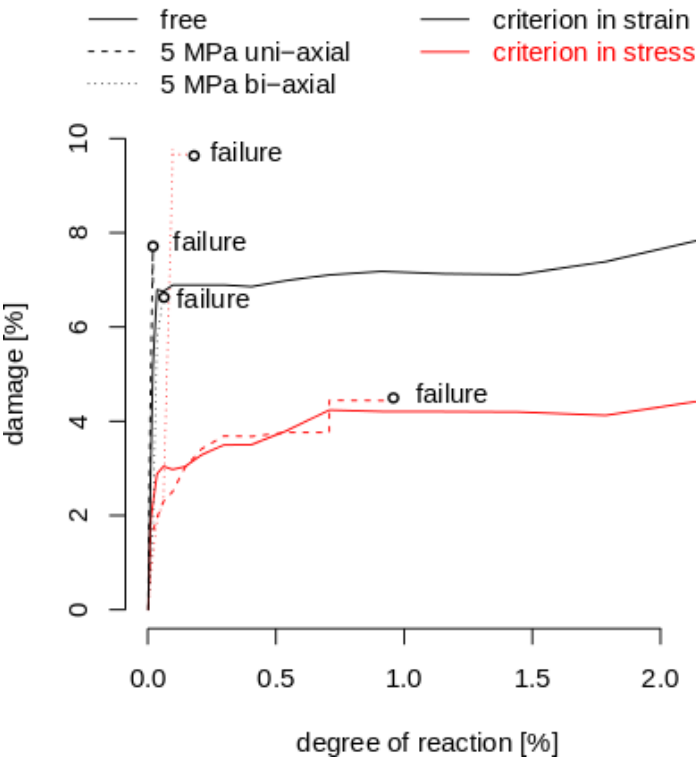


Figure 6.10: Quantity of damage induced by ASR in a single aggregate under uni-axial or bi-axial load.

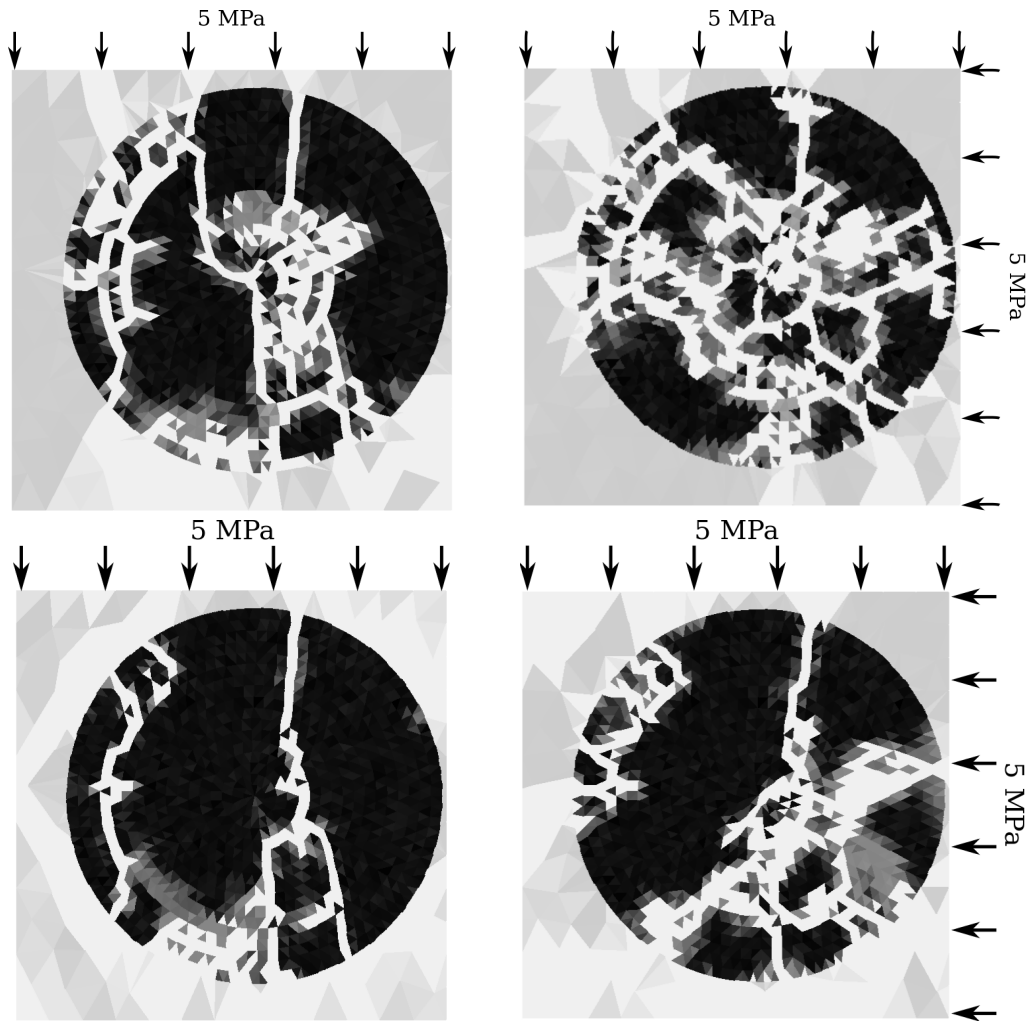


Figure 6.11: Pattern of damage induced by ASR in a single aggregate under 5 MPa uni-axial (left) or 5 MPa bi-axial load (right) with the stress-based (top) and the strain-based criterion (bottom).

6.3.3 Effect of creep and damage in the cement paste

Considering that in the microscopic observations of Ben Haha or Dunant little damage was found in the cement paste, one could assume that the creep of the cement paste is predominant compared to cracking, and that any loss of mechanical properties is mostly driven by the damage in the aggregates.

Here, the paste is simulated as a purely visco-elastic material, and results are compared with the stress-based criterion. The damage induced as a function of the degree of reaction and for different kinetics is shown in Figure 6.12. The final damage pattern for the different scenarios is shown in Figure 6.13.

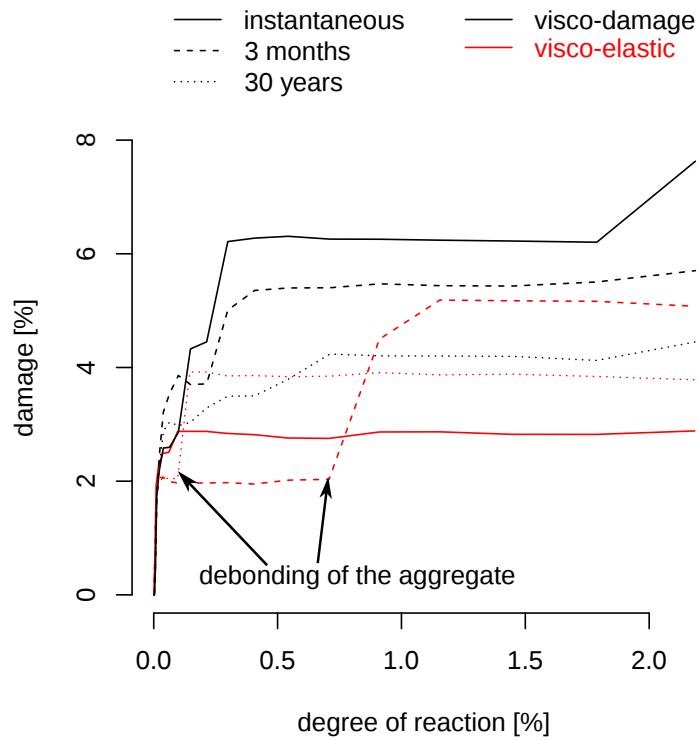


Figure 6.12: Quantity of damage induced by ASR in a single aggregate as a function of the degree of reaction with different reaction kinetics. The cement paste is either purely visco-elastic (red curves) or visco-elastic with damage (black curves).

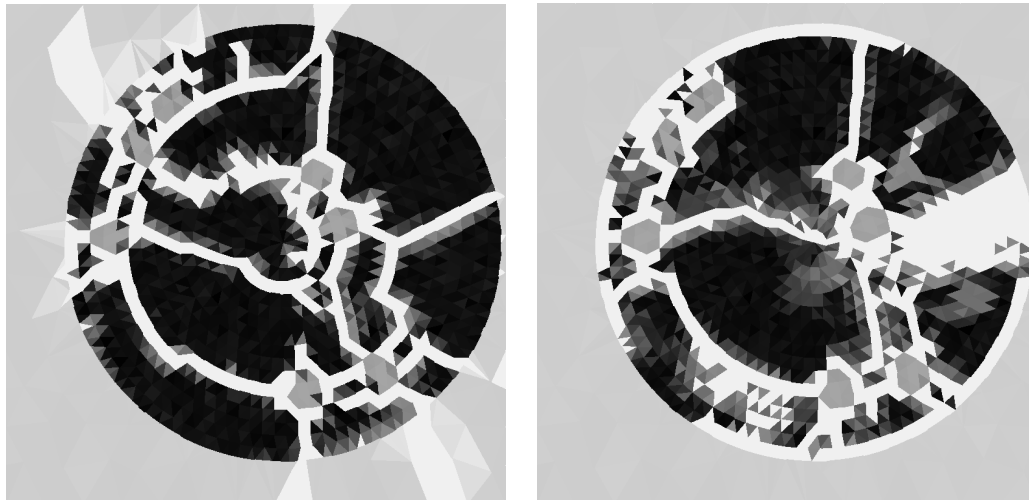


Figure 6.13: Pattern of damage induced by ASR in a single aggregate with damage in the cement paste (left) and without (right).

6.4. Combined effect of creep and ASR on concrete microstructures

The overall damage is lower with the visco-elastic cement paste than when the paste is also damaged. Furthermore, we observe debonding of the aggregates in the visco-elastic case, which does not happen in the damage case. This is caused by the creep of the cement paste: it redistributes the stresses inside the microstructure, up to the point that the aggregate fails in tension. This event corresponds to the steep rises in damage seen in Figure 6.12. It does not occur in the instantaneous case as the paste cannot creep in these conditions, nor with the visco-brittle cement paste as the paste breaks first.

These small simulations show that creep has the following effects on the simulated damage caused by ASR:

- The creep in the cement paste reduces the overall damage when the rate of reaction is slower.
- The instant at which the aggregate split is not affected.
- The stability of the crack growth in the cement paste depends on the fracture criterion: unstable for the strain, stable for stress.
- The load affects the orientation of the damage but also increases it up to the failure of the sample.
- The creep in the cement paste cannot be accounted for without damage.

These effects are verified on concrete microstructures in the next section.

6.4 Combined effect of creep and ASR on concrete microstructures

Concrete is simulated with a full microstructure using the complete model. The damage can occur in the aggregates and the visco-elastic cement paste. The previous sections highlighted the influence of the fracture criterion, and it is expected that the behaviour of concrete will also vary following similar trends.

The criterion in stress should reduce the damage in the material as the rate of reaction decreases. The mechanical setup corresponds to a relaxation test in which the displacement is imposed by the reaction: therefore the stress relaxation in the cement paste will be more predominant with the slowest kinetics than with the fastest.

The strain-based criterion should lead to a failure of the cement paste even for low degrees of reaction. The creep in the cement paste increases the strain in the material, and therefore the risk of cracking. In fact, an element will always fail under any load after a long enough time, even in compression: in that case the lateral tensile strain will lead to delayed fracture of the element.

These two material behaviours do not capture fully the properties of concrete. Indeed, neither of them can reproduce the effects of the strain rate or sustained load on the fracture of the material. The two criteria in strain and in stress provide bounds of the real material behaviour. Several studies have shown that the stress intensity factor (or the ultimate tensile strength, depending on the author) decreases with the strain rate, and reaches an asymptotic non-zero value. The ratio between the highest strength (obtained for a strain rate of 1 s^{-1}) and the minimum strength (defined as the asymptotic value when the strain rate reaches 0) for different studies are gathered in Table 6.3 and compared with the two criteria with the material parameters chosen in this study.

Table 6.3: Ratio between maximum and minimum strength from different studies

Authors	Ratio
Bažant and Gettu [144]	2.0 ± 0.3
Malvar and Crawford [145]	1.9 ± 0.4
Chen and co-workers [146]	2.5 ± 0.4
Strain-based criterion	6.666
Stress-based criterion	1.000

The values obtained from experiment presents a certain scatter, but remain in all cases well within the bounds given the strain- and stress-based criteria. The existence of the asymptote suggests that the failure mode changes with the strain rate, and that the strain-based criterion might be more appropriate for high strain rates and the stress-based criterion for low strain rates.

From a practical perspective, this might indicate that the relevant criterion changes during the course of ASR: the strain-based criterion might be more appropriate at the beginning, when the strain rate is relatively high, and the stress-based criterion at the end of the reaction when the strain rate decreases. Furthermore, this change of regime should depend on the time scale of the reaction, and is likely to happen earlier for the fastest kinetics.

In this work the two criteria are investigated. The data were insufficient to calibrate properly a fracture criterion which accounts for the shift in failure mode with the strain rate. All criteria will yield a global behaviour between the bounds defined by the two laws tested here.

The results obtained with the model are compared to experimental results of Ben Haha [6, 7]. He measured the expansion of concrete prisms as a function of the degree of degradation in the aggregates. In fact, the image analysis technique he used cannot separate the advancement of the chemical reaction from the mechanical damage. The method consists in counting the darkest pixels contained in the aggregates¹, and therefore measures the area fraction of voids in the aggregates.

¹The results of Ben Haha are sensitive to the threshold chosen, but this is beyond the scope of the current study.

6.4. Combined effect of creep and ASR on concrete microstructures

In the following simulations, the results are expressed in terms of expansion as a function of damaged area in the aggregate. The expansion is defined as the average displacement on the boundaries of the sample. The damaged area \mathcal{A} is calculated with (6.2), where a_e is the area of an element e and a_{agg} the total area of aggregates in the sample.

$$\mathcal{A} = \frac{1}{a_{\text{agg}}} \left[\sum_{e \in \text{agg}} \frac{9}{16} d_e \cdot a_e \right] \quad (6.2)$$

The factor 9/16 is used to account for the percolation of microcracks in the element. Indeed, d characterises the loss of stiffness in the material, but not the damaged area. Budiansky found in a landmark paper that with micro-cracks randomly oriented in an elastic specimen, the stiffness of the material is linear with respect to the damaged area and vanishes when the volume fraction of voids reaches 9/16 [147]. However, this value is certainly too high when comparing the characteristic size of the element in the simulation and the opening of the cracks in experiments.

Ben Haha showed that the relation between expansion and damage in the aggregates did not depend on the chemical and environmental conditions, and therefore not on the rate of the reaction or rate of damage.

In the numerical simulations, the shape of the damage-expansion curve is dominated by the nature of the failure criterion, and not the reaction or damage rate, as shown in Figure 6.14. This is in agreement with the experimental results of Ben Haha [7], and the scatter observed in the simulations is in the range of the experimental scatter.

In these simulations, the simulations predict a larger initial damage than what is experimentally observed. However, the morphology of the damage varies in a way similar to what was observed with the simulations of a single aggregate. This initial discrepancy is likely caused by the fact that in real aggregates, pre-existing cracks are first opened, and only then does damage increase. In his measure, Ben Haha removed the initial porosity of the aggregates, which is in the order of 1-2 %.

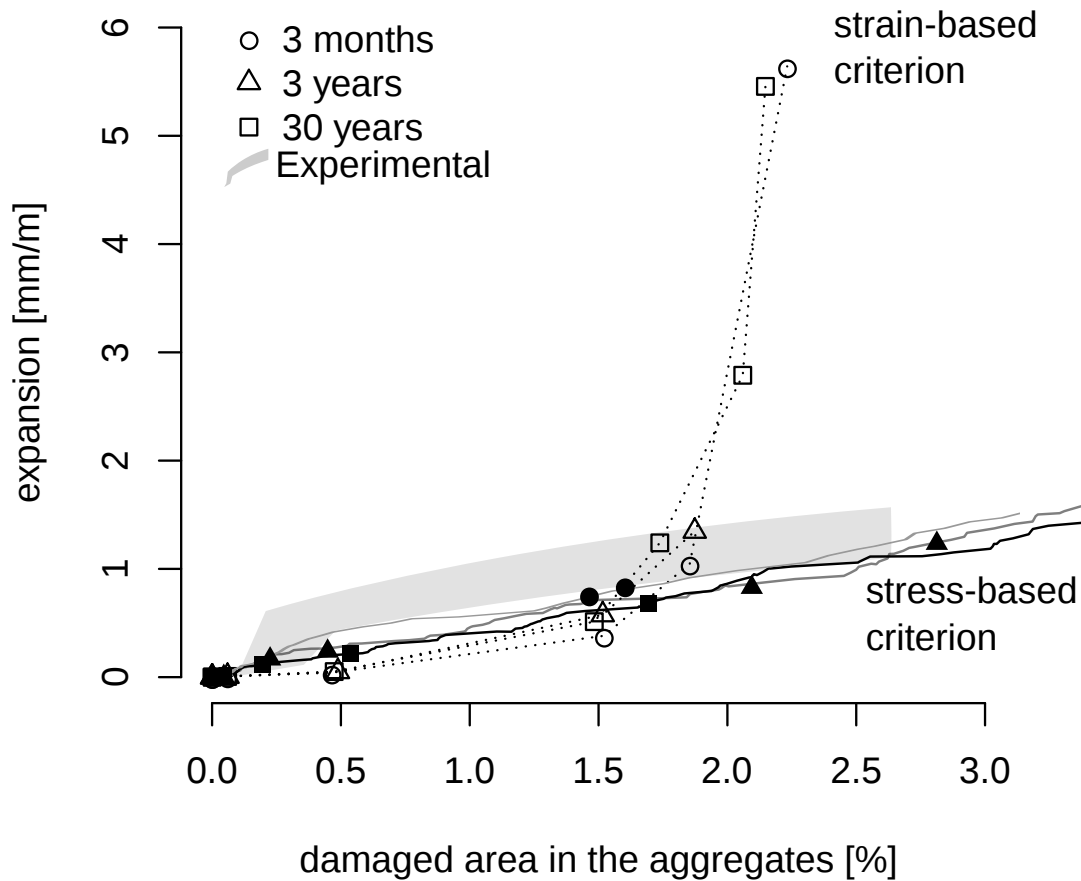
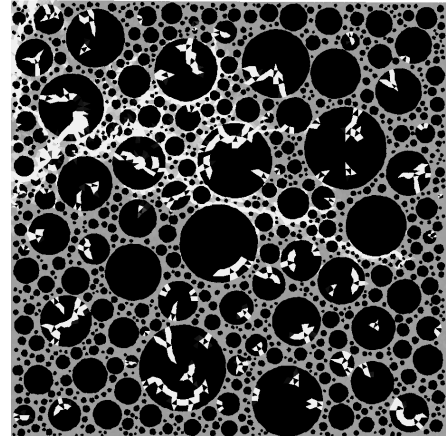
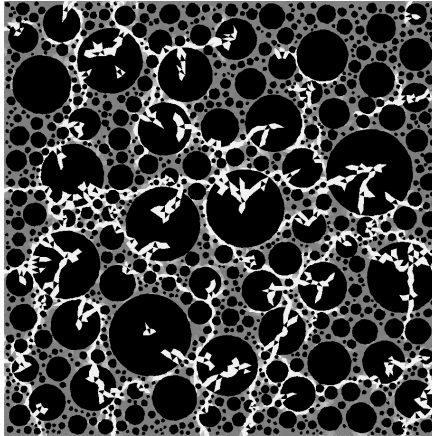


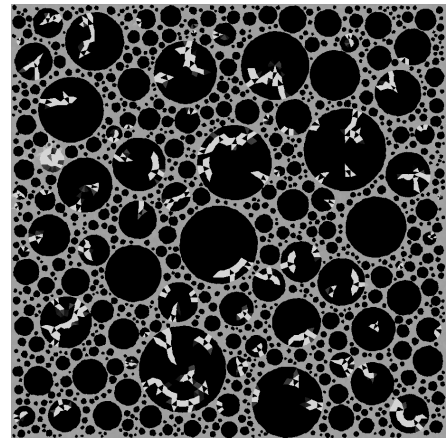
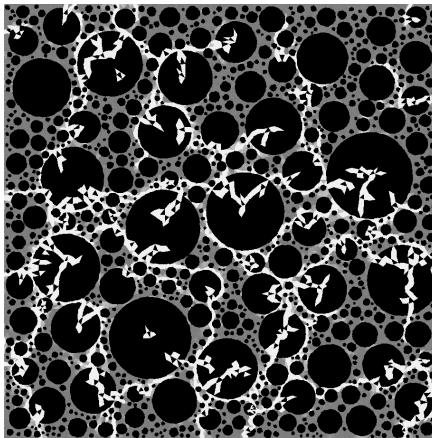
Figure 6.14: Expansion as a function of the damage in the aggregates in a simulated concrete microstructure with the complete ASR-creep model for three different kinetics and the two fracture criteria. Comparison with experimental data from Ben Haha [7]

With the strain-based criterion, the aggregates and the paste are damaged very rapidly: there are no intermediate states before the propagation of the damage in the cement paste. With all reaction kinetics, cracks have propagated through the sample paste even though the damage in the aggregates remains small. After that point, a small increase in the degree of reaction (and therefore, the damage in the aggregates) will cause a large increase in expansion.

3 months



3 years



30 years

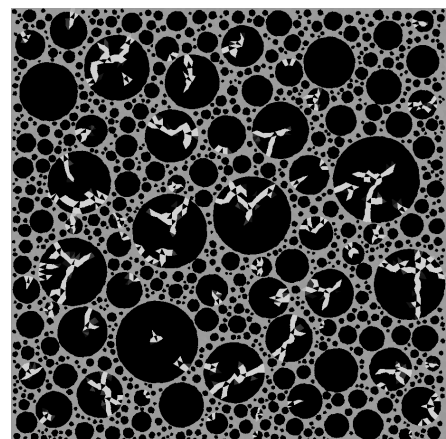
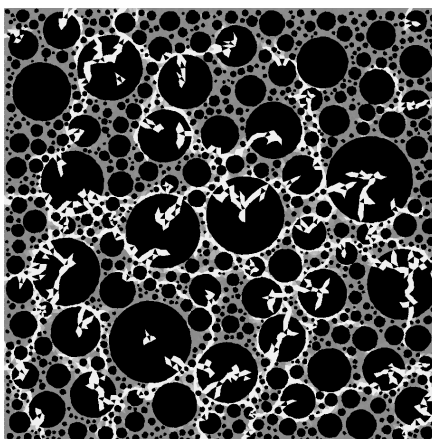


Figure 6.15: Damage patterns induced by ASR at 0.02 % of reaction with the strain-based (left) and stress-based (right) criteria and for the three different kinetics.

With the stress-based criterion, the damage propagation occurs in two stages. The aggregates break first while the paste remains intact, and thereafter the paste is progressively damaged. In this second stage, the propagation of the damage in the cement paste is stable, and so therefore an increase in the degree of reaction will cause a smaller expansion (compared to the strain-based criterion). The material can then reach higher amounts of damage in the aggregates and show a lower expansion.

The initial expansion is slightly lower than what Ben Haha measured. This effect is caused by the distribution of the reactive material in the simulated sample, as no zones were nucleated in the smallest aggregates. Indeed, small aggregates are split for lower degree of reaction, as shown for example by the model of Reinhardt [54]. A simulation with reactive small aggregates would therefore impose a larger initial expansion than in the present simulations.

The damage patterns at the same advancement of the chemical reaction are shown in Figure 6.15. At that degree of reaction, the damage has propagated through the simulated sample using the strain-based criterion and for all kinetics, and using the stress-based criterion with the fastest rate of reaction only. In the two later cases, the stress relaxation delays the point at which the paste fails, as was expected with the simple simulations without damage.

The damage in the aggregates and the cement paste as a function of the degree of reaction are both decreased when the rate of reaction slows down, as shown in Figure 6.16. However, the overall expansion as a function of the degree of reaction remains similar, indicating that for the slowest kinetics, part of the deformation is attributed to creep. The reduction of the damage with respect to the reaction kinetics seems small, but will be increased with a material behaviour in which the very short-term and very long-term responses are better captured. Indeed, the short-term creep (before 1 day) is counted as elastic in the current cement paste model, and the long-term creep reaches its asymptotic value after 3 years.

These simulations show that creep has the following influence on ASR:

- The relation between expansion and damage in the aggregates is only marginally affected by creep or the rate of the reaction.
- The choice of fracture criterion dominates the shape of the expansion-damage curve for the long-term consequences of the reaction.
- A criterion in stress delays the propagation of damage for the slowest kinetics, notably by stabilising the crack propagation in the cement paste.
- Results by Dunant were equivalent to using a stress-based criterion and represent a bound of possible behaviour. The current work highlights possible important physical effects not taken into account by the previous work.

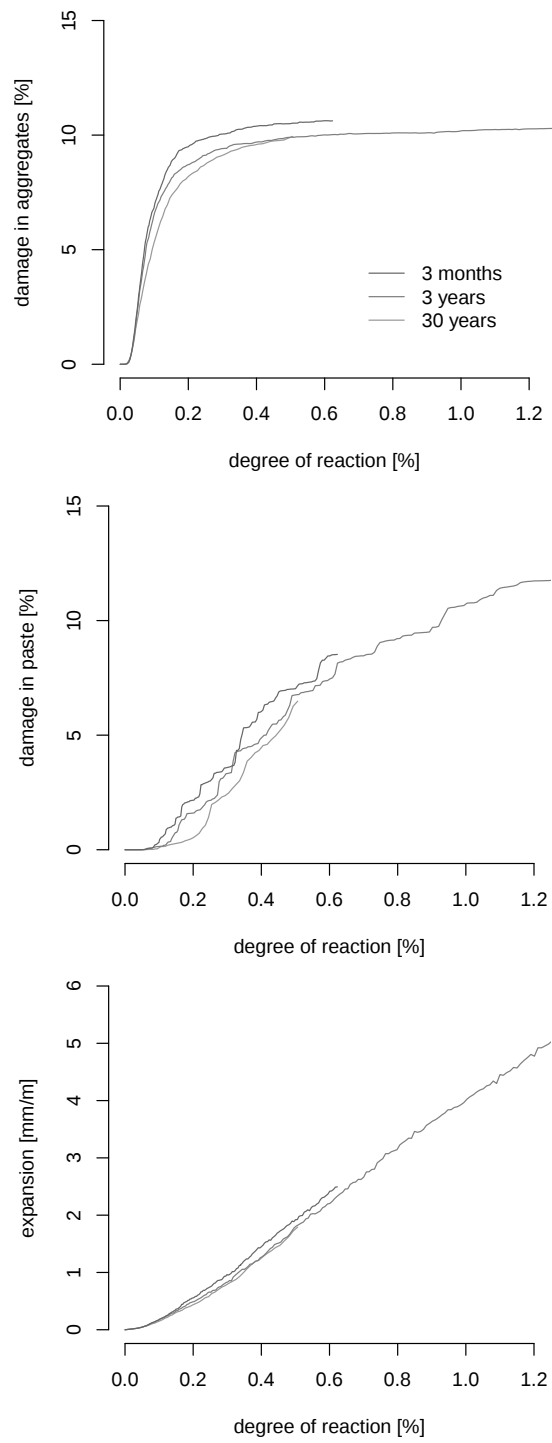


Figure 6.16: Damage in the aggregate (top), in the cement paste (middle) and expansion (bottom) as a function of the amount of reacted material, for the stress-based criterion and the three different kinetics.

6.5 Conclusions

ASR was simulated in a concrete microstructure with a coupled creep-damage algorithm. The relation between damage and expansion was confirmed in the presence of creep. However, the relation between the degree of reaction and damage is modified by the visco-elastic process in the case of a stress-based criterion: for the same degree of reaction, there is less damage in the microstructure when the kinetics of the reaction decrease. Notably, the damage in the cement paste is significantly reduced for the slower rates of reaction.

In chapter 3, the anisotropy of the ASR free expansion was simulated with this microstructural model by modelling the aggregates as oriented ellipses. Furthermore, this reduced the damage spread in the cement paste because of stress concentration in the aggregates. Combined together, these effects explain the integrity of the cement paste during the early stages of the reaction. The damage at the material level remains small, and the cement paste is progressively damaged. Extensive material-level damage, with macroscopically observable cracks on the surface of the samples still occurs, but at later stages of the simulations. In structures, map cracking is observed, which is typically caused by differential expansion between the core and the surface of the members. The cracks observed in this latter case are separated by distances significantly larger than the characteristic size of the samples simulated here, indicating that at the material level, the concrete remains sound. This is therefore in accordance with these simulations, which indicate that the material integrity of the concrete is not affected until high degrees of reaction are reached.

Overall, the model could be used to explain how concrete affected by ASR can maintain its integrity despite large expansions. This is of practical importance in field evaluations. Furthermore, the space-time formulation proposed in this work can be used to integrate the effect of progressive weakening of paste and aggregates on the apparent creeping behaviour of concrete affected by ASR, which should lead to practical, physics-based simulations at the structure level.

The proposed model can be used to simulate ASR under load. In the uni-axial simulations of Dunant, a crack propagated through the cement paste and lead to an early failure of the sample. The contribution of stress relaxation and shape of aggregate should reduce this effect and allow the simulation of ASR under load.

7 Conclusion

This thesis followed the study of Dunant on the relation between the stress, the expansion and damage induced by ASR. This relation depends on both the applied mechanical boundary conditions and the stress relaxation in the cement paste.

A tri-axial apparatus was designed to study the influence of applied load on ASR-affected samples. The cells can apply independent vertical and radial load on samples in conditions favorable for the reaction to occur: high temperature, high alkali concentration, and abundance of moisture. The strains are measured in-situ with fibre-optic sensors that were specifically designed to withstand the aggressive environmental conditions. Each cell can accommodate two reactive samples to verify the repeatability of the measures and one non-reactive for control. Six cells were built to investigate loads ranging from 5 to 15 MPa in both directions. Given the aggregates used in this study, experimental results are expected in one or two years.

The micro-mechanical model of Dunant was complemented with a visco-elastic model for the cement paste to simulate the effect of creep on the expansion and degradation caused by ASR. The microstructure of the sample is explicitly described in the simulation, including the continuous growth of silica gel pockets. This model is notably able to simulate the anisotropy of the free expansion of ASR by considering the aggregates as oriented ellipses.

A numerical method for visco-elastic materials was developed based on finite elements in space and time. The method can be used to simulate any material described by springs and dashpots assembled in series or in parallel. It is unconditionally stable in time, and can represent geometries that change in time such as the silica gel pockets.

The damage is characterised with an algorithm that accounts explicitly for the damage propagation in time. The thermodynamics of the system are verified at any point in time, which ensures the accurate coupling between creep and damage. With simple examples we show the importance of the order in which the elements are damaged, and validate this algorithm.

The visco-elastic model and damage algorithm are combined to simulate ASR at the microstructure level. The mechanical parameters used in this model have all a physical basis and can be measured or back-calculated from appropriate experiments. With this model we show that creep reduces the damage spread in the microstructure, and therefore the macroscopic expansion.

Perspectives

- The model can be used as a framework for a sensitivity analysis. Indeed, the damage pattern is not very sensitive to the material properties measured experimentally, reinforcing the notion that the damage-expansion relation is general. However, the failure mode of the cement paste is a key parameter. In this work, criteria in stress or in strain are used as upper or lower bounds of the material behaviour. The use of a mixed criterion would give a better representation of the effect of the strain rate on the material degradation.
- The damage model can be used to investigate various classes of irreversible mechanical behaviours. It can be used to investigate the failure behaviour of visco-elastic materials, and for example simulate the coupling between visco-elasticity and damage inside the microstructure of the cement paste. From a more general perspective, it can also be adapted to simulate plasticity and visco-plasticity.
- The model can be extended in three dimensions to capture more accurately the damage propagation in space. Notably, this might delay the crack coalescence observed in the simulated cement paste, and be required for the analysis of the multi-axial experiments. However, it might not be feasible from a computational perspective to represent the complete particle size distribution of the concrete in three dimensions, which might limit the scope of application of a three-dimensional model.
- The model can be used to analyse the experimental results of the tri-axial experiments, notably by decoupling the creep deformation from the ASR-induced expansion. The results can then be extrapolated to the time scale of field conditions, or to time-dependent loading cases.
- The experimental results, combined to the micro-mechanical model, can serve as a basis to formulate a macroscopic constitutive law for ASR-affected concrete which would include the influence of visco-elasticity and damage orientation on the material behaviour.

Bibliography

- [1] T. Stanton, Expansion of concrete through reaction between cement and aggregate, in: Proceedings of the American Society of Civil Engineers, Vol. 66, American Society of Civil Engineers, 1940, pp. 1781–1811.
- [2] C. Tambelli, J. Schneider, N. Hasparyk, P. Monteiro, Study of the structure of alkali-silica reaction gel by high-resolution nmr spectroscopy, *Journal of non-crystalline solids* 352 (32) (2006) 3429–3436.
- [3] S. Poyet, A. Sellier, B. Capra, G. Thèvenin-Foray, J.-M. Torrenti, H. Tournier-Cognon, E. Bourdarot, Influence of water on alkali-silica reaction: Experimental study and numerical simulations, *Journal of Materials in civil Engineering* 18 (4) (2006) 588–596.
- [4] J. Ponce, O. Batic, Different manifestations of the alkali-silica reaction in concrete according to the reaction kinetics of the reactive aggregate, *Cement and Concrete Research* 36 (6) (2006) 1148–1156.
- [5] C. Dunant, K. Scrivener, Effects of uniaxial stress on alkali-silica reaction induced expansion of concrete, *Cement and concrete research* 42 (3) (2012) 567–576.
- [6] M. Ben Haha, Mechanical effects of alkali silica reaction in concrete studied by sem-image analysis, Ph.D. thesis, Ecole Polytechnique Fédérale de Lausanne, n°3516 (2006).
- [7] M. Ben Haha, E. Gallucci, A. Guidoum, K. Scrivener, Relation of expansion due to alkali silica reaction to the degree of reaction measured by sem image analysis, *Cement and Concrete Research* 37 (8) (2007) 1206–1214.
- [8] A. Le Roux, E. Massieu, B. Godart, Evolution under stress of a concrete affected by aar. application to the feasibility of strengthening a bridge by prestressing, in: The ninth international conference on alkali-aggregate reaction in concrete, Volume 2, London, 1992, pp. 599–606.
- [9] C. Larive, Apports combinés de l'expérimentation et de la modélisation à la compréhension de l'alcali-réaction et de ses effets mécaniques, Ph.D. thesis, Ecole nationale des ponts et chaussees (1997).

Bibliography

- [10] S. Multon, F. Toutlemonde, Effect of applied stresses on alkali-silica reaction-induced expansions, *Cement and Concrete Research* 36 (5) (2006) 912–920.
- [11] C. Dunant, K. Scrivener, Micro-mechanical modelling of alkali-silica-reaction-induced degradation using the amie framework, *Cement and Concrete research* 40 (4) (2010) 517–525.
- [12] C. Dunant, Experimental and modelling study of the alkali-silica reaction in concrete, Ph.D. thesis, Ecole Polytechnique Fédérale de Lausanne, n°4510 (2009).
- [13] J. McGowan, H. Vivian, Studies in cement-aggregate reaction. 23. the effect of superincumbent load on mortar bar expansion, *Australian Journal of Applied Science* 6 (1955) 94–99.
- [14] D. Hobbs, *Alkali-silica reaction in concrete*, Telford, 1988, Ch. 3, pp. 56–72.
- [15] B. Baulande, Contribution à la détermination des poussées de gonflement dues aux alcali-réactions, Ph.D. thesis, Université Paul Sabatier, Toulouse (1993).
- [16] R. Helmuth, D. Stark, S. Diamond, M. Moranville-Regourd, Alkali-silica reactivity: an overview of research, *Contract* 100 (1993) 202.
- [17] C. Dunant, K. Scrivener, Effects of aggregate size on alkali-silica-reaction induced expansion, *Cement and concrete research* 42 (6) (2012) 745–751.
- [18] D. Inaudi, Fiber optic sensor network for the monitoring of civil engineering structures, Ph.D. thesis, Ecole Polytechnique Fédérale de Lausanne, n°1612 (1997).
- [19] M. Berra, G. Faggiani, T. Mangialardi, A. Paolini, Influence of stress restraint on the expansive behaviour of concrete affected by alkali-silica reaction, *Cement and Concrete Research* 40 (9) (2010) 1403–1409.
- [20] En 1992-1-1 eurocode 2 – design of concrete structures – part 1-1: General rules and rules for buildings.
- [21] G. Giaccio, R. Zerbino, J. Ponce, O. Batic, Mechanical behavior of concretes damaged by alkali-silica reaction, *Cement and Concrete Research* 38 (7) (2008) 993–1004.
- [22] C. Gravel, G. Ballivy, K. Khayat, M. Quirion, M. Lachemi, Expansion of aar concrete under tri-axial stresses: simulation with instrumented concrete blocks, in: *Proceedings of the Eleventh International Conference on Alkali-Aggregate Reaction*, Quebec, 2000, pp. 959–968.
- [23] L. Charpin, Modèle micromécanique pour l'étude de la réaction alcali-silice, Ph.D. thesis, Université Paris Est (2013).
- [24] E. Hoek, J. Franklin, A simple triaxial cell for field or laboratory testing of rock, Imperial College of Science and Technology, University of London, 1967.

-
- [25] H. Kupfer, K. Gerstle, Behavior of concrete under biaxial stresses, *Journal of the Engineering Mechanics Division* 99 (4) (1973) 853–866.
- [26] C. Wang, Z. Guo, X. Zhang, Experimental investigation of biaxial and triaxial compressive concrete strength, *ACI Materials Journal* 84 (2).
- [27] I. Imran, S. Pantazopoulou, Experimental study of plain concrete under triaxial stress, *ACI Materials Journal-American Concrete Institute* 93 (6) (1996) 589–601.
- [28] X. Vu, Y. Malecot, L. Daudeville, E. Buzaud, Experimental analysis of concrete behavior under high confinement: Effect of the saturation ratio, *International Journal of Solids and Structures* 46 (5) (2009) 1105–1120.
- [29] A. El-Dieb, R. Hooton, A high pressure triaxial cell with improved measurement sensitivity for saturated water permeability of high performance concrete, *Cement and concrete research* 24 (5) (1994) 854–862.
- [30] D. Inaudi, B. Glisic, Long-range pipeline monitoring by distributed fiber optic sensing, *Journal of pressure vessel technology* 132 (1) (2010) 011701.
- [31] T. Chrisp, P. Waldron, J. Wood, Development of a non-destructive test to quantify damage in deteriorated concrete, *Magazine of Concrete Research* 45 (165) (1993) 247–256.
- [32] Angst+Pfister, *Technische Grundlagen* (2013).
- [33] N. Aeronautics, Space Administration, Buckling of thin-walled circular cylinder (1968).
- [34] B. Glisic, Fibre optic sensors and behaviour in concrete at early age, Ph.D. thesis, Ecole Polytechnique Fédérale de Lausanne, n°2186 (2000).
- [35] T. Chappex, The role of aluminium from supplementary cementitious materials in controlling alkali-silica reaction, Ph.D. thesis, Ecole Polytechnique Fédérale de Lausanne, n°5429 (2012).
- [36] J. Bolomey, Granulation et prévision de la résistance probable des bétons, *Travaux* 19 (30) (1935) 228–232.
- [37] P. Léger, R. Tinawi, N. Mounzer, Numerical simulation of concrete expansion in concrete dams affected by alkali-aggregate reaction: state-of-the-art, *Canadian journal of civil engineering* 22 (4) (1995) 692–713.
- [38] Z. Bažant, A. Steffens, Mathematical model for kinetics of alkali-silica reaction in concrete, *Cement and Concrete Research* 30 (3) (2000) 419–428.
- [39] B. Capra, J.-P. Bournazel, Modeling of induced mechanical effects of alkali-aggregate reactions, *Cement and Concrete Research* 28 (2) (1998) 251–260.
- [40] V. Saouma, L. Perotti, Constitutive model for alkali-aggregate reactions, *ACI materials journal* 103 (3) (2006) 194–202.

- [41] D. Bulteel, E. Garcia-Diaz, C. Vernet, H. Zanni, Alkali-silica reaction: a method to quantify the reaction degree, *Cement and concrete research* 32 (8) (2002) 1199–1206.
- [42] M. Biot, Theory of elasticity and consolidation for a porous anisotropic solid, *Journal of Applied Physics* 26 (2) (1955) 182–185.
- [43] K. Li, Modélisation chimico-mécanique du comportement des bétons affectés par la réaction d'alcali-silice et expertise numérique des ouvrages d'art dégradés, Ph.D. thesis, Ecole des Ponts ParisTech (2002).
- [44] B. Capra, A. Sellier, Orthotropic modelling of alkali-aggregate reaction in concrete structures: numerical simulations, *Mechanics of materials* 35 (8) (2003) 817–830.
- [45] E. Grimal, A. Sellier, S. Multon, Y. Le Pape, E. Bourdarot, Concrete modelling for expertise of structures affected by alkali aggregate reaction, *Cement and Concrete Research* 40 (4) (2010) 502–507.
- [46] R. O'Connell, B. Budiansky, Viscoelastic properties of fluid-saturated cracked solids, *Journal of Geophysical Research* 82 (36) (1977) 5719–5735.
- [47] E. Denarié, C. Cécot, C. Huet, Characterization of creep and crack growth interactions in the fracture behavior of concrete, *Cement and concrete research* 36 (3) (2006) 571–575.
- [48] F. Bangert, D. Kuhl, G. Meschke, Chemo-hygro-mechanical modelling and numerical simulation of concrete deterioration caused by alkali-silica reaction, *International Journal for Numerical and Analytical Methods in Geomechanics* 28 (7-8) (2004) 689–714.
- [49] F. Pesavento, D. Gawin, M. Wyrzykowski, B. Schrefler, L. Simoni, Modeling alkali-silica reaction in non-isothermal, partially saturated cement based materials, *Computer Methods in Applied Mechanics and Engineering*.
- [50] Z. Bažant, G. Zi, C. Meyer, Fracture mechanics of asr in concretes with waste glass particles of different sizes, *Journal of engineering mechanics* 126 (3) (2000) 226–232.
- [51] A. Suwito, W. Jin, Y. Xi, C. Meyer, A mathematical model for the pessimum size effect of asr in concrete, *Concrete Science and Engineering* 4 (13) (2002) 23–34.
- [52] O. Pierard, C. Friebel, I. Doghri, Mean-field homogenization of multi-phase thermo-elastic composites: a general framework and its validation, *Composites Science and Technology* 64 (10) (2004) 1587–1603.
- [53] L. Charpin, A. Ehrlacher, A computational linear elastic fracture mechanics-based model for alkali-silica reaction, *Cement and Concrete Research* 42 (4) (2012) 613–625.
- [54] H. Reinhardt, O. Mielich, A fracture mechanics approach to the crack formation in alkali-sensitive grains, *Cement and Concrete Research* 41 (3) (2011) 255–262.

-
- [55] I. Comby-Peyrot, F. Bernard, P.-O. Bouchard, F. Bay, E. Garcia-Diaz, Development and validation of a 3d computational tool to describe concrete behaviour at mesoscale. application to the alkali-silica reaction, *Computational Materials Science* 46 (4) (2009) 1163–1177.
- [56] F. Dupray, Y. Malecot, L. Daudeville, E. Buzaud, A mesoscopic model for the behaviour of concrete under high confinement, *International journal for numerical and analytical methods in geomechanics* 33 (11) (2009) 1407–1423.
- [57] E. Schlangen, O. Çopuroglu, Concrete damage due to asr: a new method to determine the properties of the expansive gel, in: *Proceedings Framcos6*, June, 2007, pp. 17–22.
- [58] E. Schlangen, E. Garboczi, Fracture simulations of concrete using lattice models: computational aspects, *Engineering fracture mechanics* 57 (2) (1997) 319–332.
- [59] D. Lu, B. Fournier, P. Grattan-Bellew, Z. Xu, M. Tang, Development of a universal accelerated test for alkali-silica and alkali-carbonate reactivity of concrete aggregates, *Materials and Structures* 41 (2) (2008) 235–246.
- [60] O. Çopuroglu, E. Schlangen, Modelling of effect of asr on concrete microstructure, *Key Engineering Materials* 348 (2007) 809–812.
- [61] C. Dunant, S. Bordas, P. Kerfriden, K. Scrivener, T. Rabczuk, An algorithm to compute damage from load in composites, *Frontiers of Architecture and Civil Engineering in China* 5 (2) (2011) 180–193.
- [62] E. Garcia-Diaz, J. Riche, D. Bulteel, C. Vernet, Mechanism of damage for the alkali-silica reaction, *Cement and concrete research* 36 (2) (2006) 395–400.
- [63] A. Leemann, P. Lura, E-modulus of the alkali-silica-reaction product determined by micro-indentation, *Construction and Building Materials* 44 (2013) 221–227.
- [64] S. Poyet, Etude de la dégradation des ouvrages en béton atteints par la réaction alcali-silice: Approche expérimentale et modélisation numérique, Ph.D. thesis, Université de Marne-La-Vallée (2004).
- [65] J. Willis, Crack propagation in viscoelastic media, *Journal of the Mechanics and Physics of Solids* 15 (4) (1967) 229–240.
- [66] C. Cécot, Etude micromécanique par simulation numérique en éléments finis des couplages viscoélasticité-croissance des fissures dans les composites granulaires de type béton, Ph.D. thesis, Ecole Polytechnique Fédérale de Lausanne, n°2365 (2001).
- [67] A. Giorla, K. Scrivener, C. Dunant, Finite elements in space and time for the analysis of generalized visco-elastic materials, *International Journal for Numerical Methods in Engineering*.

Bibliography

- [68] R. Roscoe, Mechanical models for the representation of visco-elastic properties, *British Journal of Applied Physics* 1 (7) (1950) 171.
- [69] M. Biot, Theory of stress-strain relations in anisotropic viscoelasticity and relaxation phenomena, *Journal of Applied Physics* 25 (11) (1954) 1385–1391.
- [70] M. Biot, Linear thermodynamics and the mechanics of solids, in: *Proceedings of the Third US National Congress of Applied Mechanics*, American Society of Mechanical Engineers, Citeseer, 1958.
- [71] A. Neville, *Creep of concrete: plain, reinforced, and prestressed*.
- [72] Z. Bažant, F. Wittmann, *Creep and shrinkage in concrete structures*, Wiley Chichester, 1982.
- [73] A. Drozdov, *Mechanics of viscoelastic solids*, John Wiley Sons, 1998.
- [74] B. Tamtsia, J. Beaudoin, Basic creep of hardened cement paste a re-examination of the role of water, *Cement and Concrete Research* 30 (9) (2000) 1465–1475.
- [75] P. Acker, F.-J. Ulm, Creep and shrinkage of concrete: physical origins and practical measurements, *Nuclear Engineering and Design* 203 (2) (2001) 143–158.
- [76] G. De Schutter, Degree of hydration based kelvin model for the basic creep of early age concrete, *Materials and Structures* 32 (4) (1999) 260–265.
- [77] M. Vandamme, F. Ulm, Nanogranular origin of concrete creep, *Proceedings of the National Academy of Sciences* 106 (26) (2009) 10552–10557.
- [78] D. Davydov, M. Jirásek, Modeling of nanoindentation by a visco-elastic porous model with application to cement paste, in: *Nanotechnology in Construction 3*, Springer, 2009, pp. 187–192.
- [79] Q. Do, S. Bishnoi, K. Scrivener, Microstructural modelling of ageing basic creep in early age cement paste, *Modelling and Simulation in Materials Science and Engineering*.
- [80] O. Bernard, F.-J. Ulm, E. Lemarchand, A multiscale micromechanics-hydration model for the early-age elastic properties of cement-based materials, *Cement and Concrete Research* 33 (9) (2003) 1293–1309.
- [81] C.-B. Du, L.-G. Sun, Numerical simulation of aggregate shapes of two-dimensional concrete and its application 1, *Journal of Aerospace Engineering* 20 (3) (2007) 172–178.
- [82] J. Escoda, F. Willot, D. Jeulin, J. Sanahuja, C. Toulemonde, Estimation of local stresses and elastic properties of a mortar sample by fft computation of fields on a 3d image, *Cement and Concrete Research* 41 (5) (2011) 542–556.
- [83] O. Zienkiewicz, M. Watson, I. King, A numerical method of visco-elastic stress analysis, *International Journal of Mechanical Sciences* 10 (10) (1968) 807–827.

-
- [84] Z. Bažant, S. Wu, Rate-type creep law of aging concrete based on maxwell chain, *Matériaux et Construction* 7 (1) (1974) 45–60.
- [85] A. Guidoum, Simulation numérique 3d des comportements des bétons en tant que composites granulaires, Ph.D. thesis, Ecole Polytechnique Fédérale de Lausanne, n°1310 (1994).
- [86] M. Zocher, S. Groves, D. Allen, A three-dimensional finite element formulation for thermoviscoelastic orthotropic media, *International Journal for Numerical Methods in Engineering* 40 (12) (1997) 2267–2288.
- [87] O. Zienkiewicz, W. Wood, N. Hine, R. Taylor, A unified set of single step algorithms. part 1: General formulation and applications, *International Journal for Numerical Methods in Engineering* 20 (8) (1984) 1529–1552.
- [88] W. Wood, A unified set of single step algorithms. part 2: theory, *International journal for numerical methods in engineering* 20 (12) (1984) 2303–2309.
- [89] M. Katona, O. Zienkiewicz, A unified set of single step algorithms part 3: The beta-m method, a generalization of the newmark scheme, *International Journal for Numerical Methods in Engineering* 21 (7) (1985) 1345–1359.
- [90] N. Newmark, A method of computation for structural dynamics, in: *Proc. ASCE*, Vol. 85, 1959, pp. 67–94.
- [91] J. Argyris, D. Scharpf, Finite elements in time and space, *Nuclear Engineering and Design* 10 (4) (1969) 456–464.
- [92] I. Fried, M. Cremer, P. McMurtry, Finite-element analysis of time-dependent phenomena., *AIAA Journal* 7 (6) (1969) 1170–1173.
- [93] T. Hughes, G. Hulbert, Space-time finite element methods for elastodynamics: formulations and error estimates, *Computer methods in applied mechanics and engineering* 66 (3) (1988) 339–363.
- [94] D. French, A space-time finite element method for the wave equation, *Computer methods in applied mechanics and engineering* 107 (1) (1993) 145–157.
- [95] C. Bajer, B. Dyniewicz, Space-time approach to numerical analysis of a string with a moving mass, *International journal for numerical methods in engineering* 76 (10) (2008) 1528–1543.
- [96] L. Adélaide, F. Jourdan, C. Bohatier, Méthodes des éléments finis espace-temps et remaillage, *Revue Européenne des Eléments* 12 (4) (2003) 427–458.
- [97] A. Idesman, R. Niekamp, E. Stein, Continuous and discontinuous galerkin methods with finite elements in space and time for parallel computing of viscoelastic deformation, *Computer methods in applied mechanics and engineering* 190 (8) (2000) 1049–1063.

Bibliography

- [98] A. Idesman, R. Niekamp, E. Stein, Finite elements in space and time for generalized viscoelastic maxwell model, *Computational Mechanics* 27 (1) (2001) 49–60.
- [99] A. Idesman, Solution of linear elastodynamics problems with space–time finite elements on structured and unstructured meshes, *Computer methods in applied mechanics and engineering* 196 (9) (2007) 1787–1815.
- [100] C. Bajer, Notes on the stability of non-rectangular space–time finite elements, *International journal for numerical methods in engineering* 24 (9) (1987) 1721–1739.
- [101] C. Bajer, B. Dyniewicz, Virtual functions of the space–time finite element method in moving mass problems, *Computers & Structures* 87 (7) (2009) 444–455.
- [102] G. Howard, J. Penny, The accuracy and stability of time domain finite element solutions, *Journal of Sound and Vibration* 61 (4) (1978) 585–595.
- [103] O. Zienkiewicz, R. Taylor, J. Zhu, *The Finite Element Method: Its Basis and Fundamentals*, Vol. 1, Butterworth-Heinemann, 2005.
- [104] O. Zienkiewicz, R. Taylor, J. Zhu, *The Finite Element Method: Solid Mechanics*, Vol. 2, Butterworth-heinemann, 2005.
- [105] J. Burgers, *First Report on Viscosity and Plasticity*, Royal Netherlands Academy of Sciences, Amsterdam, 1935.
- [106] A. Bengougam, *Déformations différées et effets d'échelle des bétons de barrage*, Ph.D. thesis, Ecole Polytechnique Fédérale de Lausanne, n°2624 (2003).
- [107] S. Scheiner, C. Hellmich, Continuum microviscoelasticity model for aging basic creep of early-age concrete, *Journal of engineering mechanics* 135 (4) (2009) 307–323.
- [108] J. Sanahuja, C. Toulemonde, Numerical homogenization of concrete microstructures without explicit meshes, *Cement and Concrete Research* 41 (12) (2011) 1320–1329.
- [109] G. Dhatt, G. Touzot, *Une présentation de la méthode des éléments finis*, Maloine; Québec: Presses de l'Université Laval, 1981.
- [110] N. Moës, J. Dolbow, T. Belytschko, A finite element method for crack growth without remeshing, *Int. J. Numer. Meth. Engng* 46 (1999) 131–150.
- [111] N. Sukumar, D. Chopp, N. Moës, T. Belytschko, Modeling holes and inclusions by level sets in the extended finite-element method, *Computer methods in applied mechanics and engineering* 190 (46) (2001) 6183–6200.
- [112] N. Moës, M. Cloirec, P. Cartraud, J.-F. Remacle, A computational approach to handle complex microstructure geometries, *Computer methods in applied mechanics and engineering* 192 (28) (2003) 3163–3177.

-
- [113] J. Wang, Development and application of a micromechanics-based numerical approach for the study of crack propagation in concrete, Ph.D. thesis, Ecole Polytechnique Fédérale de Lausanne, n°1233 (1994).
- [114] M. Jirásek, B. Patzàk, Consistent tangent stiffness for nonlocal damage models, *Computers & structures* 80 (14) (2002) 1279–1293.
- [115] E. Budyn, G. Zi, N. Moës, T. Belytschko, A method for multiple crack growth in brittle materials without remeshing, *International journal for numerical methods in engineering* 61 (10) (2004) 1741–1770.
- [116] P. Areias, T. Belytschko, Analysis of three-dimensional crack initiation and propagation using the extended finite element method, *International Journal for Numerical Methods in Engineering* 63 (5) (2005) 760–788.
- [117] L. Kachanov, Time of the rupture process under creep conditions, *Isv. Akad. Nauk. SSR. Otd Tekh. Nauk* 8 (1958) 26–31.
- [118] J. Mazars, A description of micro-and macroscale damage of concrete structures, *Engineering Fracture Mechanics* 25 (5) (1986) 729–737.
- [119] R. de Borst, Some recent issues in computational failure mechanics, *International Journal for Numerical Methods in Engineering* 52 (1-2) (2001) 63–95.
- [120] M. Jirásek, P. Grassl, Evaluation of directional mesh bias in concrete fracture simulations using continuum damage models, *Engineering Fracture Mechanics* 75 (8) (2008) 1921–1943.
- [121] J. Rice, A path independent integral and the approximate analysis of strain concentration by notches and cracks, *Tech. rep., DTIC Document* (1967).
- [122] G. Pijaudier-Cabot, Z. Bažant, Nonlocal damage theory, *Journal of Engineering Mechanics* 113 (10) (1987) 1512–1533.
- [123] R. de Borst, Fracture in quasi-brittle materials: a review of continuum damage-based approaches, *Engineering Fracture Mechanics* 69 (2) (2002) 95–112.
- [124] C. Dunant, E. Bentz, Algorithmically imposed thermodynamic compliance for material models in mechanical simulations using the AIM method, submitted in *International Journal for Numerical Methods in Engineering*.
- [125] Y.-R. Kim, D. Allen, D. Little, Computational constitutive model for predicting nonlinear viscoelastic damage and fracture failure of asphalt concrete mixtures, *International Journal of Geomechanics* 7 (2) (2007) 102–110.
- [126] R. Abu Al-Rub, M. Darabi, A thermodynamic framework for constitutive modeling of time-and rate-dependent materials. part i: Theory, *International Journal of Plasticity* 34 (2012) 61–92.

Bibliography

- [127] M. Darabi, R. Abu Al-Rub, E. Masad, D. Nittle, A thermodynamic framework for constitutive modeling of time-and rate-dependent materials. part ii: Numerical aspects and application to asphalt concrete, *International Journal of Plasticity* 35 (2012) 67–99.
- [128] E. Prado, J. Van Mier, Effect of particle structure on mode i fracture process in concrete, *Engineering fracture mechanics* 70 (14) (2003) 1793–1807.
- [129] B. Oh, Z. Bažant, Crack band theory for fracture of concrete, *Materials and Structures*, January-February (1983) 155–177.
- [130] A. Berthollet, J.-F. Georgin, J.-M. Reynouard, Fluage tertiaire du béton en traction: Modélisation d'éprouvettes entaillées sous chargement de traction maintenu élevé, *Revue française de génie civil* 8 (2-3) (2004) 235–260.
- [131] N. Challamel, C. Lanos, C. Casandjian, Creep failure in concrete as a bifurcation phenomenon, *International Journal of Damage Mechanics* 14 (1) (2005) 5–24.
- [132] E. Brühwiler, F. Wittmann, The wedge splitting test, a new method of performing stable fracture mechanics tests, *Engineering Fracture Mechanics* 35 (1) (1990) 117–125.
- [133] E. Denarié, Etude expérimentale des couplages viscoélasticité-croissance des fissures dans les bétons de ciment, Ph.D. thesis, Ecole Polytechnique Fédérale de Lausanne, n°2195 (2000).
- [134] M. Jirásek, Nonlocal models for damage and fracture: comparison of approaches, *International Journal of Solids and Structures* 35 (31) (1998) 4133–4145.
- [135] R. Peerlings, M. Geers, R. De Borst, W. Brekelmans, A critical comparison of nonlocal and gradient-enhanced softening continua, *International Journal of Solids and Structures* 38 (44) (2001) 7723–7746.
- [136] S. Bishnoi, K. Scrivener, μic : A new platform for modelling the hydration of cements, *Cement and Concrete Research* 39 (4) (2009) 266–274.
- [137] R Core Team, R: A Language and Environment for Statistical Computing, R Foundation for Statistical Computing, Vienna, Austria, ISBN 3-900051-07-0 (2012).
URL <http://www.R-project.org/>
- [138] H. Tsien, A generalization of alfreys theorem for visco-elastic media, *Quarterly of Applied Mathematics* 8 (1) (1950) 104–106.
- [139] T. Mori, K. Tanaka, Average stress in matrix and average elastic energy of materials with misfitting inclusions, *Acta metallurgica* 21 (5) (1973) 571–574.
- [140] C. Dunant, B. Bary, A. Giorla, C. Péniguel, J. Sanahuja, C. Toulemonde, A.-B. Tran, F. Willot, J. Yvonnet, A critical comparison of several numerical methods for computing effective properties of highly heterogeneous materials, *Advances in Engineering Software* 58 (2013) 1–12.

- [141] A.-B. Tran, Développement de méthodes numériques multi échelle pour le calcul des structures constituées de matériaux fortement hétérogènes élastiques et viscoélastiques, Ph.D. thesis, Université Paris-Est (2011).
- [142] C. Yi, C. Ostertag, Mechanical approach in mitigating alkali-silica reaction, *Cement and concrete research* 35 (1) (2005) 67–75.
- [143] B. Pichler, C. Hellmich, Upscaling quasi-brittle strength of cement paste and mortar: A multi-scale engineering mechanics model, *Cement and Concrete Research* 41 (5) (2011) 467–476.
- [144] Z. Bazant, R. Gettu, Rate effects and load relaxation in static fracture of concrete, *ACI Materials Journal* 89 (5) (1992) 456–468.
- [145] L. Malvar, J. Crawford, Dynamic increase factors for concrete, Tech. rep., DTIC Document (1998).
- [146] R. Chen, K. Xia, F. Dai, F. Lu, S. Luo, Determination of dynamic fracture parameters using a semi-circular bend technique in split hopkinson pressure bar testing, *Engineering Fracture Mechanics* 76 (9) (2009) 1268–1276.
- [147] B. Budiansky, R. O’connell, Elastic moduli of a cracked solid, *International Journal of Solids and Structures* 12 (2) (1976) 81–97.
- [148] S. Park, R. Kim, R. Schapery, A viscoelastic continuum damage model and its application to uniaxial behavior of asphalt concrete, *Mechanics of Materials* 24 (4) (1996) 241–255.
- [149] A. Tran, J. Yvonnet, Q.-C. He, C. Toulemonde, J. Sanahuja, A simple computational homogenization method for structures made of linear heterogeneous viscoelastic materials, *Computer Methods in Applied Mechanics and Engineering* 200 (45) (2011) 2956–2970.
- [150] Abaqus 6.11 theory manual (2011).
- [151] C. Chazal, R. Moutou Pitti, An incremental constitutive law for ageing viscoelastic materials: a three-dimensional approach, *Comptes Rendus Mécanique* 337 (1) (2009) 30–33.
- [152] V. Šmilauer, Z. Bažant, Identification of viscoelastic csh behavior in mature cement paste by fft-based homogenization method, *Cement and Concrete Research* 40 (2) (2010) 197–207.

A Mechanical design of the tri-axial cells

The designs for the tri-axial cells are gathered in the following pages. Their respective role is briefly outlined below:

- A.1 Top plate: maintains the verin in place
- A.2 Intermediate plate: the channels are used to drain the air out of the cell
- A.3 Bottom plate: the channels are used to fill the cell and extract the fibre-optic wires
- A.4 Cell wall
- A.5 Piston: transmits the force from the verin (outside the cell) to the support plate (inside the cell)
- A.6 Support plate: transmits the force from the piston to the samples
- A.7 Ball joint support plate: maintains the samples and the ball joints in place
- A.8 Aluminium base: placed under the cell; is used to maintain the bottom bolts in place and guide the fibre-optic wires

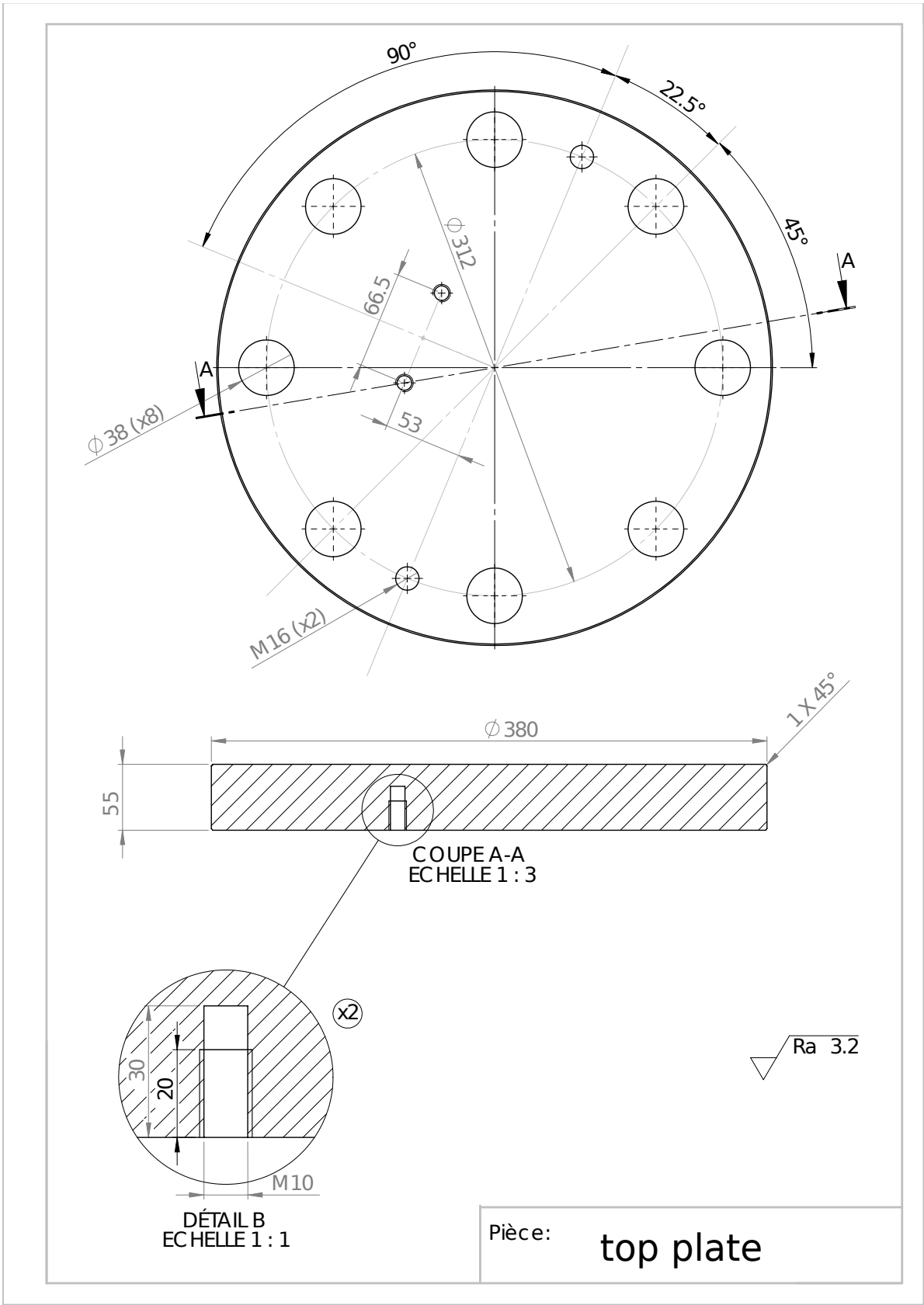


Figure A.1

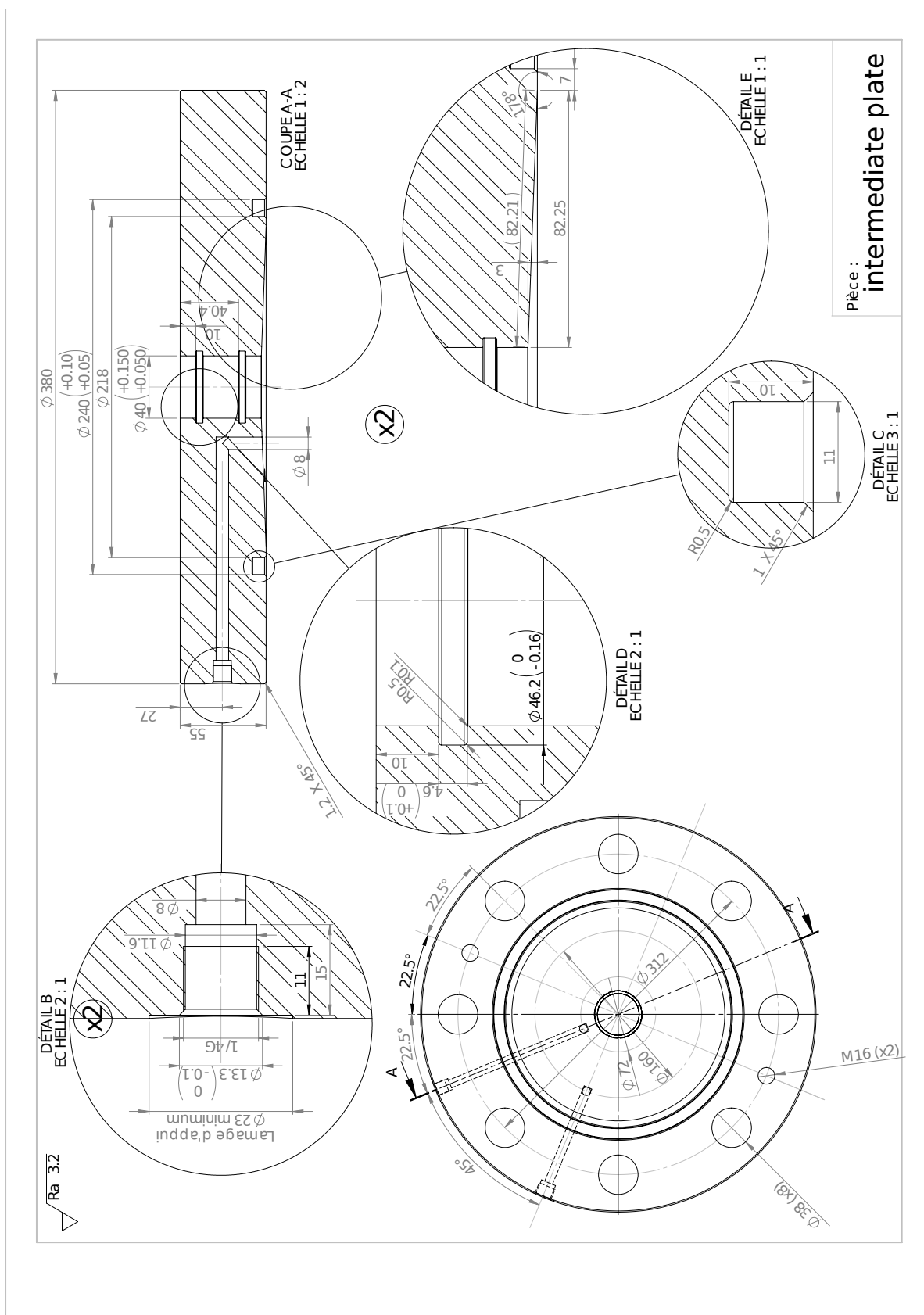


Figure A.2

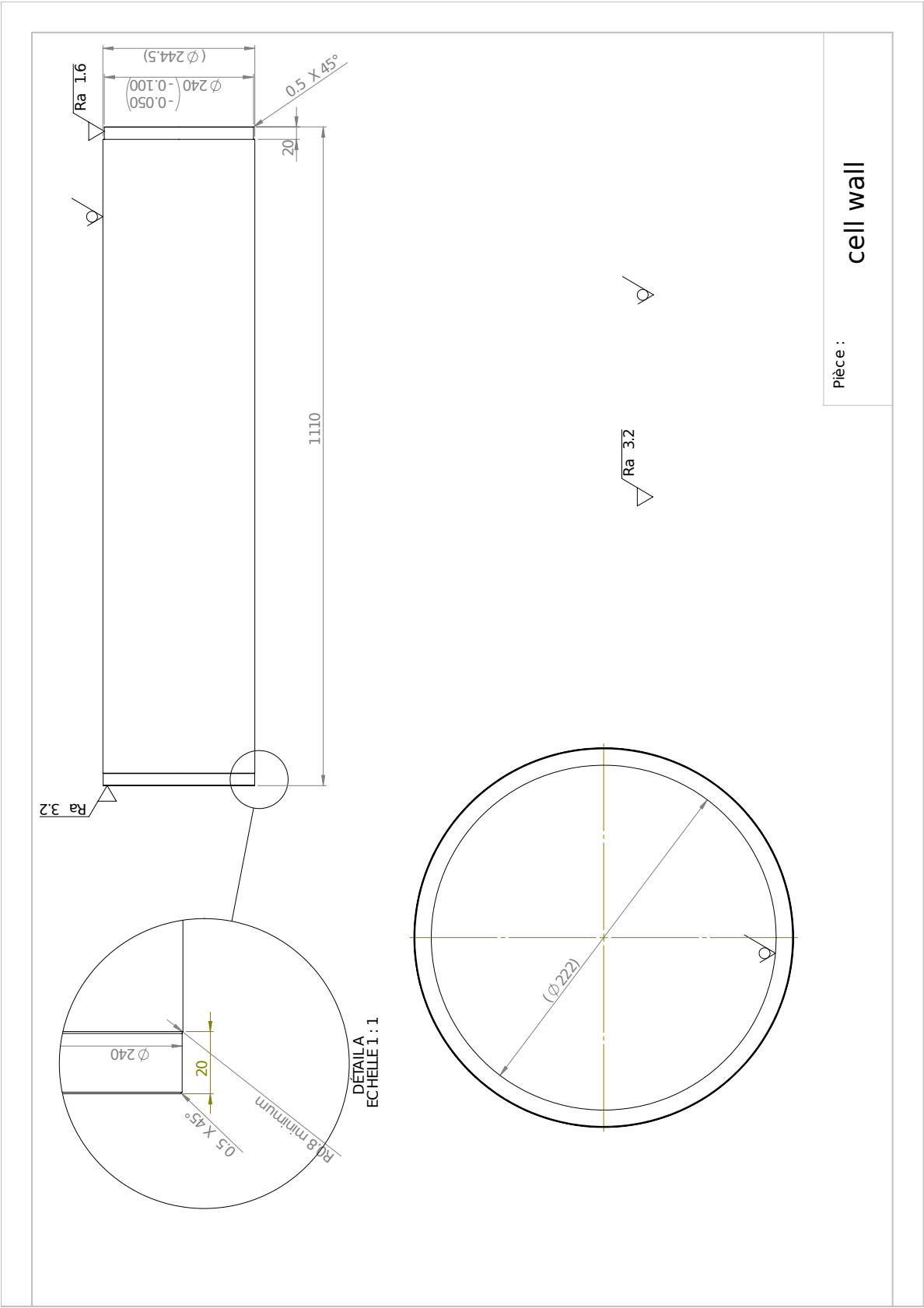


Figure A.4

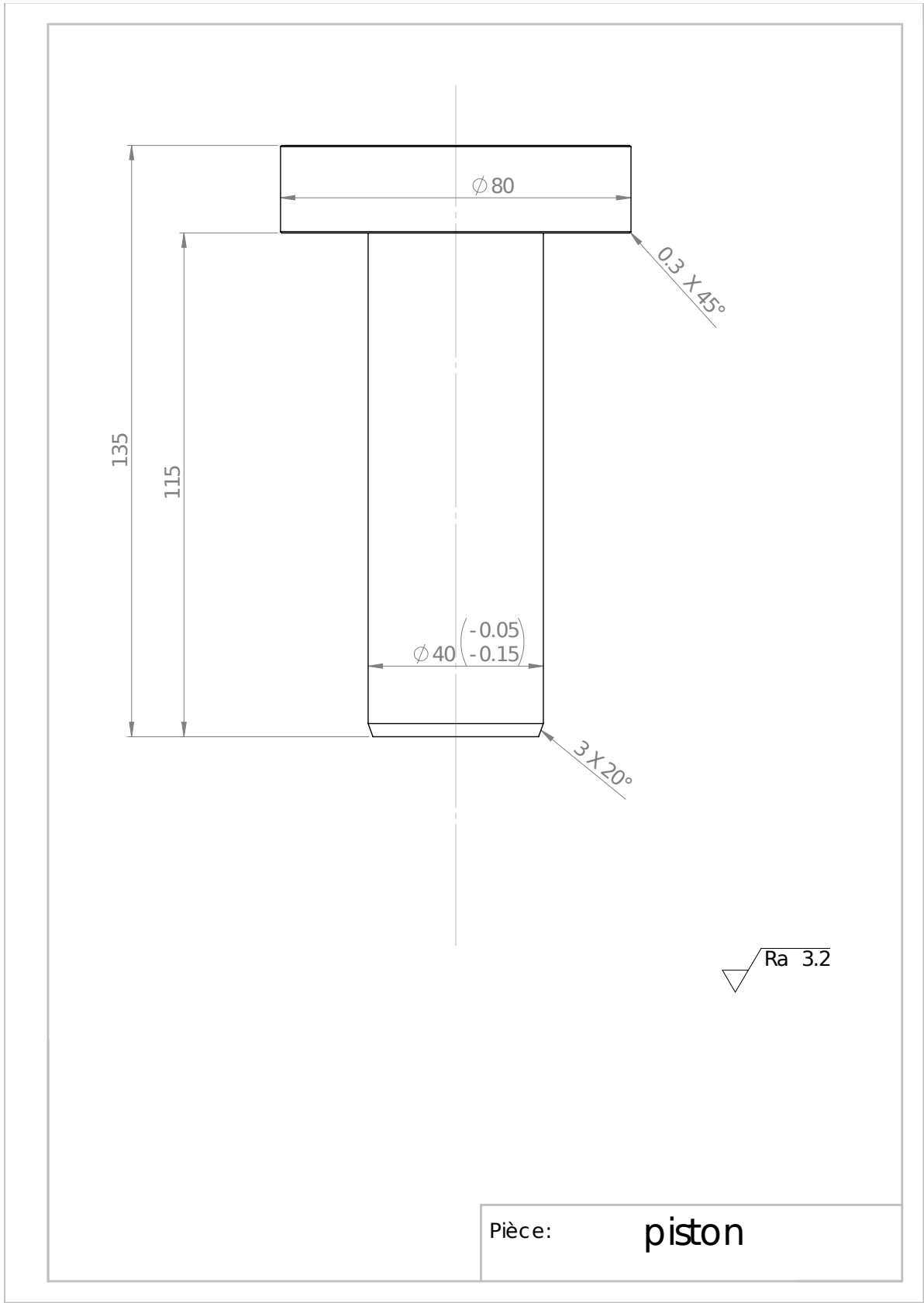


Figure A.5

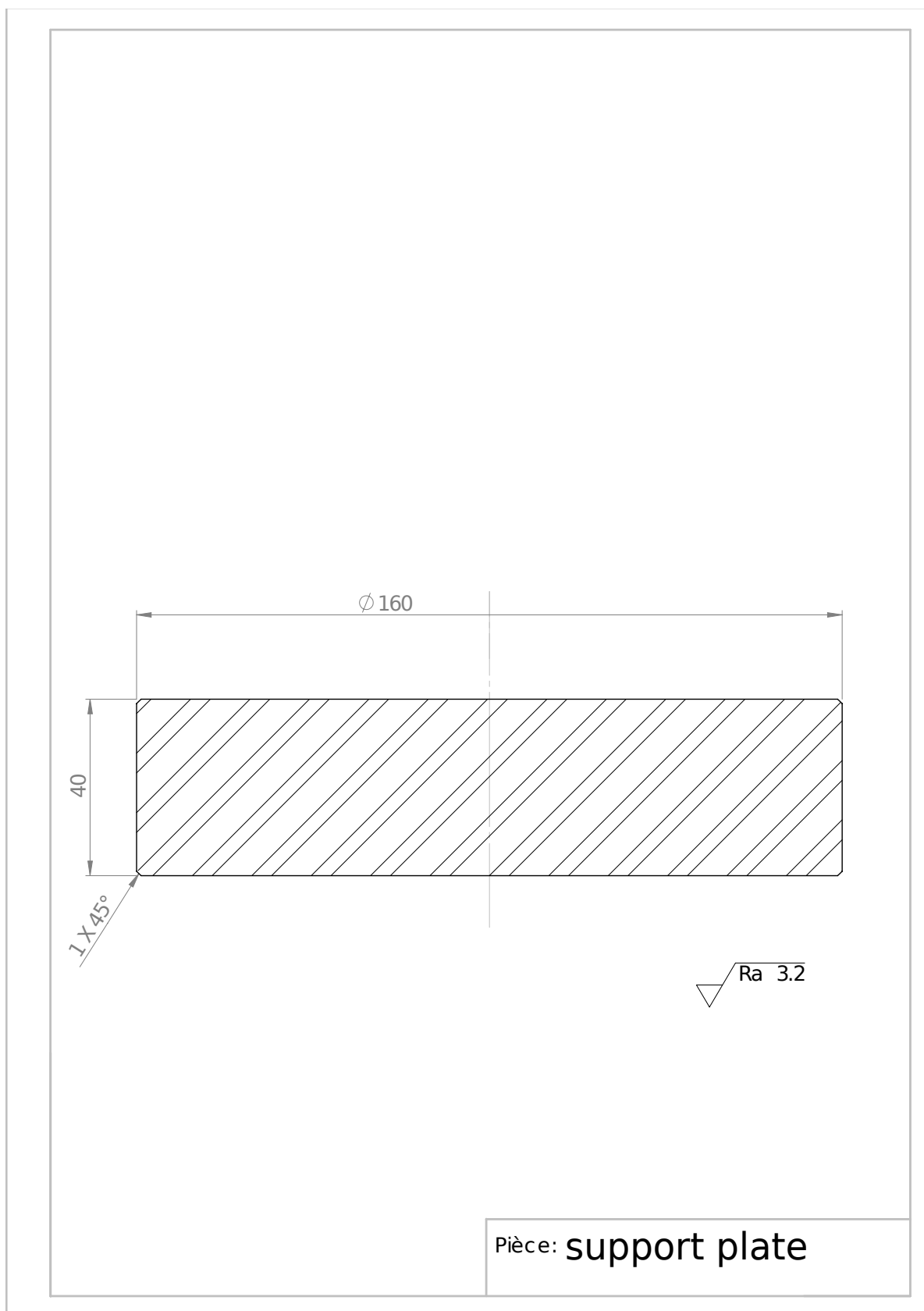


Figure A.6

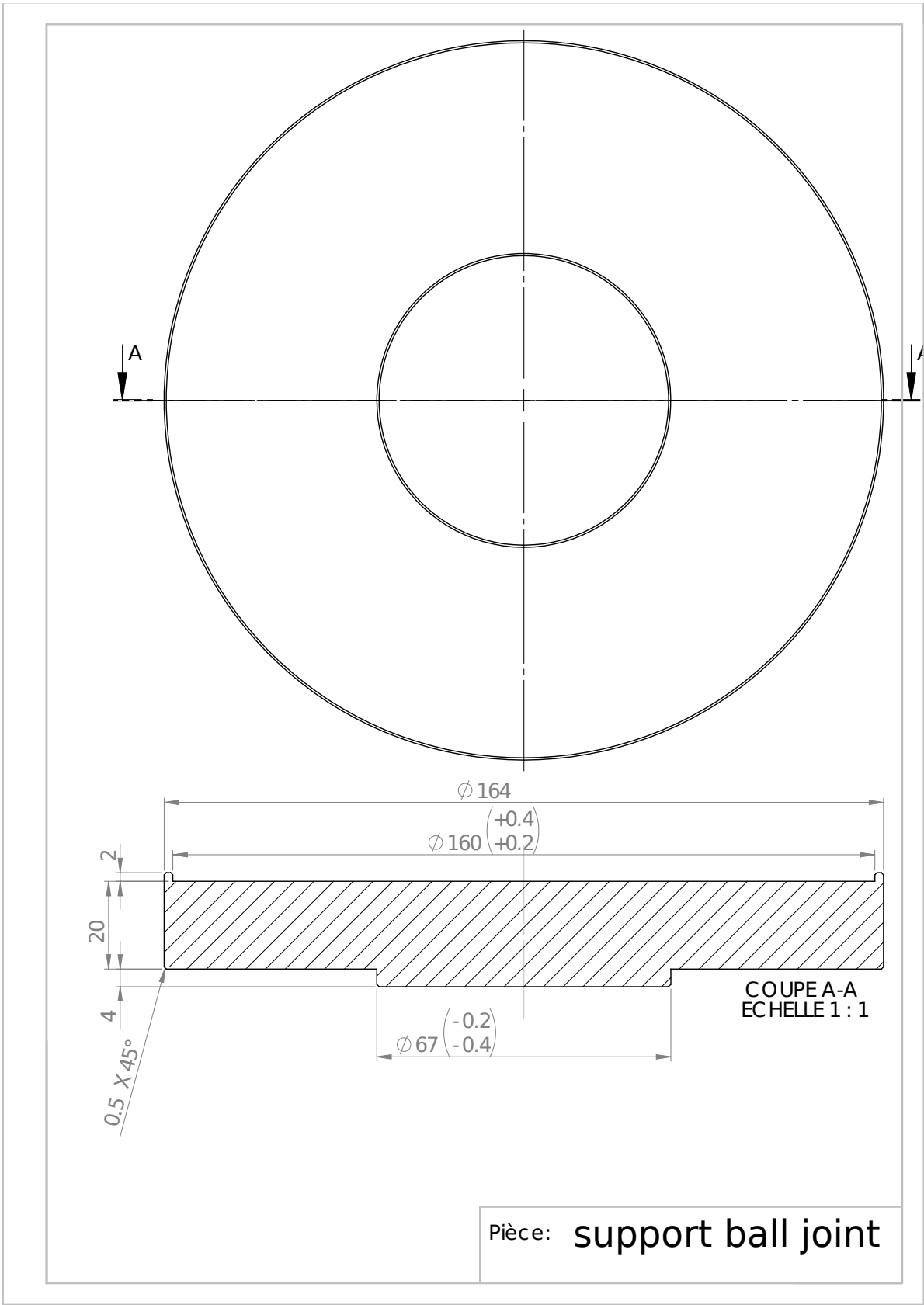


Figure A.7

B Finite Differences scheme for visco-elastic materials

In this section we show a Finite Differences scheme adapted for generalised Maxwell materials. The scheme is based on the general framework proposed by Zienkiewicz and co-workers [87, 88, 89]. We show that the schemes proposed independently by Guidoum [85], Park [148], Zocher [86] or Tran [141, 149] are specific cases of this formulation.

We consider a generalized Maxwell model composed by one spring (\mathbb{C}_0) and m Maxwell chains ($\mathbb{C}_i, \mathbb{E}_i$) placed in parallel. α_i is the internal strain of the dashpot of the i^{th} Maxwell branch. The material law is given by:

$$\sigma(t) = \mathbb{C}_0 : \varepsilon(t) + \sum_{i=1}^m \mathbb{C}_i : [\varepsilon(t) - \alpha_i(t)] \quad (\text{B.1})$$

$$0 = \mathbb{C}_i : [\alpha_i(t) - \varepsilon(t)] + \mathbb{E}_i : \dot{\alpha}_i(t), \forall i \quad (\text{B.2})$$

The time is decomposed in a series of instants (t_n). The value of the internal strains and strain rates at instant (t_{n+1}) are predicted from their previous values using the interval between two instants Δt_{n+1} and a scalar parameter θ_i arbitrarily taken between 0 and 1:

$$\alpha_i(t_{n+1}) = \alpha_i(t_n) + (1 - \theta_i) \Delta t_{n+1} \dot{\alpha}_i(t_n) + \theta_i \Delta t_{n+1} \dot{\alpha}_i(t_{n+1}), \forall i \quad (\text{B.3})$$

Insertion of (B.3) in (B.2) at t_{n+1} gives a relation which depends only on the internal strain rate at the previous instant and not its current value. All relations (B.2) can be then inserted in (B.1), which then gives the current stress and strain as a function of the inelastic strain and

Appendix B. Finite Differences scheme for visco-elastic materials

strain rates at the previous time step.

$$\sigma(t_{n+1}) = \left[\mathbb{C}_0 + \sum_{i=1}^m \mathbb{C}_i^{\text{eq}}(t_{n+1}) \right] : \varepsilon(t_{n+1}) - \sum_{i=1}^m \mathbb{C}_i^{\text{eq}}(t_{n+1}) : \alpha_i^{\text{eq}}(t_n) \quad (\text{B.4})$$

Where

$$\mathbb{C}_i^{\text{eq}}(t_{n+1}) = [\mathbb{C}_i : \mathbb{E}_i] \left[\frac{1}{\theta_i \Delta t_{n+1}} \mathbb{C}_i + \mathbb{E}_i \right]^{-1} \quad (\text{B.5})$$

$$\alpha_i^{\text{eq}}(t_{n+1}) = \alpha_i(t_n) + (1 - \theta_i) \Delta t_{n+1} \dot{\alpha}_i(t_n) \quad (\text{B.6})$$

Relation (B.4) can then be inserted in a FE software to obtain the spatial distribution of strains at instant t_{n+1} . Application of (B.2-B.3) after the FE procedure gives the distribution of internal strains and strain rates at instant t_{n+1} , which are then used for the next iteration.

This method has well-defined convergence and stability properties which depend solely on the choice of θ and Δt [90, 88]. Notably, if $1/2 \leq \theta \leq 1$, then the scheme is stable in time for any value of Δt , and the exact value of θ has little influence over the final results (see Figure B.1).

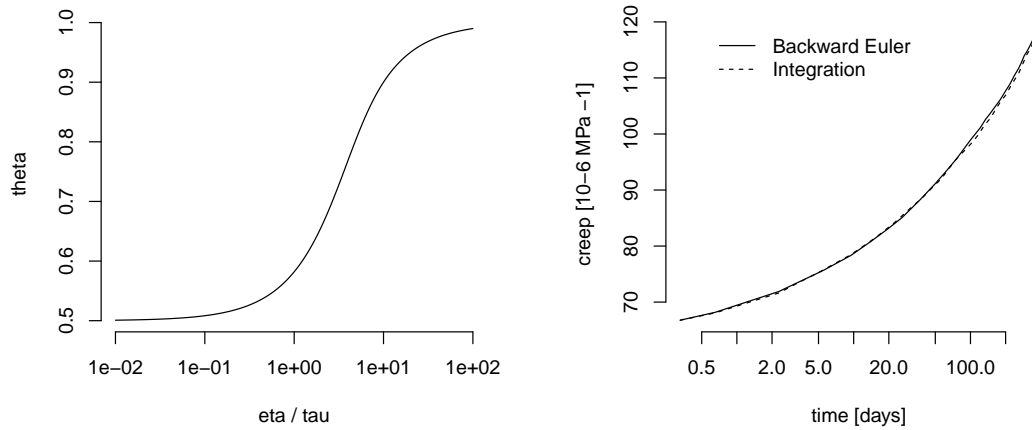


Figure B.1: Values of $\theta_i(\Delta t_{n+1})$ as a function of the ratio $\tau_i / \Delta t_{n+1}$ (left), and comparison between numerical creep curves obtained for elastic aggregates embedded in a generalized Maxwell cement paste for $\theta_i = 1$ (backward Euler) and $\theta_i(\Delta t_{n+1})$ obtained from integration as found in [85].

Furthermore, if $\mathbb{E}_i = \tau_i \mathbb{C}_i$, $\forall i$, and if the strain rate is constant between t_n and t_{n+1} , then (B.2) can be analytically integrated as it is the case in the work of Guidoum or Tran, among others. Doing so gives the following value of $\theta_i(t_{n+1})$:

$$\theta_i(t_{n+1}) = \frac{1}{1 - e^{-\Delta t_{n+1}/\tau_i}} - \frac{\tau_i}{\Delta t_{n+1}} \quad (\text{B.7})$$

As both Δt_{n+1} and τ_i are always positive, $\theta_i(t_{n+1})$ is always stricly higher than 1/2 (see Figure B.1), which ensures the stability and convergence of the scheme independently of the time step size.

The FE form of the constitutive law (B.4) follows the traditionnal FE formulation for linear elastic materials, and is implemented in most commercial FE softwares such as ABAQUS [150].

Similar schemes for the generalised Kelvin-Voigt model can be found in the work of Zienkiewicz [83], Chazal [151], or Šmilauer [152].

ALAIN GIORLA

✉ ECOLE POLYTECHNIQUE FÉDÉRALE DE LAUSANNE
LABORATOIRE DES MATÉRIAUX DE CONSTRUCTION
STI-IMX-LMC-MXG 241
STATION 12
1015 Lausanne, VD – Suisse
alain.giorla@epfl.ch
☎ +41 21 69 34 382

PROFESSIONNAL EXPERIENCE

Ph.D. in Civil Engineering – EPFL, 2009 – present. *Experimental and numerical study of Alkali-Silica-Reaction under multi-axial load.* Under the supervision of Prof. K.L. Scrivener and Dr. C.F. Dunant.

Research: Design of an experimental set-up for the study of the expansion induced by alkali-silica reaction (ASR) under multi-axial load. Development of a space-time finite element method for the modelling of coupled continuum damage and visco-elasticity in ASR-affected concrete. Development of image analysis tools for the microscopy of cement and concrete (porosimetry, ASR, sulfate attack, hydration degree of slags).

Teaching: Organisation of seminars on ASR for managers of dams in Switzerland; supervision of exercise sessions and laboratory courses for undergraduate students *construction materials* and *numerical analysis*

Master Internship – EDF R&D / IFMB Karlsruhe – 2009: *Modelling autogenous shrinkage of cement and concrete.* Under the supervision of Y. Le Pape and I. Burkart. **Research:** Multiscale modelling of autogenous shrinkage with analytical homogenisation. Proof of the need to include creep and relaxation for the modelling of early age properties of cement-based materials.

Internship – EDF R&D – 2008 : *Modélisation de l'hydratation du ciment avec le logiciel Vi(CA)2T.* Under the supervision of Y. Le Pape.

Research: Modelling hydration of cement paste using an adaptative time-stepping integration scheme.

Worker Internship – Snecma – 2007.

EDUCATION

Master in Engineering – Ecole Centrale Nantes, 2006–2009. *Computer Sciences – Research & Development.*

Research: Modelling coupling between diffusion and damage induced by external sulfate attack in concrete. Development of a visualisation tool for a geographical database system.

Preparatory Courses for Engineering Schools Physics-Chemistry – 2004–2006.
Lycée Janson-de-Sailly.

Baccalauréat – Scientific Series, 2004.

SKILLS

Experimental Methods: ASR expansion test, mechanical tests (creep, modulus, strength), fibre-optic sensing, electronix microscopy

Programming and Modelling: C/C++, Java, Scilab/Matlab/Octave, R, \LaTeX , SolidWorks, Linux, Office, finite elements, finite differences, micro-mechanical homogenisation, image analysis.

Languages : Fluent in French and English (both written and oral). Knowledge of German (both written and oral).

OTHER EXPERIENCE

Interests: music (played the violin in student orchestra), reading, writing.

Driving Licence B.

PUBLICATIONS

Peer-Reviewed Journal Papers

Y. Le Pape, C. Toulemonde, J. Sanahuja, **A. B. Giorla**. Upscaling concrete properties: a rational approach to account for the material complexity and variability. *International Journal of Materials and Structural Integrity*, 2009.

C. F. Dunant, B. Bary, **A. B. Giorla**, C. Péniguel, J. Sanahuja, C. Toulemonde, A.-B. Tran, F. Willot, J. Yvonnet. A critical comparison of several numerical methods for computing effective properties of highly heterogeneous materials. *Advances in Engineering Software*, 2013.

A. B. Giorla, K. L. Scrivener, C. F. Dunant. Finite elements in space and time for the analysis of generalized visco-elastic materials. *International Journal for Numerical Methods in Engineering*, submitted.

Peer-Reviewed Conference Papers With Talks

A. B. Giorla, C. F. Dunant, A. Guidoum, K. L. Scrivener. Experimental and numerical study of alkali-silica reaction under load. *ICAAR*, 2012.

A. B. Giorla, K. L. Scrivener, C. F. Dunant. Modeling the visco-elasticity of concrete with the space-time finite element method. *W(h)yDoc*, 2012.